NASA TECHNICAL NOTE

EFFECT OF NONLIFTING EMPENNAGE SURFACES ON SINGLE-ENGINE AFTERBODY/NOZZLE DRAG AT MACH NUMBERS FROM 0.5 TO 2.2

Bobby L. Berrier

Langley Research Center
Hampton, Va. 23665

ERRATA

NASA Technical Note D-8326

EFFECT OF NONLIFTING EMPENNAGE SURFACES ON
SINGLE-ENGINE AFTERBODY/NOZZLE DRAG AT
MACH NUMBERS FROM 0.5 TO 2.2

Bobby L. Berrier
February 1977

The data reduction constants used to compute aft-end drag data on two
equivalent-body configurations are in error. Replace pages 16, 51, 52, 53,
54, 164, and 165 with the attached corrected pages.

Issued January 1978

ERRATA

NASA Technical Note D-8326

EFFECT OF NONLIFTING EMPENNAGE SURFACES ON SINGLE-ENGINE AFTERBODY/NOZZLE DRAG AT MACH NUMBERS FROM 0.5 TO 2.2

Bobby L. Berrier
February 1977

The attached pages (pp. 25, 26, 166, 167, 168, 169, 170) should be substituted for the corresponding pages in this report.

Issued April 1977

0134027

1. Report No. NASA TN D-8326	2. Government Accession No.	3. Recipient's Catalog No.
4. Title and Subtitle EFFECT OF NONLIFTING EMPENNAGE SURFACES ON SINGLE-ENGINE AFTERBODY/NOZZLE DRAG AT MACH NUMBERS FROM 0.5 TO 2.2		5. Report Date February 1977
		6. Performing Organization Code
7. Author(s) Bobby L. Berrier		8. Performing Organization Report No. L-11014
		10. Work Unit No. 505-04-11-01
9. Performing Organization Name and Address NASA Langley Research Center Hampton, VA 23665		11. Contract or Grant No.
		13. Type of Report and Period Covered Technical Note
12. Sponsoring Agency Name and Address National Aeronautics and Space Administration Washington, DC 20546		14. Sponsoring Agency Code

15. Supplementary Notes

16. Abstract

An investigation has been conducted to determine the effect of empennage interference on the drag characteristics of a model with a single-engine-fighter aft end with convergent-divergent nozzles. Two nozzle power settings, dry and maximum afterburning, were investigated. A high-pressure air system was used to provide jet total pressure ratios up to 20.0. In an attempt to quantify and reduce adverse empennage interference and decrease aft-end drag, several empennage arrangements (variable tail surface location), "contour" bump configurations, and locally contoured afterbodies were investigated.

The results of the investigation indicate that empennage interference effects can be significant at transonic and supersonic speeds. The most effective means of reducing adverse empennage interference was the proper relocation of individual tail surfaces. The aft or conventional empennage arrangement produced the highest aft-end drag at all conditions investigated.

17. Key Words (Suggested by Author(s)) Interference Nozzle Afterbody Tails	18. Distribution Statement Unclassified - Unlimited Subject Category 02

19. Security Classif. (of this report) Unclassified	20. Security Classif. (of this page) Unclassified	21. No. of Pages 181	22. Price* $7.00

EFFECT OF NONLIFTING EMPENNAGE SURFACES ON

SINGLE-ENGINE AFTERBODY/NOZZLE DRAG AT

MACH NUMBERS FROM 0.5 TO 2.2

Bobby L. Berrier
Langley Research Center

SUMMARY

An investigation has been conducted to determine the effect of empennage interference on the drag characteristics of a model with a single-engine-fighter aft end with convergent-divergent nozzles. Two nozzle power settings, dry and maximum afterburning, were investigated. A high-pressure air system was used to provide jet total pressure ratios up to 20.0. In an attempt to quantify and reduce adverse empennage interference and decrease aft-end drag, several empennage arrangements (variable tail surface location), "contour" bump configurations, and locally contoured afterbodies were investigated.

The results of the investigation indicate that empennage interference effects can be significant at transonic and supersonic speeds. The most effective means of reducing adverse empennage interference was found to be the proper relocation of individual tail surfaces. The aft or conventional empennage arrangement produced the highest aft-end drag at all conditions investigated. At subsonic speeds, staggered empennage arrangements appear to produce the lowest adverse interference effects. At supersonic speeds, the forward empennage arrangement produced the least adverse interference effects.

INTRODUCTION

Past experimental investigations (refs. 1 to 3) on current, high-performance fighter aircraft have shown that sizable airplane performance penalties are associated with the installation of the propulsion system into the airframe. These penalties can be associated with both the inlet and nozzle installation. The afterbody/nozzle drag problem has been addressed by several large government and private industry experimental programs (refs. 4 to 12). These experimental programs have shown that afterbody/nozzle installation drag penalties, for both single-engine and multiengine configurations, can result from interference effects orginating from base areas, horizontal and vertical tails, ventral fins, tail actuator housings, and structural booms to support empennage surfaces. Additional complexity exists for multiengine configurations as a result of mutual interference effects and the additional boattail or base area between the engines. These penalties can be especially acute during the cruise portion of the airplane mission when the nozzle is in a dry power (closed down) mode. Most of the referenced experimental programs, especially those which examined empennage variables, concentrated on twin-engine ccnfigurations.

Adverse interference effects originating from empennage surfaces have been found to be a major contributor to the afterbody/nozzle drag problem (refs. 3, 4, 7, and 13). However, in past aircraft designs, the major consideration for tail location has probably been stability and control considerations rather than configuration drag. These considerations tend to force the tail location to the most aft position in order to obtain maximum tail volume for a given tail area. For conventional fighter aircraft, this generally places the empennage surfaces close to nozzle boattail surfaces.

Because of the possible large effect of empennage surfaces on afterbody/nozzle drag and the recent emphasis on small, lightweight fighters, an experimental program to determine the effects of nonlifting empennage surfaces on single-engine afterbody/nozzle drag has been conducted at Langley Research Center. Objectives of this program were to provide a parametric data base on the effects of nonlifting empennage surfaces on single-engine aft-end drag and to investigate three methods for reducing adverse empennage interference on aft-end drag. These methods were primarily used to smooth the aft-fuselage normal-area distribution which reference 6 indicates to be a desirable feature at both subsonic and supersonic speeds. Bumps in the aft-end normal-area distribution, caused by addition of empennage surfaces, were reduced either by relocating the empennage surfaces or by local afterbody contouring. Valleys in the aft-end normal-area distribution were filled by addition of "contour" bumps.

The investigation was conducted in the Langley 16-foot transonic tunnel at Mach numbers from 0.5 to 1.2 with nozzle throat areas corresponding to dry power and maximum afterburning power and in the Langley 4-foot supersonic pressure tunnel at a Mach number of 2.2 with the nozzle at maximum afterburning power (max. A/B). Jet total pressure ratio was varied from approximately 1.0 (jet off) to 7 in the transonic facility and to approximately 20 in the supersonic tunnel. All configurations were tested at 0° tail deflection.

SYMBOLS

A	cross-sectional area, meters^2
A_{an}	area of annular clearance gap at model base, meters^2
A_e	nozzle exit area, meters^2
A_{int}	internal cross-sectional area of afterbody/nozzle outer shell, meters^2
A_{ref}	reference area (cross-sectional area at metric break), 0.0273 meter^2
A_t	nozzle throat area, meters^2
C_D	drag coefficient
$C_{D,a}$	afterbody drag coefficient, $D_a/q_\infty A_{ref}$
$C_{D,n}$	nozzle drag coefficient (pressure + friction), $D_n/q_\infty A_{ref}$

2

$C_{D,pn}$	nozzle pressure drag coefficient, $D_{p,n}/q_\infty A_{ref}$
$C_{D,t}$	total aft-end drag coefficient, $D_t/q_\infty A_{ref}$
$C_{D,tails}$	tail drag coefficient, $D_{tails}/q_\infty A_{ref}$
$\Delta C_{D,ia}$	afterbody-empennage interference drag coefficient increment, $\Delta D_{i,a}/q_\infty A_{ref}$
$\Delta C_{D,in}$	nozzle-empennage interference drag coefficient increment, $\Delta D_{i,n}/q_\infty A_{ref}$
$\Delta C_{D,it}$	total aft-end—empennage interference drag coefficient increment, $\Delta D_{i,t}/q_\infty A_{ref}$
C_p	static-pressure coefficient, $(p_l - p_\infty)/q_\infty$
D_a	afterbody drag, newtons
D_{bal}	drag measured by balance, positive downstream, newtons
D_n	nozzle drag (pressure + friction), newtons
$D_{p,n}$	nozzle pressure drag, newtons
D_t	total aft-end (afterbody/nozzle/tail) drag, newtons
D_{tails}	tail drag, newtons
$\Delta D_{i,a}$	afterbody-empennage interference-drag increment, newtons
$\Delta D_{i,n}$	nozzle-empennage interference-drag increment, newtons
$\Delta D_{i,t}$	total aft-end—empennage interference-drag increment, newtons
d_{ref}	reference diameter (diameter at metric break), meters
d_{th}	nozzle throat diameter, meters
l	length of model with dry power nozzle installed, meters
M	free-stream Mach number
M_{av}	average free-stream Mach number
p_{an}	local pressure at nozzle annular clearance gap, newtons/meter^2
p_{int}	internal static pressure, newtons/meter^2
p_l	local static pressure, newtons/meter^2
$p_{t,j}$	jet total pressure, newtons/meter^2

$(p_{t,j}/p_\infty)_{av}$ average jet total pressure ratio

p_∞ free-stream static pressure, newtons/meter^2

q_∞ free-stream dynamic pressure, newtons/meter^2

r radius, meters

r_h distance from model center line to horizontal tail "contour" bump external surface, meters

r_{ref} reference radius (radius at metric break), meters

r_v distance from model center line to vertical tail "contour" bump external surface, meters

S_w wing reference area for typical fighter, meters^2

t/c empennage surface thickness ratio (ratio of local maximum thickness to local chord)

x axial distance from model nose, positive downstream, meters

x_h axial distance from start of horizontal tail "contour" bump, meters

x_v axial distance from start of vertical tail "contour" bump, meters

y_h half-width of horizontal tail "contour" bump, meters

y_v half-width of vertical tail "contour" bump, meters

Λ_{le} sweep angle at leading edge, degrees

ϕ meridian angle about model axis, degrees (positive for clockwise direction when facing upstream; $\phi = 0^o$ at top of model)

Abbreviations:

L.E.   leading edge

max. A/B   maximum afterburning

sta.   station

APPARATUS AND METHODS

Wind Tunnels

The experimental investigation was conducted in the Langley 16-foot transonic tunnel and in the Langley 4-foot supersonic pressure tunnel. The Langley 16-foot transonic tunnel is a single-return, atmospheric tunnel with a slotted,

4

octagonal test section and continuous air exchange. The tunnel has a continuously variable speed range from M = 0.20 to M = 1.30. The Langley 4-foot supersonic pressure tunnel is a single-return continuous-flow wind tunnel with a stagnation-pressure range from 27.58 kN/m² to 206.84 kN/m² and a stagnation-temperature range from 310.9 K to 322.2 K. By mechanically deflecting the tunnel floor and ceiling between fixed sidewalls to form a divergent nozzle, the Mach number can be varied from 1.25 to 2.20.

Model and Support System

A sketch of the sting-strut-supported single-engine model with the dry-power nozzle installed is presented in figure 1, and photographs of the model installed in the Langley 16-foot transonic tunnel are shown in figure 2. The overall model arrangement represents a typical single-engine-fighter aft end and is composed of four major parts, located as follows:

	Model station, cm	x/ι
Forebody	0 to 89.38	0 to 0.533
Afterbody	89.38 to 150.34	0.533 to 0.897
Nozzle:		
Dry power	150.34 to 167.64	0.897 to 1.000
Max. A/B	150.34 to 164.88	0.897 to 0.984
Empennage surfaces	Variable	Variable

The term aft end, as used in this paper, is the metric portion of the model (that portion of the model on which forces and moments are measured) beginning at the metric break or seal station (sta. 89.38 cm) and includes the afterbody, nozzle, and empennage surfaces when present. The axisymmetric forebody was non-metric. As shown in figure 1, a 0.15-cm gap in the external skin at the metric-break station prevented fouling between the nonmetric forebody and metric aft end. A Teflon strip inserted into grooves machined into the nonmetric forebody and the metric aft end was used as a seal to prevent internal flow in the model. The metric aft end was attached to a six-component strain-gage balance which was grounded to the nonmetric internal air system (high-pressure air plenum, tail-pipe, and inner nozzle). A nominal 0.16-cm annular clearance gap between the external and inner nozzle parts was required to prevent fouling between the metric aft end and the nonmetric internal air system.

The center line of the model was located on the wind-tunnel center line. The center line of the sting, which supports the strut in the 16-foot transonic tunnel (see fig. 2), was 55.88 cm below the wind-tunnel center line. The sting portion of the support system was 5.08 cm by 10.16 cm in cross section, with the top and bottom capped by half-cylinders of 2.54-cm radius. The strut was 5 percent thick with a 50.8-cm chord (see fig. 1) in the streamwise direction. The strut leading and trailing edges were swept 45°. In the 4-foot supersonic tunnel, only the strut support was used and the model was mounted from the tunnel sidewall.

The single-engine model used for this investigation utilized the single-engine simulator air system described in reference 14. An external high-pressure air supply provides the model with a continuous flow of clean, dry air at a controlled temperature of about 306 K, which is used to simulate exhaust flow over a range of jet total pressure.

Normal-cross-sectional-area distributions for each configuration investigated are presented in figure 3. In addition to the regular configurations with empennage surfaces, two tailless equivalent bodies (bodies of revolution) representing two different tail-on configurations were investigated. One equivalent body (staggered-tail equivalent body) had a normal-area distribution identical to the basic afterbody with the dry power nozzle, the forward vertical tail, and the aft horizontal tail (see fig. 3(d)); the other equivalent body (aft-tail equivalent body) had a normal-area distribution identical to the basic afterbody with the dry power nozzle, the aft vertical tail, and the aft horizontal tail (see fig. 3(e)).

Figure 4 presents a sketch and geometry details of the basic axisymmetric afterbody (sta. 89.38 cm to 150.34 cm). The afterbody had provisions for mounting a vertical tail at two different axial locations (forward and aft), a mid (model center line) horizontal tail at two different axial locations (forward and aft), and a low horizontal tail at a single axial location (forward). Sketches showing geometric details of the empennage surfaces are presented in figure 5. The vertical and horizontal tails were sized with the afterbody and nozzle areas to be representative of a typical single-engine-fighter configuration.

Nozzle geometry simulated a variable-geometry, balanced-beam, convergent-divergent nozzle typical of those currently in use on modern fighter aircraft. The external nozzle shell attached directly to the afterbody at station 150.34 cm. Two nozzle power settings, one representing dry operation and one representing afterburning operation, were investigated. Sketches showing external and internal nozzle geometry are presented in figure 6.

In addition to the basic axisymmetric afterbody (see fig. 4), two afterbodies with varying amounts of local contouring were also investigated to examine the effect of aft-end normal-area distribution. For these afterbodies, the vertical and horizontal tails were fixed in the forward and aft locations, respectively (staggered empennage arrangement). Sketches showing geometric details of these afterbodies are presented in figure 7. These afterbodies were locally contoured in the region of the empennage surfaces by removing afterbody volume to compensate for normal-area-distribution lumps created by addition of empennage surfaces. (See figs. 3(f) and 3(g).) A minimum afterbody radius equal to the nozzle maximum radius (7.62 cm) was used as a design constraint for these afterbodies. This constraint resulted in a normal-area-distribution bump in the x/l range from 0.825 to 0.95 for these configurations. The partially contoured afterbody was designed to account for only a portion of the empennage-surface volume. The fully contoured afterbody was designed, within the above constraint, to account for the total empennage volume. For these afterbodies, tail span was held constant by addition of root fillers such that empennage wetted area increased slightly with increased amounts of contouring.

6

The effect of normal-area distribution was also investigated by adding "contour" bumps around the empennage surfaces on three different aft-end configurations. Figure 8 presents sketches of the contour bumps showing their location and important dimensions. These bumps were designed to eliminate defects in the aft-end normal-area distribution. (See figs. 3(d), 3(e), and 3(g).) The partial contour bumps (see fig. 8(a)) were designed to only partially fill aft-end normal-area-distribution defects, whereas the full contour bumps completely filled the normal-area-distribution defects. Since the contour bumps were added around the base of the empennage surfaces, empennage wetted area varied slightly for each aft-end configuration with contour bumps.

Instrumentation

External static-pressure orifices were located on the afterbodies at the locations indicated in figures 4 and 7. External static-pressure orifice locations on the nozzles are shown in figure 6. Two separate dry power nozzles with identical external and internal geometries were investigated. The baseline nozzle had 20 external static-pressure orifices and was installed for all force and moment tests; the alternate pressure nozzle had 56 external static-pressure orifices and was installed for pressure tests only. Internal pressures were measured in the afterbody cavity at six internal orifice locations. Four total pressures and the stagnation temperature of the jet flow were measured in each nozzle at locations indicated in figure 6.

Forces and moments on the external shell of the metric aft end (afterbody, nozzle, and tails) were measured with a six-component strain-gage balance. Forces on the internal flow system (thrust) were not measured. An electronic turbine flow meter was used to obtain the air mass-flow rate to the nozzle.

Tests

Data were obtained in the Langley 16-foot transonic tunnel at Mach numbers from 0.50 to 1.30 and in the Langley 4-foot supersonic pressure tunnel at a Mach number of 2.20 at a stagnation pressure of 124 kN/m^2 and at a stagnation temperature of 317 K. Angle of attack and tail deflection angle were held constant at 0° during the entire investigation. Reynolds number based on model length varied from approximately 1.53×10^7 at M = 0.50 to 2.08×10^7 at M = 1.30 in the Langley 16-foot transonic tunnel and was 2.11×10^7 at M = 2.20 in the Langley 4-foot supersonic pressure tunnel. The ratio of jet total pressure to free-stream static pressure was varied from approximately 1.0 (jet off) to about 20.0, depending on Mach number. To insure a turbulent boundary layer over the afterbody, a 0.38-cm-wide transition strip of No. 100 carborundum grit was fixed 5.72 cm from the model nose. Transition strips 0.13 cm wide of No. 90 carborundum grit were fixed 2.08 cm and 1.61 cm from the leading edges of the vertical and horizontal tails, respectively.

In addition to the normal (force and moment measurements with limited external pressure instrumentation) tunnel run made for each configuration investigated, two additional tunnel runs were made on several of the dry power nozzle configurations. For these configurations, a pressure run and a flow-

visualization run were made with the alternate dry power pressure nozzle
installed. The pressure run (no balance data) was required for the alternate
dry power pressure nozzle because of the added restraint created by additional
pressure tubing for 56 pressure orifices. (See fig. 6(a).) Surface-flow-
visualization runs were accomplished by pumping water tinted with ink through
orifices equally spaced in a circumferential tube buried in the afterbody at
station 93.98 cm (see fig. 4) and by adding tufts to the empennage surfaces.
Because of tuft drag, restraint of the ink flow tube, and the possibility of
orifice blockage, no data were obtained during these runs except for photo-
graphs, tunnel parameters, and internal exhaust flow parameters.

Data Reduction

All data for both the model and the wind-tunnel facilities were recorded
simultaneously on magnetic tape. Approximately 10 frames of data, taken at a
rate of 1 frame per second, were used for each data point; average values were
used in computations. The recorded data were used to compute standard force and
pressure coefficients. All force coefficients in this report are referenced to
the forebody maximum cross-sectional area (cross-sectional area at metric-break
station).

Aft-end drag was obtained directly from the six-component balance and com-
puted from the equation

$$D_t = D_{bal} - \sum_{k=1}^{4} (p_{int,k} - p_\infty)A_{int,k} - \sum_{k=1}^{2} (p_{an,k} - p_\infty)A_{an,k} \qquad (1)$$

Included in the balance term D_{bal} are external and internal axial forces on
the afterbody/nozzle external shell (including nozzle base drag, jet effects on
external drag, and tail drag when tails are installed). Included in the aft-end
drag D_t but not felt by the balance term D_{bal} is a pressure-area term to
account for the annulus between the nozzle internal and external pieces. (See
fig. 6.)

Nozzle drag D_n was obtained for each configuration by adding nozzle pres-
sure drag to a computed value of nozzle skin-friction drag. Nozzle pressure
drag was obtained by a pressure-area integration using measured nozzle static
pressures over the external nozzle boattail surface (sta. 150.34 cm to end of
model). Nozzle skin-friction drag was computed by using the Sommer and Short
reference temperature method as outlined in reference 15.

Tail drag D_{tails} was computed for each tail-on configuration. Tail drag
was composed of friction drag plus form drag at subsonic speeds ($M < 0.89$) and
friction drag plus wave drag at supersonic speeds ($M > 1.00$). For M greater
than 0.89 and less than 1.00, a smooth fairing between the subsonic and super-
sonic values was used to obtain tail drag. Friction drag and wave drag were
computed from methods outlined in references 15 and 16, respectively. Subsonic
form factors for the tails were obtained from empirical data correlations of
unpublished NASA data and may be obtained from the equation

8

$$\text{Form factor} = 1 + 1.44(t/c) + 2(t/c)^2 \tag{2}$$

Afterbody drag D_a was obtained for each configuration from the equation

$$D_a = D_t - D_n - D_{tails} \tag{3}$$

One of the primary objectives of this investigation was to determine empennage interference. Empennage interference-drag increments on the total aft end were obtained from the equation

$$\Delta D_{i,t} = (D_t)_{tails\ on} - (D_t)_{tails\ off} - D_{tails} \tag{4}$$

where $(D_t)_{tails\ on}$ is the experimentally measured value of tails-on aft-end drag (afterbody/nozzle/tails), $(D_t)_{tails\ off}$ is the experimentally measured value of tails-off aft-end drag (afterbody/nozzle) for the same configuration, and D_{tails} is the computed value of tail drag. Positive values of $\Delta D_{i,t}$ indicate adverse interference effects of empennage surfaces on aft-end drag. It can be noted from equation (4) that absolute values of aft-end—empennage interference-drag increments can be obtained only for those configurations which were tested with empennage surfaces off and on. Empennage interference-drag increments on the nozzle alone were obtained from the equation

$$\Delta D_{i,n} = (D_n)_{tails\ on} - (D_n)_{tails\ off} \tag{5}$$

Empennage interference-drag increments on the afterbody alone were then computed from the equation

$$\Delta D_{i,a} = \Delta D_{i,t} - \Delta D_{i,n} \tag{6}$$

It should be noted that any interference effects on the tails themselves (assumed to be negligible) are included in the afterbody interference-drag term $\Delta D_{i,a}$.

DISCUSSION

Basic Data

Figure 9 presents the basic drag data as a function of jet total pressure ratio for all configurations at all Mach numbers investigated. An index of the configurations presented in figure 9 is given as table I. For tail-off configurations (e.g., see fig. 9(a)), total aft-end and nozzle pressure drag coefficients are shown; for tail-on configurations (e.g., see fig. 9(f)), the computed value of tail drag coefficient is also given. Since tail friction, form, and wave drags are not a function of jet total pressure ratio, tail drag remains constant with varying $p_{t,j}/p_\infty$.

Both aft-end drag and nozzle pressure drag exhibit typical variations with increasing jet total pressure ratio. (For example, see refs. 8 to 10.) As a result of a base-bleed effect, a significant drag reduction generally occurs with initial jet operation. As jet total pressure ratio is increased from very low values, aft-end drag and nozzle pressure drag increase as a result of the

9

aspiration caused by the pumping action of the jet exhaust. At a jet total pressure ratio generally between 2.0 and 3.0, a maximum value of jet-on drag was reached, and any further increase in jet total pressure ratio reduced drag as the compression region at the nozzle exit increased in strength with jet exhaust plume growth.

Pressure Distributions

Effect of support system.- The effect of the support system (strut) on afterbody/nozzle pressure distributions is shown in figure 10. Pressure distributions at four meridian angles on a tails-off aft end are shown for several combinations of Mach number and jet total pressure ratio. Pressure distributions on the model top ($\phi = 0^o$) are usually considered to be free of support interference. As indicated in references 17 and 18, differences between the pressure distributions directly behind the support system ($\phi = 180^o$) and the model top could indicate undesirable support interference on the metric aft end. Examination of the pressure distributions around the model used for the current investigation (see fig. 10) indicate little or no effect of the model support system on the metric aft-end measurements.

Effect of jet total pressure ratio.- The effects of jet total pressure ratio on afterbody/nozzle pressure distributions at four meridian angles and several Mach numbers are shown in figures 11 to 13. Tails-off data on the basic afterbody with the dry power nozzle are presented in figure 11, and tails-on (staggered tails with vertical tail forward) data on the basic afterbody with the dry power nozzle and the max. A/B power nozzle are presented in figures 12 and 13, respectively. Jet operation generally increased the pressure coefficients near the end of the model; several exceptions are noted at $M > 1.0$. The force data presented in figure 9 exhibit this characteristic in that the jet-on drag coefficients are generally lower than the jet-off drag coefficient. For $M < 1.0$, jet interference effects carried forward of station $x/l = 0.833$, whereas at low supersonic speeds, jet interference effects were limited to areas aft of station $x/l = 0.940$ to 0.952 for the dry-power configurations and station 0.959 for the max. A/B configuration. At $M = 2.20$, jet interference effects were much smaller and limited to areas aft of station $x/l = 0.959$.

Empennage arrangement.- Afterbody/nozzle static-pressure distributions at $\phi = 315^o$, showing the effect of empennage arrangement, are presented in figures 14 and 15 for the dry power and max. A/B power nozzles, respectively, on the basic afterbody. Data are presented for three empennage arrangements: tails off, aft tails, and staggered tails (vertical tail forward). The pressure distributions shown are characterized by low pressures on the afterbody followed by recovery on the nozzle boattail. The pressure recovery on the dry power nozzle (fig. 14) is sufficient to create a negative drag (thrust) on the nozzle at subsonic speeds. (See fig. 9.) The sharp compression indicated by the pressures on the max. A/B nozzle at $x/l = 0.925$ (fig. 15) is caused by a discontinuity in the external contour of the max. A/B power nozzle (see fig. 6(b)). This discontinuity is created when the nozzle flap rotates to change the nozzle power setting from dry to max. A/B.

The pressure distributions for both nozzle power settings indicate identical trends with varying empennage arrangement. At subsonic speeds, addition of empennage surfaces generally reduced afterbody static pressures and increased nozzle static pressures aft of station $x/\iota = 0.909$. At supersonic speeds, addition of empennage surfaces was generally adverse on all pressures measured. The favorable effect at subsonic speeds of empennage surfaces on nozzle static pressure increases as each empennage surface is moved closer to the nozzle boat-tail. This effect is more clearly seen in figure 16 which presents the pressure distribution around the nozzle circumference ($\phi = 270^{\circ}$ to 360°) at station $x/\iota = 0.935$ for the dry power nozzle. The pressure measured at $\phi = 270^{\circ}$ is directly behind the horizontal tail and the pressure measured at $\phi = 360^{\circ}$ is directly behind the vertical tail. Addition of empennage surfaces in a forward location produces a small favorable effect on all nozzle static pressures measured at this station. Moving the horizontal tail to an aft location to produce a staggered empennage arrangement results in a favorable increase in the static pressures close to the horizontal tail surface ($\phi = 270^{\circ}$ to 306°); static pressures close to the forward vertical tail ($\phi = 324^{\circ}$ to 360°) were unaffected and remain at the level for the forward empennage arrangement. Moving the vertical tail to an aft position with the horizontal tail (aft empennage arrangement) resulted in a substantial increase of the static pressures close to the vertical tail; static pressures close to the horizontal tail were also increased slightly.

Although complete afterbody pressure distributions were not obtained, the pressure distributions obtained indicate a possible large unfavorable empennage interference effect on afterbody drag but a favorable effect, at subsonic speeds, on nozzle drag.

Contour bumps.- Figures 17 and 18 present the effect of contour bumps on the pressure distributions of the basic afterbody and dry power nozzle combination ($\phi = 315^{\circ}$) with a staggered empennage arrangement (vertical tail forward) and an aft empennage arrangement, respectively. Addition of contour bumps produced mixed results on the afterbody pressures ($x/\iota = 0.833$ to 0.864). Because of the limited pressure instrumentation on the afterbody, it is impossible to establish trends about afterbody drag from the pressure data shown. Contour bumps have little or no effect on nozzle pressure distributions and hence nozzle drag may be expected to be relatively insensitive to this feature.

Afterbody contouring.- The effects of afterbody contouring on afterbody/ nozzle pressure distributions ($\phi = 315^{\circ}$) are presented in figures 19 and 20 for the dry power and max. A/B power nozzles, respectively. Afterbody contouring was investigated with the staggered empennage arrangement (vertical tail forward) only. Afterbody contouring generally produced larger variations in the static-pressure distributions than did the addition of contour bumps. Similar to the contour bump feature, afterbody contouring produced mixed results on afterbody static pressures and it is impossible to establish possible trends of afterbody drag. However, unlike the contour bump feature, afterbody contouring did affect the nozzle static-pressure distributions; afterbody contouring generally decreased nozzle static pressure and an increase in nozzle drag may be expected when the afterbody is contoured.

In order to simplify data analysis, drag data have been cross-plotted at selected jet total pressure ratios. Figure 21 presents a typical variation of turbofan-engine total pressure ratio with Mach number for a turbofan engine (maximum dry power), which was used for comparison purposes in this investigation. Although discussion for this particular schedule of $p_{t,j}/p_\infty$ as a function of M would generally be true for other schedules, the relative differences between comparisons may vary.

For the summary figures shown hereafter, cross-plotted values of total aft-end (afterbody/nozzle/tails) drag, nozzle drag, afterbody drag, and tail drag coefficients will be presented as a function of Mach number. An explanation of how these coefficients were obtained is included in the section "Data Reduction." In addition, for afterbody/nozzle configurations which were investigated with tails off, empennage interference-drag coefficient increments (see the section "Data Reduction") on the total aft end, nozzle, and afterbody are also presented. It should be noted that the curves shown in these summary figures between $M = 1.2$ and $M = 2.2$ do not represent actual data but were faired according to past experience with data in this Mach range.

Empennage arrangement.- The effects of empennage arrangement on aft-end drag characteristics are presented in figures 22 and 23 for the dry power nozzle and the max. A/B power nozzle, respectively. Total aft-end drag coefficient $C_{D,t}$ and its components $C_{D,n}$, $C_{D,a}$, and $C_{D,tails}$ are presented for several empennage arrangements as a function of Mach number (figs. 22(a), 22(b), 23(a), and 23(b)) at the scheduled values of $p_{t,j}/p_\infty$. It should be noted that these drag components include empennage interference effects when present. Also shown for both nozzle power settings (figs. 22(c) and 23(c)) are the absolute values of empennage interference-drag coefficients acting on the total aft end, nozzle, and afterbody as obtained by the procedures outlined previously in the section "Data Reduction."

For $M < 1.0$, these data indicate that the majority of aft-end drag originates on the afterbody (46 to 65 percent of $C_{D,t}$) and tails (26 to 51 percent of $C_{D,t}$), although these two components together comprise only approximately 51 percent and 64 percent of the total aft-facing projected area for the dry and max. A/B configurations, respectively; the remaining aft-facing projected area (approximately 49 percent for the dry power configuration and 36 percent for max. A/B power configuration) occurs on the nozzle boattail. Although a significant portion of the total aft-facing area consists of nozzle boattail, nozzle drag contributes very little to the total aft-end drag for $M < 1.0$ (maximum of 12 percent of $C_{D,t}$). In fact, as a result of the static-pressure recovery over the nozzle surface discussed in the section "Pressure Distributions," the nozzle reduces the total aft-end drag (up to 19 percent) by providing a negative drag (thrust) over much of the subsonic Mach number range for the dry power nozzle configurations and for a limited Mach number range for the max. A/B nozzle configurations. At supersonic speeds, the total aft-end drag $C_{D,t}$ is more nearly equally divided among the afterbody (28 to 38 percent of $C_{D,t}$), tails (36 to 51 percent of $C_{D,t}$), and nozzle (32 to 39 percent of $C_{D,t}$ for the dry power nozzle and 15 to 23 percent $C_{D,t}$ for the max. A/B power nozzle) components.

Examination of total aft-end empennage interference-drag coefficient incre-
ments $\Delta C_{D,it}$ (see figs. 22(c) and 23(c)) indicates that empennage interference
is generally small for $M < 0.85$ (5 to 8 percent of $C_{D,t}$) but comprises a sig-
nificant portion of the total aft-end drag at transonic (4 to 54 percent of
$C_{D,t}$) and supersonic (11 to 20 percent of $C_{D,t}$) speeds. Based on the wing area
($S_w/A_{ref} = 16.0$) and drag of a typical single-engine fighter, empennage inter-
ference (aft tails) could account for 8 to 39 percent of airplane drag at Mach
numbers above 0.85. Empennage interference effects on nozzle drag were gener-
ally favorable (negative values of $\Delta C_{D,in}$) at subsonic speeds but unfavorable
at supersonic speeds. The negative values of $\Delta C_{D,in}$ at subsonic speeds indi-
cate that the low and sometimes negative nozzle drag (see figs. 22(a) and 23(a))
discussed earlier results not only from excellent static-pressure recovery char-
acteristics of the basic afterbody/nozzle (see fig. 11) but also from favorable
empennage interference acting on the nozzle (see figs. 22(c) and 23(c)). These
favorable empennage interference effects on nozzle drag at subsonic speeds
increased as each empennage surface was moved aft closer to the nozzle surface.
At supersonic speeds, an opposite trend is indicated; adverse (positive $\Delta C_{D,in}$)
empennage interference decreased as each empennage surface was moved forward
away from the nozzle surface. These results are consistent with the nozzle
static-pressure distributions discussed earlier. (See figs. 14 to 16.) Adverse
empennage interference on the afterbody more than offset any favorable effects
on the nozzle such that, with one exception at low subsonic Mach numbers, empen-
nage interference always had an adverse effect on total aft-end drag (positive
values of $\Delta C_{D,it}$).

Empennage arrangement had a large effect on aft-end drag (total drag and
its components). In fact, for the configurations of this investigation, varying
the longitudinal location of individual tail surfaces was found to be the most
consistent and effective method for reducing adverse empennage interference and
thus aft-end drag, particularly in the transonic speed range ($0.90 \leq M \leq 1.20$)
where adverse empennage interference effects were found to be largest. For
$M < 1.0$, adverse empennage interference and total aft-end drag were signifi-
cantly reduced by staggering the empennage surfaces (vertical tail forward,
horizontal tail aft). Both configurations with empennage surfaces located in
the same approximate axial location (forward or aft) produced more adverse
empennage interference and higher total aft-end drag. At supersonic speeds, the
forward empennage arrangement produced the least adverse empennage interference
and the lowest aft-end drag. This result probably stems from the fact that the
forward empennage arrangement produces negligible empennage interference on the
nozzle boattail at supersonic speeds. However, examination of the max. A/B con-
figuration data (fig. 23), which would apply to most aircraft during supersonic
flight, indicates that the forward empennage arrangement was only marginally
better than the staggered empennage arrangement. It should be noted that the
aft (conventional) empennage arrangement produced the most adverse empennage
interference and highest total aft-end drag at all conditions investigated.

Method of staggering empennage surfaces.- The effect of two different meth-
ods of staggering the empennage surfaces on aft-end drag characteristics is pre-
sented in figure 24. One configuration presented has a forward vertical tail
with an aft horizontal tail (solid line); the other configuration presented has
an aft vertical tail with a forward horizontal tail (dashed line). The method
of staggering the empennage surfaces generally had only a small effect on total

aft-end drag. The aft-end drag of the configuration with the forward vertical tail and the aft horizontal tail was slightly lower than the aft-end drag of the configuration with the aft vertical tail and the forward horizontal tail for $M < 1.0$. Negligible effects were measured at low supersonic speeds and at $M = 2.2$ (see fig. 23).

Horizontal tail vertical location.- The effect on aft-end drag characteristics of changing the horizontal tail from a mid to a low position is presented in figure 25. The low horizontal tail was investigated in the forward axial location with the forward vertical tail only. For the configuration tested, horizontal tail vertical location had little or no effect on empennage interference or aft-end drag.

Contour bumps.- Addition of empennage surfaces to a smoothly contoured aft end creates nonoptimum bumps in the aft-end area distribution (see figs. 3(b), 3(c), and 3(e)). In an attempt to smooth the aft-end normal-area distribution and thereby hopefully reduce adverse empennage interference effects, contour bumps were added around the tail surfaces on several configurations (see figs. 3(d) and 3(e)). On the assumption that at subsonic speeds, tail interference originates mainly from the tail surface root area and any "fix" for adverse tail interference should account only for that portion of the tail causing the problem, a partial contour bump was also investigated which accounted for only the tail cross-sectional area near the root which was immersed in the boundary layer. Figures 26 through 28 present the effects of contour bumps on the aft-end drag characteristics. Since these configurations were not investigated with tails off, absolute values of empennage interference were not obtained. Figures 26 and 27 present contour bump data for a staggered empennage arrangement (vertical tail forward) with the dry power nozzle and the max. A/B power nozzle, respectively; figure 28 presents data for the aft empennage arrangement with the dry power nozzle.

Addition of contour bumps generally increased aft-end drag, particularly in the subsonic and cruise Mach number range where adverse empennage interference drag can have a significant impact on airplane range. It should be noted that aft-end drag $C_{D,t}$ and afterbody drag $C_{D,a}$ include drag on the contour bumps themselves which must be compensated for by reduced empennage interference in order to show a net gain. Some drag reductions attributable to the contour bumps were obtained at transonic Mach numbers ($0.90 < M < 1.2$) for the aft empennage arrangement. (See fig. 28.) Drag reductions near $M = 1.0$ were expected since the contour bumps were designed for the normal-area distribution. It is interesting to note that this "fix" reduced aft-end drag only for the configuration with the highest measured adverse empennage interference (aft empennage arrangement - see fig. 22) but was ineffective for the configuration with the lowest measured adverse empennage interference (staggered empennage arrangement - see fig. 22).

Afterbody contouring.- An alternate approach to smoothing the aft-end normal-area distribution was also investigated. Rather than adding area (contour bumps) to fill in the area distribution, the afterbody was contoured to remove lumps created by addition of empennage surfaces. (See figs. 3(f) and 3(g).) For the same reason as discussed for the contour bumps, a partially contoured afterbody was also investigated.

14

Figures 29 and 30 present the results of afterbody contouring on aft-end drag characteristics with the dry power nozzle and the max. A/B power nozzle installed, respectively. Afterbody contouring was investigated with the staggered empennage arrangement only. Since the fully contoured afterbody was investigated with the tails off (dry power nozzle only), absolute values of empennage interference were obtained for this configuration. Opposite results due to afterbody contouring were obtained at subsonic (M $\leq$ 0.90) speeds depending on nozzle power setting; afterbody contouring increased aft-end drag for the dry power configuration but reduced aft-end drag for the max. A/B power configuration. At low supersonic speeds (M = 1.2), afterbody contouring (designed for M = 1.0) reduced aft-end drag for both configurations investigated. Examination of the empennage interference-drag characteristics (see fig. 29(c)) provides insight into the reason for this drag reduction. At low supersonic Mach numbers, afterbody contouring had little effect on nozzle drag (little change in $\Delta C_{D,in}$) but produced a dramatic decrease in the empennage interference acting on the afterbody. In fact, afterbody contouring produced a beneficial empennage interference on the afterbody, as indicated by the negative values of $\Delta C_{D,ia}$. The net result on the total aft-end empennage interference $\Delta C_{D,it}$ was that afterbody contouring almost totally eliminated the adverse empennage interference produced by the staggered empennage surfaces ($\Delta C_{D,it} \approx 0.0$).

Combination contour bumps and afterbody contouring.- In order to investigate the effects of combined contour bumps and afterbody contouring, the fully contoured afterbody with the dry power nozzle and the staggered empennage arrangement was tested with a set of full contour bumps. The normal-area distribution was completely smooth with no lumps (see fig. 3(g)). A comparison of the aft-end drag characteristics of this configuration with those of the basic aft end (with and without contour bumps) and with those of the fully contoured afterbody without contour bumps is presented in figure 31. Combined use of contour bumps and afterbody contouring increased aft-end drag over the basic aft end (solid line) at all conditions tested and in fact produced the highest aft-end drag measured for the staggered empennage arrangement at 0.85 < M < 1.20.

In general, for the staggered empennage arrangement, contour bumps reduced nozzle drag and increased afterbody drag, whereas afterbody contouring increased nozzle drag and decreased afterbody drag; with one exception at M = 1.2, the net result was a drag increase on the total aft end.

Reference 6 indicates that for aircraft designed primarily for subsonic and transonic missions, two of the desirable aft-end design guidelines are a smooth area distribution and avoidance of sharp corners and steps (continuous, smooth aft-end closure rates). Results from the current investigation on contour bumps, afterbody contouring, and a combination of both indicate that the latter design guideline is more critical or important at subsonic speeds than the former guideline. Although contour bumps and afterbody contouring were used to produce a smooth area distribution, as suggested in reference 6, these modifications also produced discontinuous and sometimes steep aft-end slopes in local areas and generally increased aft-end drag in the subsonic speed range. Thus, attention to local aft-end slopes and empennage arrangement appear to be the most critical aft-end design elements at subsonic speeds. At transonic and supersonic speeds, as also suggested by reference 6, the area distribution itself also becomes critical.

15

Equivalent bodies.- In an attempt to determine whether the aft-end drag could be obtained from tests of simple bodies (no tails), two equivalent bodies were investigated at Mach numbers up to 1.20. Each equivalent body was a body of revolution with no tails and had the dry power nozzle installed. The normal-area distribution of one equivalent body was identical to the area distribution of the configuration with the basic afterbody and the aft empennage arrangement, and the other equivalent body had a normal-area distribution identical to that of the configuration with the basic afterbody and the staggered empennage arrangement (forward vertical tail). Figure 32 presents comparisons of equivalent-body aft-end drag with the aft-end drag of the tail-on configuration it represents. Also shown in figure 32 are two estimates of aft-end drag which use simple tail-off body data as a data base. One estimate is derived from the equivalent-body data (see figs. 9(c) and 9(d)). Since the equivalent-body volume includes empennage volume, the pressure drag of the empennage surfaces was assumed to be included in the equivalent-body aft-end drag values. However, the wetted area of the empennage surfaces is not included in the equivalent-body wetted area and thus tail friction drag was added. The other estimate consists of the aft-end drag of the basic configuration with tails off (see fig. 9(a)) plus tail drag computed by the method outlined in the section "Data Reduction."

Examination of figure 32 shows that neither method is adequate for estimating total aft-end (tails on) drag at Mach numbers greater than 0.90. At Mach numbers below 0.90, both methods yield reasonable configuration drag estimates with the method utilizing the equivalent body data base producing the best agreement with actual configuration drag. These results indicate that complex single engine aft-ends may be simulated with simple bodies of revolution to obtain reasonable estimates of zero-lift aft-end drag at subsonic speeds.

At transonic and supersonic speeds, actual aft-end geometry needs to be simulated to produce reasonable values of aft-end drag. The estimate utilizing the aft-end drag data of the basic configuration with tails off tends to significantly underestimate drag at transonic and supersonic speeds. The reason for this, of course, is that this method includes no estimate of empennage interference drag. Thus, the adequacy of this method depends on the amount of empennage interference drag present on the tail-on configuration (compare fig. 32(a) with fig. 32(b), for example). The method utilizing the equivalent body data base generally provides better agreement in these speed regimes but it too tends to underpredict the empennage interference drag thus producing too low aft-end drag estimates.

Flow Visualization

A combination of ink flow on the afterbody/nozzle and tufts on the empennage surfaces was used to obtain photographs of the aft-end flow characteristics. Photographs were obtained with the dry power nozzle only.

Mach number and empennage arrangement.- The effect of Mach number and empennage arrangement on jet-off aft-end flow characteristics is illustrated by the photographs shown in figure 33. The flow over the nozzle boattail appears to be attached for Mach numbers up to 0.80. Evidence of flow turning can be

16

seen by the lowest row of tufts on the aft vertical tail. Areas of flow separation on the nozzle boattail can be observed at Mach numbers of 0.90 and 0.95. The addition of empennage surfaces tended to induce flow separation at lower Mach numbers. As each empennage surface was moved aft, the region of separated flow tended to increase. At a Mach number of 0.95, a large asymmetric separated area can be observed for the staggered empennage arrangement. Also at $M = 0.95$, it appears that at least half of the nozzle boattail flow for the aft empennage arrangement is separated; this extensive separated region even extends onto the vertical tail as evidenced by the tufts.

Effect of jet total pressure ratio.- The photographs shown in figure 34 illustrate the effect of jet total pressure ratio on nozzle boattail flow. At Mach numbers for which the jet-off nozzle boattail flow was attached, jet operation tended to induce boattail flow separation. (For example, compare the photograph for $M = 0.85$ and jet off with the photograph for $M = 0.85$ and $p_{t,j}/p_\infty = 6.0$.) At Mach numbers for which the jet-off nozzle boattail flow was extensively separated (for example, $M = 0.95$), jet operation had little effect on the separated region.

Figure 35 presents nozzle static-pressure distributions for the same conditions of Mach number and jet total pressure ratio as illustrated by the photographs in figure 34. Comparison of the jet-off and jet-on pressure distributions, particularly at $M = 0.85$, indicates jet-induced separation at the last pressure orifice. Little effect of jet operation on the separated flow region at $M = 0.95$ can be identified. In general, the effects of flow separation on the nozzle static-pressure distributions were minor when compared with the large effects indicated by the flow visualization photographs.

Theoretical Comparisons

Figure 36 presents a comparison of measured aft-end drag coefficients with theoretical aft-end drag coefficients for configurations with both nozzle power settings and several empennage arrangements. Measured data are presented for jet total pressure ratios representing a jet-off condition, an on-design condition (exhaust flow fully expanded with near cylindrical plume; $p_{t,j}/p_\infty = 2.30$ for the dry power nozzle and $p_{t,j}/p_\infty = 5.75$ for the max. A/B power nozzle), and a typical engine operating jet total pressure ratio ($p_{t,j}/p_\infty = 6.00$ at $M = 1.20$). Theoretical aft-end drag values were obtained from calculations of supersonic wave drag (ref. 16) and friction drag (ref. 15). The supersonic wave drag calculations assume a slender body with a cylindrical exhaust plume. Excellent agreement between data and theory was obtained for the max. A/B power nozzle configurations, particularly for jet-on conditions. However, slender body theory was totally inadequate for the dry power nozzle configurations. This is a result of the theory's inability to handle the large closure angle (nonslender body) which terminates the dry power nozzle. Tail drag increments appear to have been satisfactorily computed for both nozzle power settings. This fact lends credibility to the technique used to obtain empennage interference in the current paper.

Comparisons of experimental afterbody/nozzle (tails off) static-pressure distributions with analytical calculations using the Neumann inviscid flow

theory (ref. 19) and an inviscid streamtube curvature method (ref. 20) are presented in figures 37 to 40. Results from the Neumann method with the boundary layer included are also presented in figure 40. Both inviscid methods overpredict the compression near the nozzle exit. This is a result of the inability to handle boundary-layer growth and separation. It was found that this deficiency rendered these theories to be almost totally inadequate for accurate nozzle pressure-drag estimates. In addition to this deficiency, it was found that both theories often overpredicted the expansion region and started pressure recovery too far downstream on the nozzle boattail.

Addition of the boundary layer to the Neumann theory (see fig. 40) resulted in a substantial improvement of the prediction of the compression level at the nozzle exit; unfortunately, it also caused an underprediction of the boattail expansion region and started pressure recovery too far upstream on the nozzle boattail.

CONCLUSIONS

An investigation has been conducted in the Langley 16-foot transonic tunnel and the Langley 4-foot supersonic pressure tunnel to determine the effects of nonlifting empennage surfaces on single-engine aft-end drag characteristics at Mach numbers up to 2.2. The jet total pressure ratio was varied from approximately 1 (jet off) to approximately 20, depending on Mach number. Three methods for minimizing adverse empennage interference effects were investigated. Results from this study indicate the following conclusions:

1. Empennage interference effects can be significant on single-engine aft-end drag at transonic and supersonic speeds.

2. Although favorable empennage interference effects were measured on nozzle drag, empennage interference was almost always adverse on total aft-end drag.

3. Relocation of individual tail surfaces was found to be the most effective method for reducing adverse empennage interference effects. For Mach numbers less than 1.0, staggered empennage arrangements appear to produce the least adverse interference effects. At supersonic speeds, the forward empennage arrangement produced the least adverse interference effects. The aft (conventional) empennage arrangement produced the highest aft-end drag at all conditions investigated.

4. In the low subsonic and cruise Mach number range, addition of "contour" bumps, designed to smooth the normal-area distribution, increased aft-end drag. Some drag reductions attributable to contour bumps were found at transonic and supersonic speeds.

5. At subsonic speeds, afterbody contouring was effective in reducing aft-end drag for the maximum afterburning power nozzle only. Results at supersonic speeds indicate that local area ruling can almost totally eliminate adverse empennage interference effects.

6. Results from this investigation indicate that attention to local aft-end details (avoidance of bumps, steep local slopes, contour discontinuities, etc.) is a more critical aft-end design criteria at subsonic speeds than producing a smooth normal-area distribution.

7. Current, existing methods for estimating aft-end drag (tails off or on) in a simple manner were found to be inadequate with one exception. This exception was the supersonic wave drag calculated by slender-body theory for the maximum afterburning power nozzle configurations; however, this theory was inadequate when attempted on dry power nozzle configurations with high closure angles.

Langley Research Center
National Aeronautics and Space Administration
Hampton, VA 23665
November 17, 1976

REFERENCES

1. Schmeer, James W.; Lauer, Rodney F., Jr.; and Berrier, Bobby L.: Performance of Blow-in-Door Ejector Nozzles Installed on a Twin-Jet Variable-Wing-Sweep Fighter Airplane Model. NASA TM X-1383, 1967.

2. Reubush, David E.; and Mercer, Charles E.: Effects of Nozzle Interfairing Modifications on Longitudinal Aerodynamic Characteristics of a Twin-Jet, Variable-Wing-Sweep Fighter Model. NASA TN D-7817, 1975.

3. Maiden, Donald L.; and Berrier, Bobby L.: Effect of Airframe Modifications on Longitudinal Aerodynamic Characteristics of a Fixed-Wing, Twin-Jet Fighter Airplane Model. NASA TM X-2523, 1972.

4. Exhaust System Interaction Program. Volumes I-XVII. D162-10467-11 (Contract No. F33615-70-C-1450), Boeing Co., Apr. 1973.

5. Program for Experimental and Analytical Determination of Integrated Airframe-Nozzle Performance - Phase II Interim Report. Volumes I-V. LR 24830 (Contract No. F33657-70-C-0511), Lockheed-California Co., Feb. 1972.

6. Glasgow, E. R.; and Santman, D. M.: Aft-End Design Criteria and Performance Prediction Methods Applicable to Air Superiority Fighters Having Twin Buried Engines and Dual Nozzles. AIAA Paper No. 72-1111, Nov.-Dec. 1972.

7. Glasgow, E. R.: Integrated Airframe-Nozzle Performance for Designing Twin-Engine Fighters. AIAA Paper No. 73-1303, Nov. 1973.

8. Mercer, Charles E.; and Berrier, Bobby L.: Effect of Afterbody Shape, Nozzle Type, and Engine Lateral Spacing on the Installed Performance of a Twin-Jet Afterbody Model. NASA TM X-1855, 1969.

9. Berrier, Bobby L.: Effect of Nozzle Lateral Spacing on Afterbody Drag and Performance of Twin-Jet Afterbody Models With Cone Plug Nozzles at Mach Numbers up to 2.20. NASA TM X-2632, 1972.

10. Lee, Edwin E., Jr.; and Runckel, Jack F.: Performance of Closely Spaced Twin-Jet Afterbodies With Different Inboard-Outboard Fairing and Nozzle Shapes. NASA TM X-2329, 1971.

11. Maiden, Donald L.; and Runckel, Jack F.: Effect of Nozzle Lateral Spacing on Afterbody Drag and Performance of Twin-Jet Afterbody Models With Convergent Nozzles at Mach Numbers up to 2.2. NASA TM X-2099, 1970.

12. Pendergraft, Odis C., Jr., and Schmeer, James W.: Effect of Nozzle Lateral Spacing on Afterbody Drag and Performance of Twin-Jet Afterbody Models With Convergent-Divergent Nozzles at Mach Numbers up to 2.2. NASA TM X-2601, 1972.

13. Swavely, C. E.; and Soileau, J. F.: Aircraft Aftbody/Propulsion System Integration for Low Drag. AIAA Paper No. 72-1101, Nov.-Dec. 1972.

14. Compton, William B., III; and Runckel, Jack F.: Jet Effects on the Boattail Axial Force of Conical Afterbodies at Subsonic and Transonic Speeds. NASA TM X-1960, 1970.

15. Peterson, John B., Jr.: A Comparison of Experimental and Theoretical Results for the Compressible Turbulent-Boundary-Layer Skin Friction With Zero Pressure Gradient. NASA TN D-1795, 1963.

16. Harris, Roy V., Jr.: An Analysis and Correlation of Aircraft Wave Drag. NASA TM X-947, 1964.

17. Reubush, David E.: Effects of Fineness and Closure Ratios on Boattail Drag of Circular-Arc Afterbody Models With Jet Exhaust at Mach Numbers up to 1.3. NASA TN D-7163, 1973.

18. Laughrey, James A.: Comparison of Testing Techniques for Isolated Axisymmetric Exhaust Nozzles in Transonic Flow. AIAA Paper No. 75-1292, Sept.-Oct. 1975.

19. Reubush, David E.; and Putnam, Lawrence E.: An Experimental and Analytical Investigation of the Effect on Isolated Boattail Drag of Varying Reynolds Number up to 130×10^6. NASA TN D-8210, 1976.

20. Ferguson, D. R.; and Keith, J. S.: Modifications to the Streamtube Curvature Program.
Volume I - Program Modifications and User's Manual. NASA CR-132705, 1975.
Volume II - Program Listing. NASA CR-132706, 1975.

TABLE I.- INDEX TO BASIC DATA

Afterbody type	Nozzle type	Horizontal tail location	Vertical tail location	Contour bumps	Figure
Basic	Dry	Off	Off	Off	9(a)
Basic	Max. A/B	Off	Off	Off	9(b)
Equivalent body	Dry	Mid, aft	Aft	Off	9(c)
Equivalent body	Dry	Mid, aft	Forward	Off	9(d)
Fully contoured	Dry	Off	Off	Off	9(e)
Basic	Dry	Mid, aft	Forward	Off	9(f)
Basic	Max. A/B	Mid, aft	Forward	Off	9(g)
Basic	Dry	Mid, aft	Aft	Off	9(h)
Basic	Max. A/B	Mid, aft	Aft	Off	9(i)
Basic	Dry	Mid, forward	Forward	Off	9(j)
Basic	Max. A/B	Mid, forward	Forward	Off	9(k)
Basic	Dry	Mid, forward	Aft	Off	9(l)
Basic	Dry	Low, forward	Forward	Off	9(m)
Basic	Dry	Mid, aft	Forward	Partial	9(n)
Basic	Dry	Mid, aft	Forward	Full	9(o)
Basic	Max. A/B	Mid, aft	Forward	Full	9(p)
Basic	Dry	Mid, aft	Aft	Full	9(q)
Fully contoured	Dry	Mid, aft	Forward	Full	9(r)
Partially contoured	Dry	Mid, aft	Forward	Off	9(s)
Fully contoured	Dry	Mid, aft	Forward	Off	9(t)
Fully contoured	Max. A/B	Mid, aft	Forward	Off	9(u)
Basic	Max. A/B	Mid, forward	Aft	Off	9(v)
Fully contoured	Max. A/B	Mid, aft	Forward	Full	9(w)
Partially contoured	Max. A/B	Mid, aft	Forward	Off	9(x)
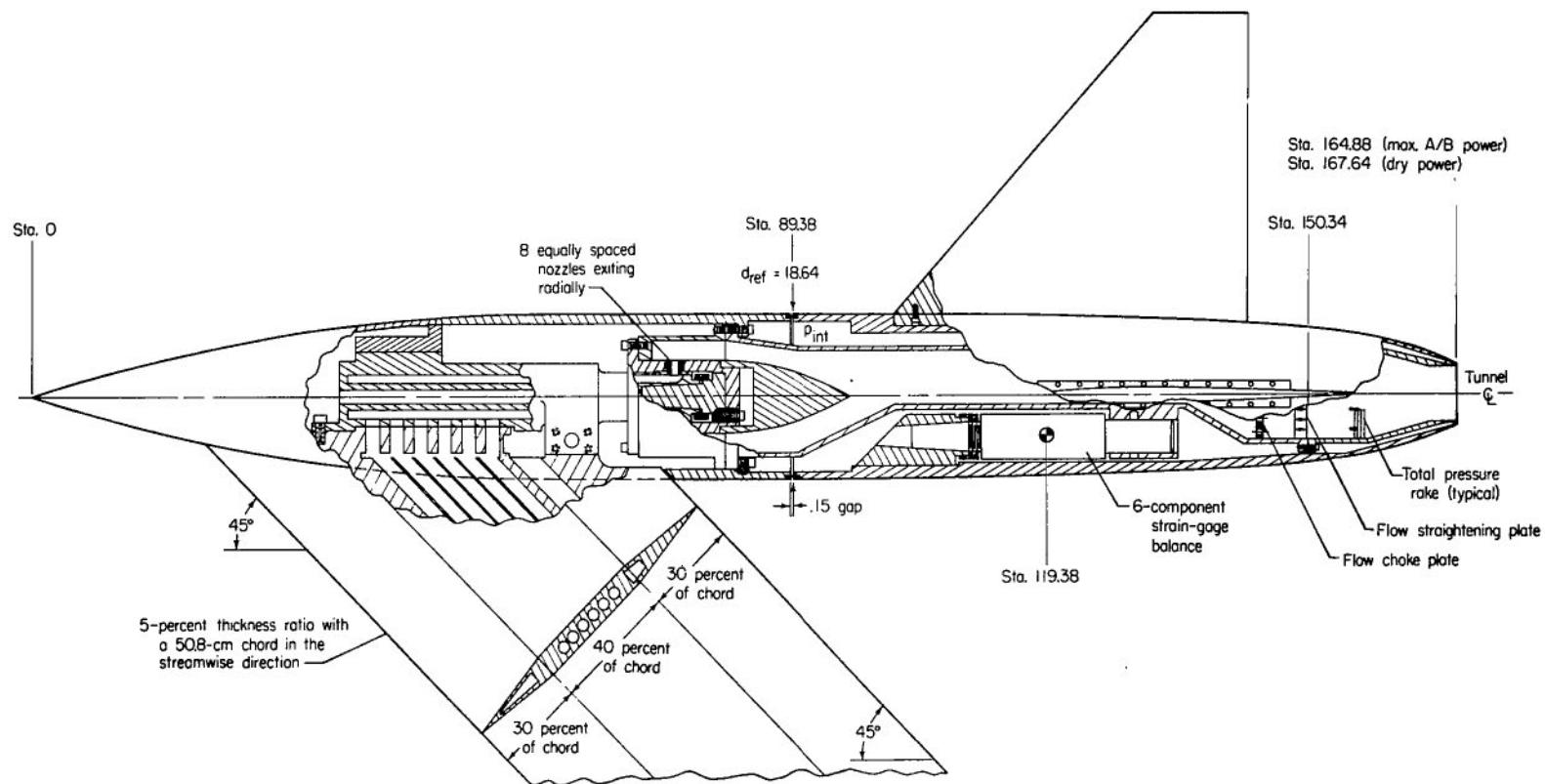
Figure 1.- Sketch of air-powered, single-engine model with dry power nozzle installed. All dimensions are in centimeters.

Sta. 164.88 (max. A/B power)
Sta. 167.64 (dry power)

Sta. 0

Sta. 89.38

Sta. 150.34

8 equally spaced nozzles exiting radially

d_{ref} = 18.64

p_{int}

Tunnel ℄

Total pressure rake (typical)

6-component strain-gage balance

Flow straightening plate

Flow choke plate

Sta. 119.38

.15 gap

45°

30 percent of chord

40 percent of chord

30 percent of chord

45°

5-percent thickness ratio with a 50.8-cm chord in the streamwise direction

L-74-3994

(a) Basic afterbody with dry power nozzle, forward vertical tail, and aft horizontal tail.

Figure 2.- Photographs of model installed in Langley 16-foot transonic tunnel test section.
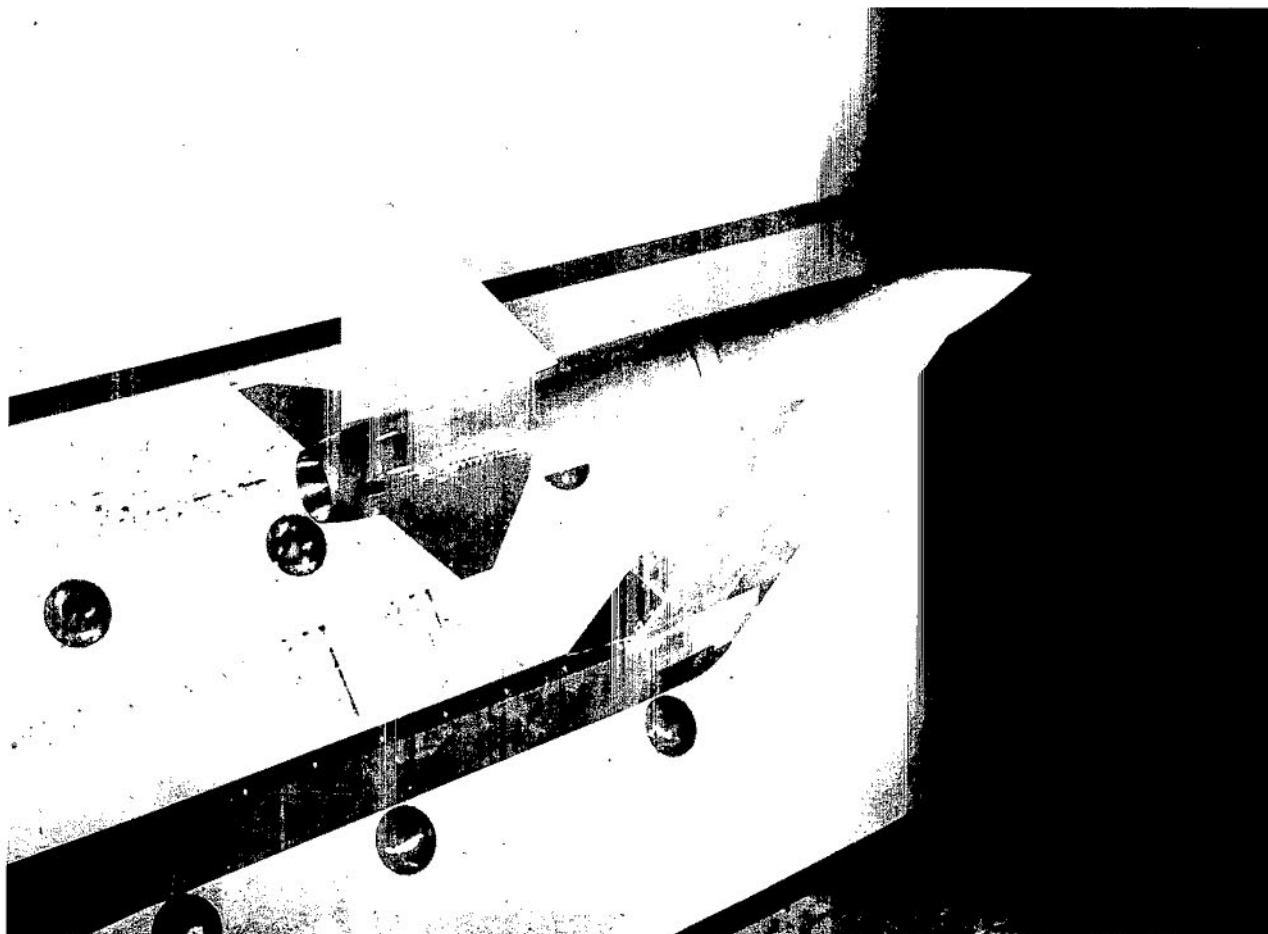
L-74-6710

(b) Basic afterbody with maximum afterburning nozzle, aft vertical tail, and aft horizontal tail.'

Figure 2.- Continued.
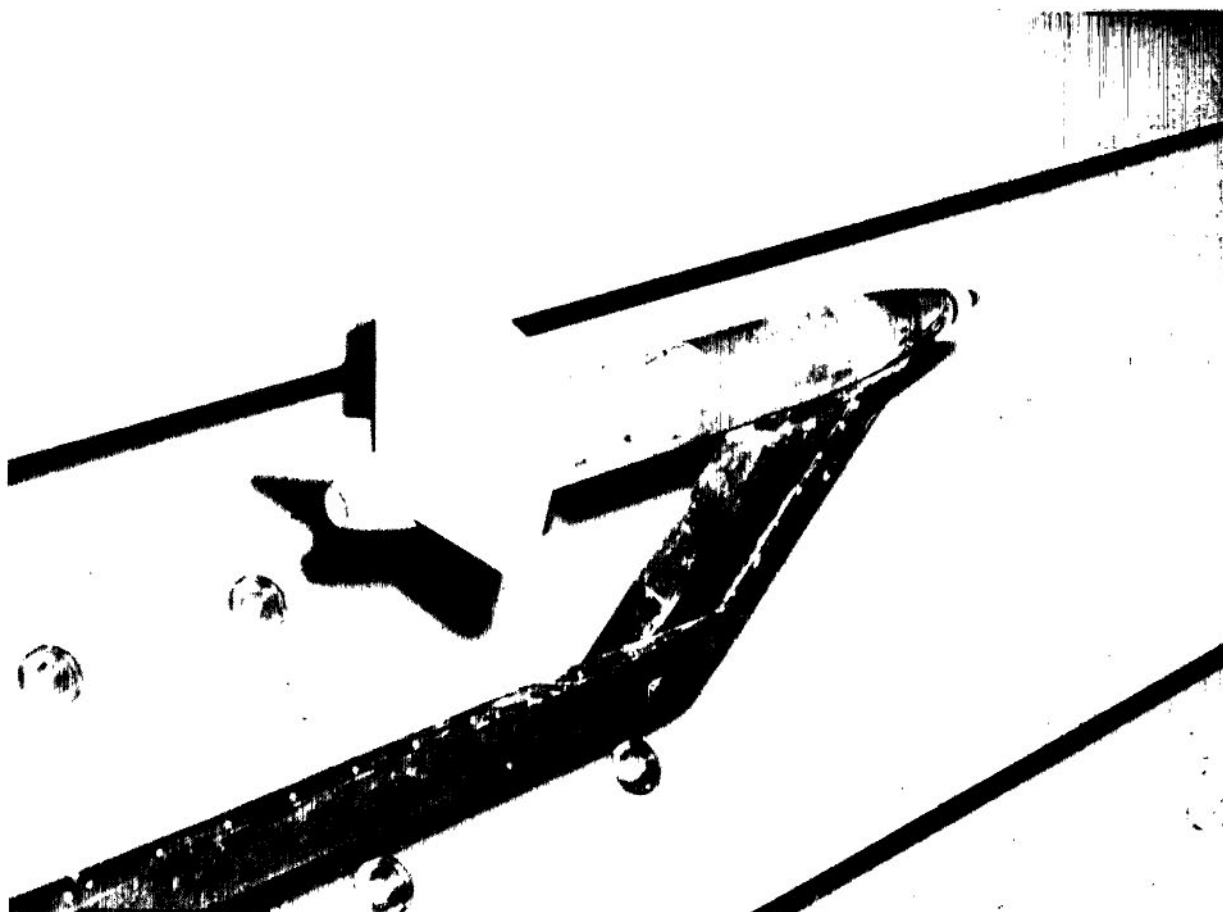
L-74-6622

(c) Basic afterbody with dry power nozzle, full contour bumps, aft vertical tail, and aft horizontal tail.

Figure 2.- Concluded.
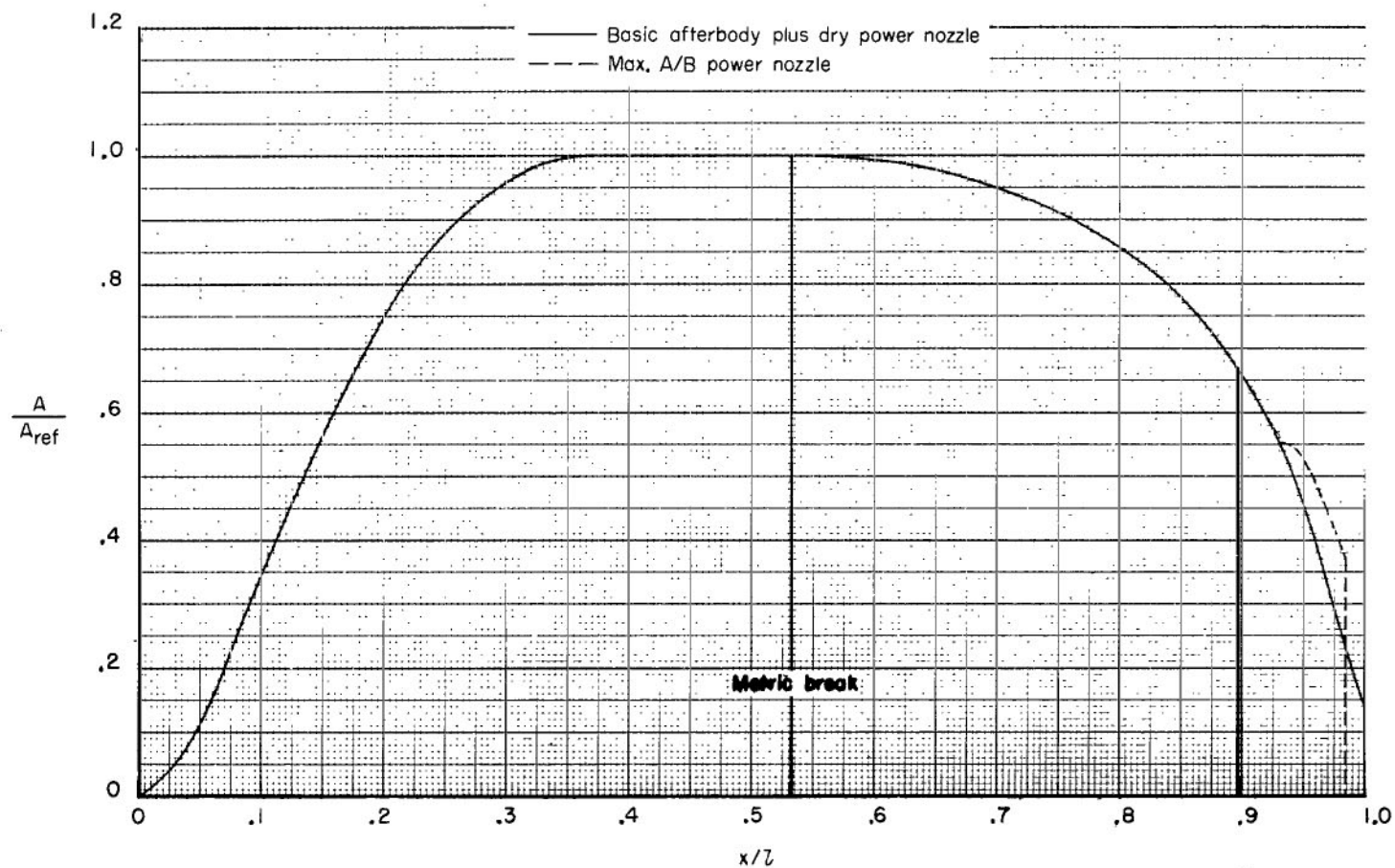
(a) Basic afterbody, tails off.

Figure 3.- Normal-area distribution of each configuration.
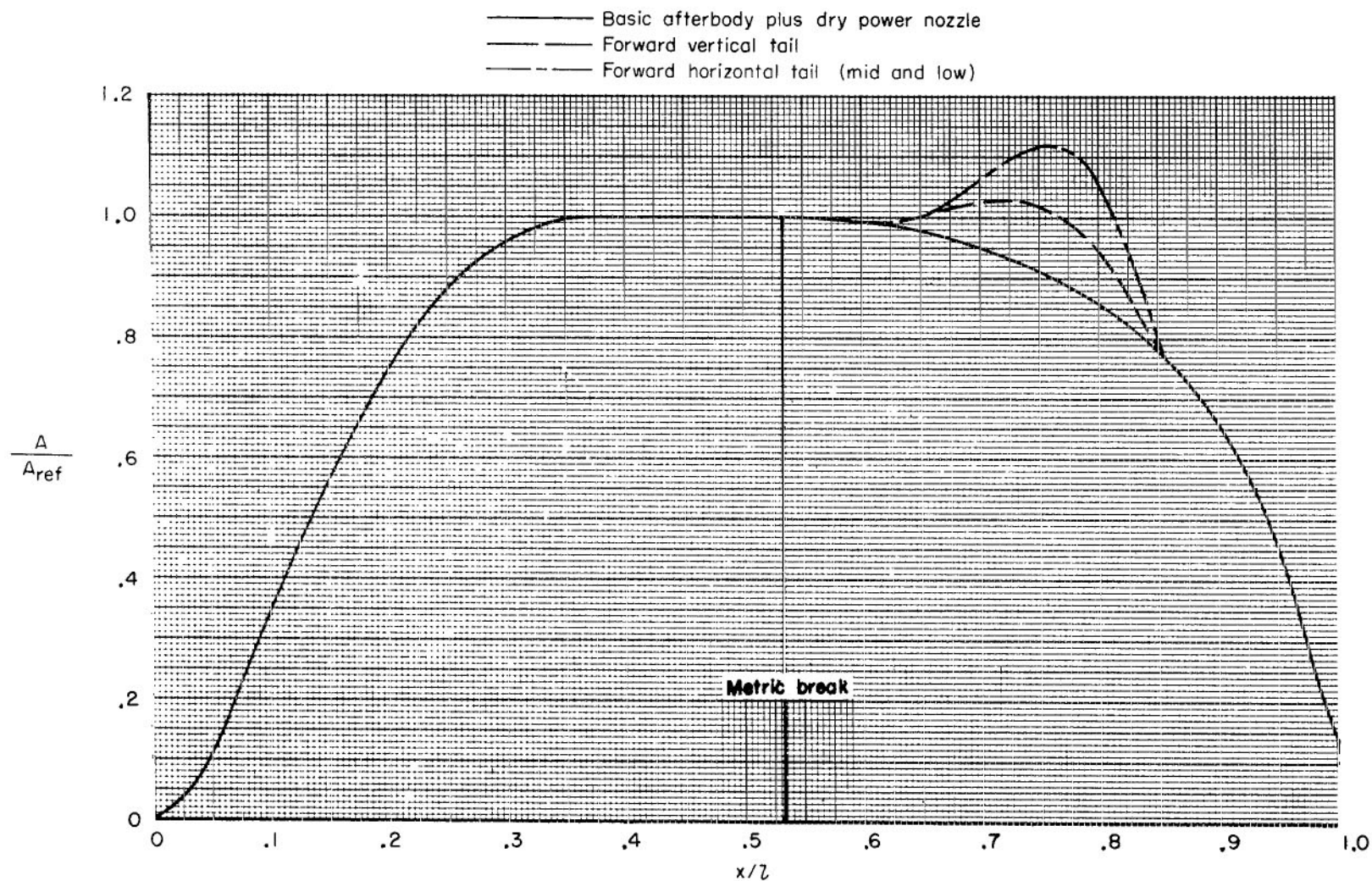
(b) Basic afterbody + forward tails.

Figure 3.- Continued.
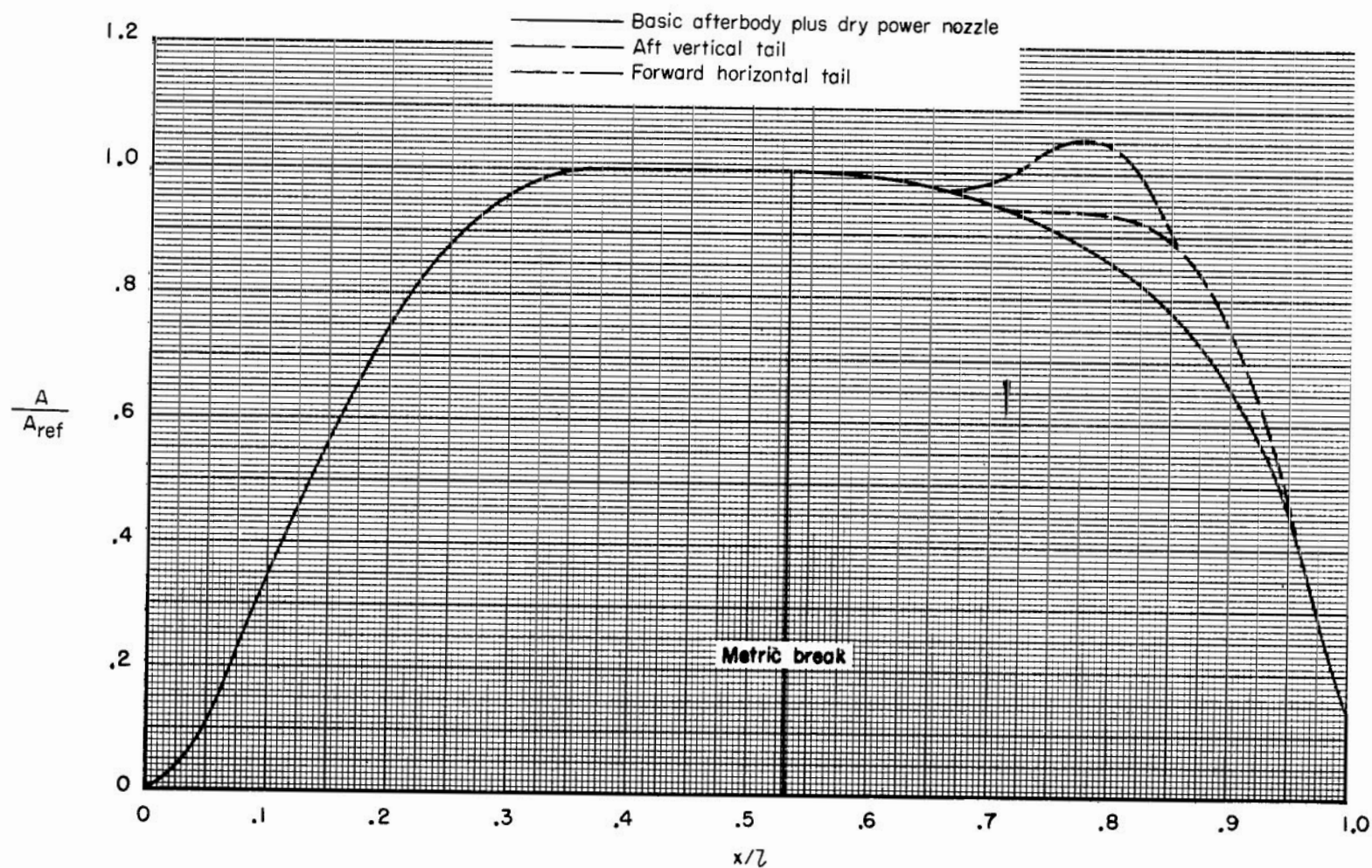
(c) Basic afterbody + staggered tails (aft vertical tail).

Figure 3.- Continued.
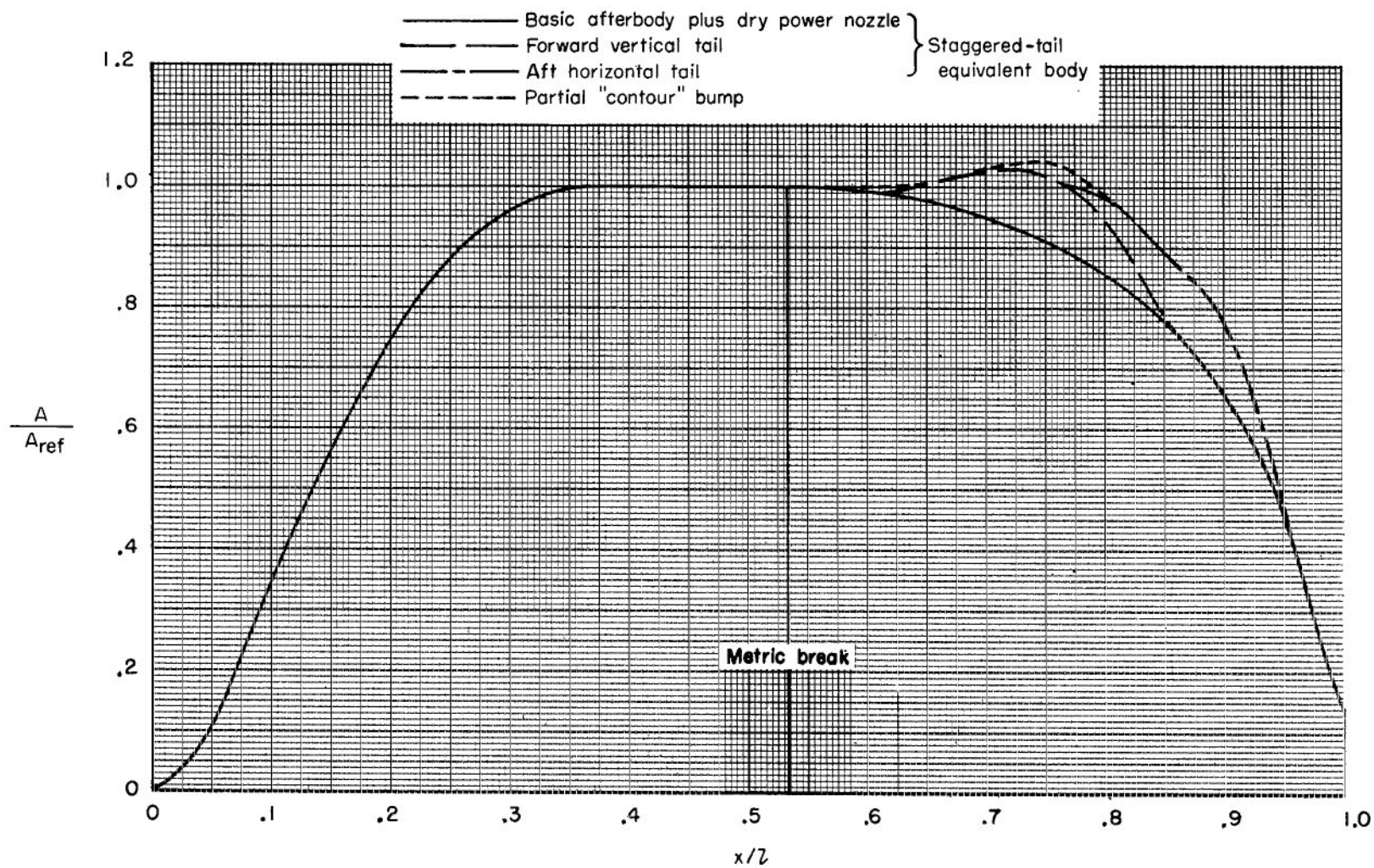
(d) Basic afterbody + staggered tails (forward vertical tail).

Figure 3.- Continued.

Basic afterbody plus forward vertical tail plus aft horizontal
tail plus dry power nozzle
Full "contour" bump
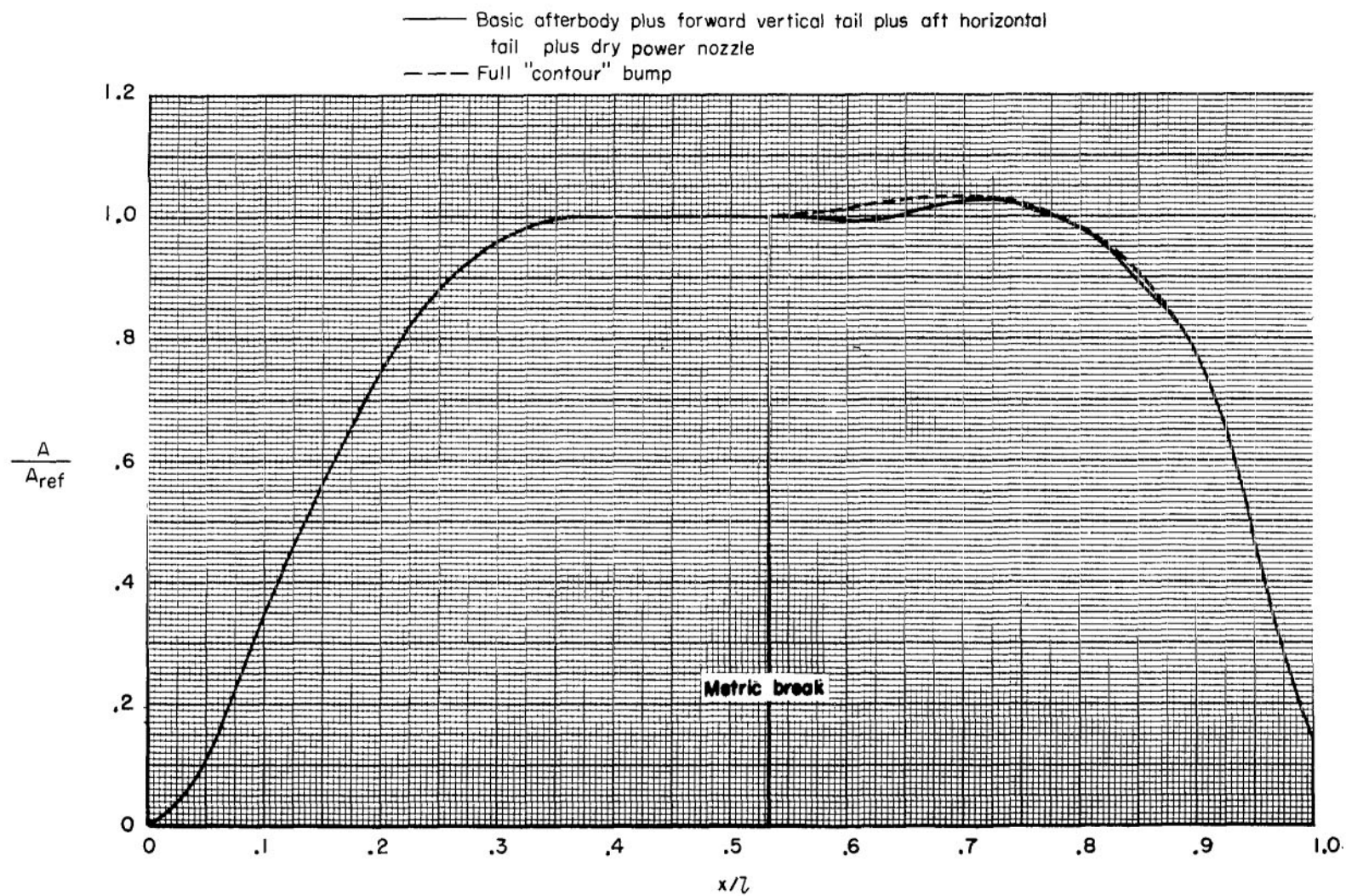
(d) Concluded.

Figure 3.- Continued.
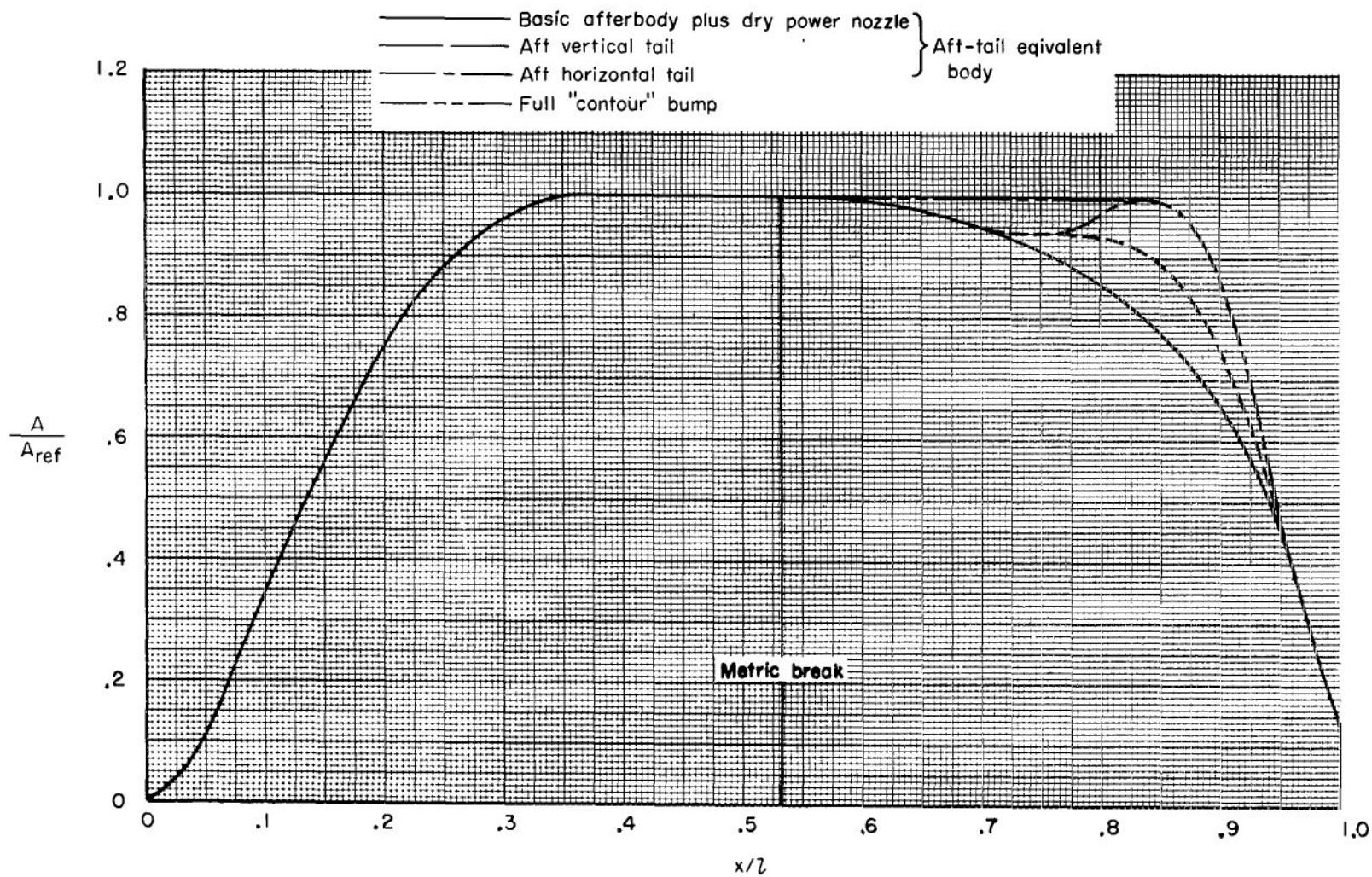
(e) Basic afterbody + aft tails.

Figure 3.- Continued.
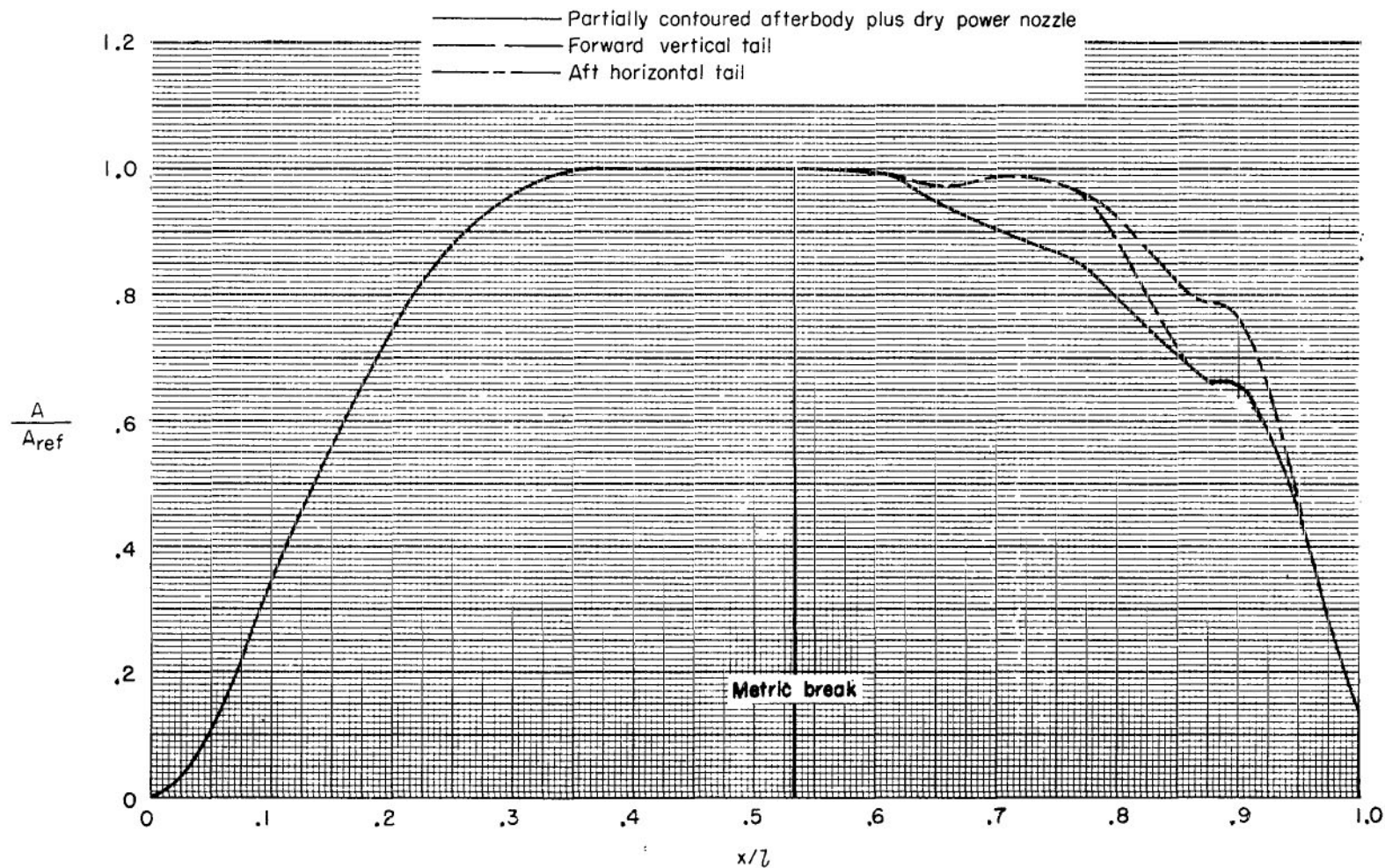
(f) Partially contoured afterbody + staggered tails (forward vertical tail).
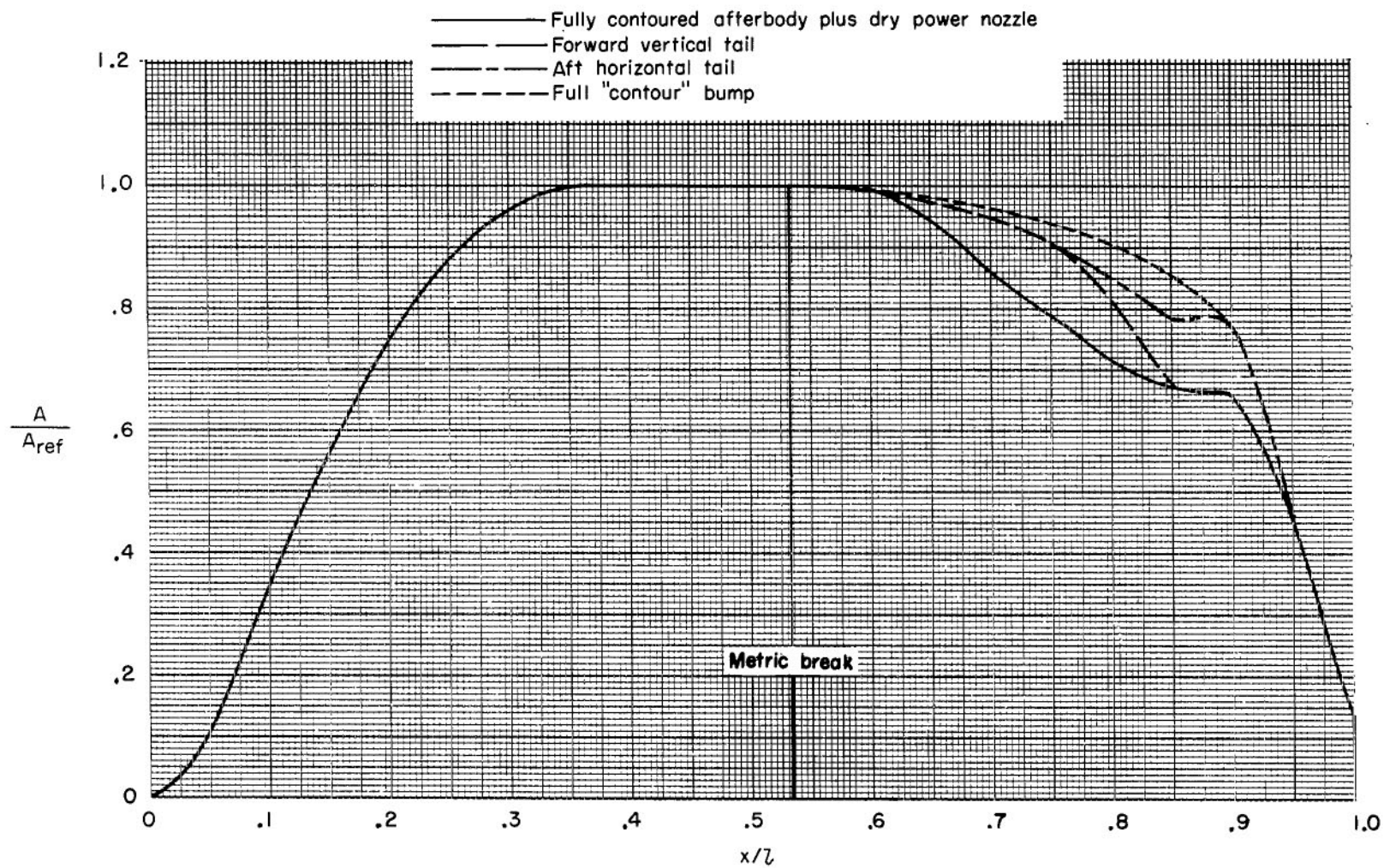
Figure 3.- Continued.

(g) Fully contoured afterbody + staggered tails (forward vertical tail).

Figure 3.- Concluded.

Afterbody geometry		Orifice locations		
x/l	r/r_{ref}	$\Phi = 292^\circ$	$\Phi = 315^\circ$	$\Phi = 338^\circ$
0.533	1.000			
.606	.996			
.697	.975			
.758	.950			
.803	.923			
.833	.900		X	
.864	.867		X	
.879	.847			
.886	—	X	X	X
.897	.817			
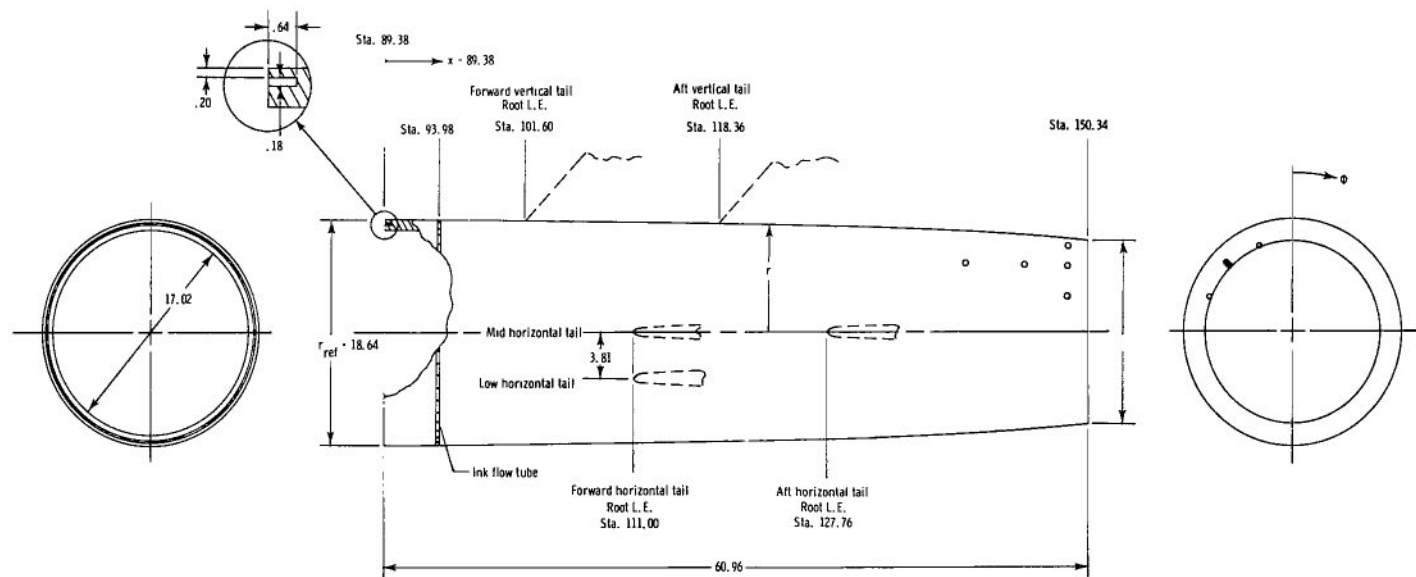
Figure 4.- Sketch of basic axisymmetric afterbody showing important dimensions, empennage locations, and orifice locations. All dimensions are in centimeters.

Vertical tail geometry

Airfoil sections

Tip .... NACA 64-003

Root .... NACA 64-005

Area (exposed, not including filler), m^2 .... 0.0881

Tail height (root to tip), cm 33.68

Tip chord, cm 10.67

Root chord, cm 41.66

Taper ratio 0.256

Aspect ratio (exposed) 1.288

Λ_{le}, deg 42.62

10.67

42.62°

33.68

41.66

Filler contoured for each tail location

Distance from model center line varies slightly with tail location

Model ₵
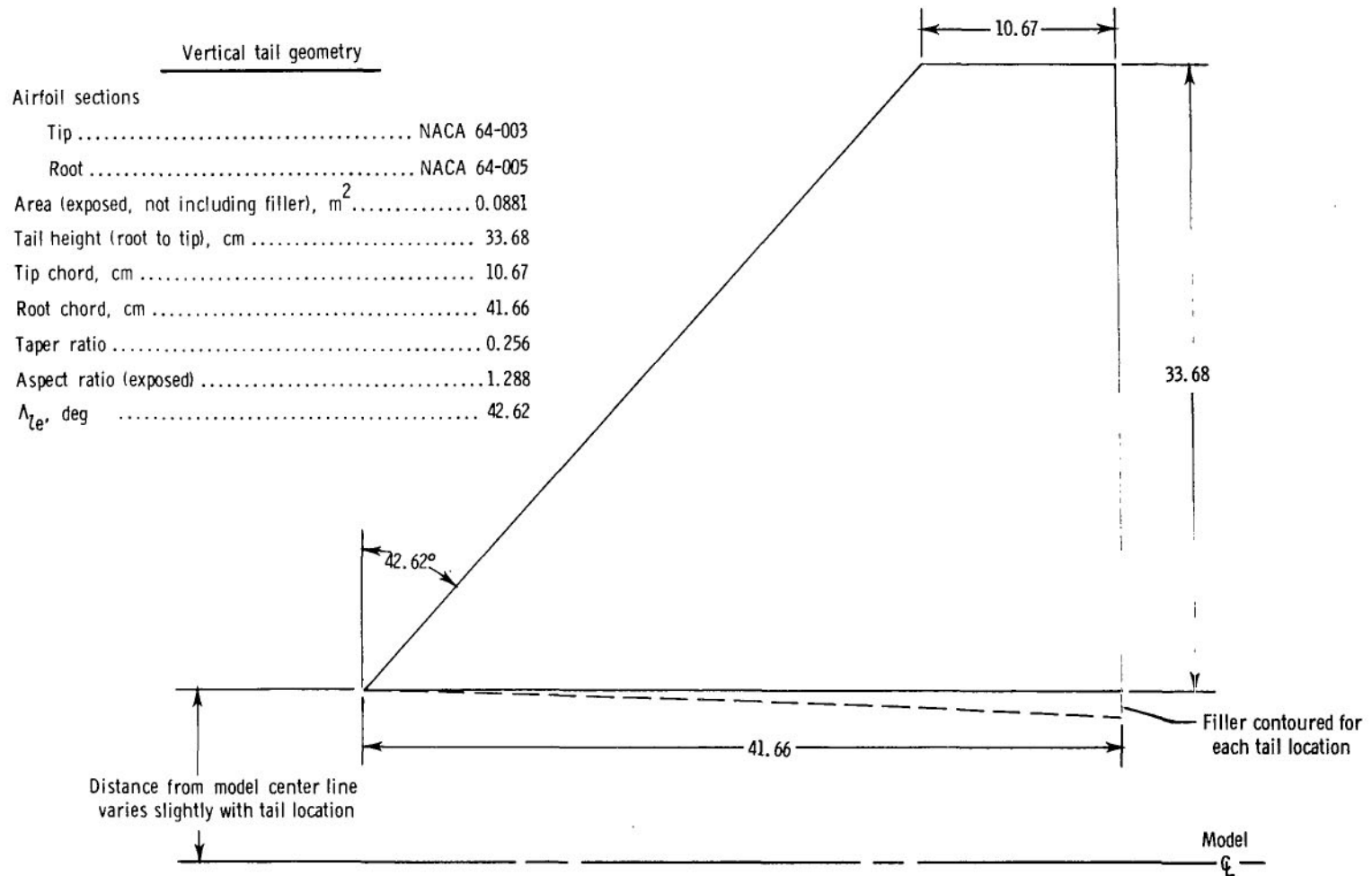
(a) Vertical tail.

Figure 5.- Sketches of empennage surfaces showing important dimensions. All dimensions are in centimeters.

Horizontal tail geometry

Airfoil sections

    Tip ....NACA 64-003

    Root...NACA 64-005

Area (one side exposed, not including filler), m^2.....0.0488

Area (total, aft tail location), m^2 ....0.1631

Span (aft tail location), cm 69.24

Tip chord, cm 5.59

Root chord, cm..32.26

Taper ratio...0.173

Aspect ratio (exposed).................................2.724

Aspect ratio (aft tail location)........................2.939

Λ_{le}, deg 45.97
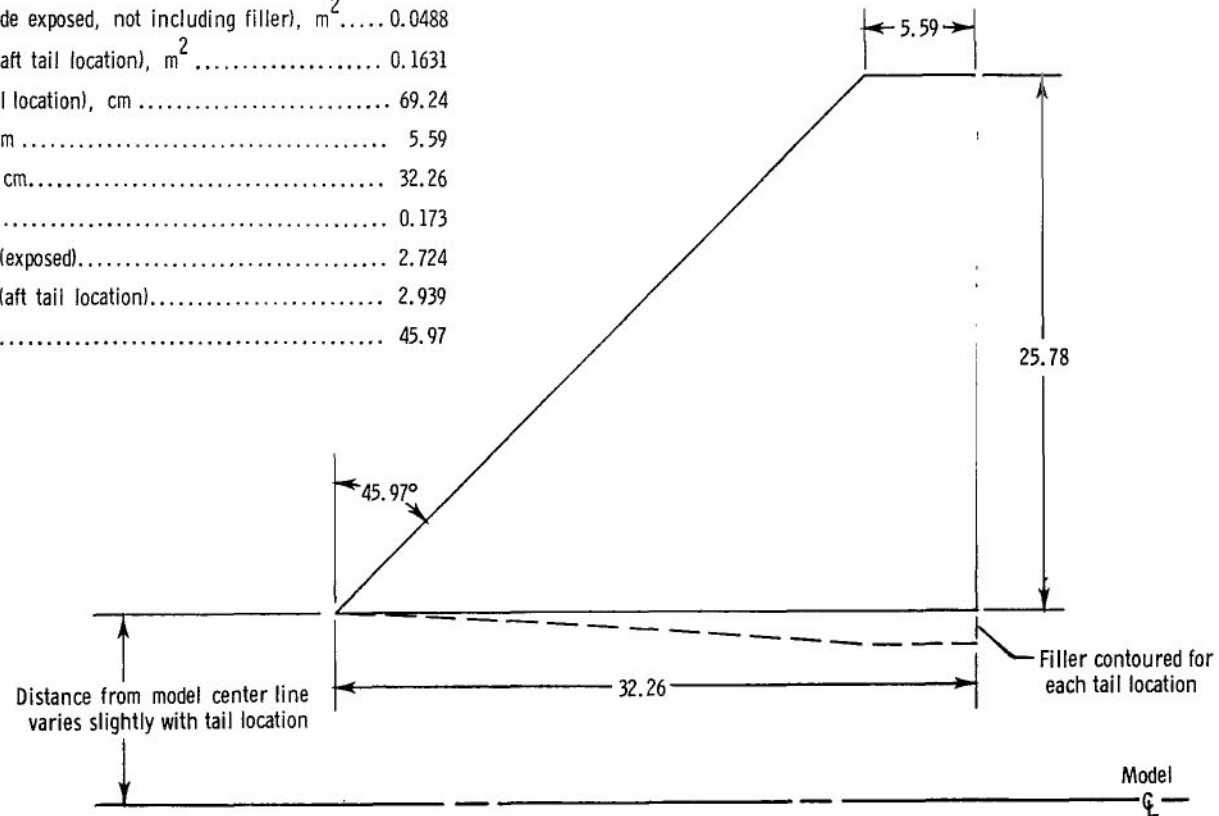
(b) Horizontal tails.

Figure 5.- Concluded.

x/l	r/r_{ref}	x/l	r/r_{ref}	x/l	r/r_{ref}
0.897	0.817	0.939	0.718	0.972	(b)
.909	a, b .795	.948	(b)	.973	(a)
.922	(b)	.952	(a)	.985	b 0.477
.930	(a)	.955	.654	.994	(a)
.932	.743	.959	(b)	.995	(b)
.935	(b)	.970	.572	1.000	.374

[a] Base line nozzle (shown) pressure orifices located at $\Phi = 0°$, $90°$, $180°$ and $315°$.

[b] Pressure nozzle (not shown, identical geometry) pressure orifices located at $\Phi = 0°$, $270°$, $279°$, $288°$, $306°$, $324°$ and $342°$.
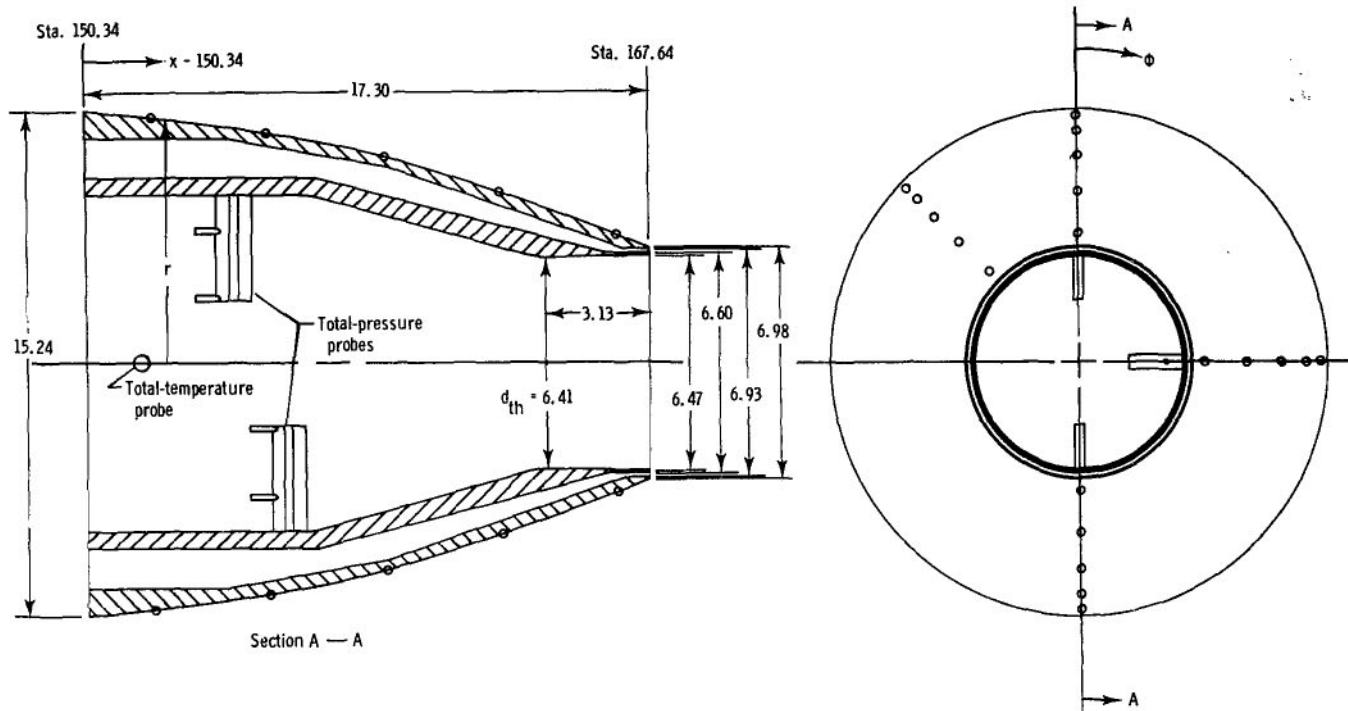
(a) Dry power ($A_e/A_t = 1.02$).

Figure 6.- Sketches of nozzle configurations showing important dimensions and orifice locations. All dimensions are in centimeters.

x/l	r/r_{ref}	x/l	r/r_{ref}
0.897	0.817	0.955	0.714
.909	[a] .795	.959	(a)
.926	(a)	.970	.665
.932	.743	.976	(a)
.939	.741	.984	.608
.942	(a)		

[a] Pressure orifices at $\Phi = 0°$, $90°$, $180°$ and $315°$.
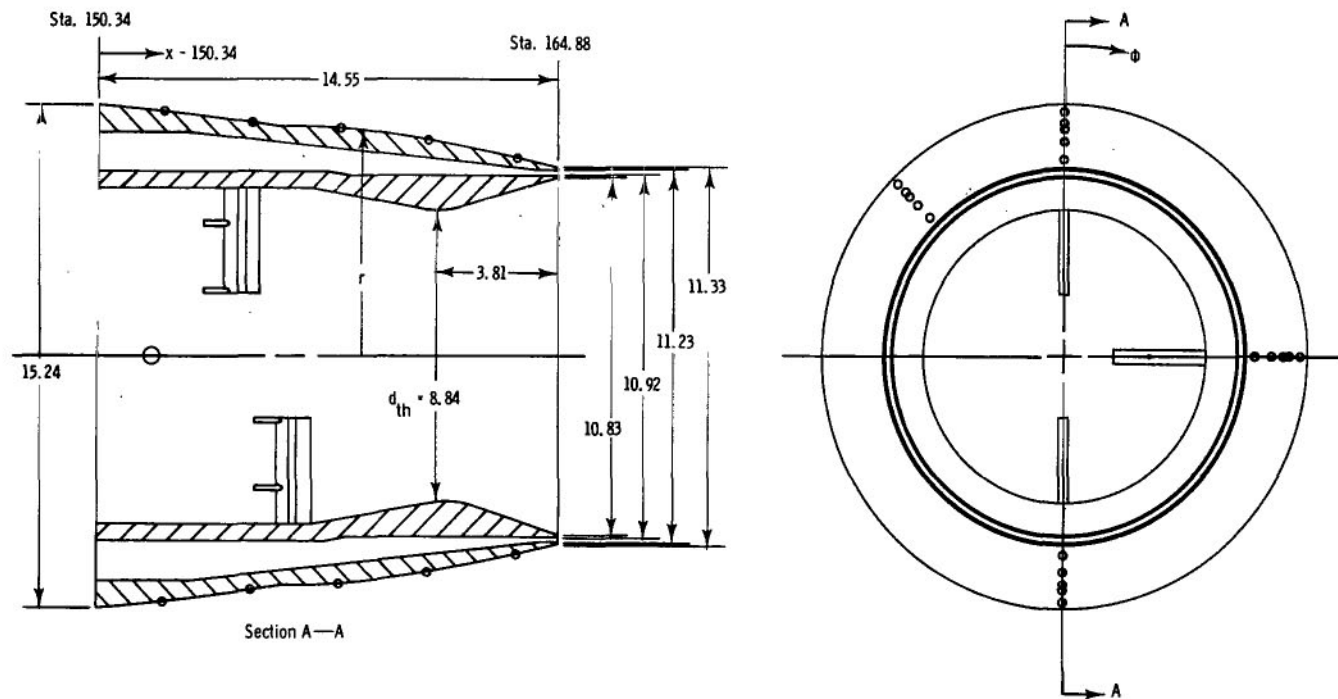
(b) Max. A/B power ($A_e/A_t = 1.50$).

Figure 6.- Concluded.

Orifice locations	
x/l	ϕ, deg
0.833	315
.864	315
.886	292, 315, 338
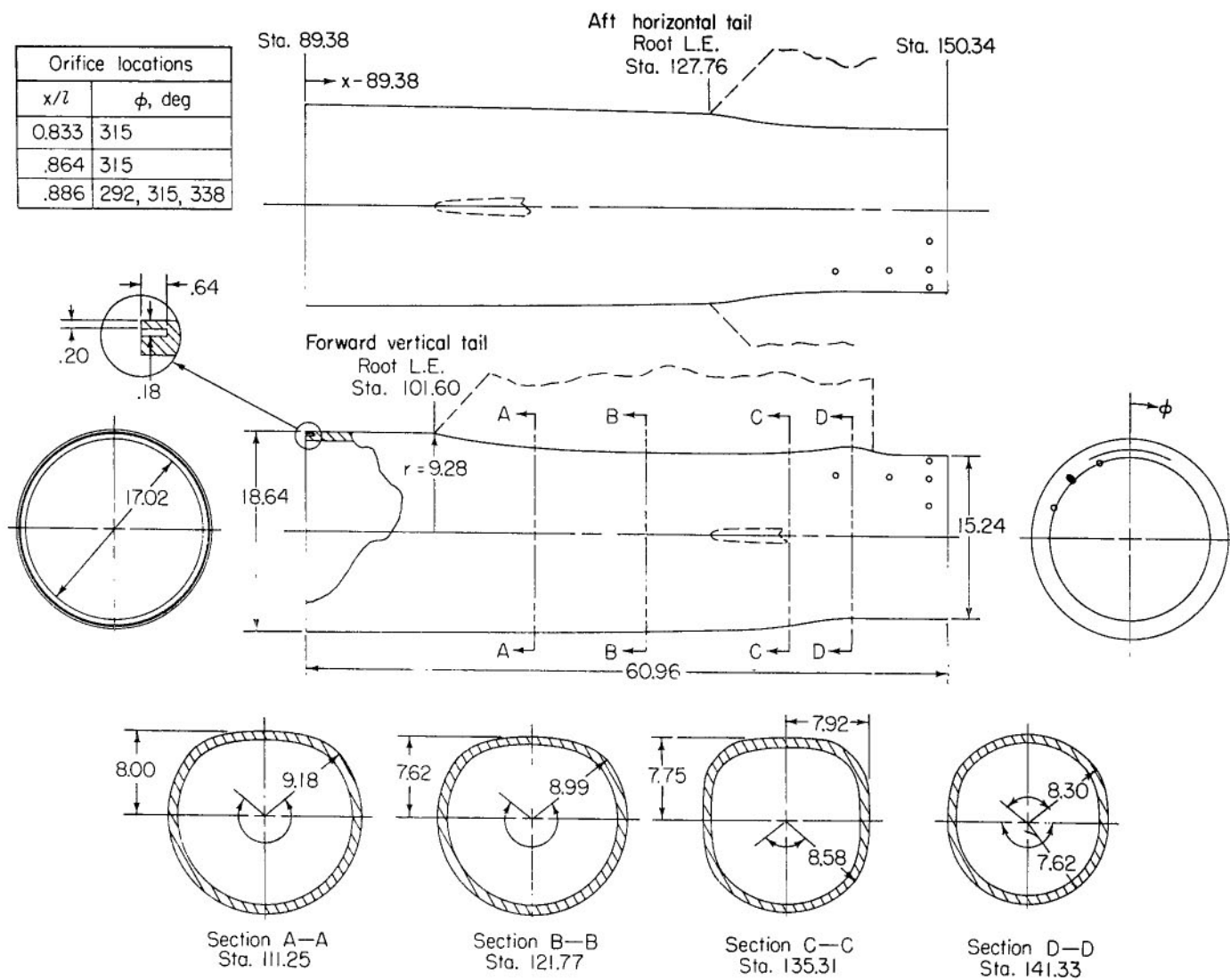
(a) Partially contoured.

Figure 7.- Sketches of locally contoured afterbodies showing geometry details and orifice locations. All dimensions are in centimeters.

Orifice locations

x/l	ϕ, deg
0.833	315
.864	315
.886	292, 315, 338

Sta. 89.38

x - 89.38

Aft horizontal tail
Root L.E.
Sta. 127.76

Sta. 150.34

.64

.20

.18

Forward vertical tail
Root L.E.
Sta. 101.60

A   B   C   D

17.02

18.64

r = 9.28

15.24

60.96

Section A—A
Sta. 111.25

7.81   9.18

Section B—B
Sta. 121.77

6.86   8.94

Section C—C
Sta. 135.31

6.86   7.95   8.20

Section D—D
Sta. 141.33

7.62   7.62
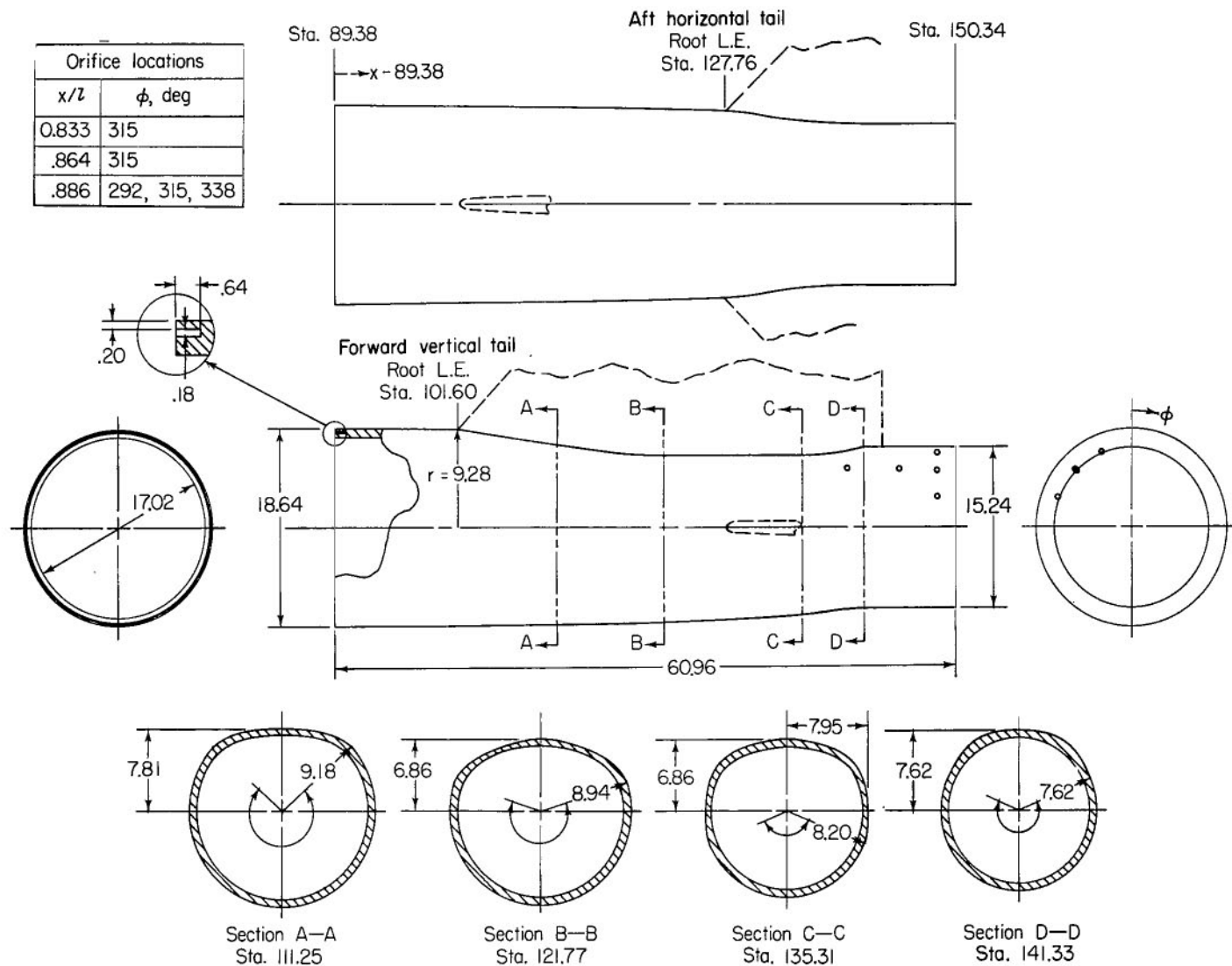
(b) Fully contoured.

Figure 7.- Concluded.

Sta. 89.38

x_v

y_v

r_h

Vertical tail bump		
x_v	r_v	y_v
0.00	9.32	0.00
5.33	9.91	1.68
8.33	10.16	2.11
12.22	10.54	2.44
14.35	10.67	2.54
17.91	10.16	1.83
21.26	9.19	.91

Horizontal tail bumps		
x_h	r_h	y_h
0.00	9.19	0.00
3.35	9.32	.89
7.72	9.42	1.57
10.64	9.58	1.91
14.45	9.86	2.34
17.12	9.96	2.67
20.12	9.91	2.54
23.47	9.45	1.40
25.50	8.56	.76

r_v

Sta. 110.64

x_h

y_h
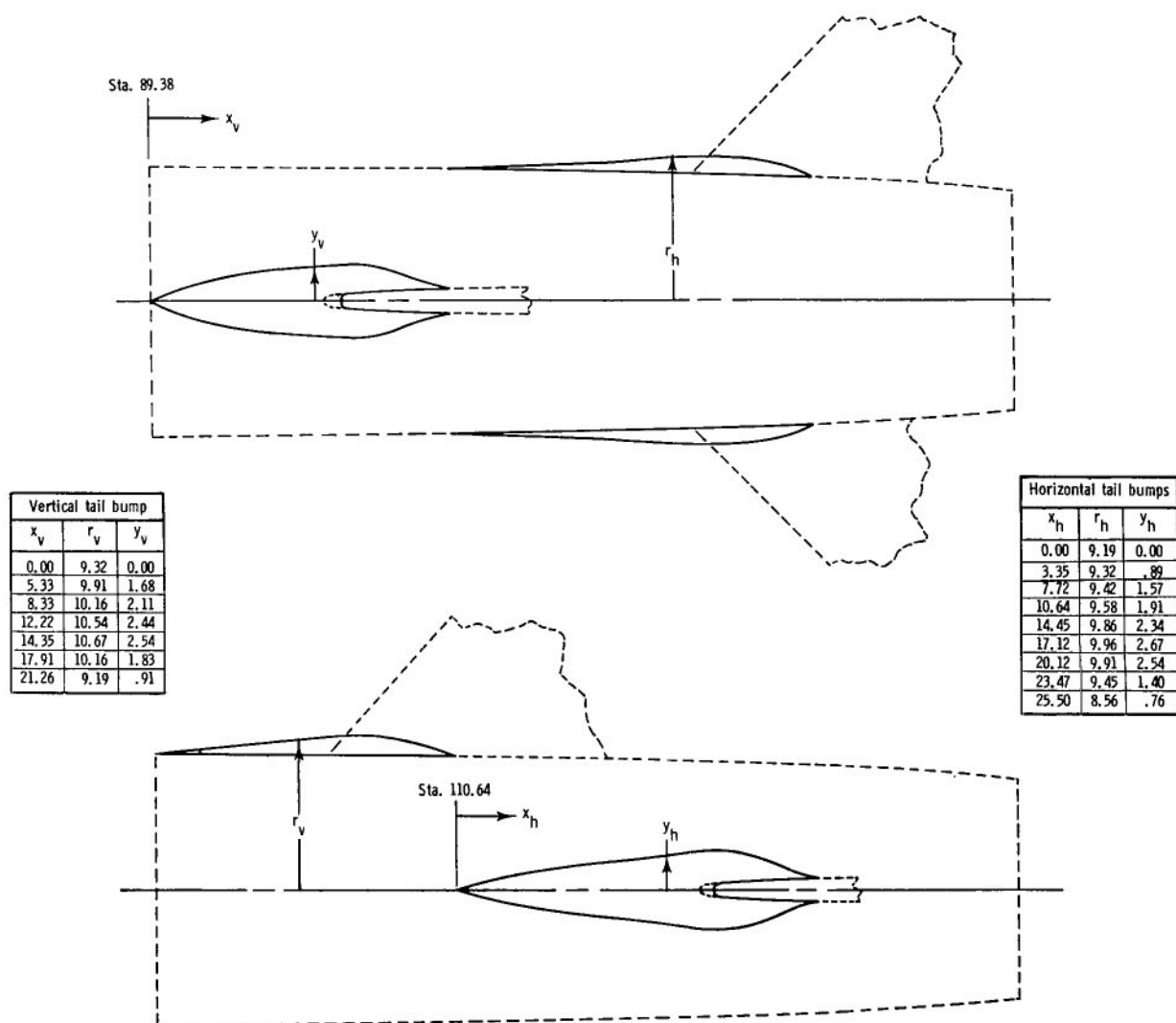
(a) Partial bumps, basic afterbody, and staggered empennage arrangement.

Figure 8.- Sketches of contour bumps showing important dimensions. All dimensions are in centimeters.

Sta. 89.38

Vertical tail bump		
x_v	r_v	y_v
0.00	9.32	0.00
5.33	10.06	2.29
8.33	10.54	2.57
12.22	11.13	2.87
14.35	11.38	3.07
17.91	11.35	3.18
21.26	11.05	2.97
24.61	10.59	2.57
28.98	9.91	1.91
31.90	8.99	1.02

Horizontal tail bumps		
x_h	r_h	y_h
0.00	8.92	0.00
2.67	9.47	.64
5.66	9.32	.94
9.02	8.64	.69
11.05	9.02	1.30
12.37	9.14	1.50
15.72	9.30	1.80
17.73	9.35	1.93
20.73	8.94	1.55
22.45	7.87	.61

Sta. 125.10

(b) Full bumps, basic afterbody, and staggered empennage arrangement.

Figure 8.- Continued.

Sta. 89.38

Vertical tail bump

x_v	r_v	y_v
0.00	9.32	0.00
7.85	9.65	1.78
11.20	9.88	2.29
17.91	10.24	2.84
21.26	10.39	3.05
24.61	0.59	3.05
28.99	1.05	2.79
31.32	11.35	2.87
34.67	11.35	2.92
38.38	10.82	2.92
41.38	10.08	2.46
44.73	8.64	1.04

Horizontal tail bumps

x_h	r_h	y_h
0.00	9.30	0.00
6.71	9.55	1.52
10.06	9.68	1.93
13.41	9.83	2.18
17.78	10.01	2.41
20.12	10.11	2.39
23.47	10.29	2.18
27.18	10.54	2.03
30.18	10.54	2.36
33.53	10.24	2.24
36.88	9.47	1.68
40.23	8.33	.81

Sta. 100.58

(c) Full bumps, basic afterbody, and aft empennage arrangement.

Figure 8.- Continued.
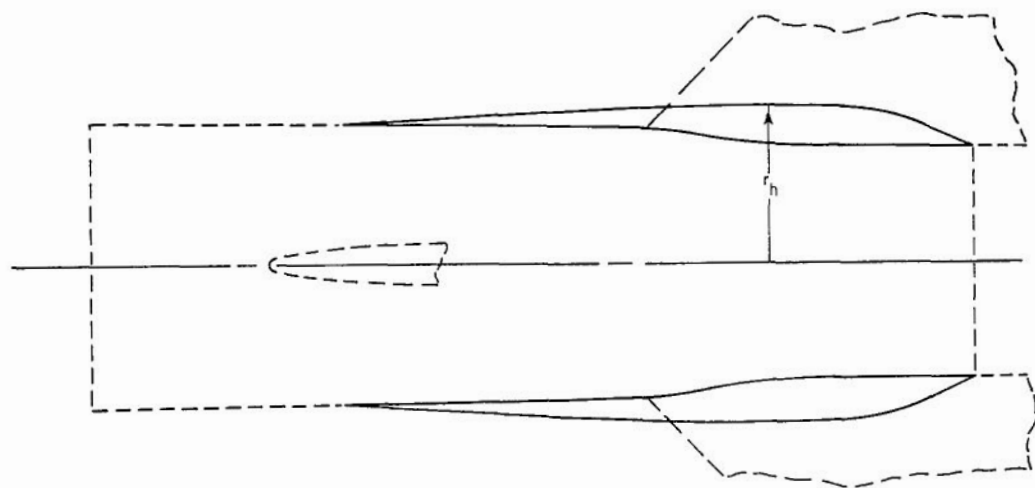
Horizontal tail bumps		
x_h	r_h	y_h
0.00	9.25	0.00
4.52	9.60	.76
10.52	9.91	1.52
15.04	10.13	1.98
21.03	10.34	2.54
24.82	10.44	2.79
28.58	10.46	2.97
30.84	10.46	3.00
33.07	10.44	3.02
34.59	10.36	3.20
36.53	10.16	3.43
39.09	9.58	3.10
40.59	8.92	2.34
43.61	7.62	.48
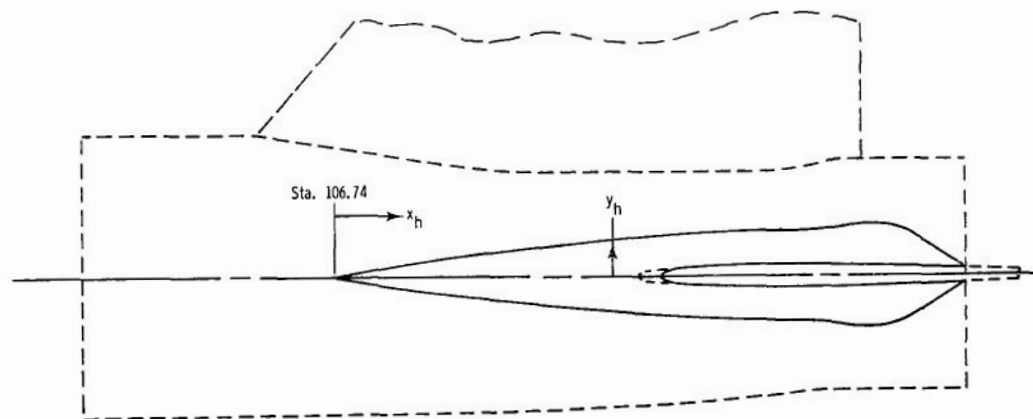
(d) Full bumps, fully contoured afterbody, and staggered empennage arrangement.

Figure 8.- Concluded.
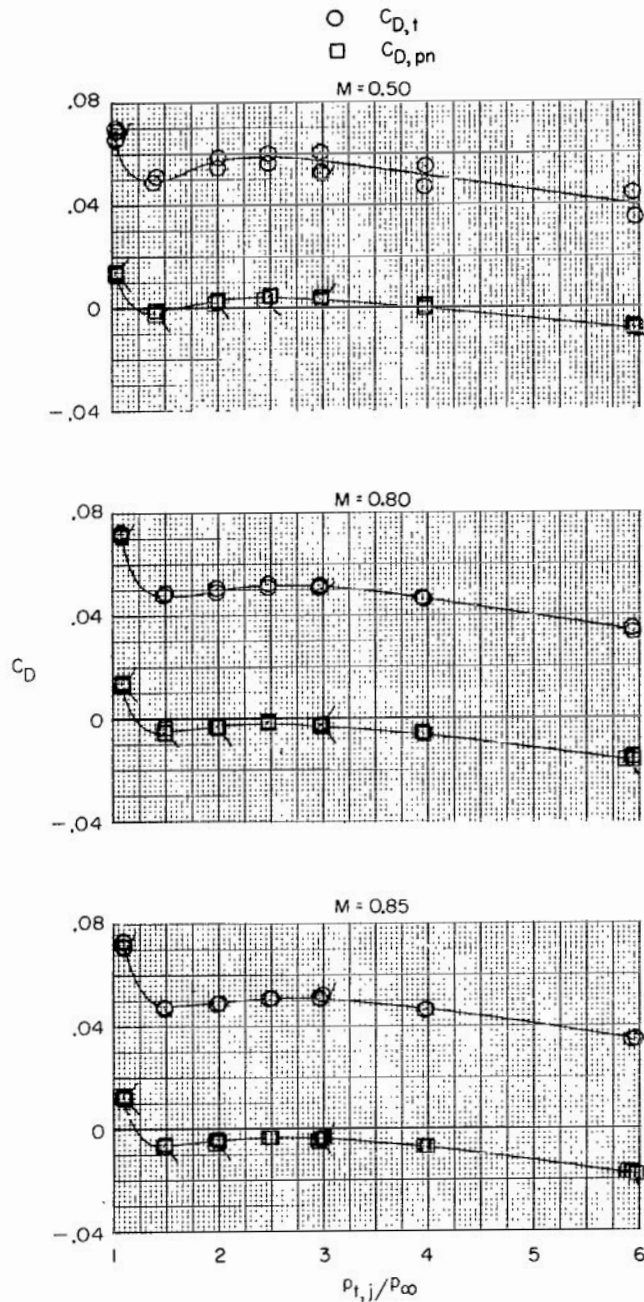
(a) Basic afterbody + dry power nozzle.

Figure 9.- Variation of total (afterbody + nozzle + tails) drag coefficient, integrated nozzle pressure drag coefficient, and computed tail drag coefficient with jet total pressure ratio at Mach numbers from 0.50 to 2.20. Flagged symbols indicate decreasing jet total pressure ratio. Tailed symbols indicate drag values from pressure nozzle.
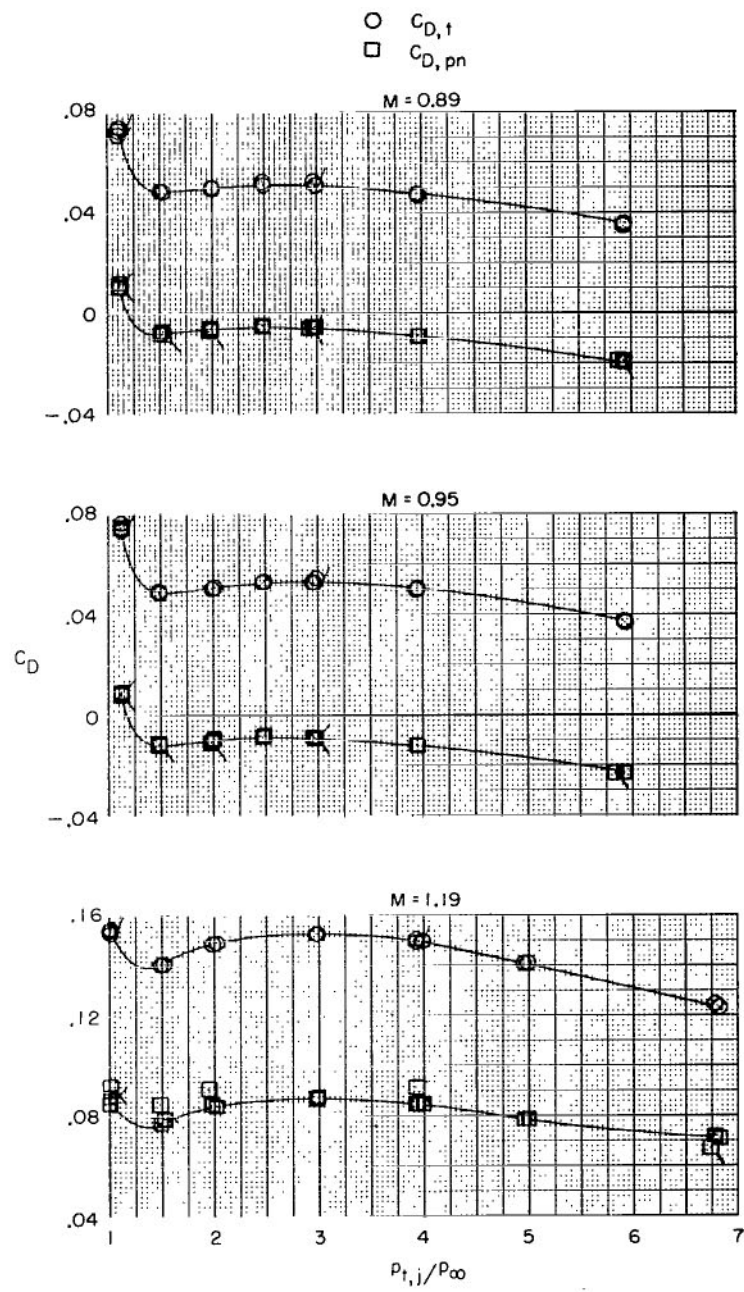
(a) Concluded.

Figure 9.- Continued.
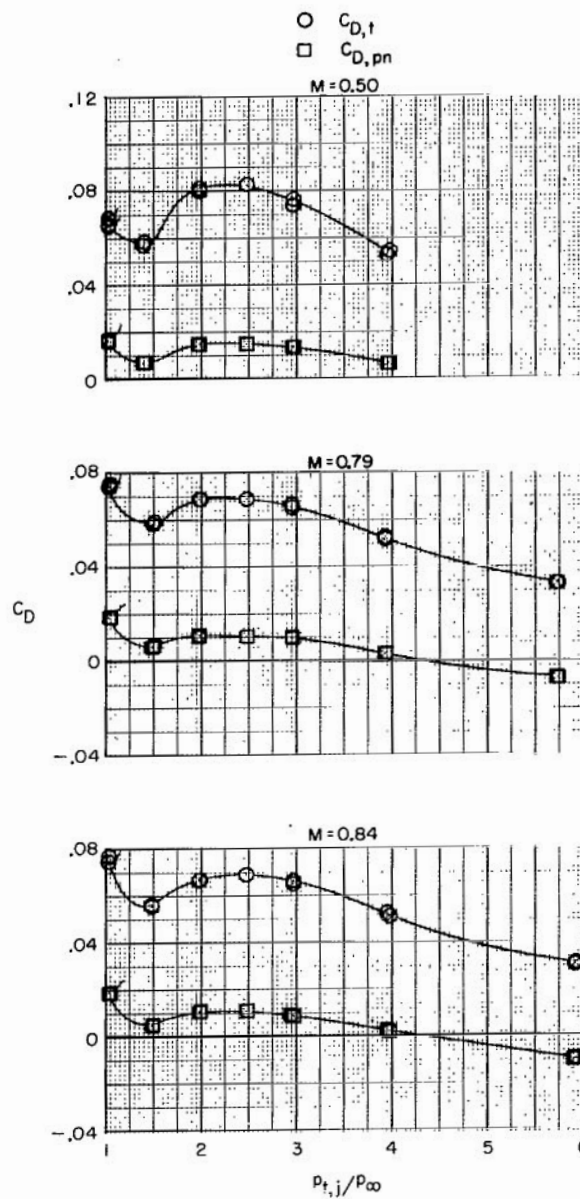
(b) Basic afterbody + max. A/B power nozzle.
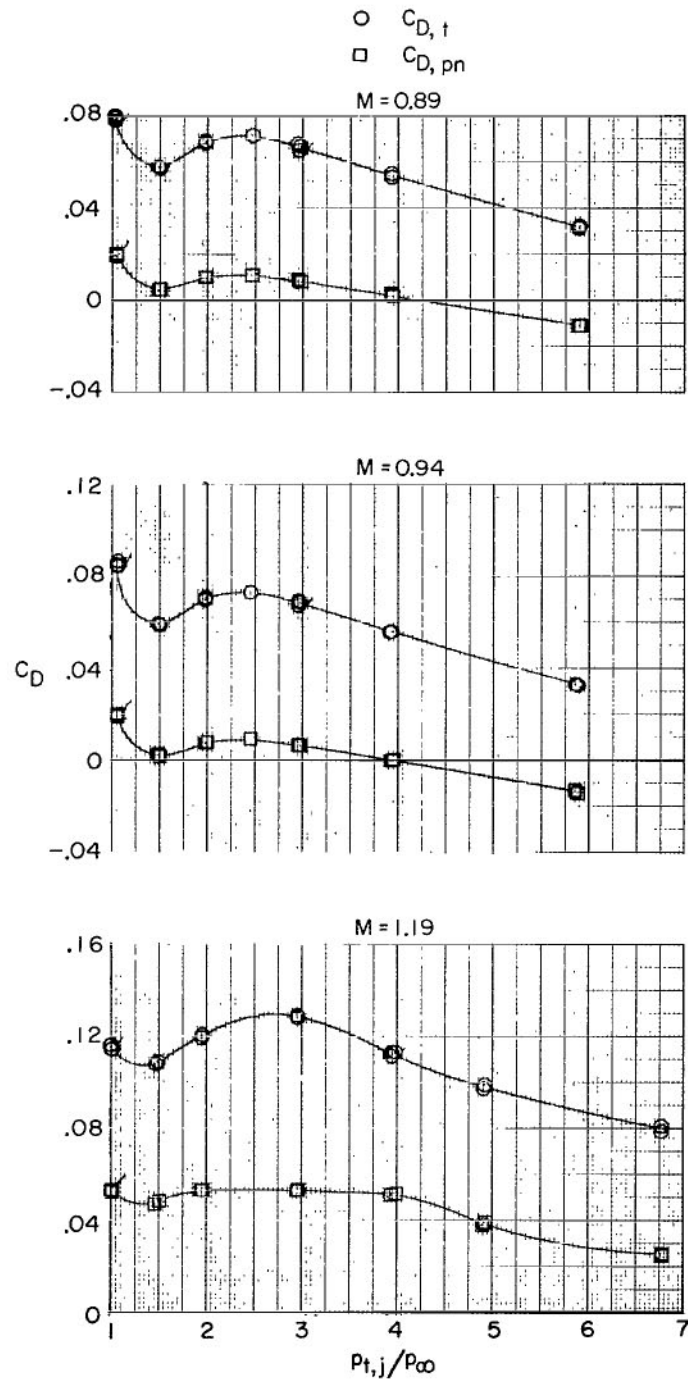
Figure 9.- Continued.

(b) Continued.

Figure 9.- Continued.
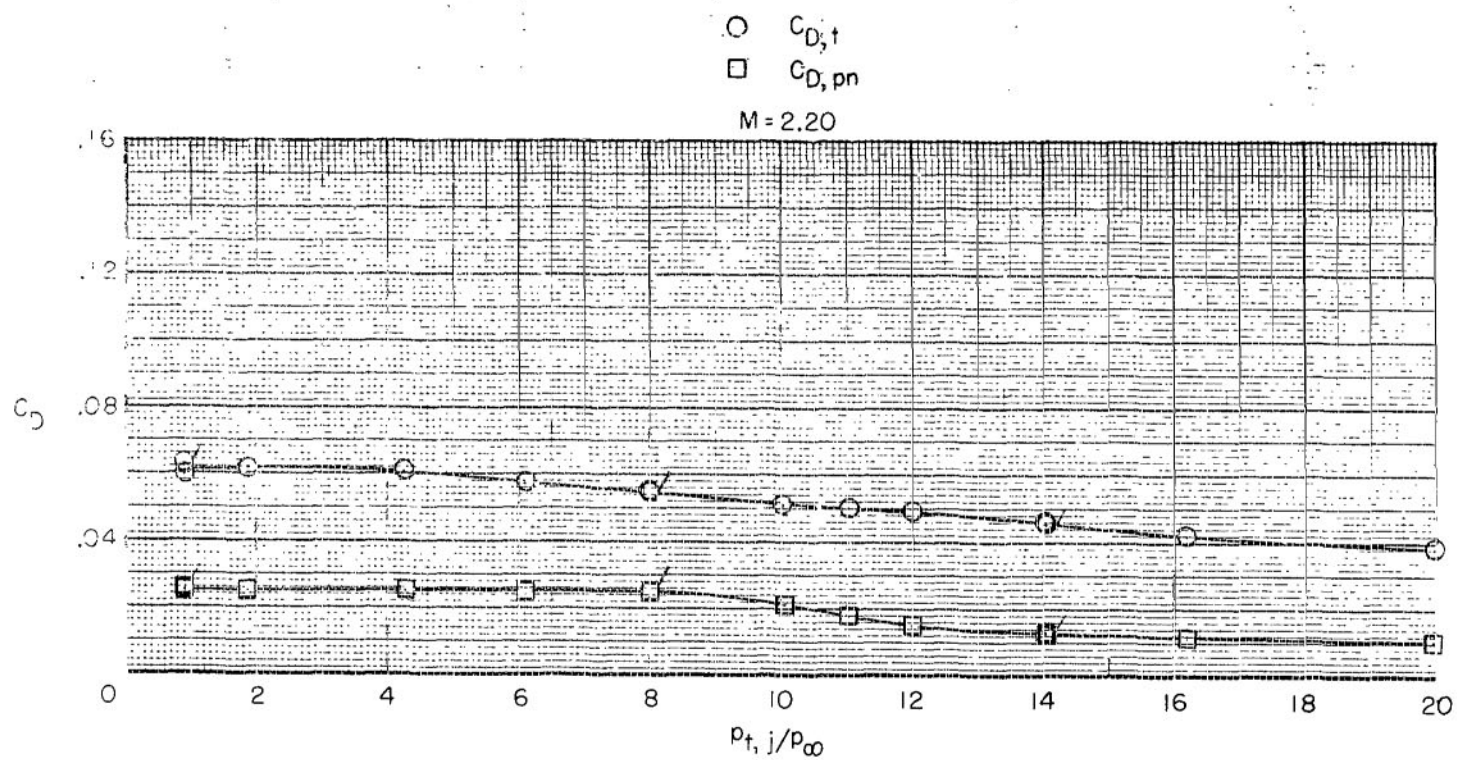
(b) Concluded.

Figure 9.- Continued.
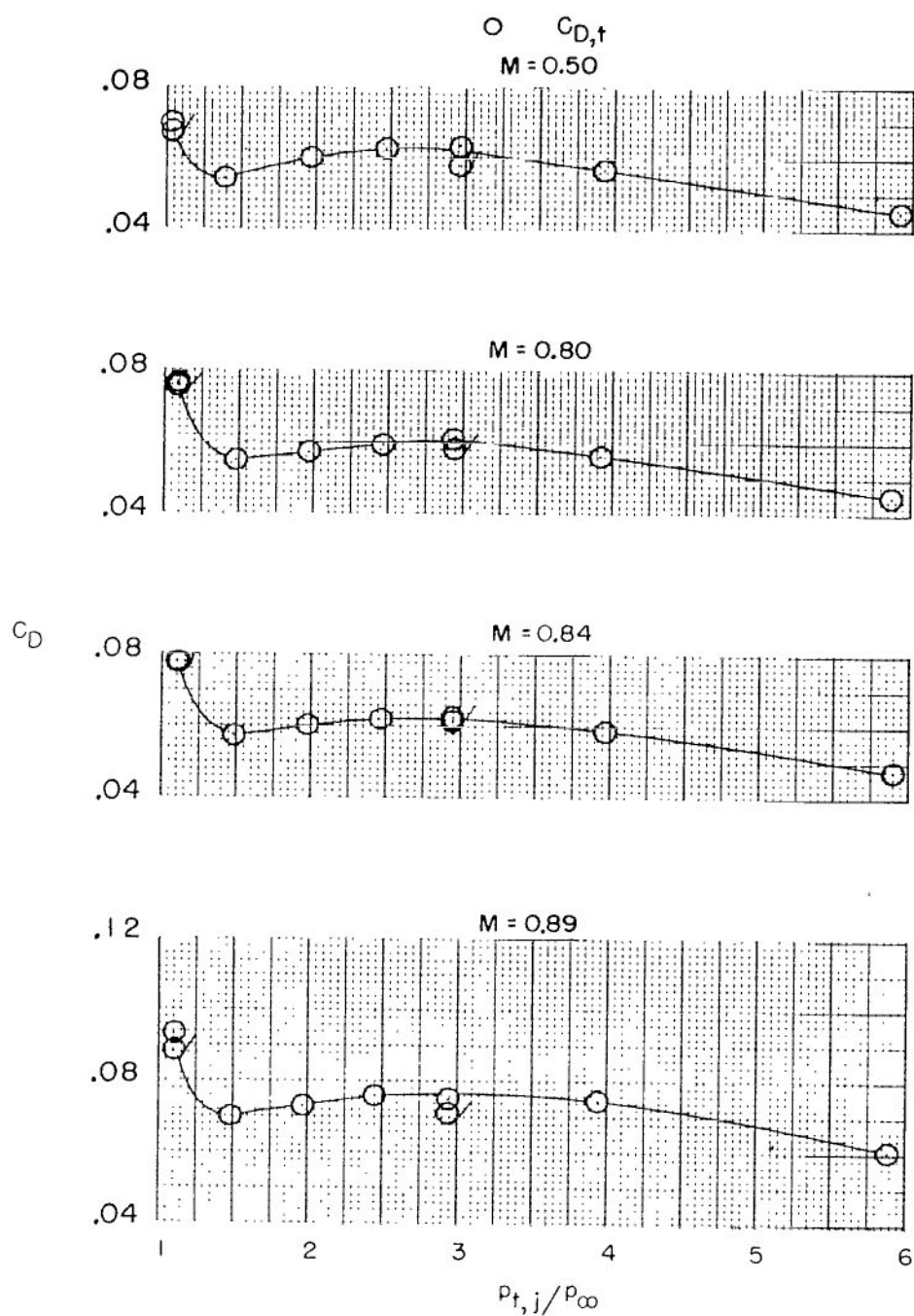
(c) Equivalent body (basic afterbody + aft vertical tail
+ aft horizontal tail + dry power nozzle).
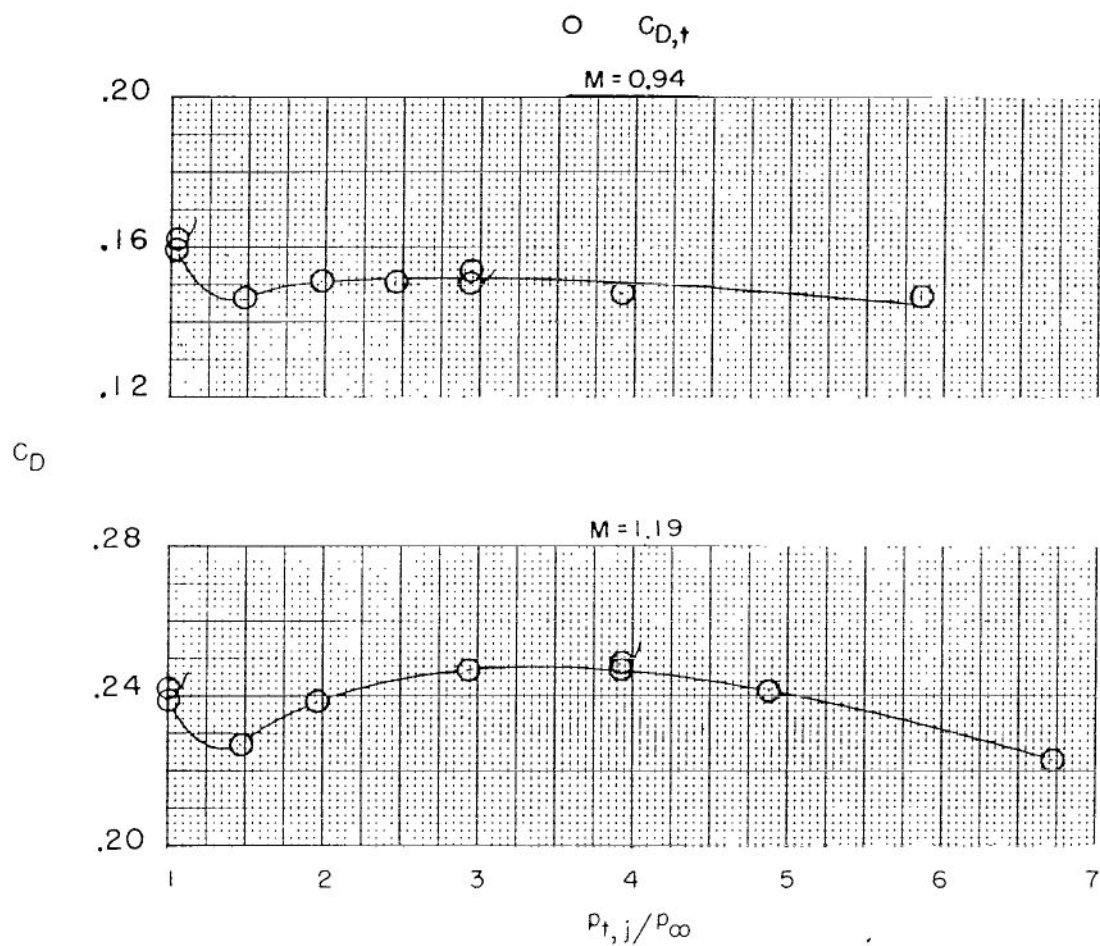
Figure 9.- Continued.

(c) Concluded.

Figure 9.- Continued.

O $c_{D,t}$

C_D

$p_{t,j}/p_\infty$
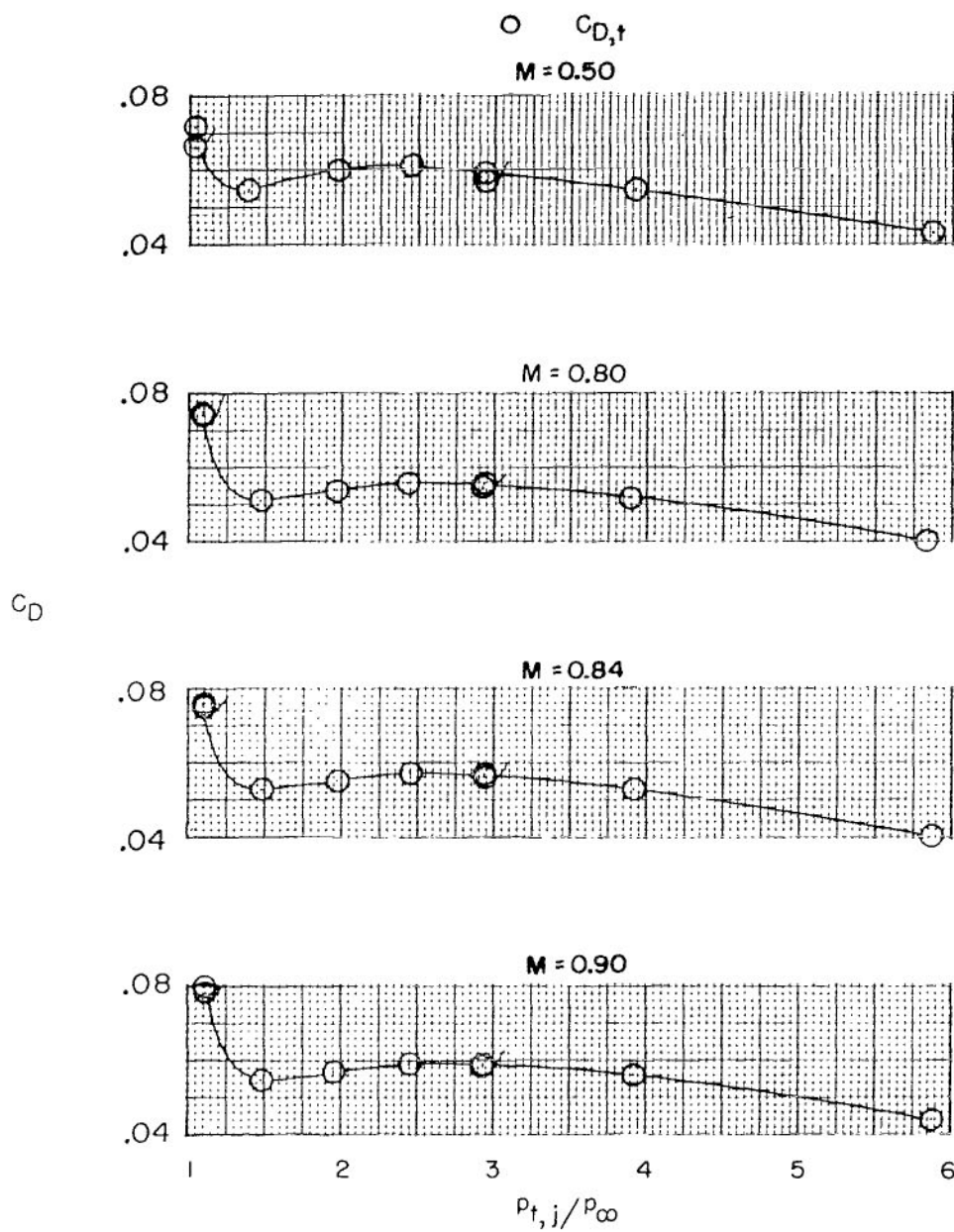
(d) Equivalent body (basic afterbody + forward vertical tail
+ aft horizontal tail + dry power nozzle).

Figure 9.- Continued.

53
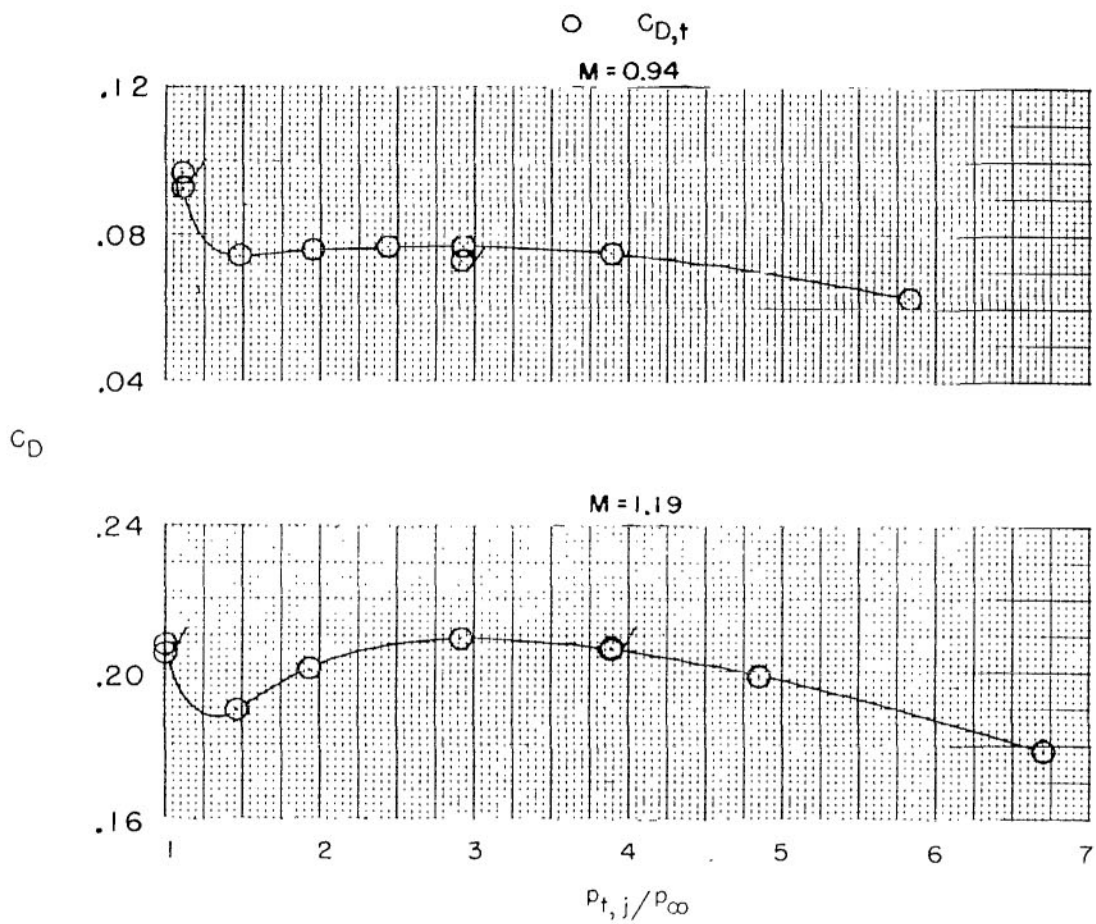
(d) Concluded.
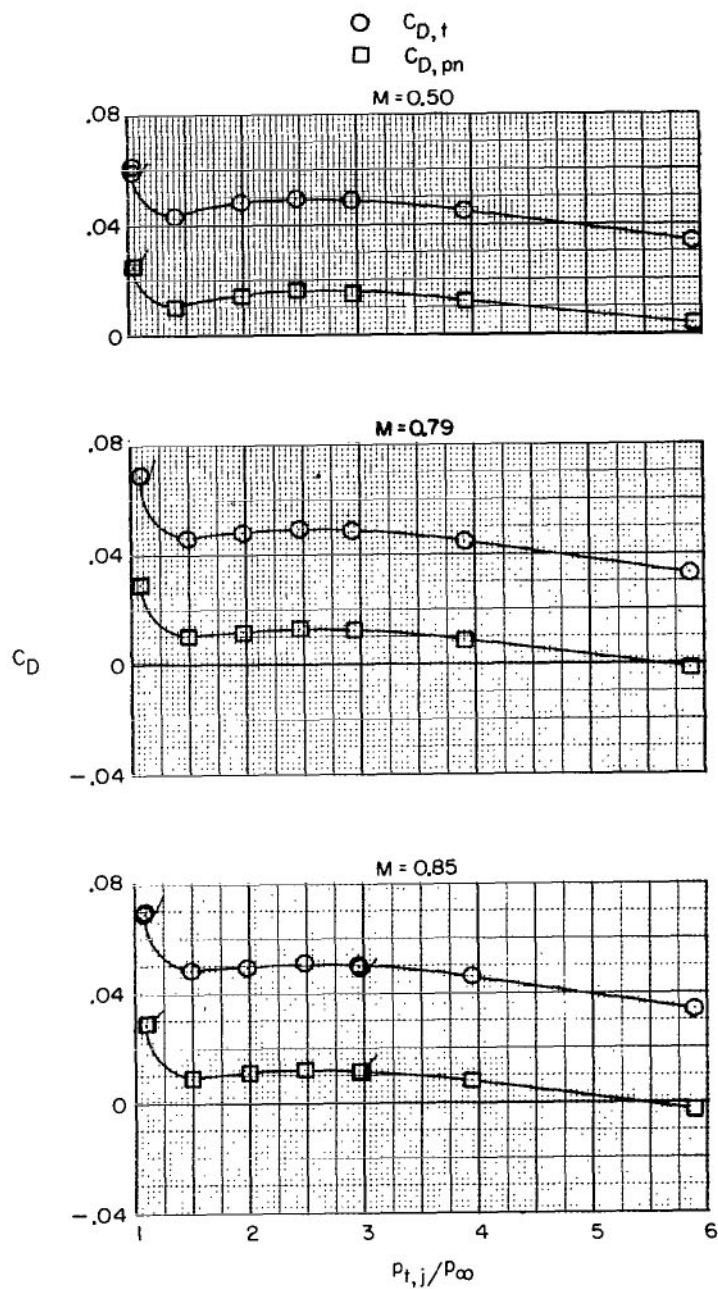
Figure 9.- Continued.

(e) Fully contoured afterbody + dry power nozzle.
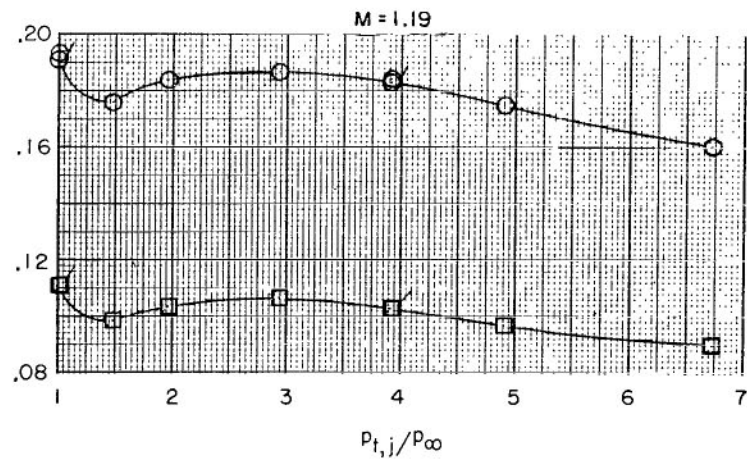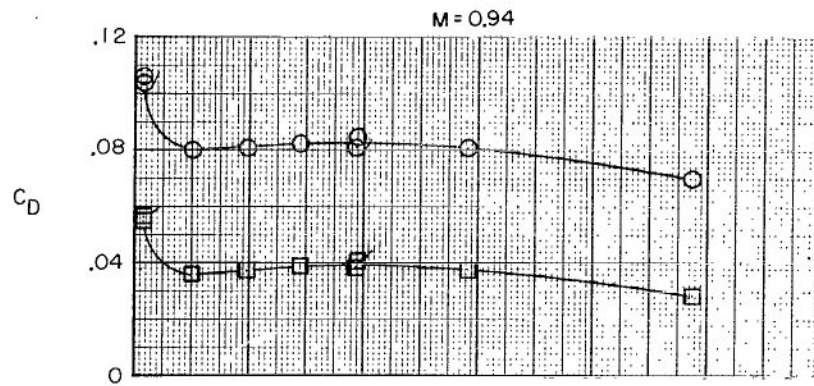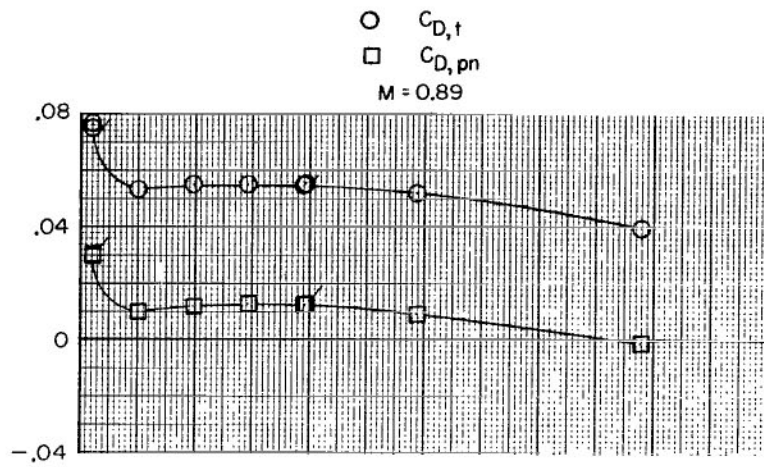
Figure 9.- Continued.

(e) Concluded.

Figure 9.- Continued.
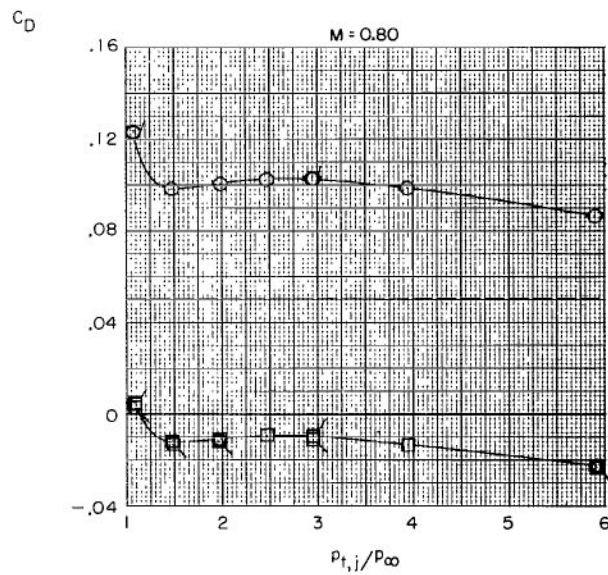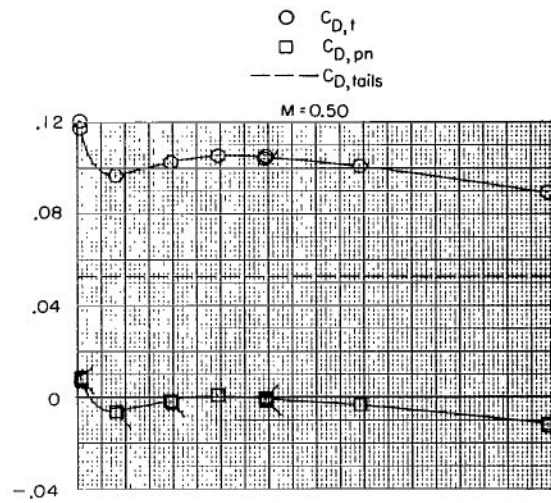
(f) Basic afterbody + forward vertical tail + aft horizontal tail + dry power nozzle.
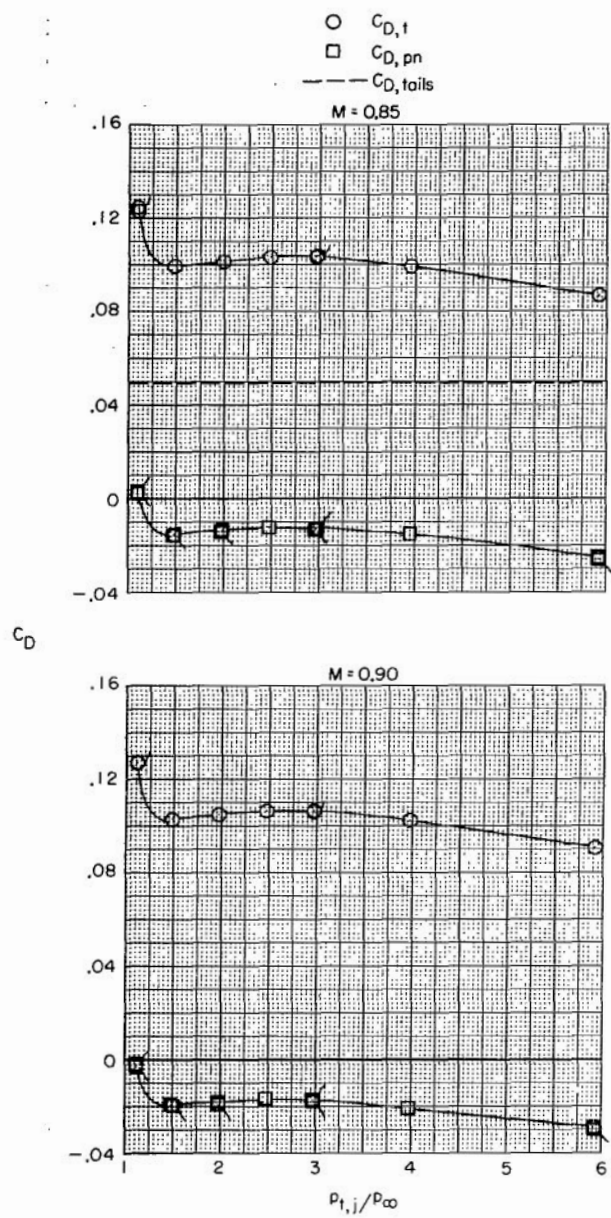
Figure 9.- Continued.

(f) Continued.

Figure 9.- Continued.
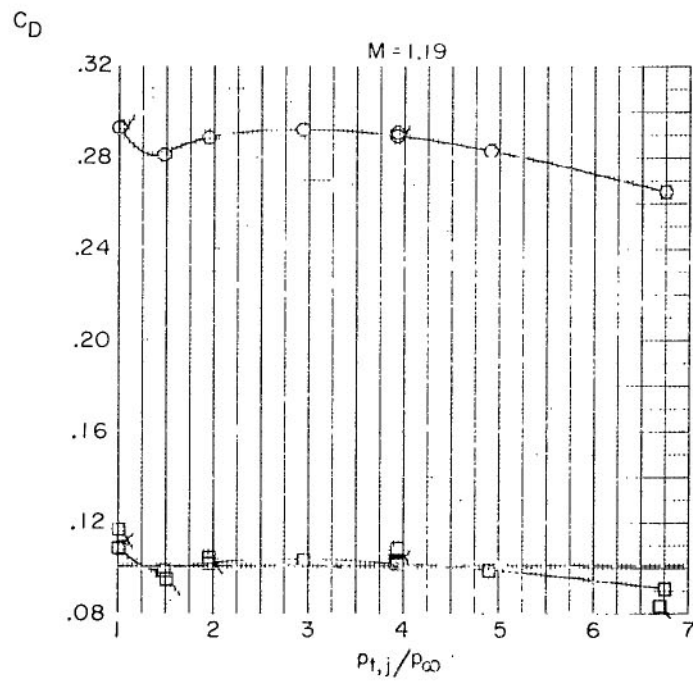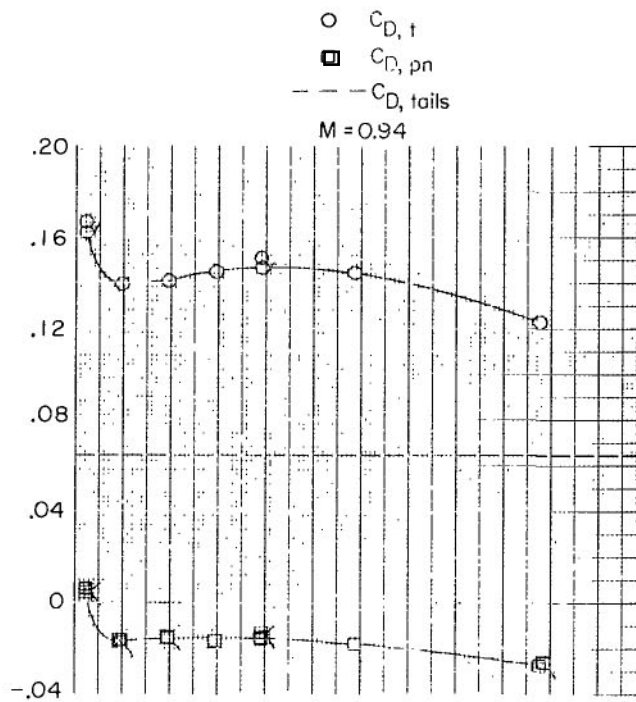
(f) Concluded.

Figure 9.- Continued.
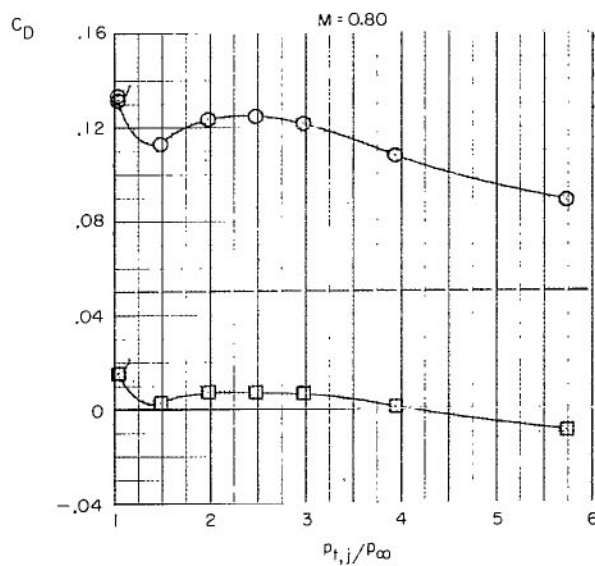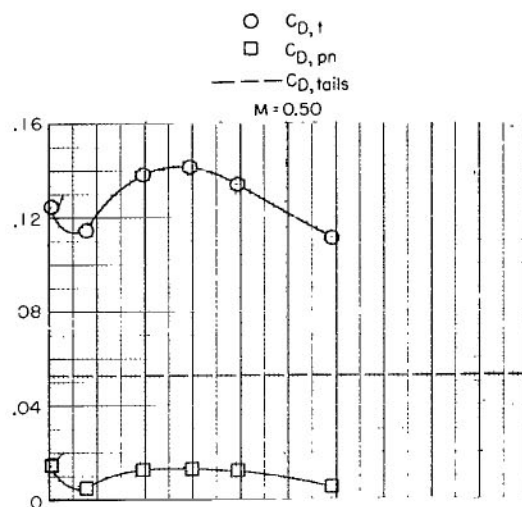
(g) Basic afterbody + forward vertical tail + aft horizontal tail
+ max. A/B power nozzle.
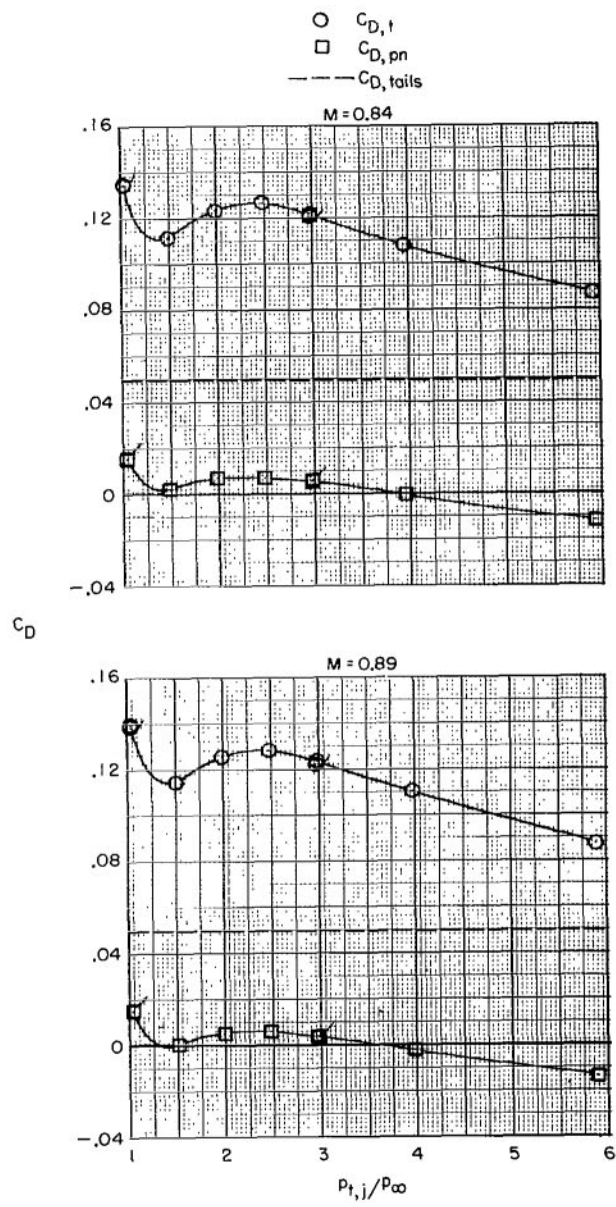
Figure 9.- Continued.

(g) Continued.

Figure 9.- Continued.

Legend:
- ○ $C_{D,t}$
- □ $C_{D,pn}$
- — — — $C_{D,tails}$

$M = 0.94$

$M = 1.19$

$p_{t,j}/p_\infty$
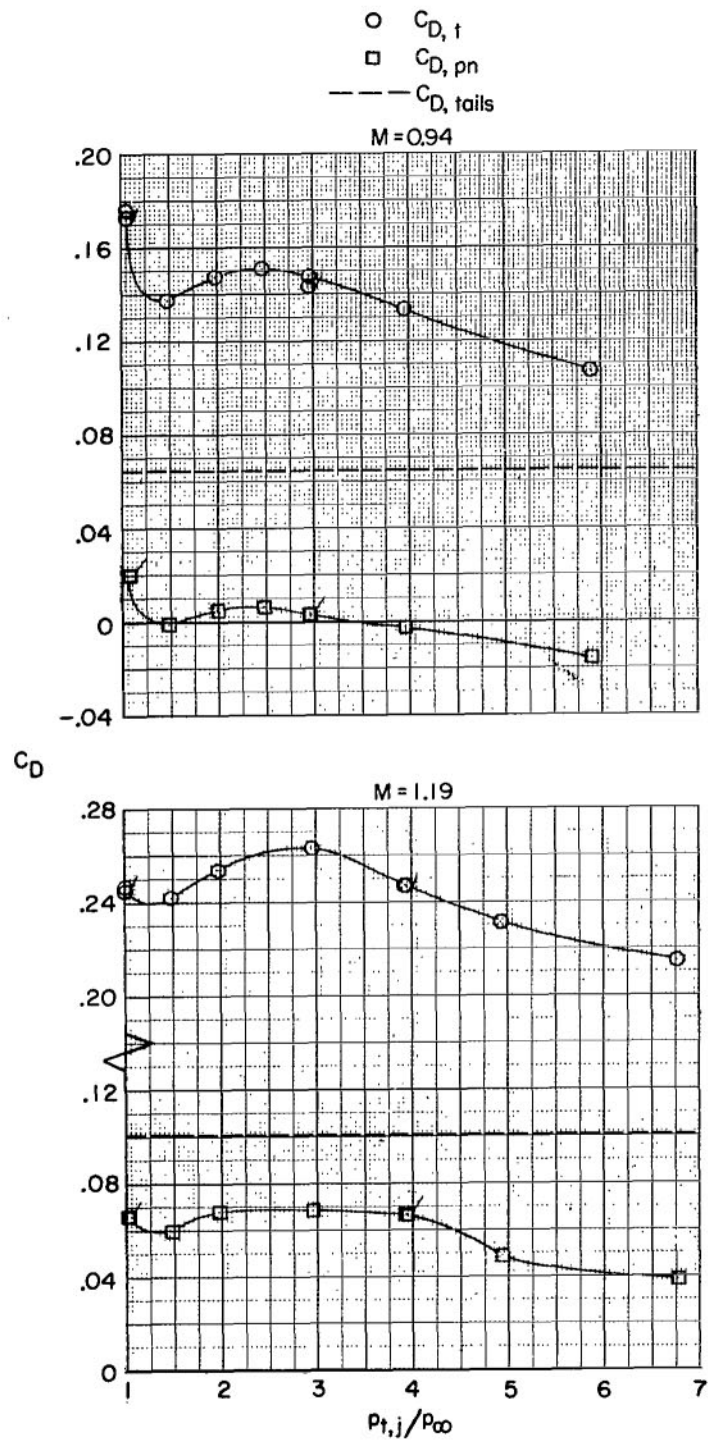
(g) Continued.
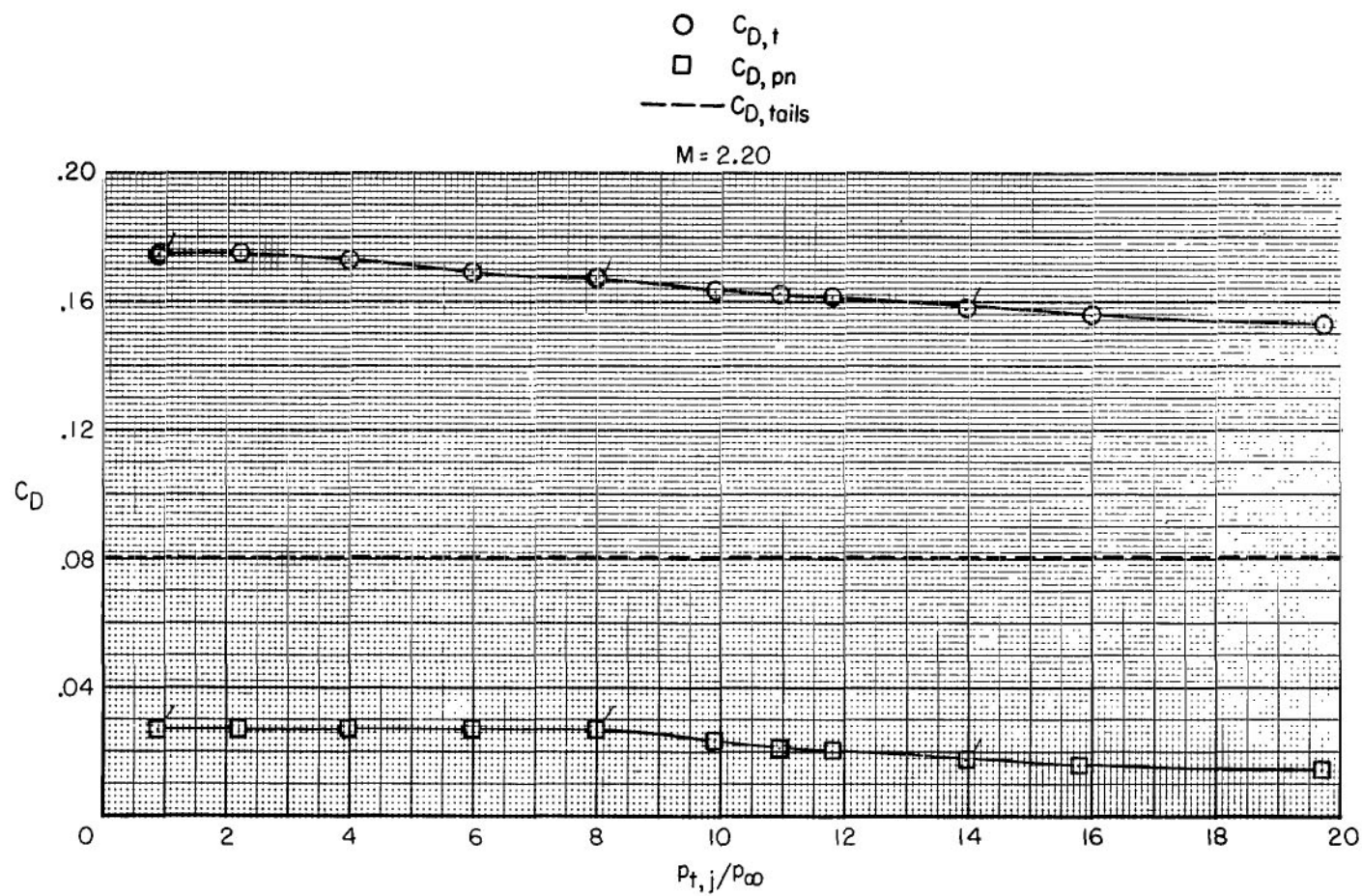
Figure 9.- Continued.

(g) Concluded.

Figure 9.- Continued.

C_D
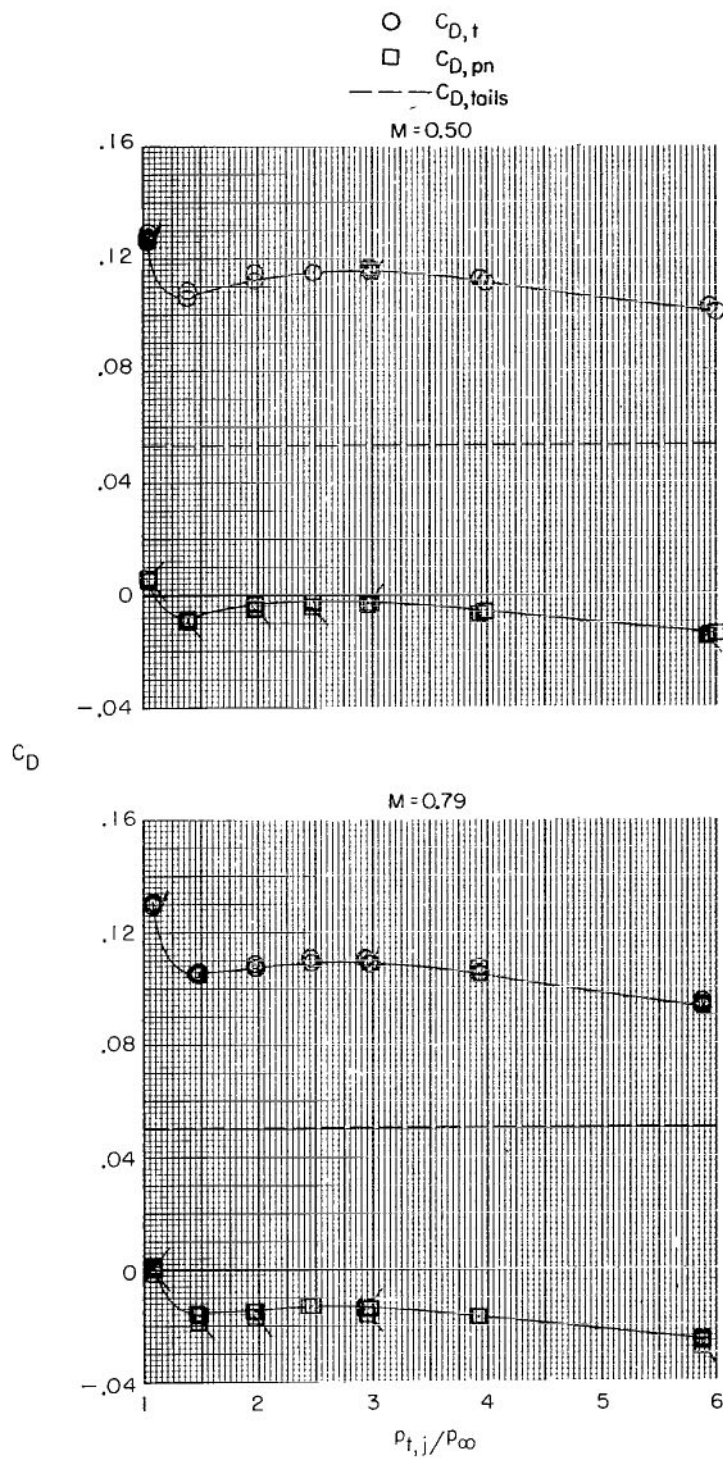
(h) Basic afterbody + aft vertical tail + aft horizontal tail
+ dry power nozzle.
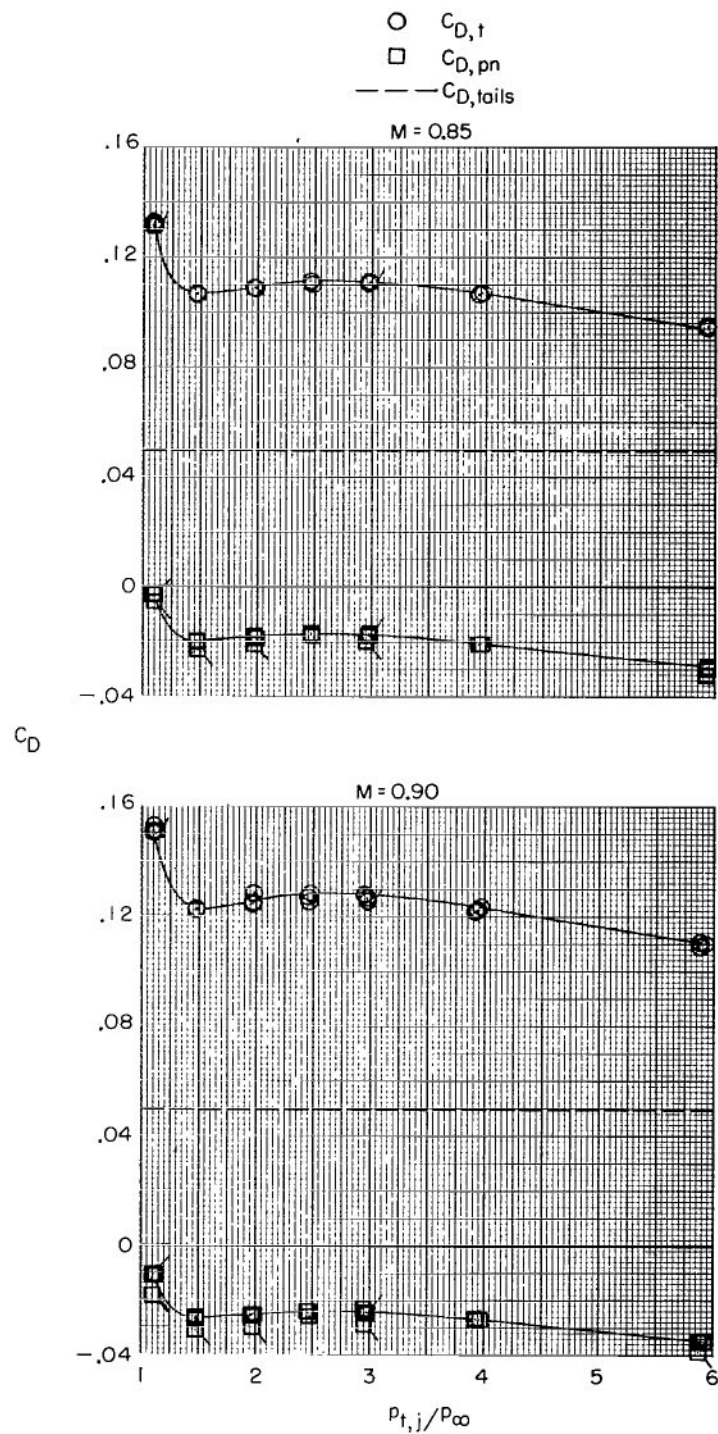
Figure 9.- Continued.

(h) Continued.

Figure 9.- Continued.
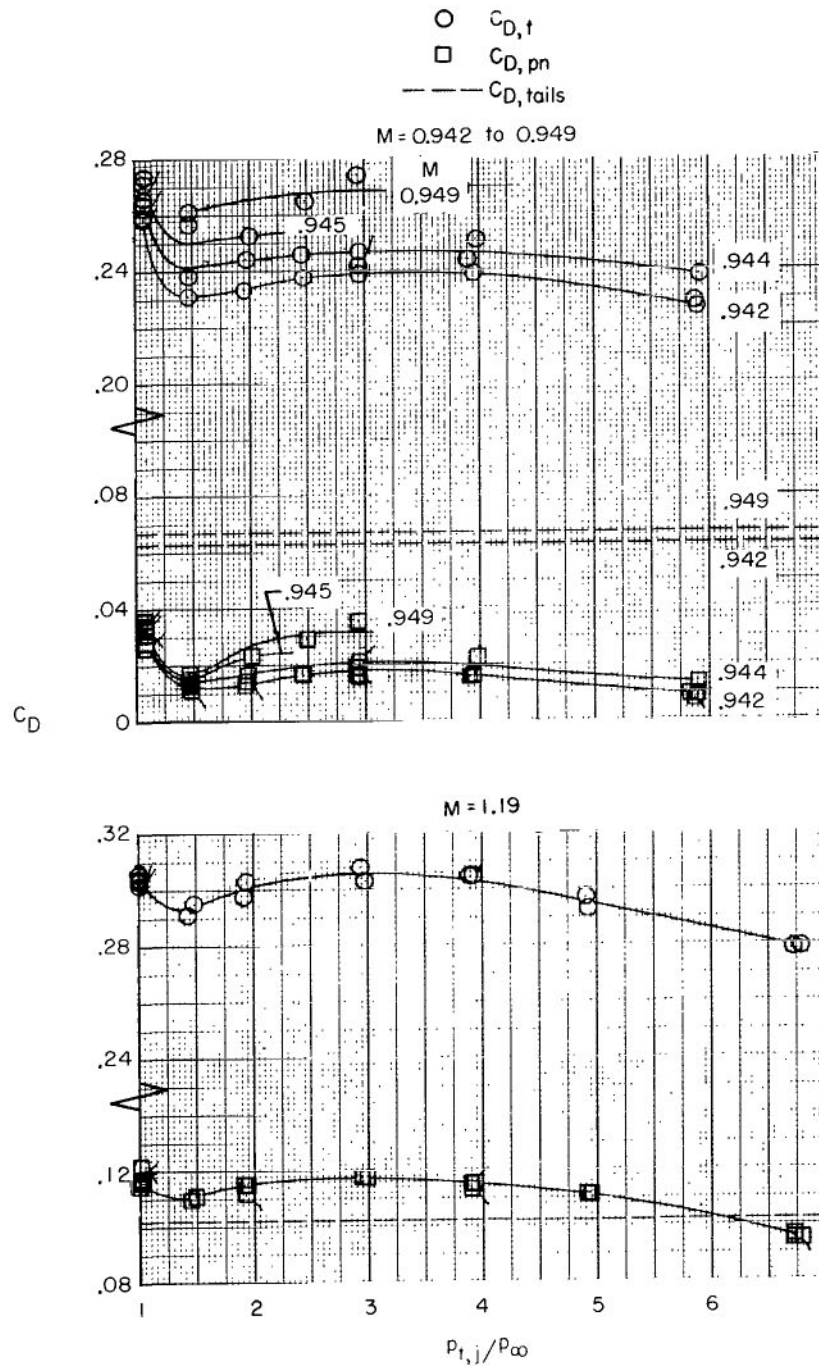
(h) Concluded.

Figure 9.- Continued.
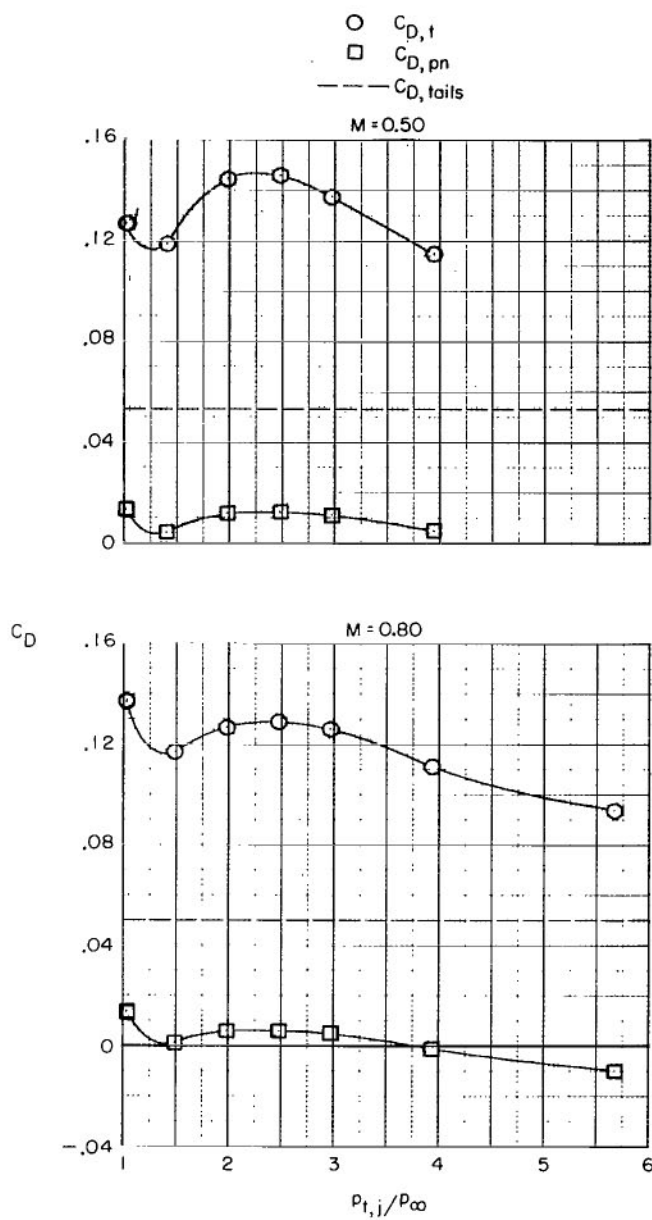
(i) Basic afterbody + aft vertical tail + aft horizontal tail
+ max. A/B power nozzle.
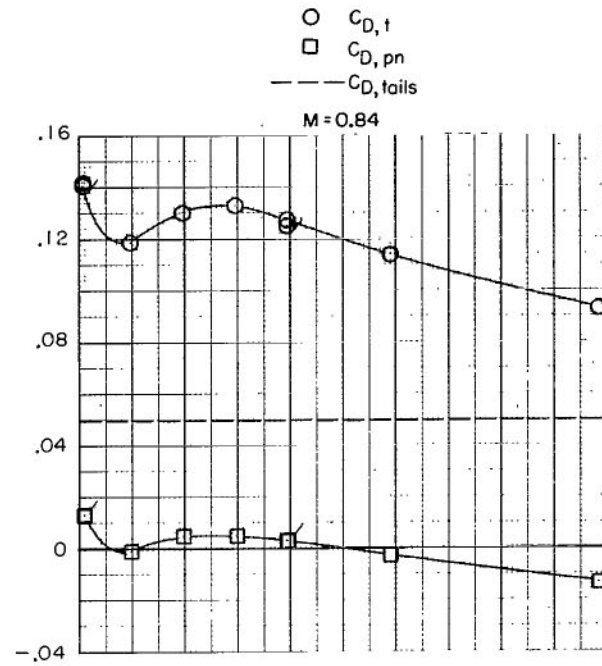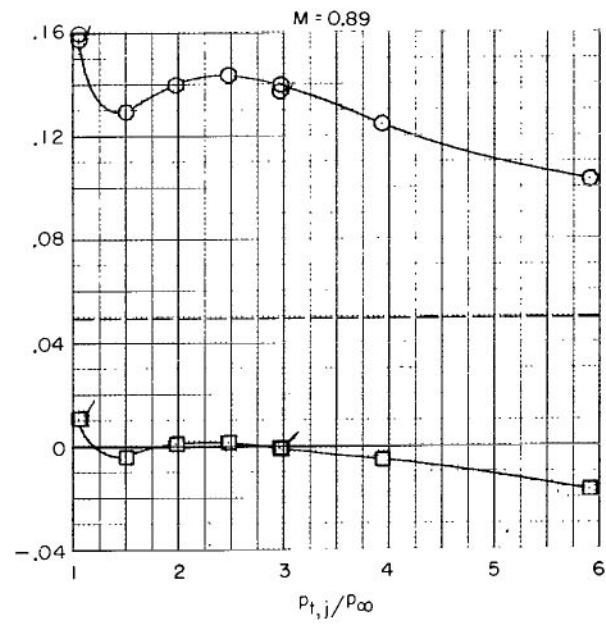
Figure 9.- Continued.

(i) Continued.

Figure 9.- Continued.

Legend:

○ $C_{D,t}$
□ $C_{D,pn}$
— — — $C_{D,tails}$

$M = 0.943$

$M = 1.18$

$\dfrac{p_{t,j}}{p_\infty}$
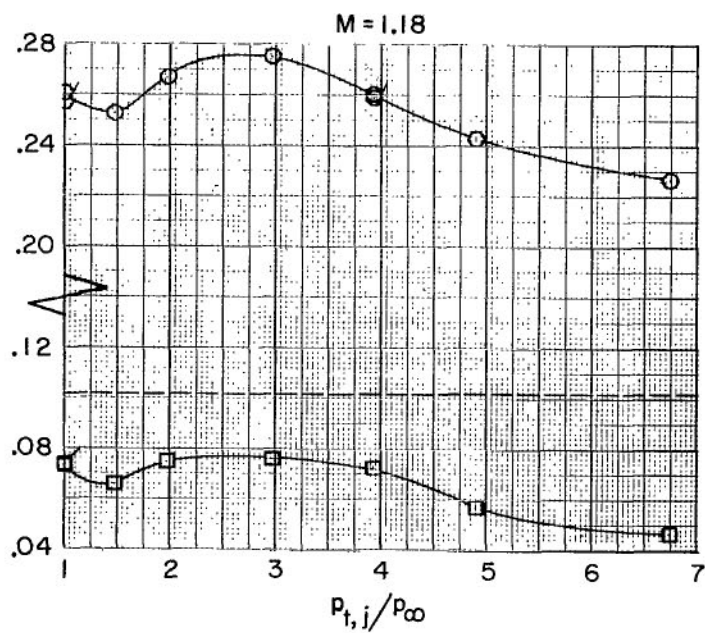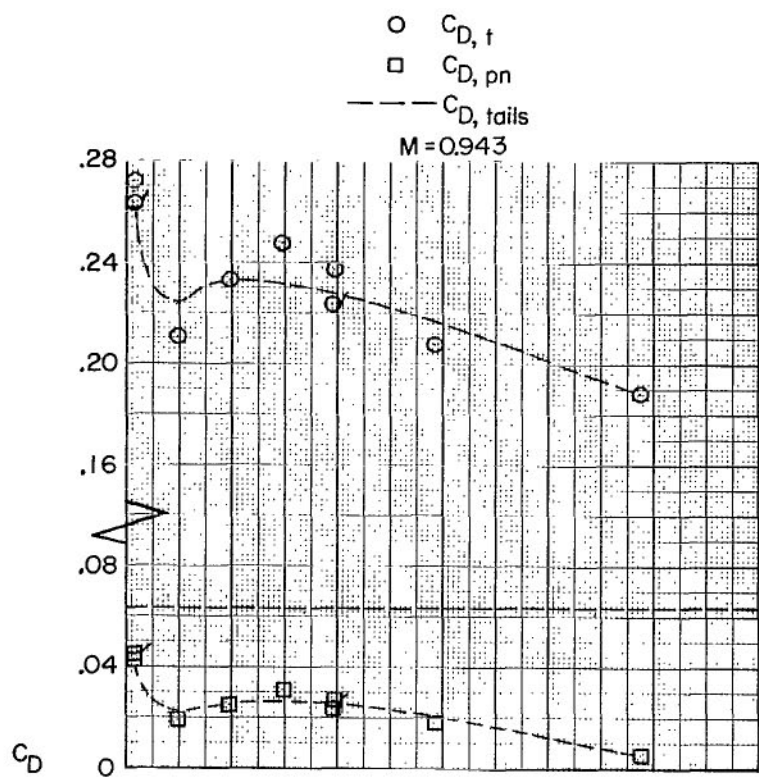
(i) Continued.
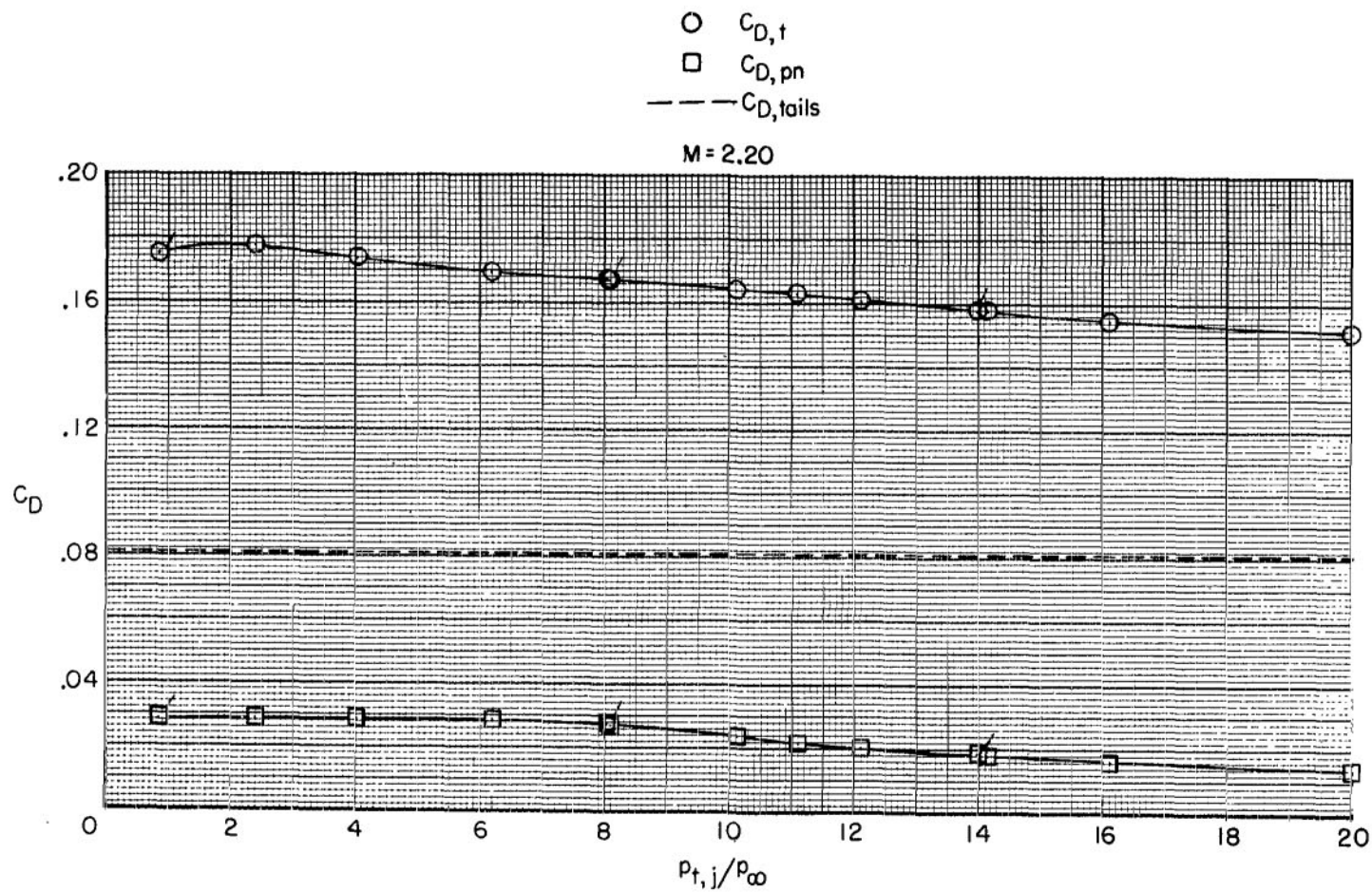
Figure 9.- Continued.

(i) Concluded.

Figure 9.- Continued.
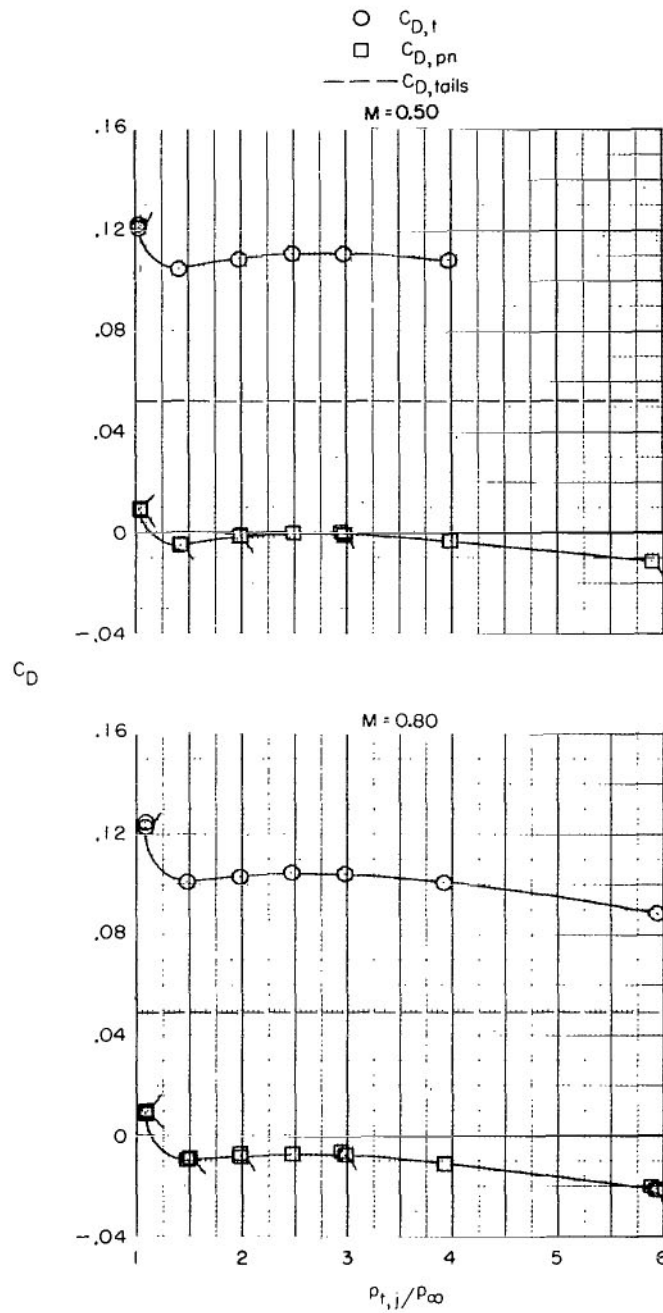
(j) Basic afterbody + forward vertical tail + forward horizontal tail + dry power nozzle.
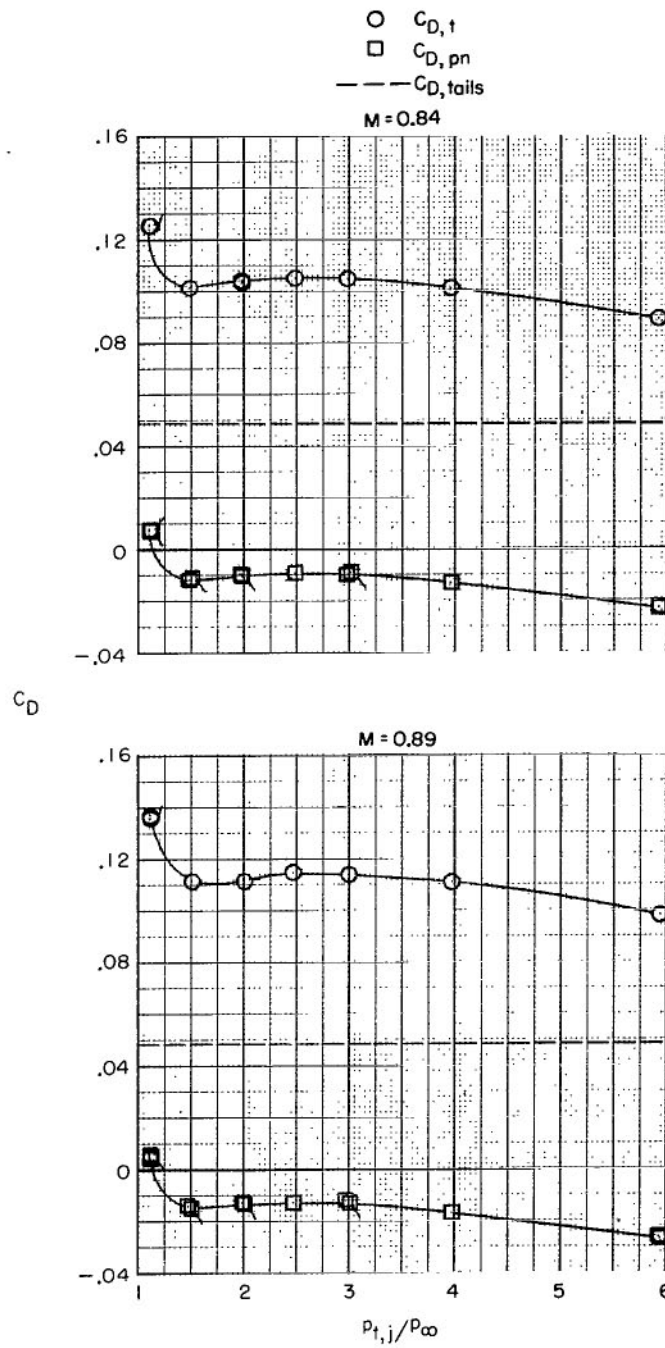
Figure 9.- Continued.

(j) Continued.

Figure 9.- Continued.
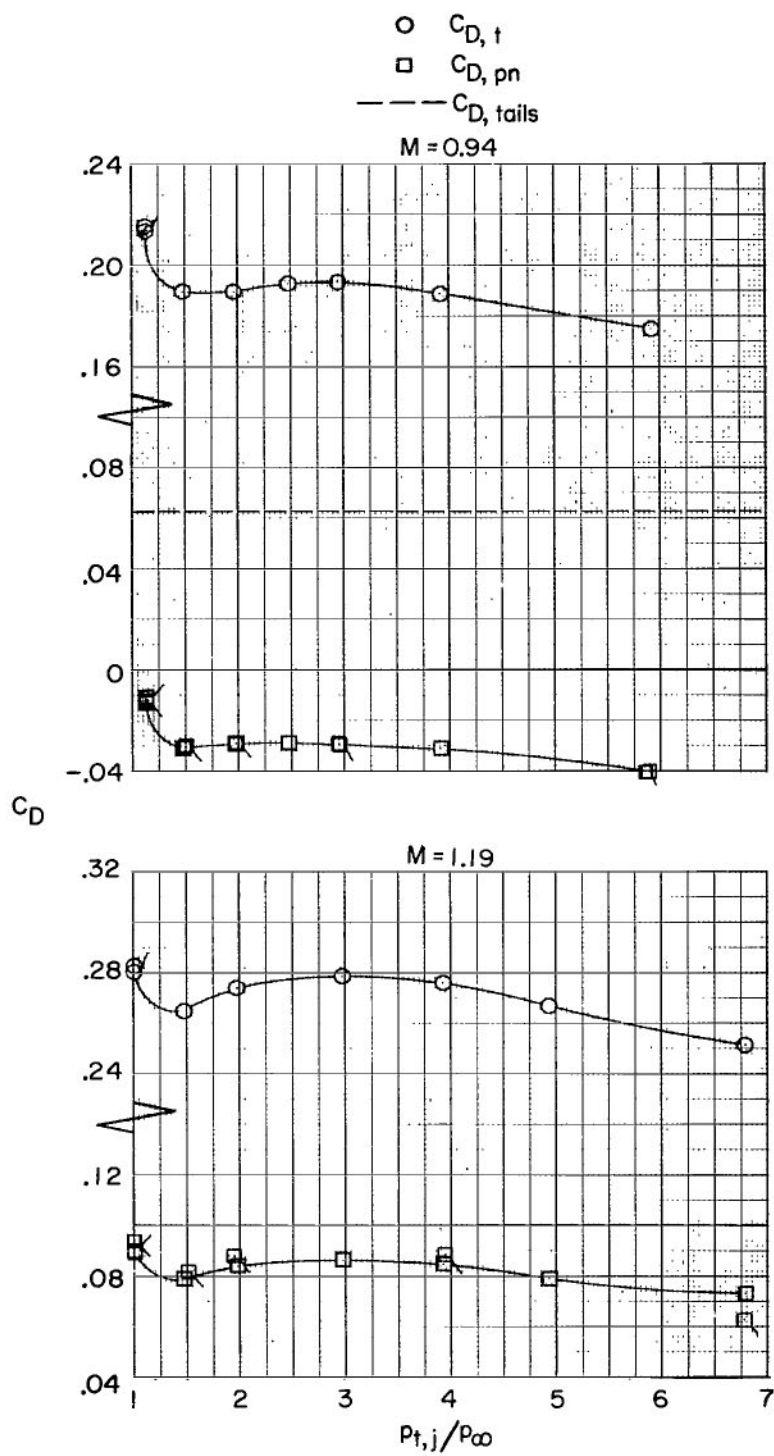
(j) Concluded.

Figure 9.- Continued.
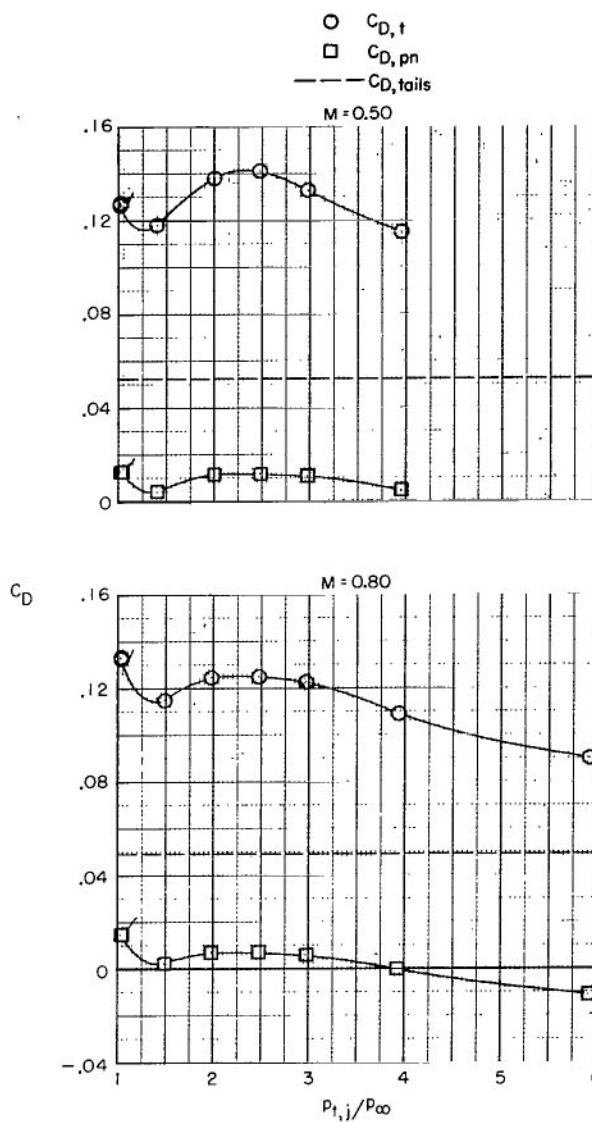
(k) Basic afterbody + forward vertical tail + forward horizontal tail
+ max. A/B power nozzle.
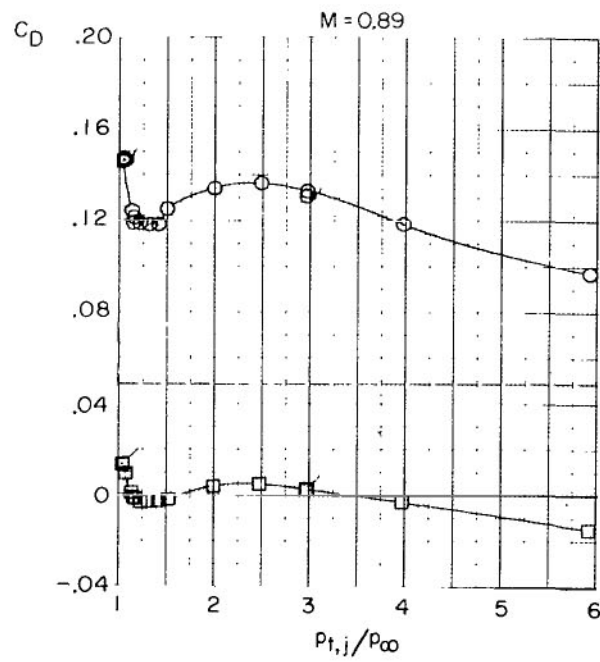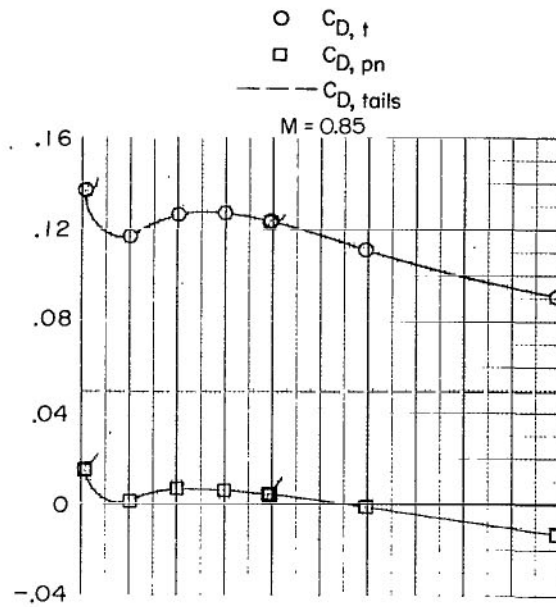
Figure 9.- Continued.

(k) Continued.
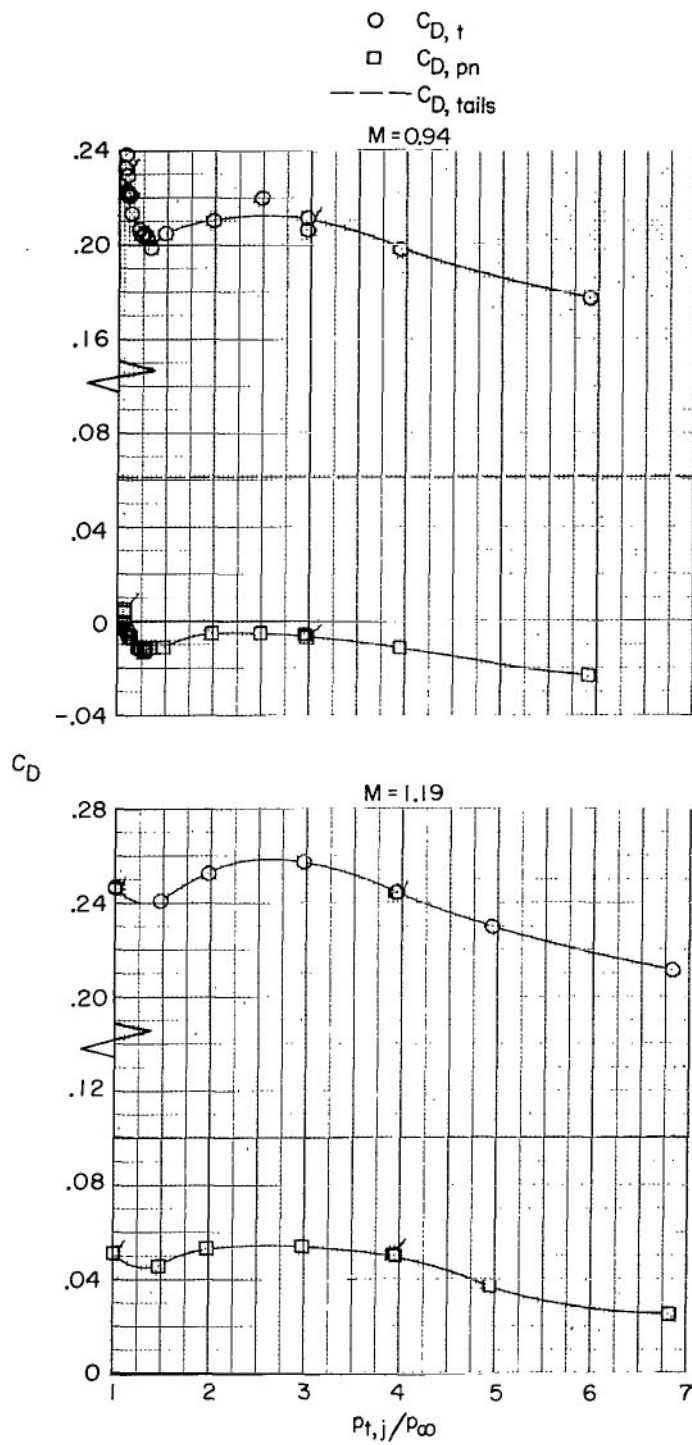
Figure 9.- Continued.

(k) Continued.
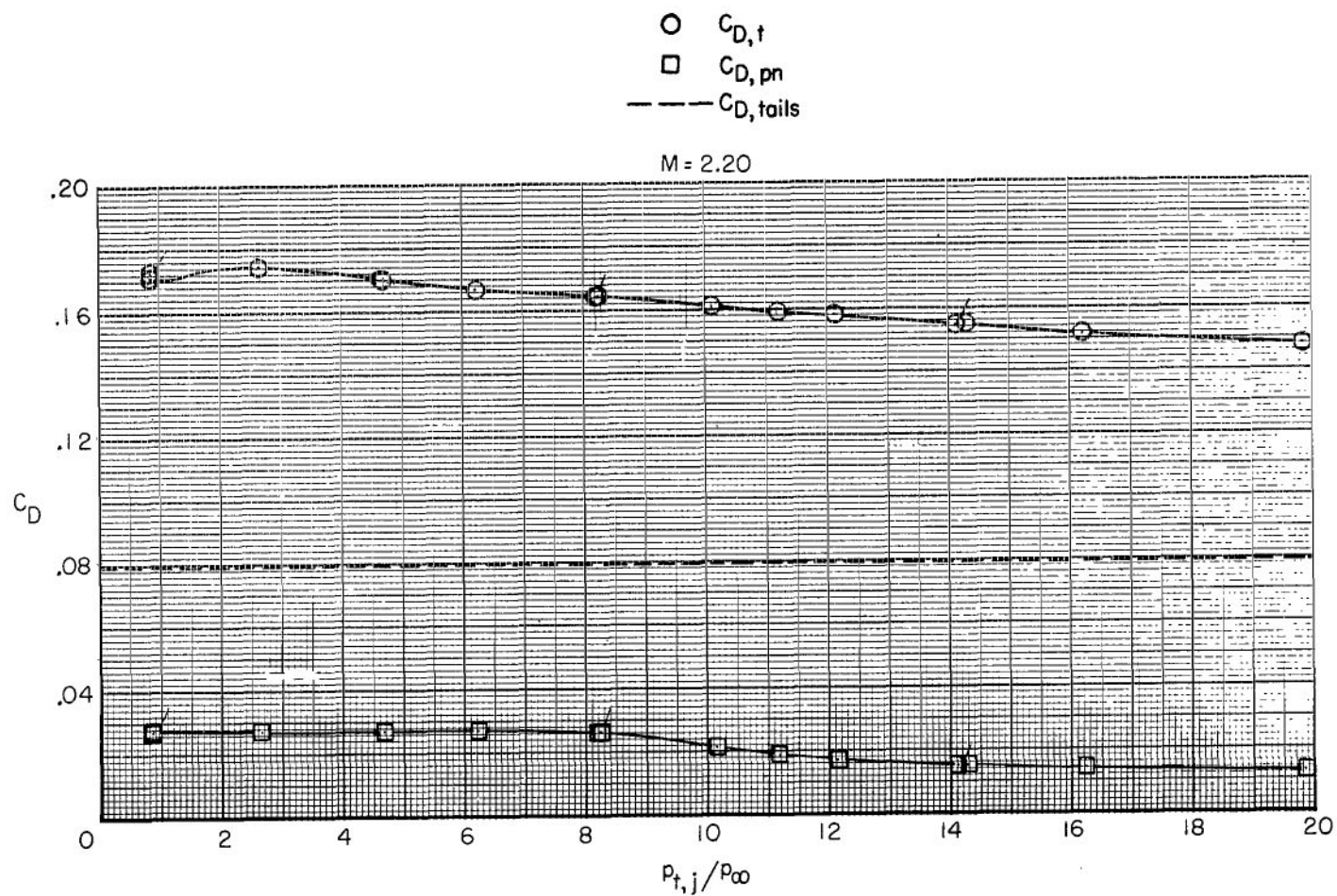
Figure 9.- Continued.

(k) Concluded.

Figure 9.- Continued.
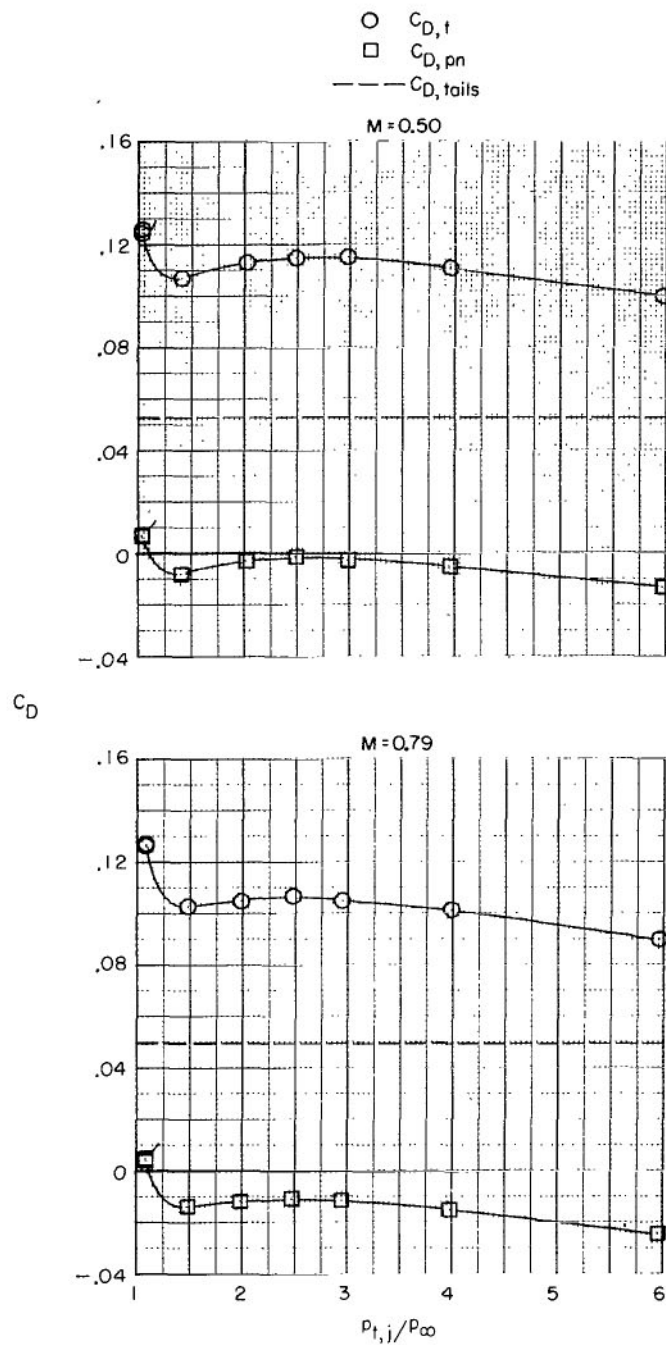
(1) Basic afterbody + aft vertical tail + forward horizontal tail
+ dry power nozzle.

Figure 9.- Continued.

(1) Continued.

Figure 9.- Continued.

Legend:
○ $C_{D,t}$
□ $C_{D,pn}$
— — — $C_{D,tails}$

M = 0.94

M = 1.18

$p_{t,j}/p_\infty$

(1) Concluded.

Figure 9.- Continued.

Legend:
- ○ $C_{D,t}$
- □ $C_{D,pn}$
- --- $C_{D,tails}$

$M = 0.50$

$M = 0.80$

C_D

$p_{t,j}/p_\infty$
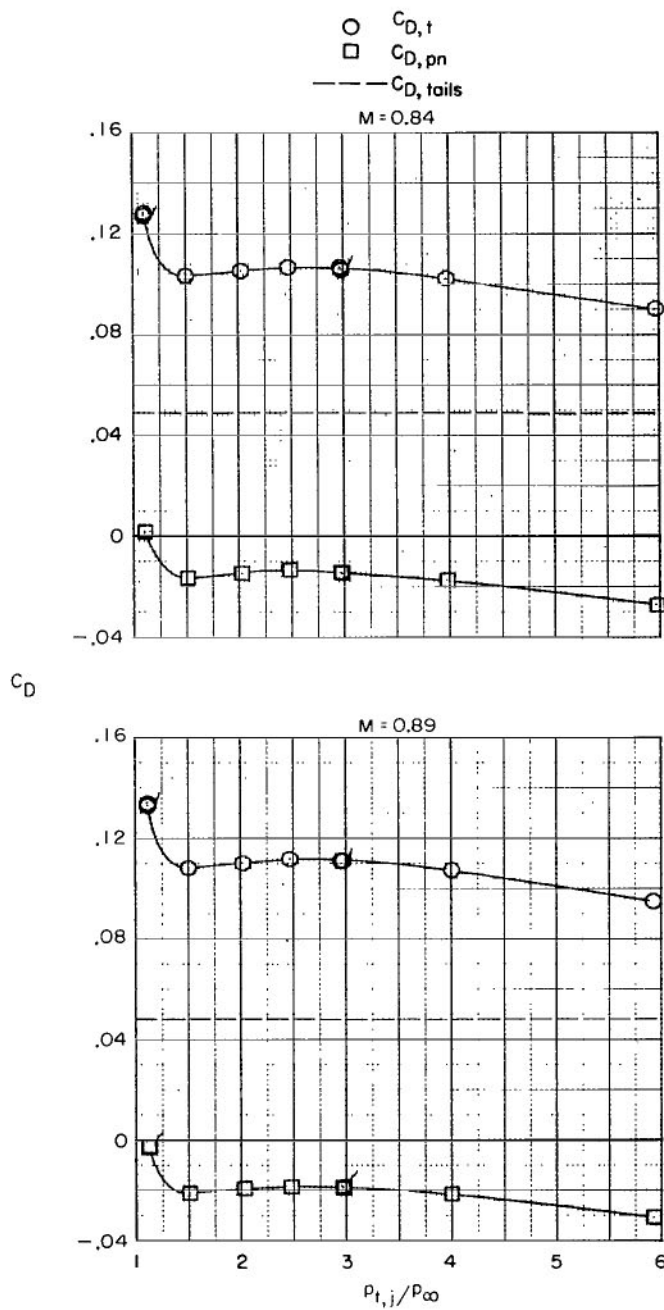
(m) Basic afterbody + forward vertical tail + low, forward horizontal tail + dry power nozzle.
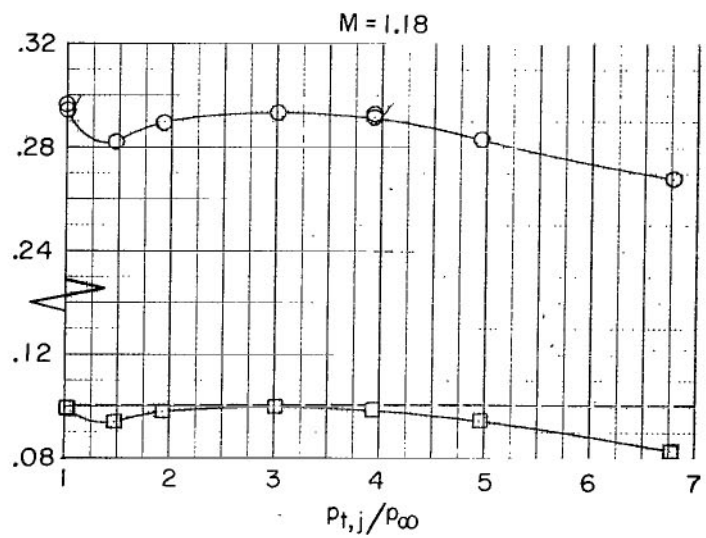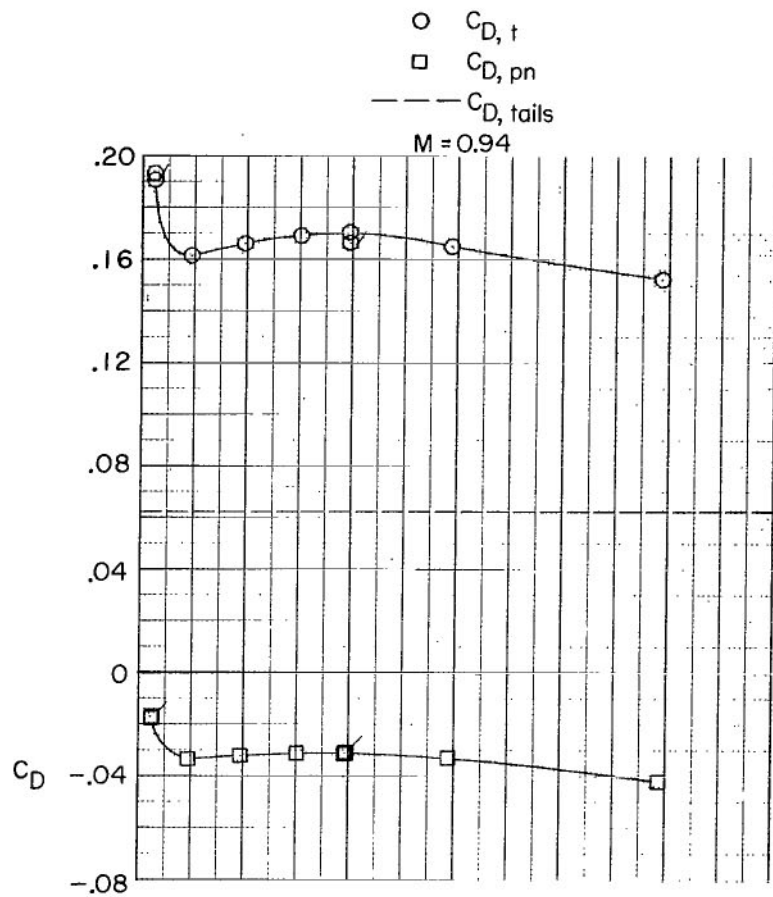
Figure 9.- Continued.

(m) Continued.

Figure 9.- Continued.

Legend:
○ $C_{D,t}$
□ $C_{D,pn}$
— — — $C_{D,tails}$

$M = 0.94$

$M = 1.18$

$p_{t,j}/p_\infty$
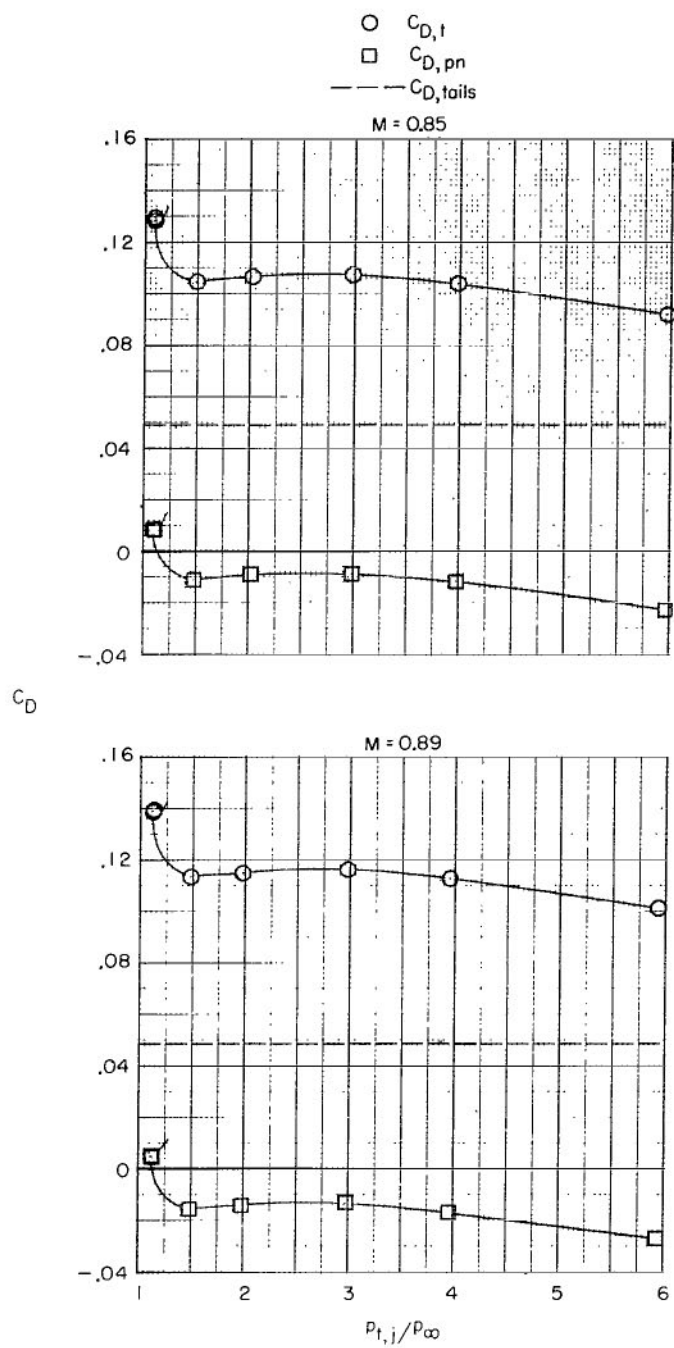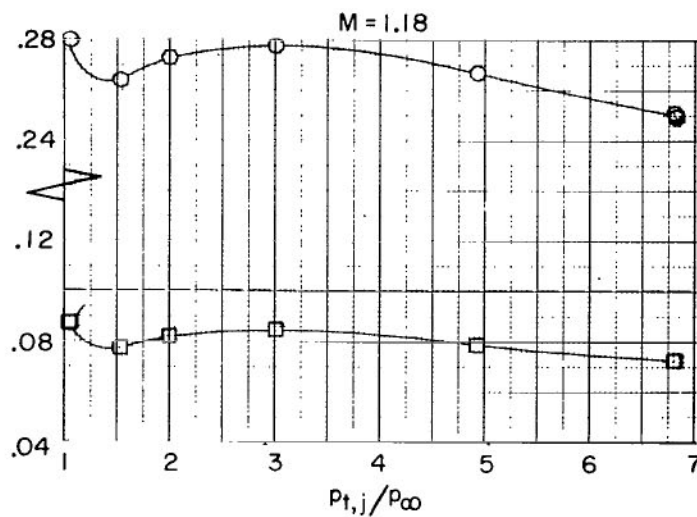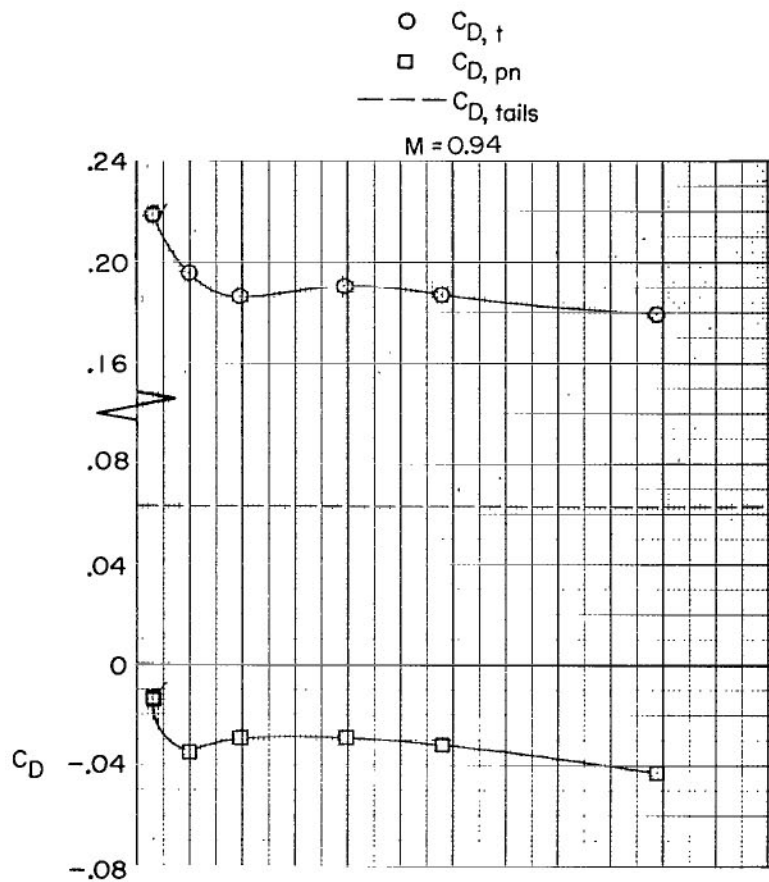
(m) Concluded.
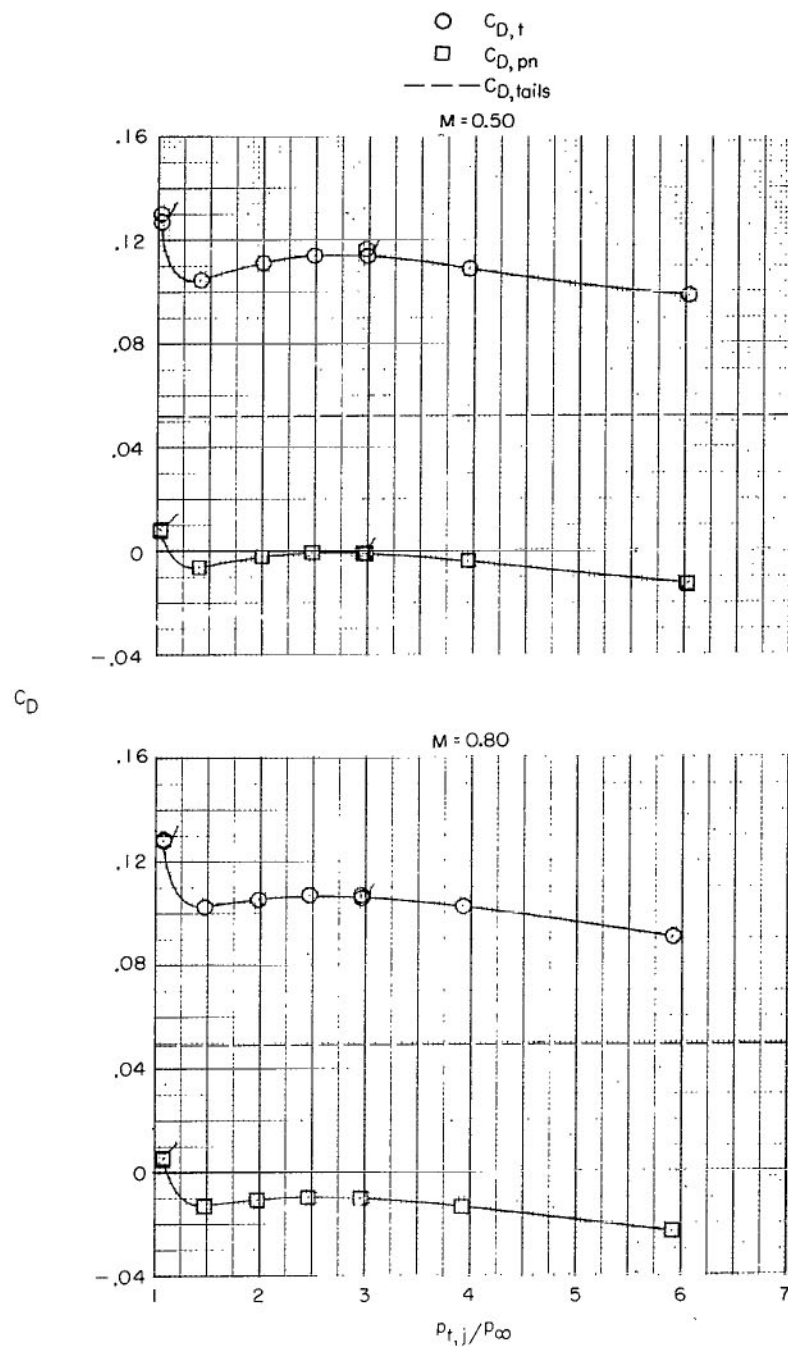
Figure 9.- Continued.

(n) Basic afterbody + forward vertical tail + aft horizontal tail
  + partial contour bumps + dry power nozzle.
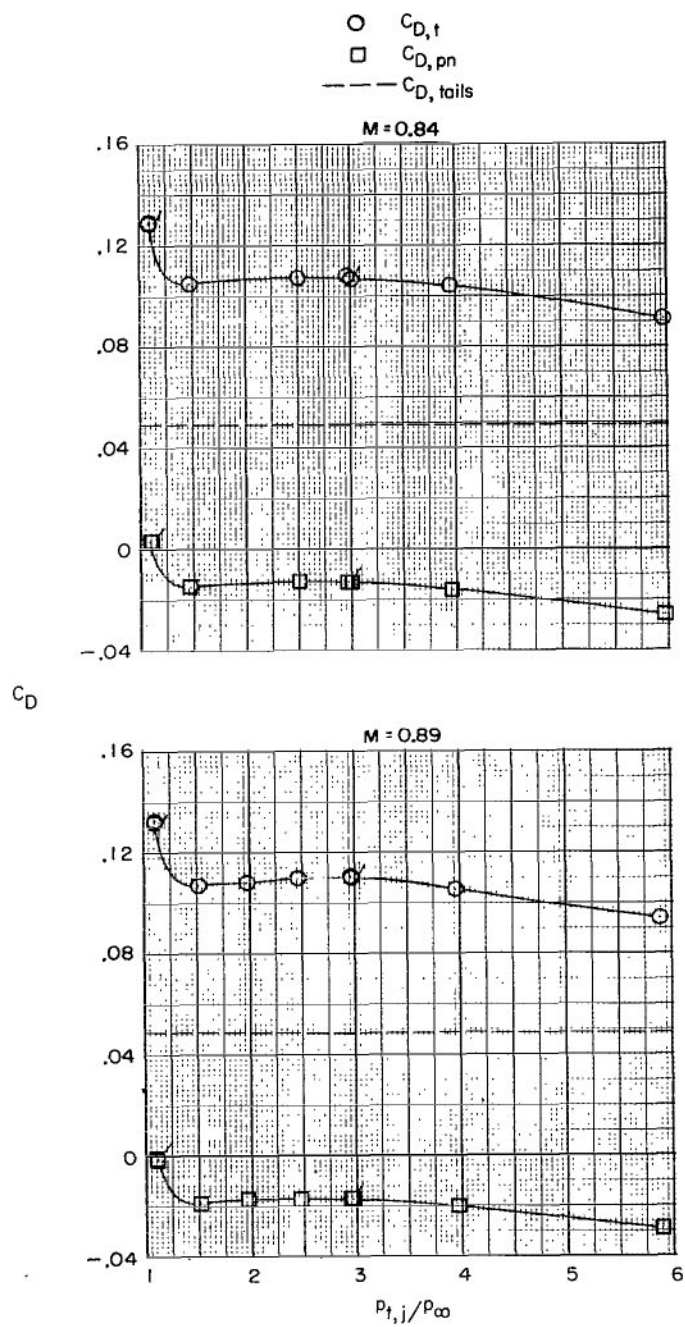
Figure 9.- Continued.

(n) Continued.

Figure 9.- Continued.
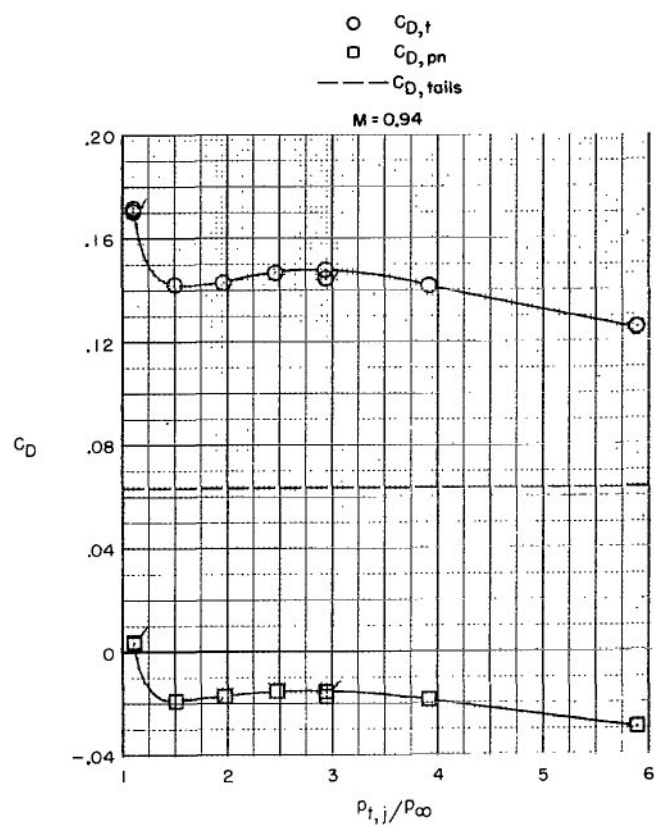
(n) Concluded.

Figure 9.- Continued.
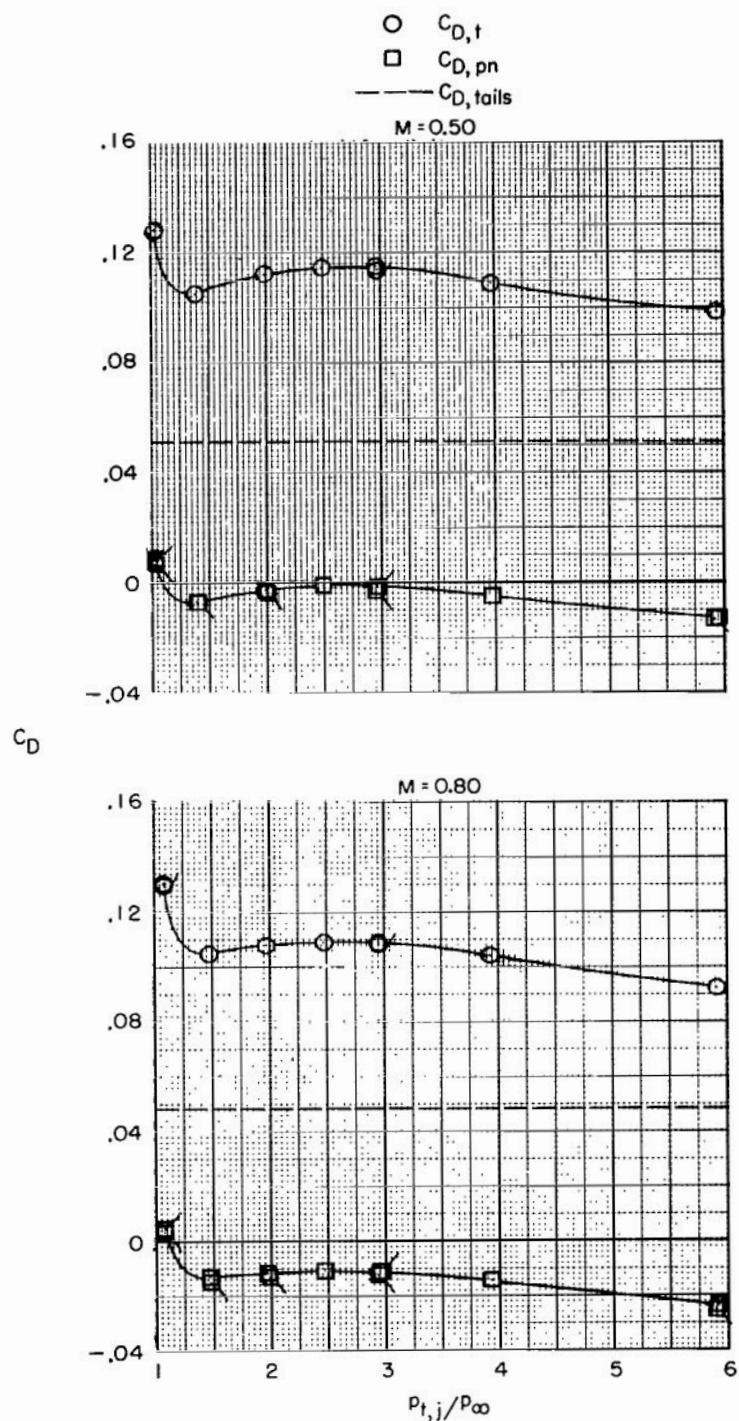
(o) Basic afterbody + forward vertical tail + aft horizontal tail
+ full contour bumps + dry power nozzle.

Figure 9.- Continued.

(o) Continued.

Figure 9.- Continued.

Legend:

○ $C_{D,t}$
□ $C_{D,pn}$
—— $C_{D,tails}$

$M = 0.94$

$M = 1.19$

C_D (vertical axis)

$p_{t,j}/p_\infty$ (horizontal axis)
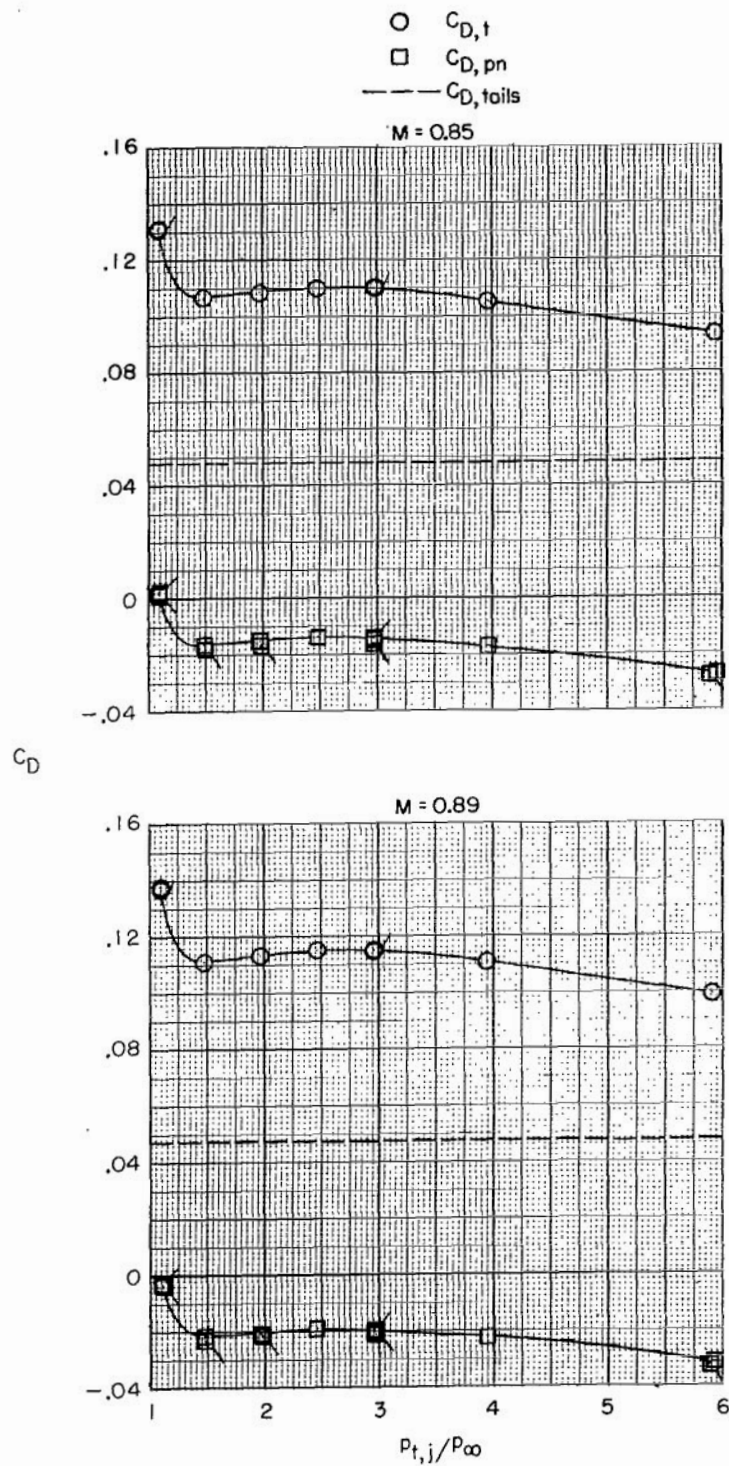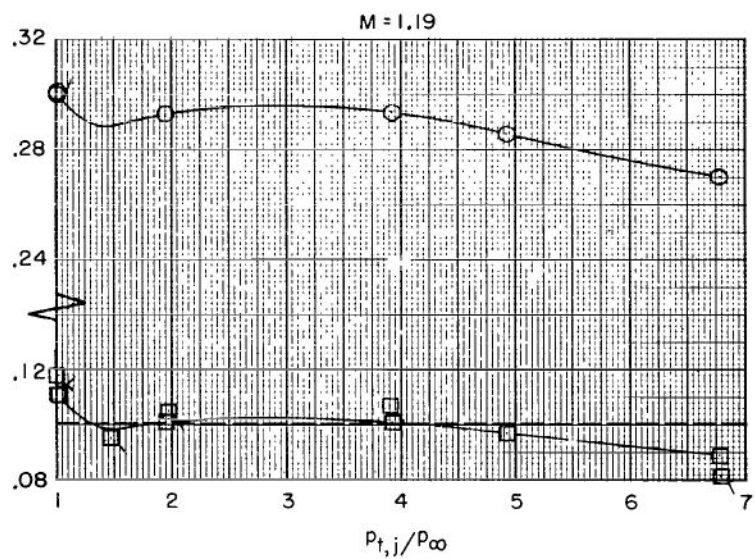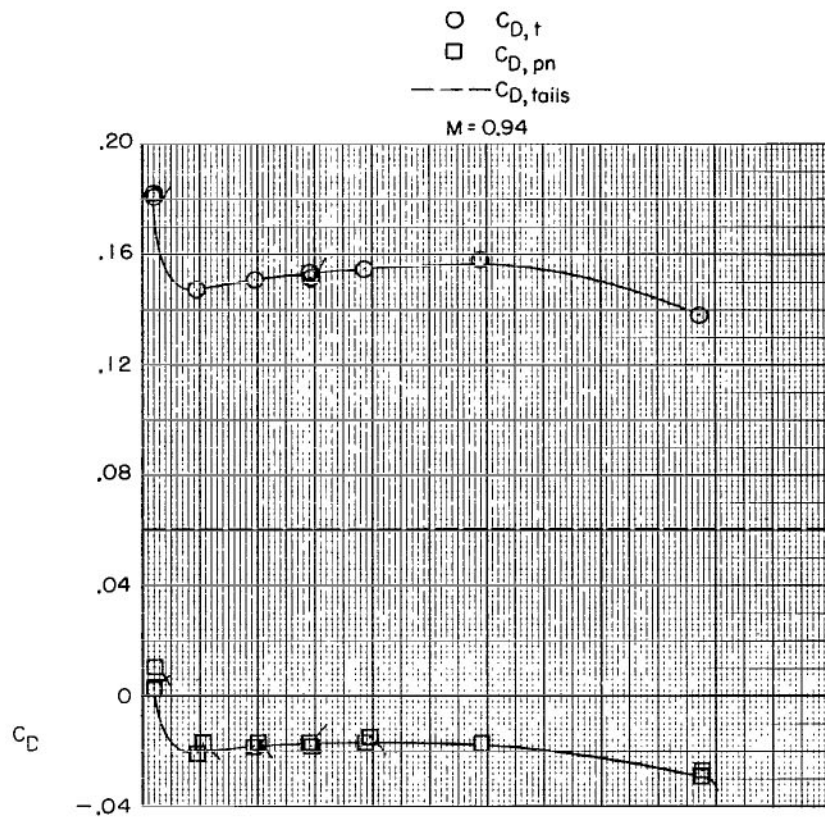
(o) Concluded.
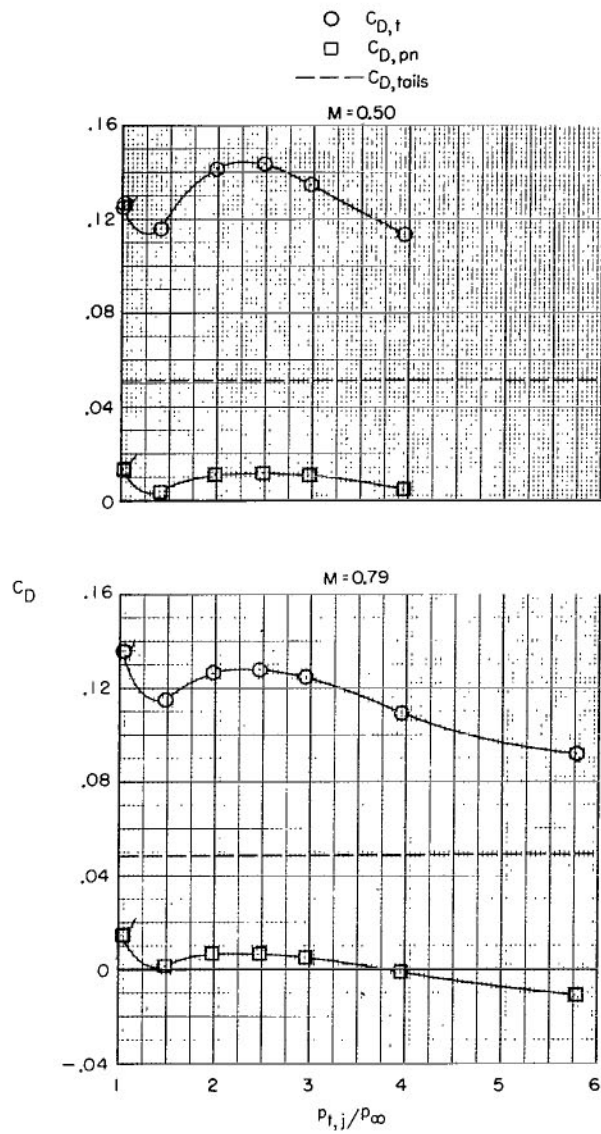
Figure 9.- Continued.

(p) Basic afterbody + forward vertical tail + aft horizontal tail
    + full contour bumps + max. A/B power nozzle.
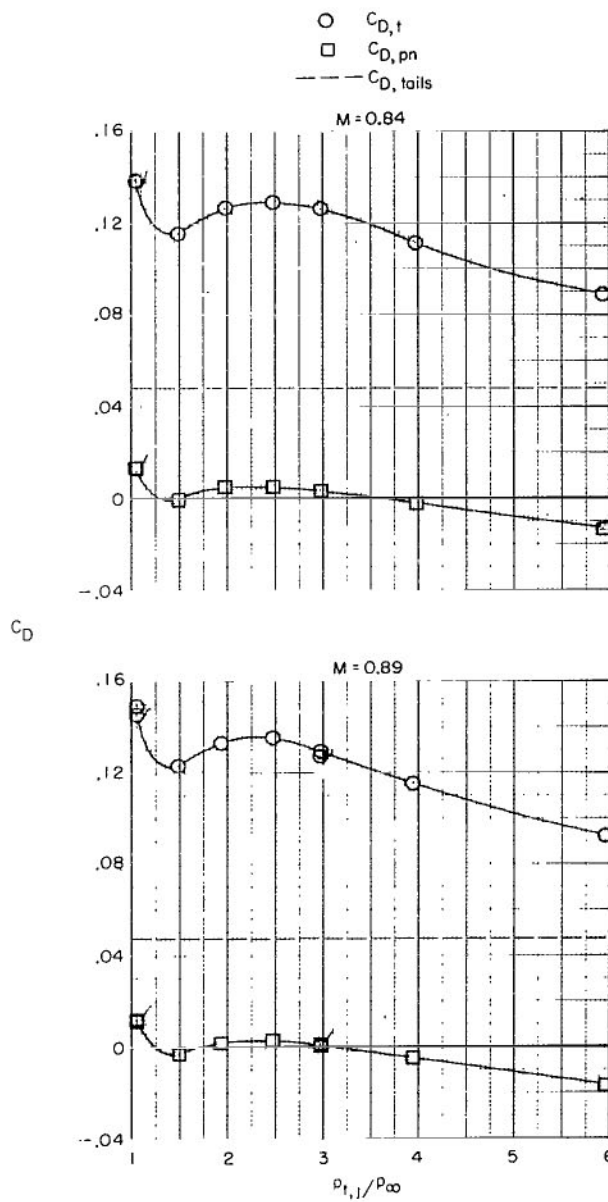
Figure 9.- Continued.

(p) Continued.
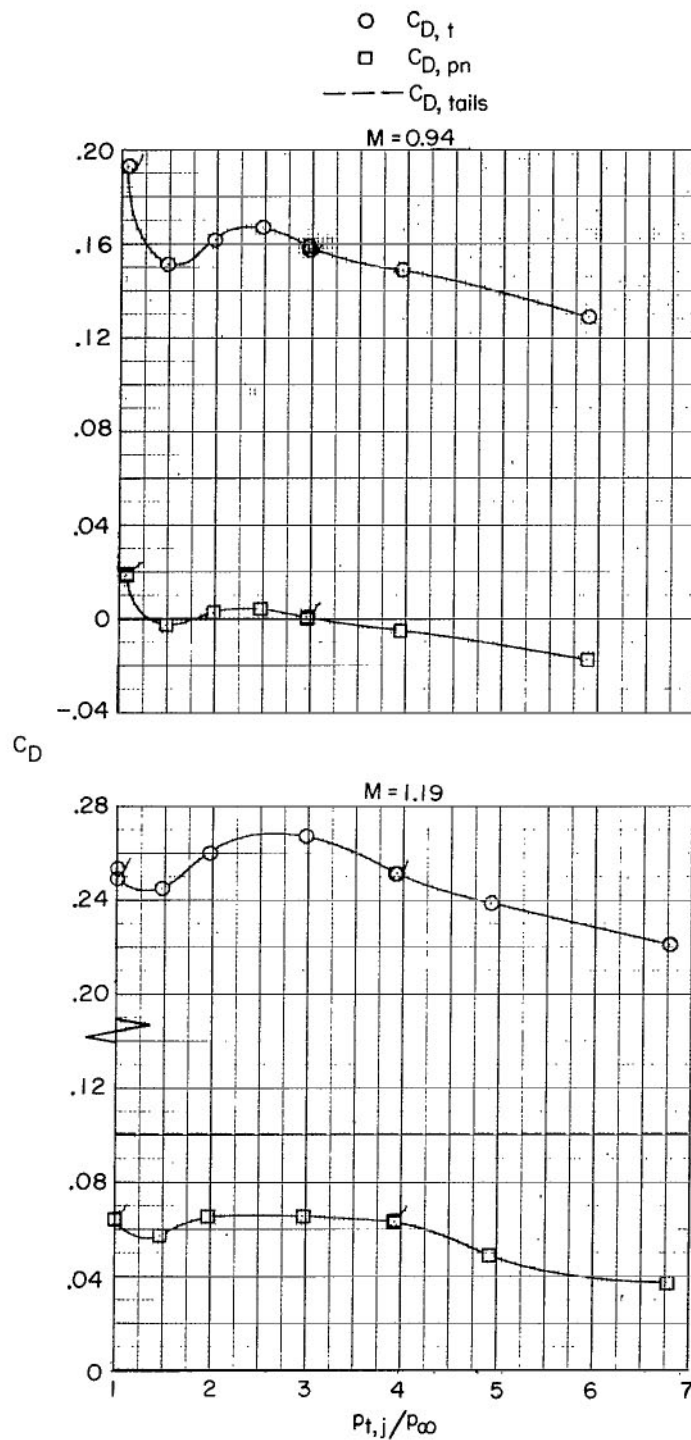
Figure 9.- Continued.

(p) Continued.
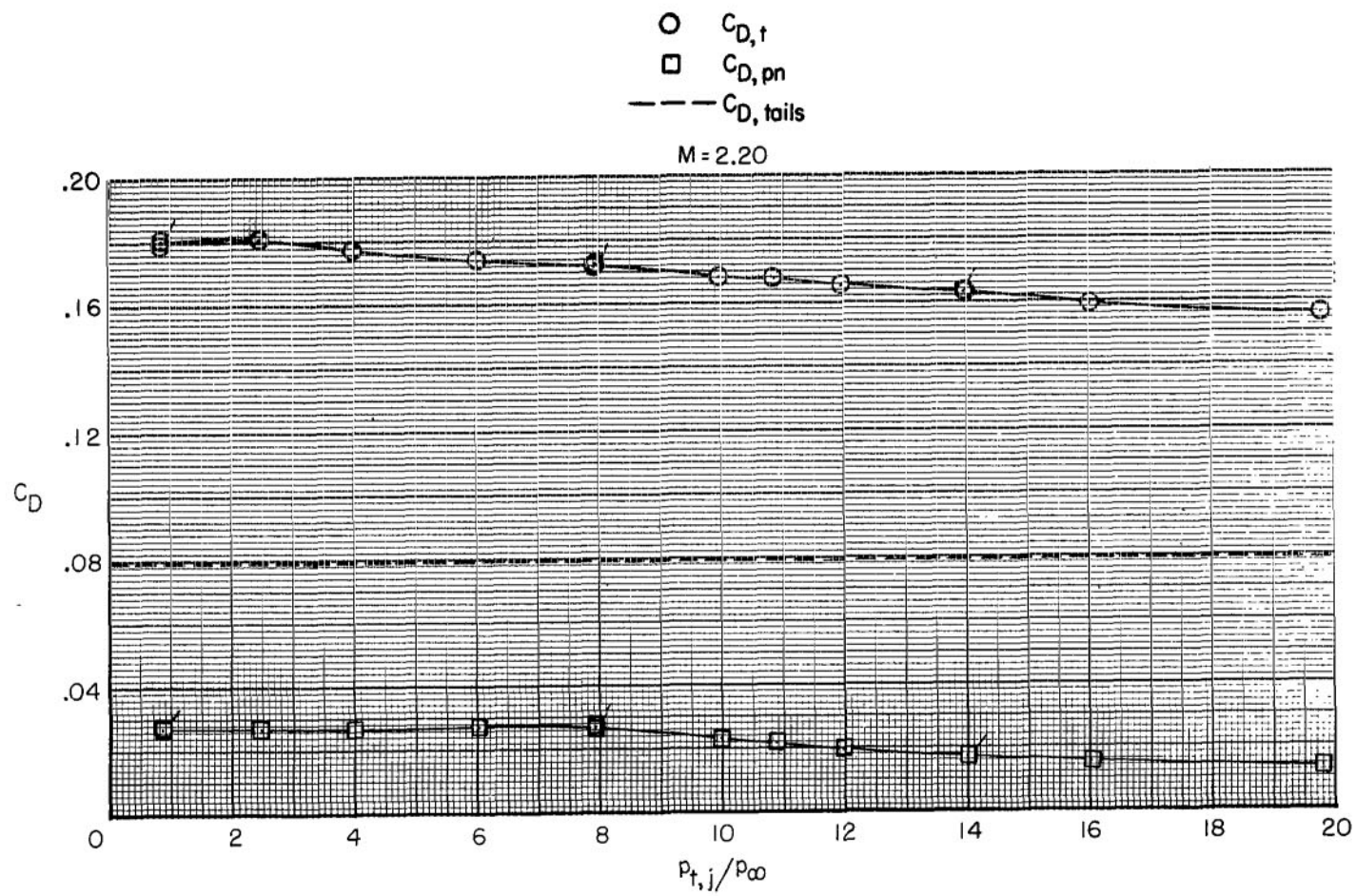
Figure 9.- Continued.

(p) Concluded.

Figure 9.- Continued.
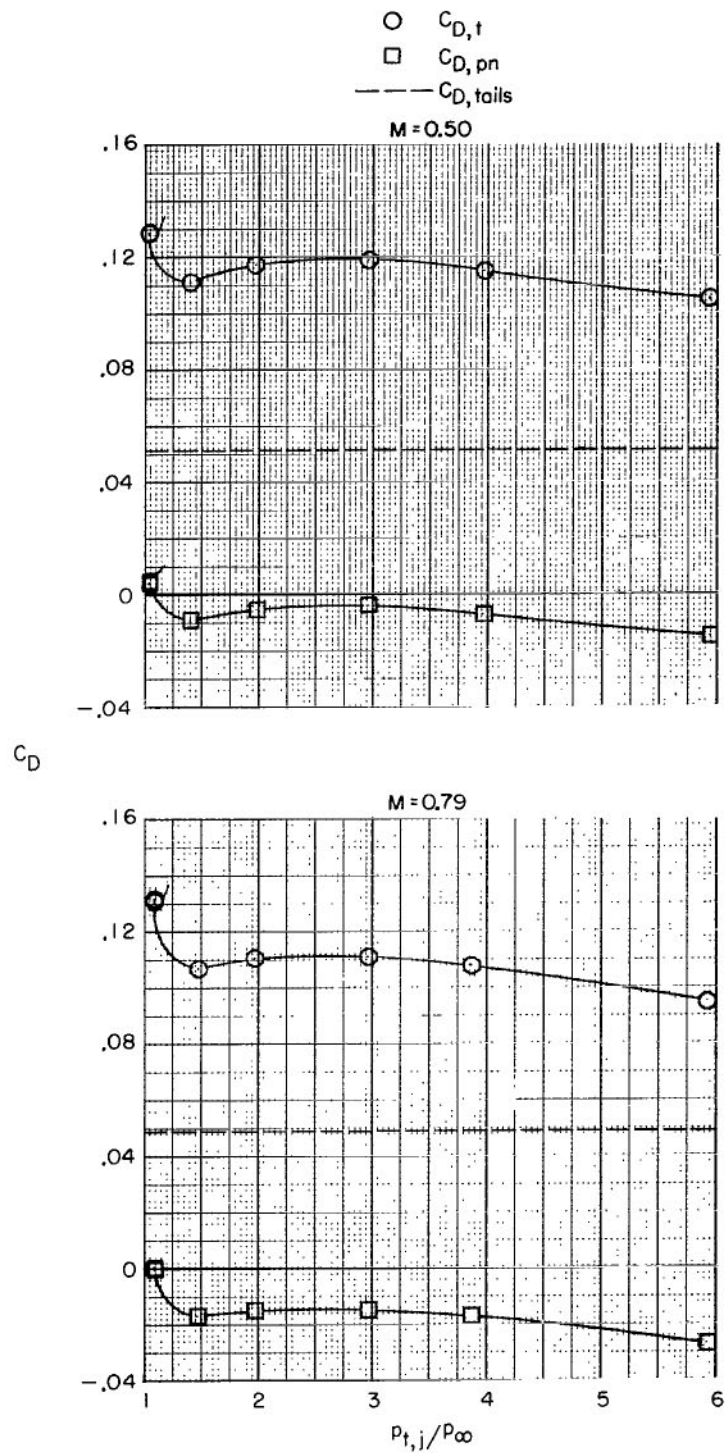
(q) Basic afterbody + aft vertical tail + aft horizontal tail
    + full contour bumps + dry power nozzle.
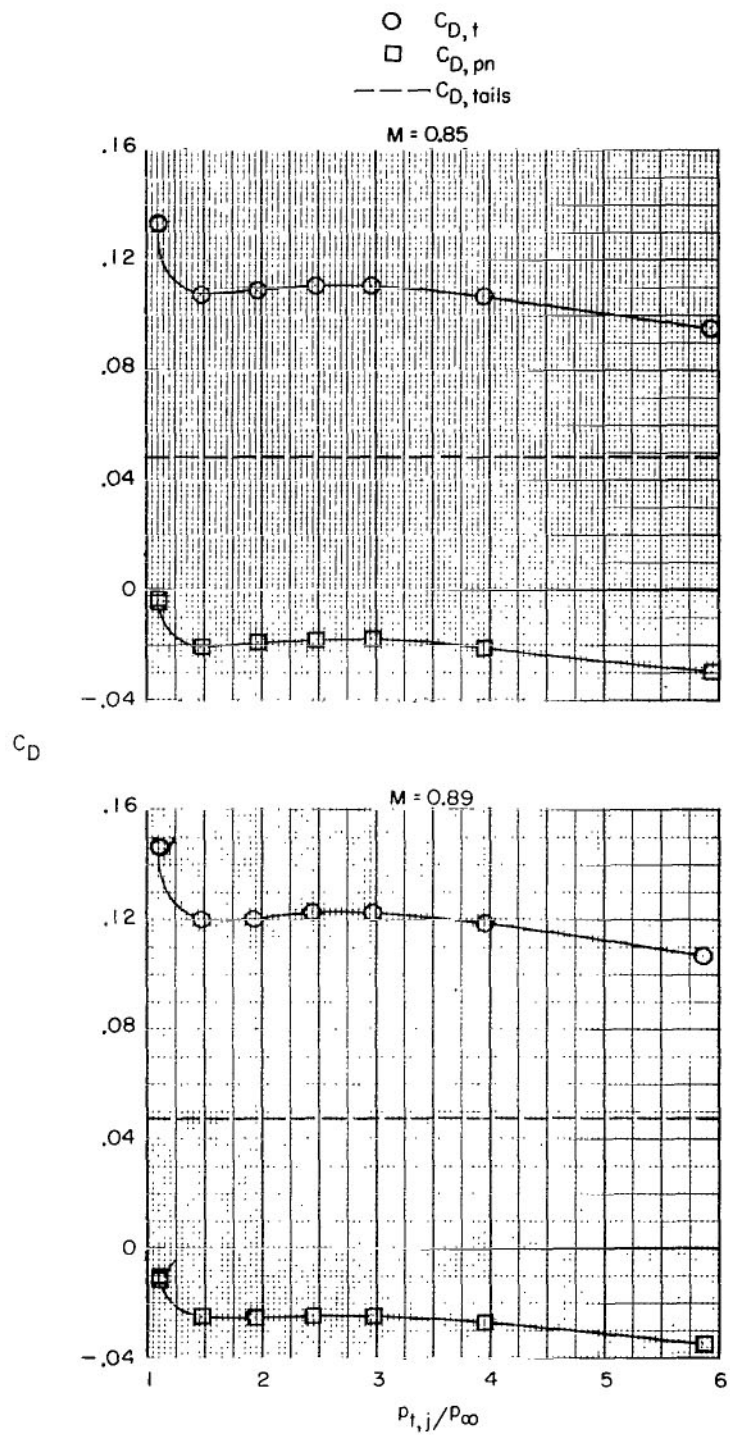
Figure 9.- Continued.

(q) Continued.

Figure 9.- Continued.
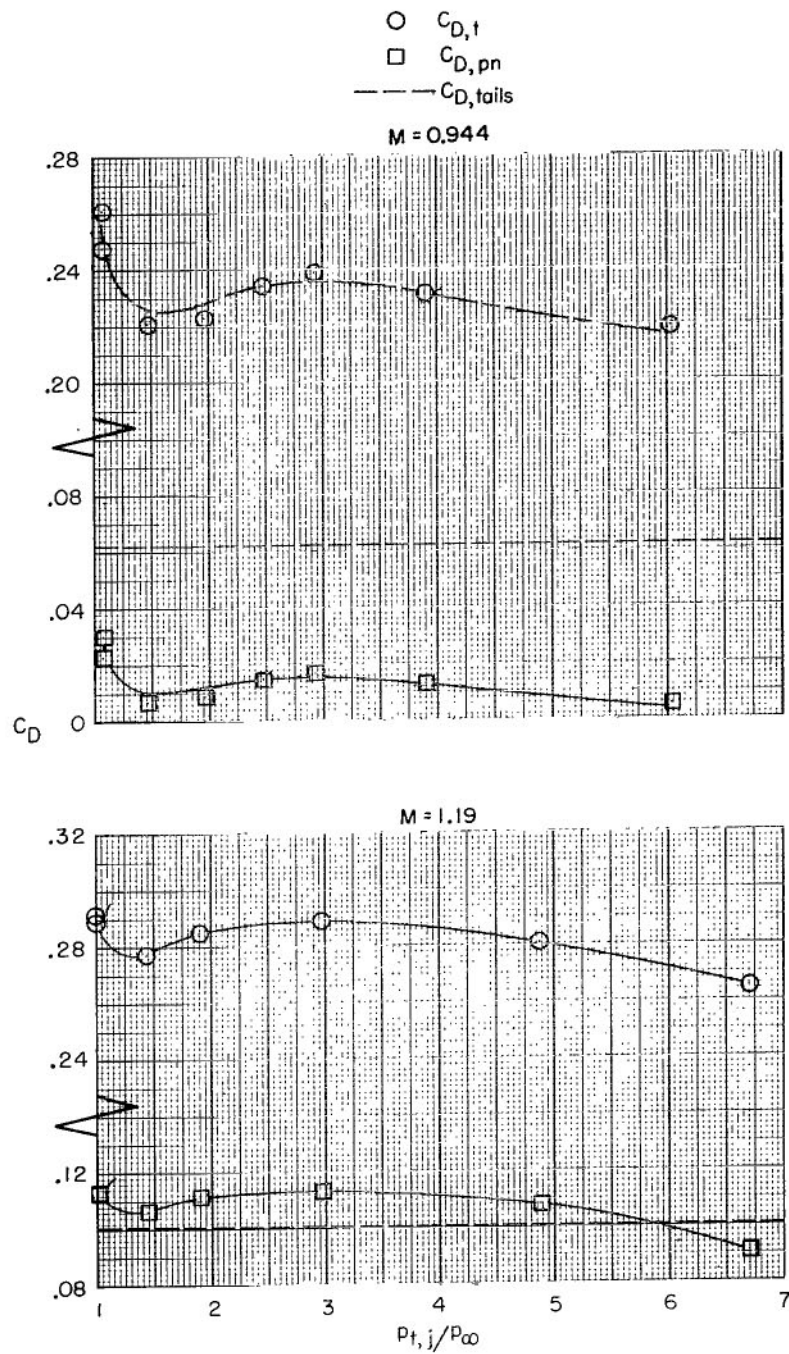
(q) Concluded.

Figure 9.- Continued.
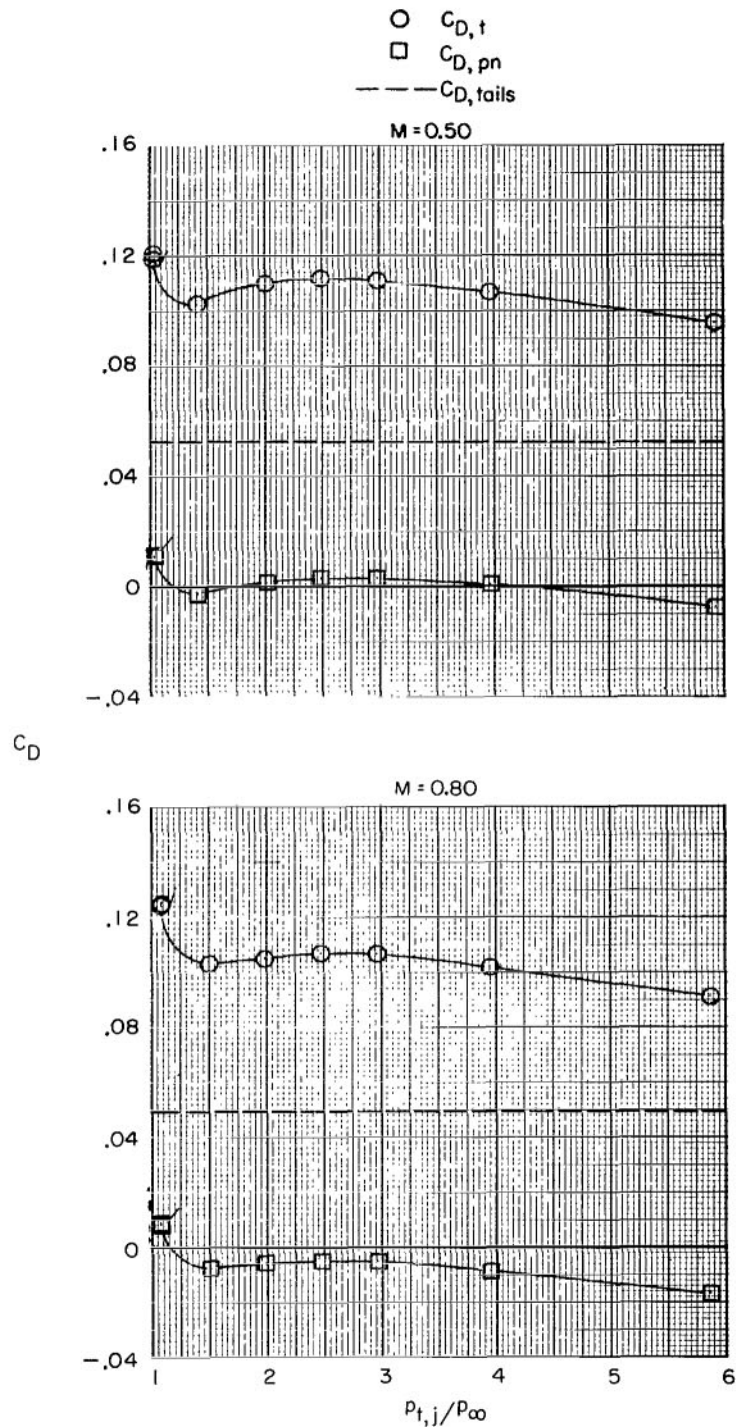
(r) Fully contoured afterbody + forward vertical tail + aft horizontal tail
+ full contour bumps + dry power nozzle.

Figure 9.- Continued.

Legend:
- ○ $C_{D,t}$
- □ $C_{D,pn}$
- — — — $C_{D,tails}$

$M = 0.84$

$M = 0.89$

C_D

$p_{t,j}/p_\infty$

(r) Continued.

Figure 9.- Continued.

Legend:
○ $C_{D,t}$
□ $C_{D,pn}$
— — — $C_{D,tails}$

$M = 0.944$

$M = 1.19$

C_D

$p_{t,j}/p_\infty$

(r) Concluded.

Figure 9.- Continued.

Legend:
○ $C_{D,t}$
□ $C_{D,pn}$
— — — $C_{D,tails}$

M = 0.50

M = 0.80

C_D

$p_{t,j}/p_\infty$
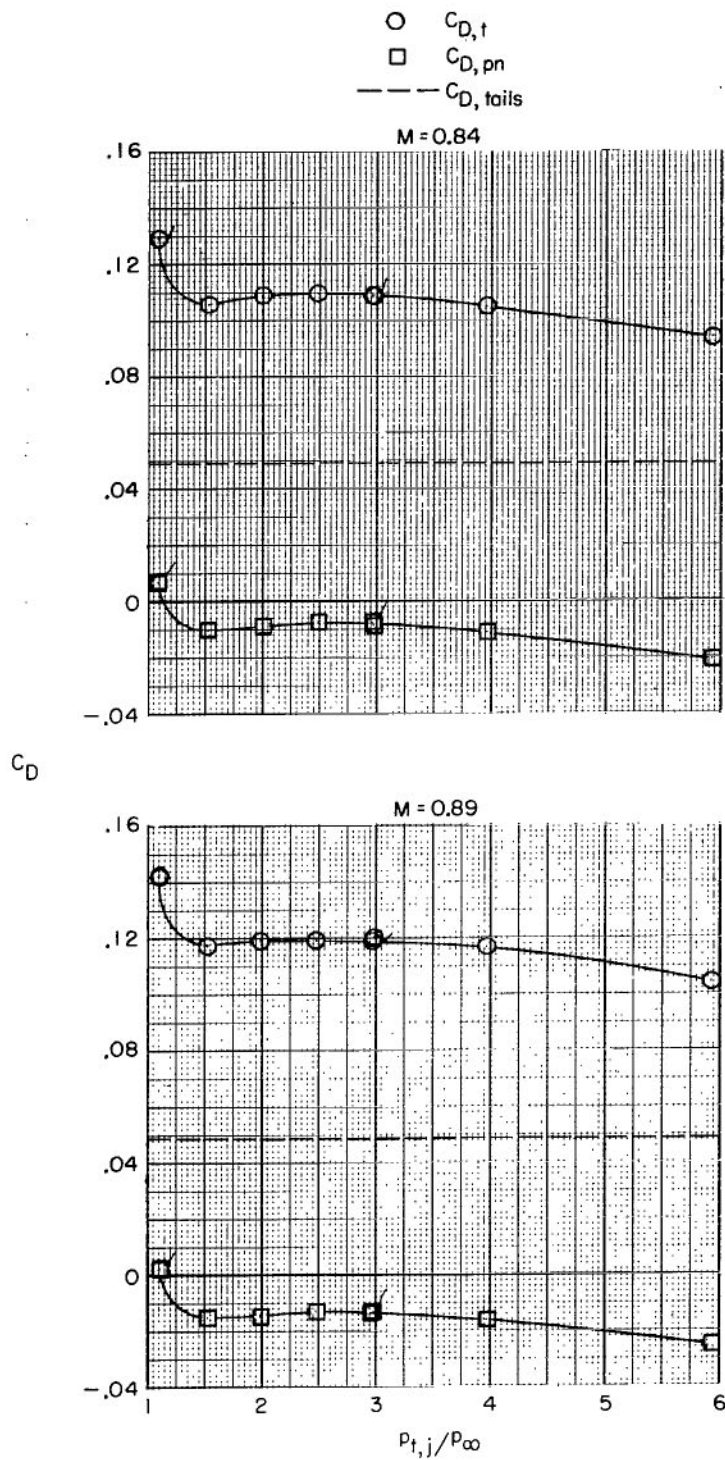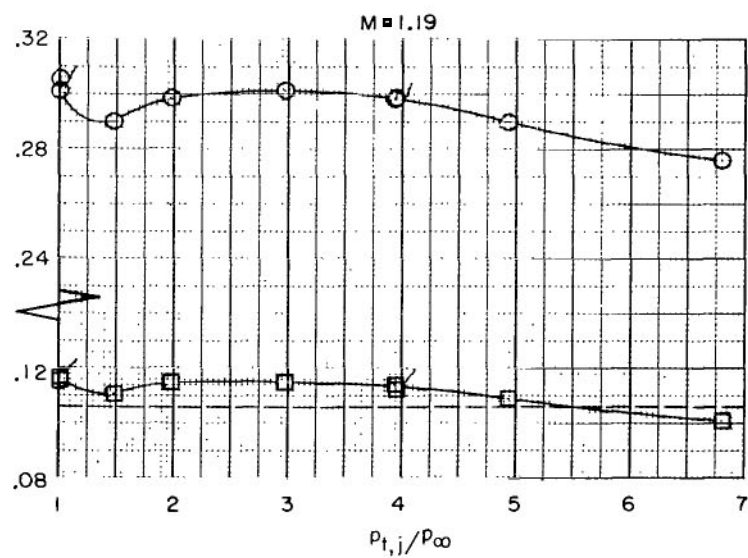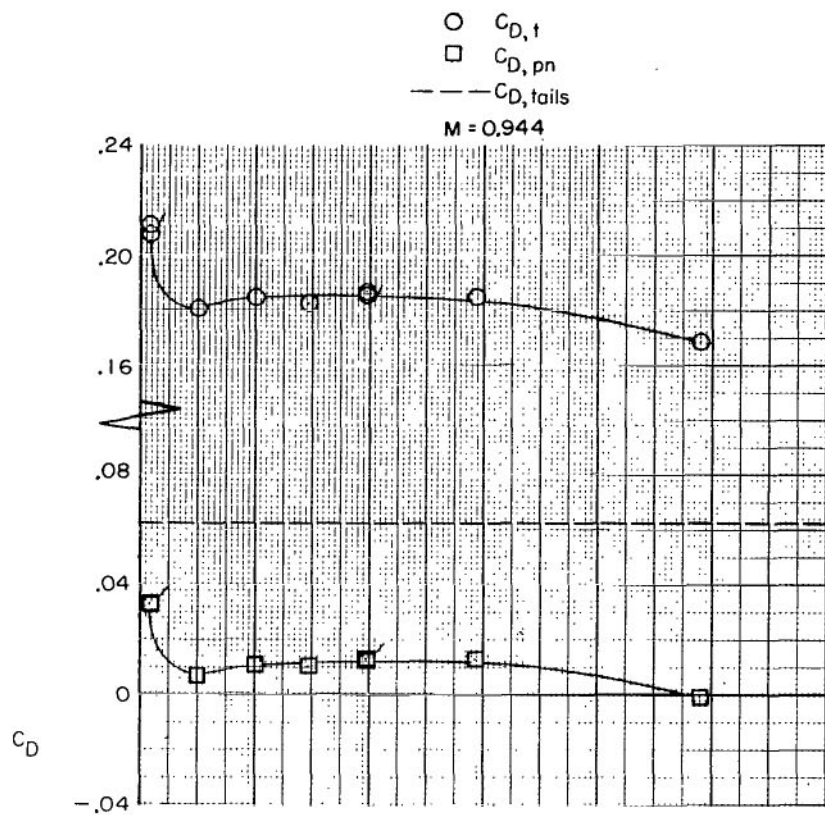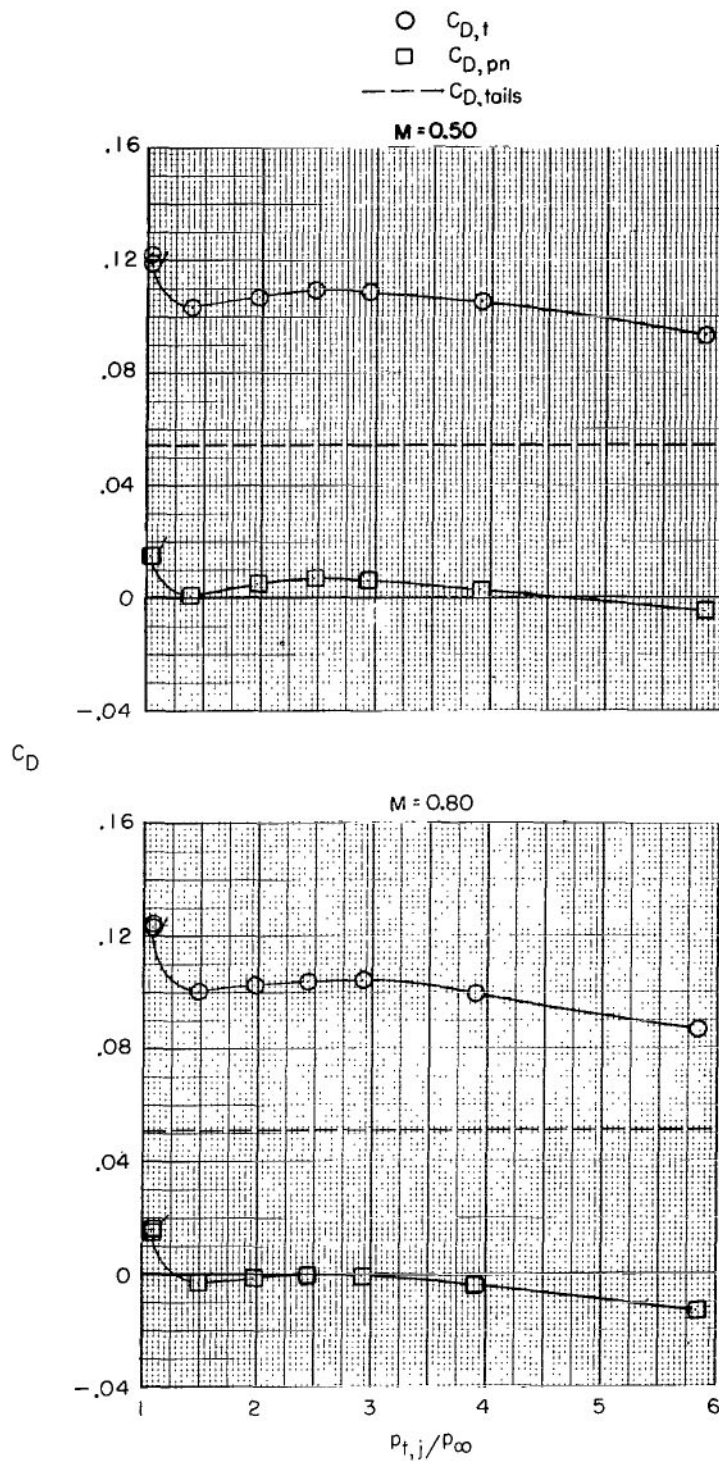
(s) Partially contoured afterbody + forward vertical tail
+ aft horizontal tail + dry power nozzle.
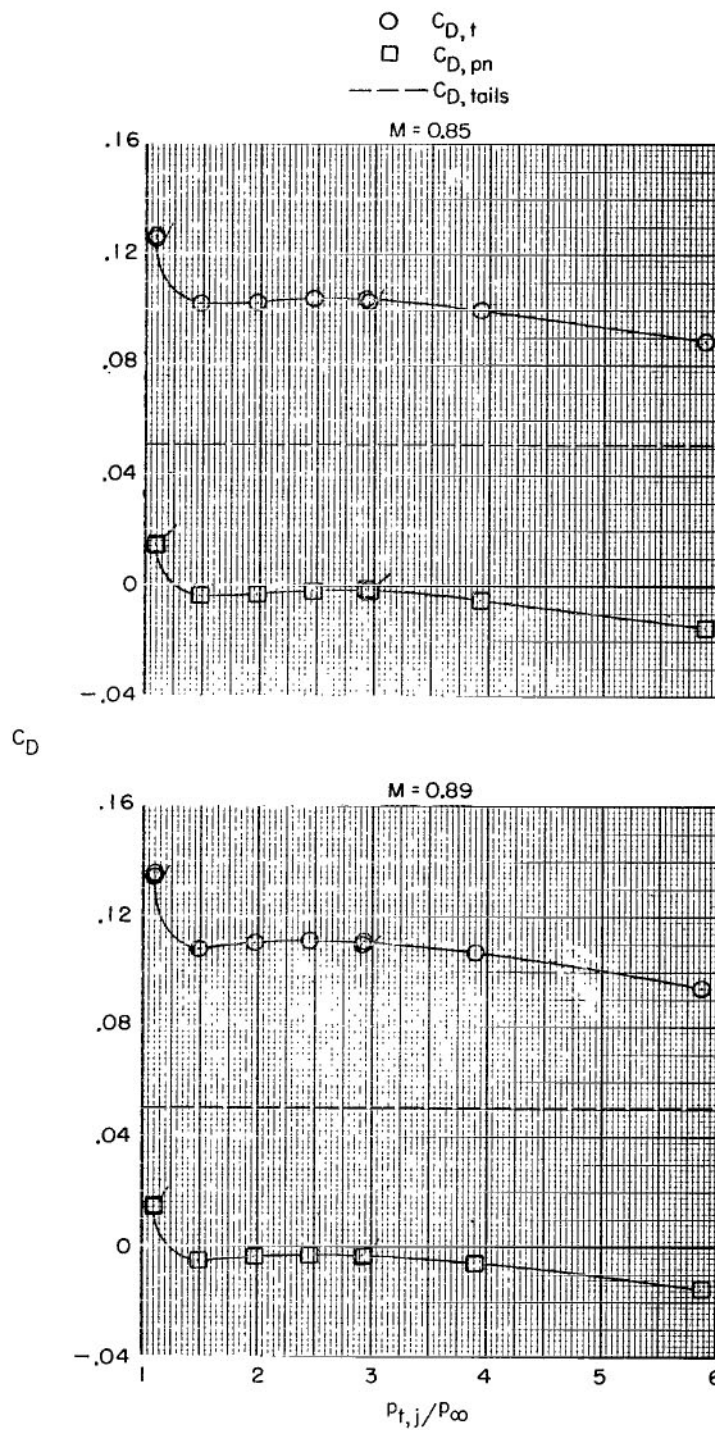
Figure 9.- Continued.

(s) Continued.

Figure 9.- Continued.
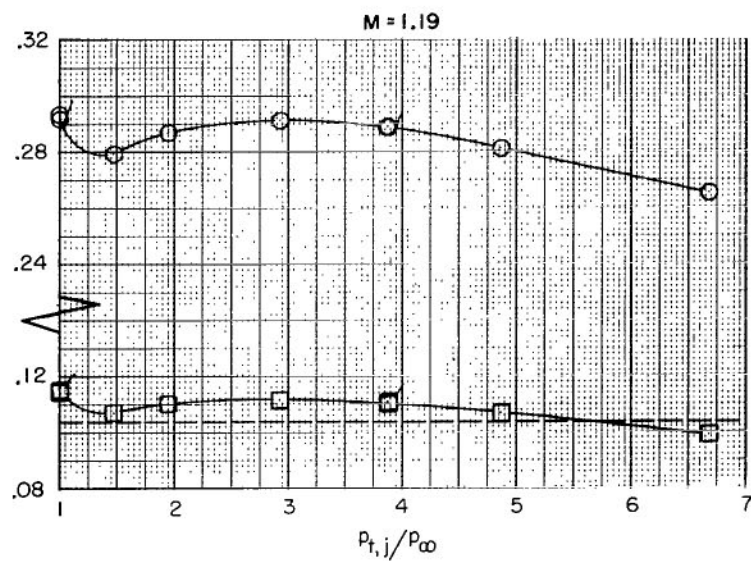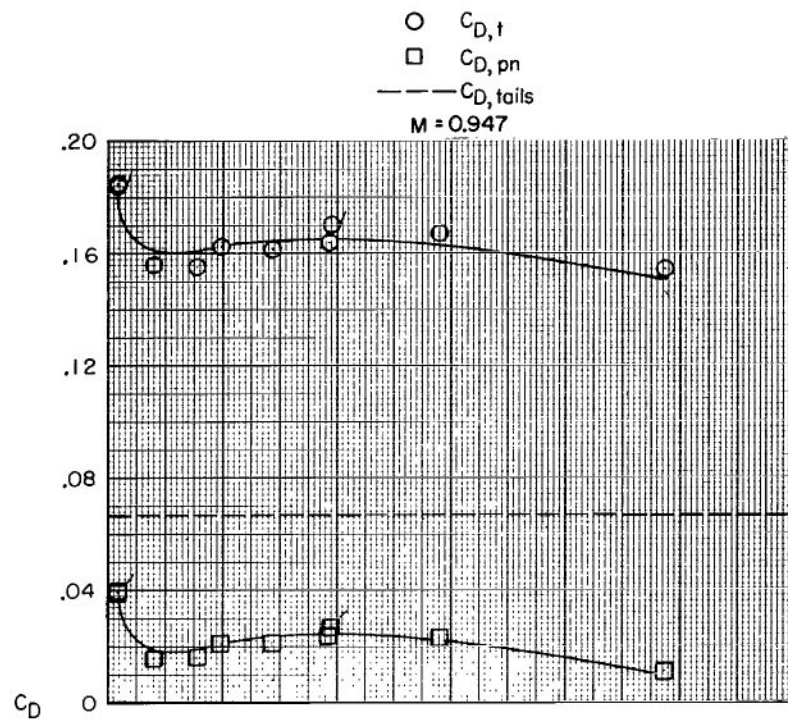
(s) Concluded.

Figure 9.- Continued.
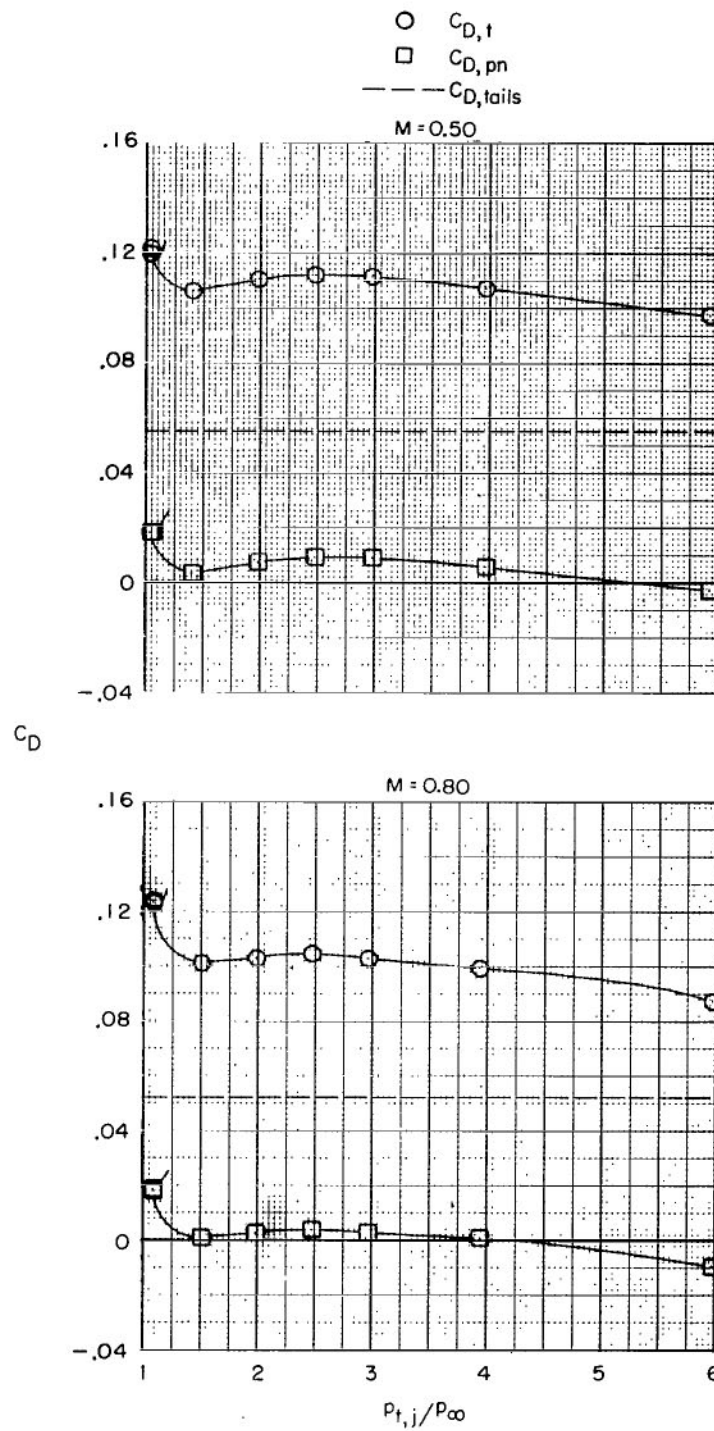
(t) Fully contoured afterbody + forward vertical tail
+ aft horizontal tail + dry power nozzle.

Figure 9.- Continued.

$$C_D$$
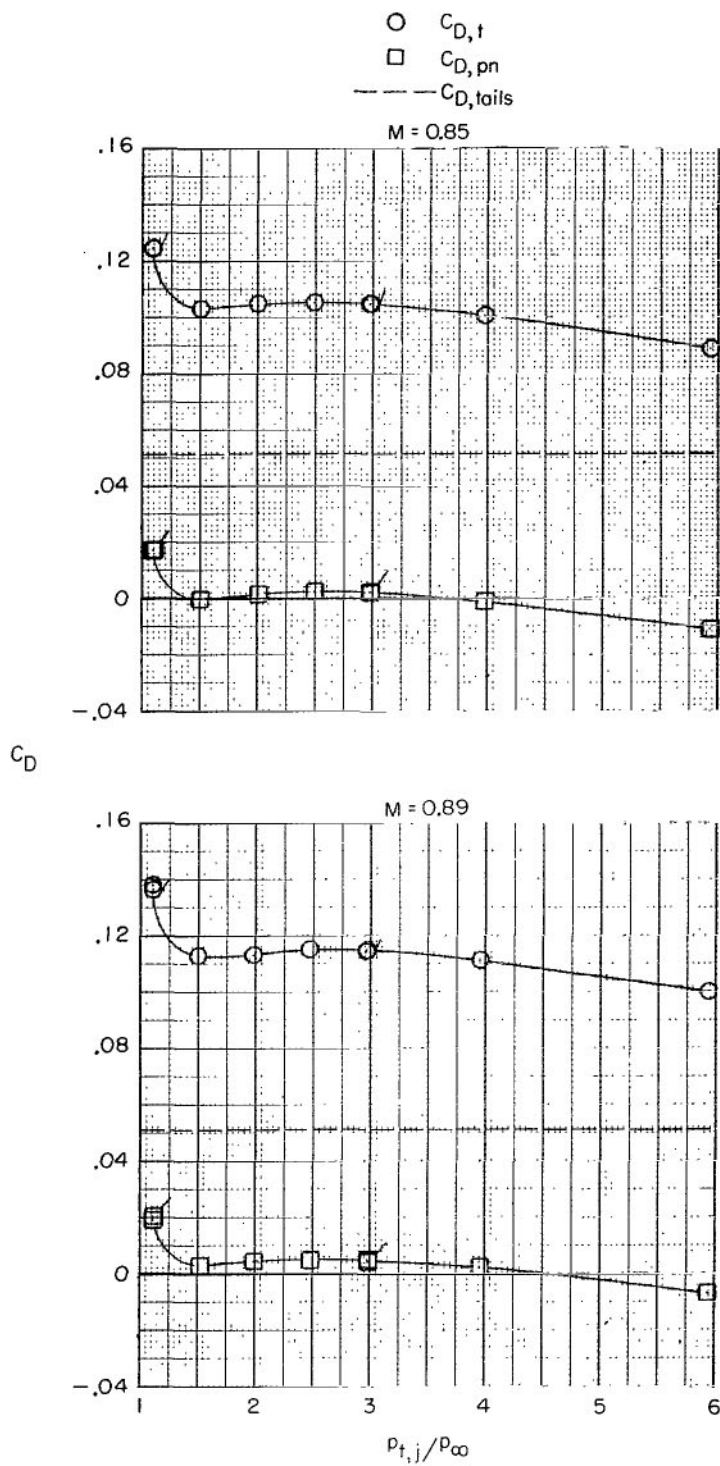
(t) Continued.

Figure 9.- Continued.

Legend:
○ $C_{D,t}$
□ $C_{D,pn}$
— — — $C_{D,tails}$

$M = 0.945$

$M = 1.18$

C_D

$p_{t,j}/p_\infty$
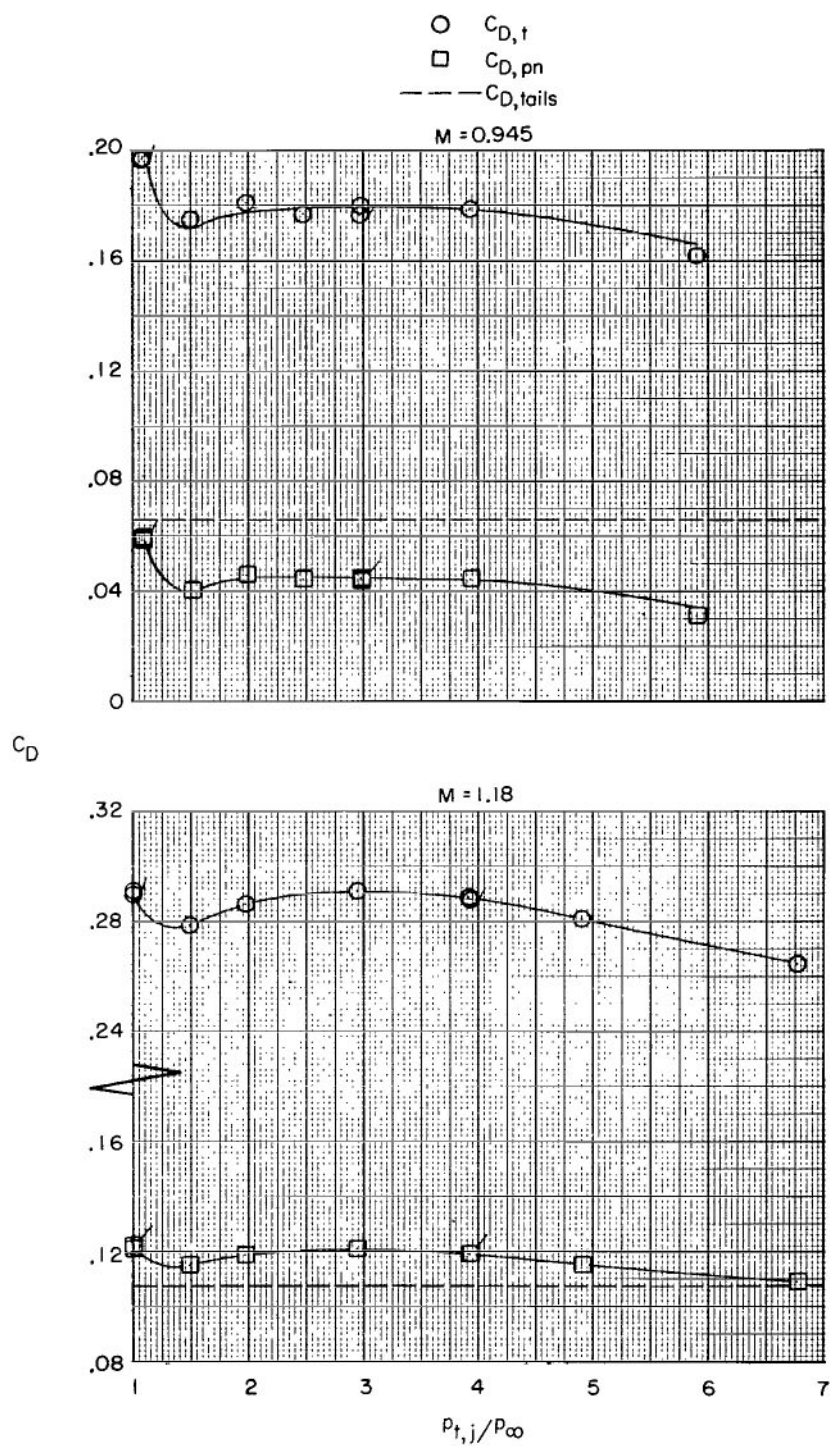
(t) Concluded.
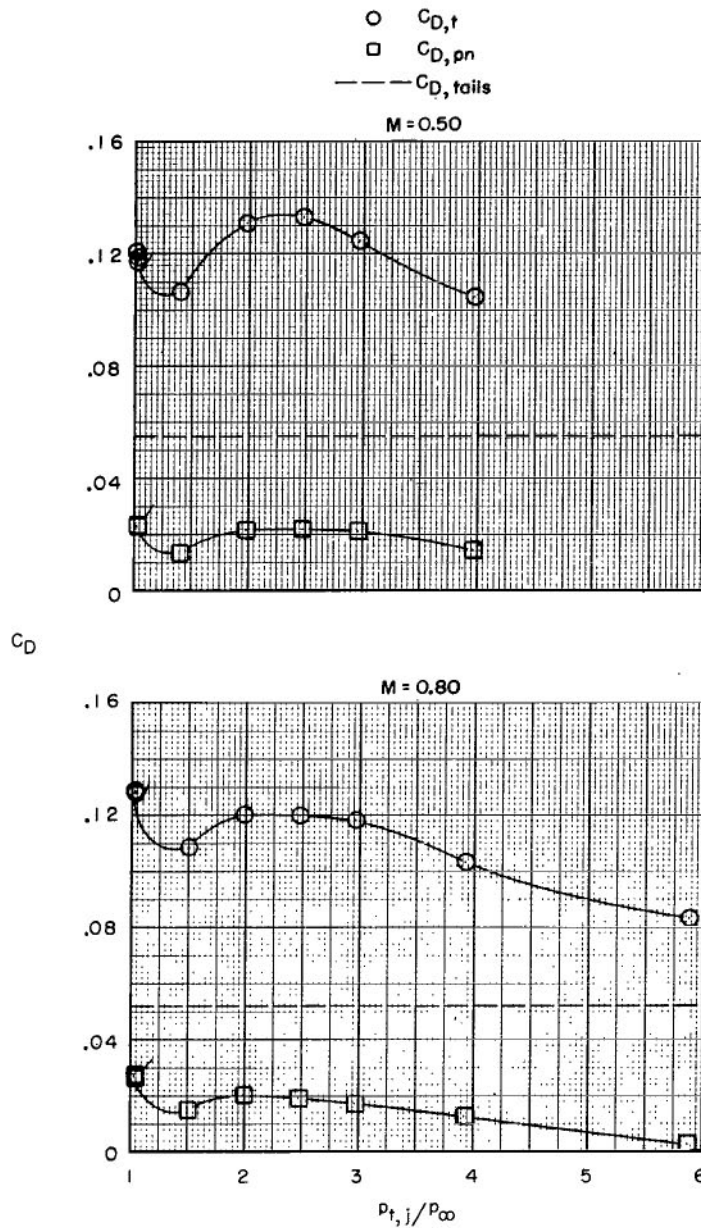
Figure 9.- Continued.

(u) Fully contoured afterbody + forward vertical tail
+ aft horizontal tail + max. A/B power nozzle.
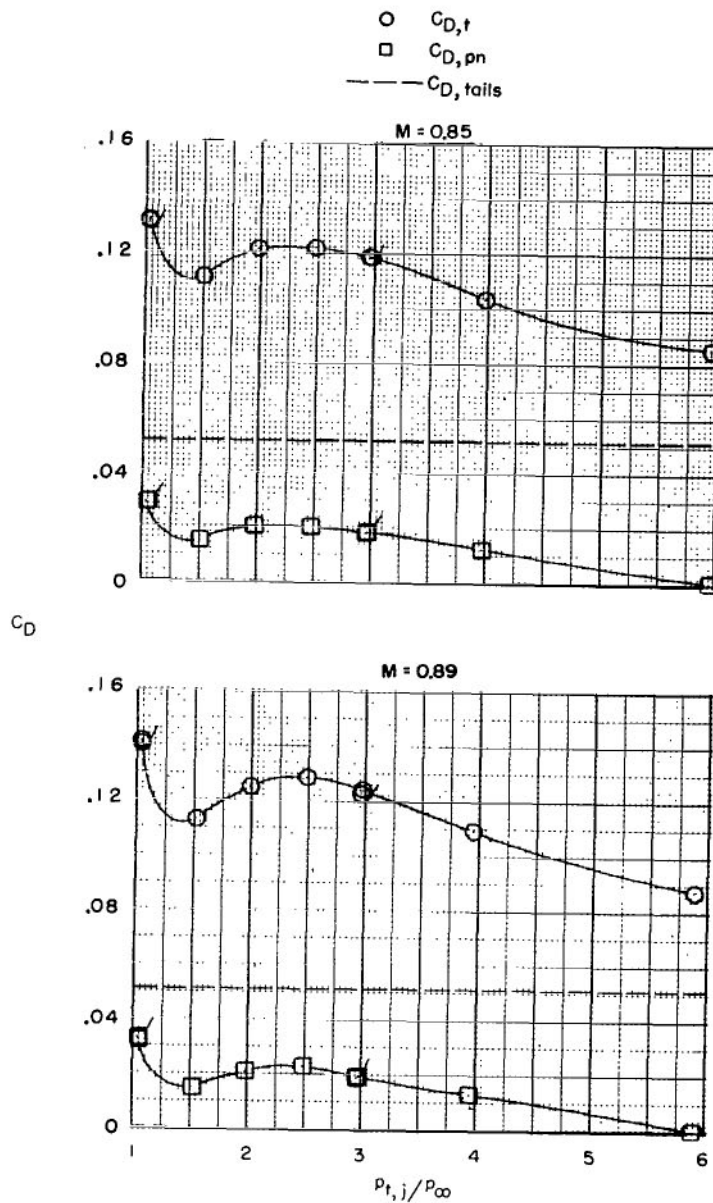
Figure 9.- Continued.

(u) Continued.

Figure 9.- Continued.

Legend:
○ $C_{D,t}$
□ $C_{D,pn}$
— — — $C_{D,tails}$

$M = 0.945$

$M = 1.19$

$p_{t,j}/p_\infty$

C_D
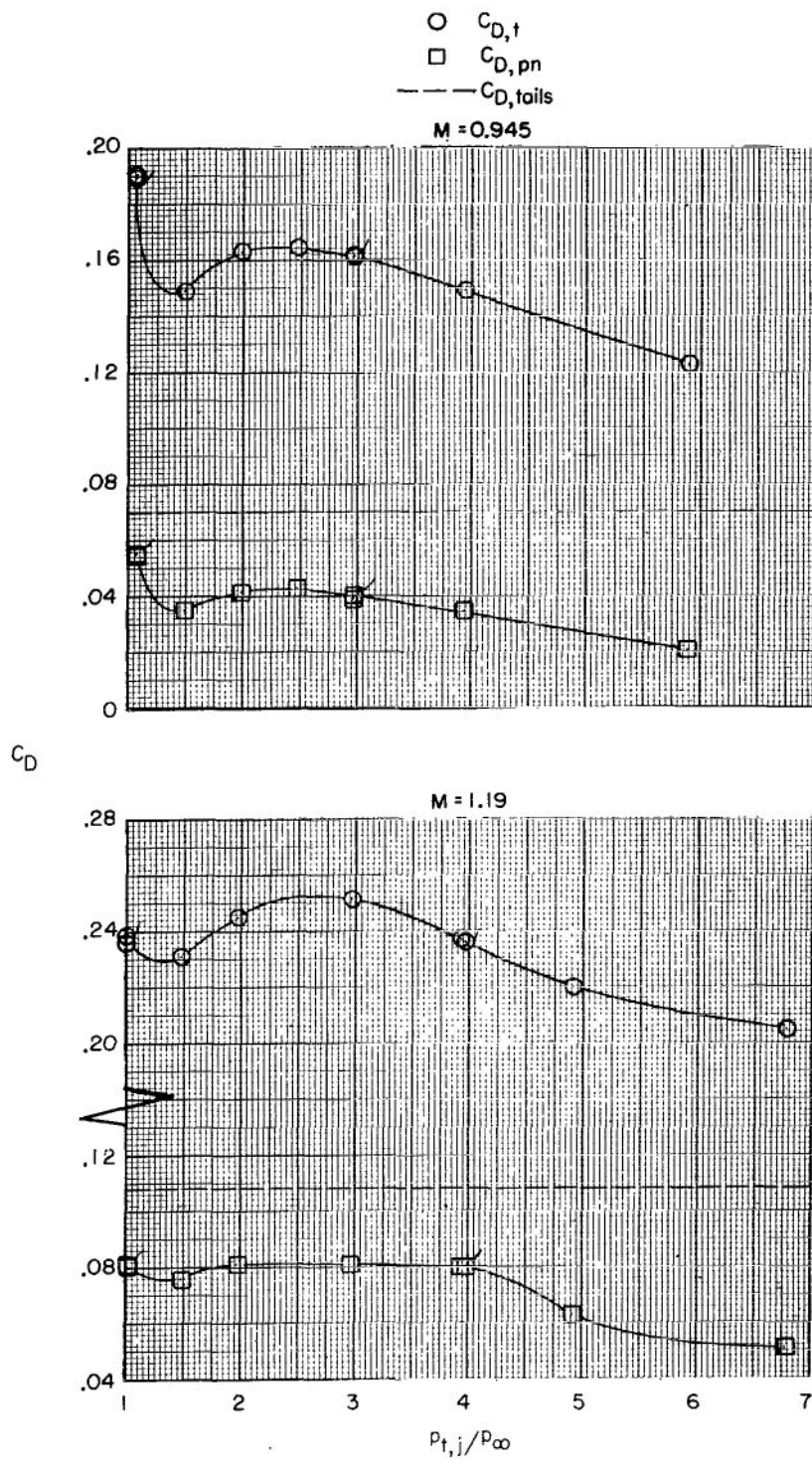
(u) Continued.
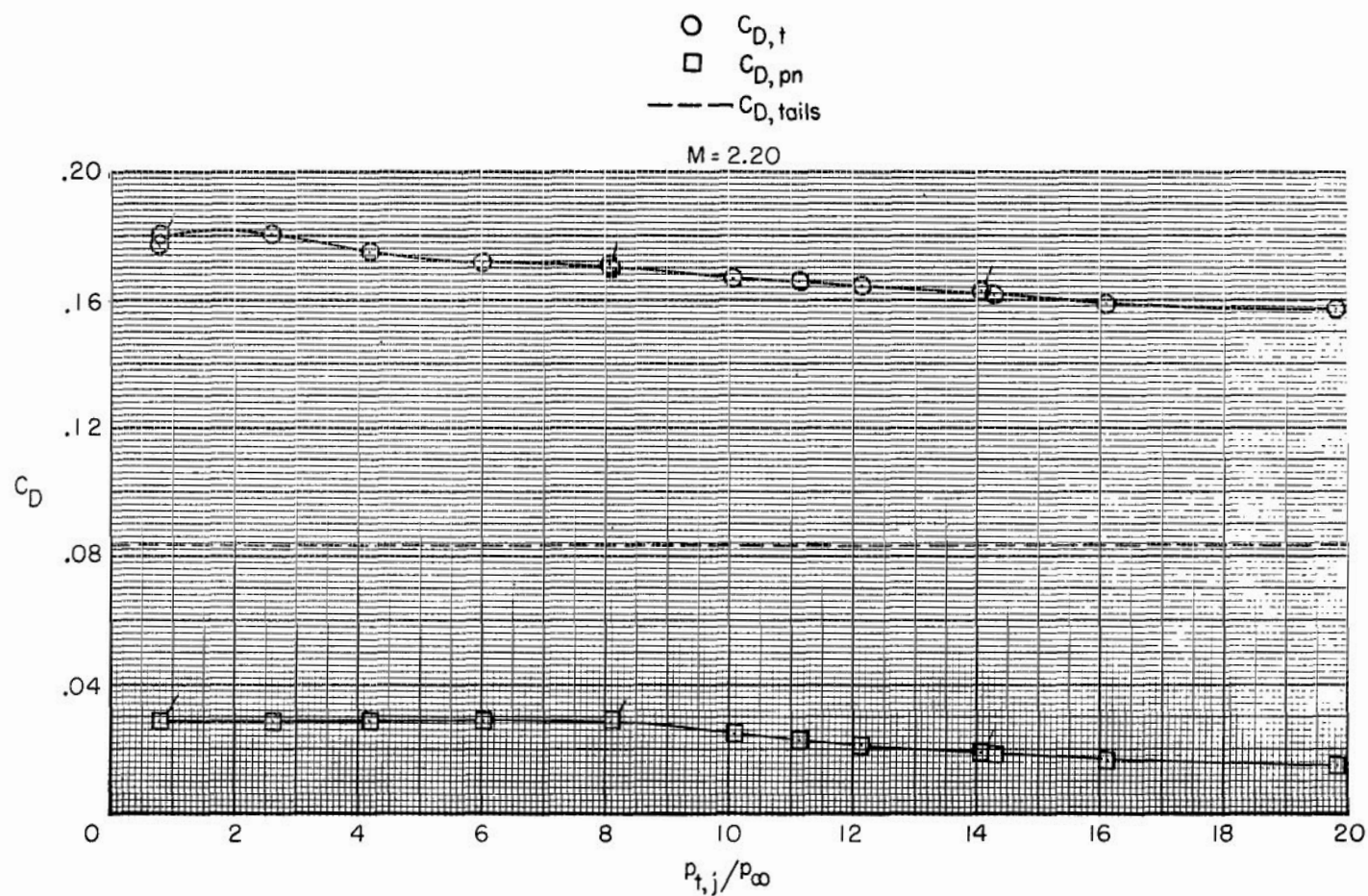
Figure 9.- Continued.

(u) Concluded.

Figure 9.- Continued.
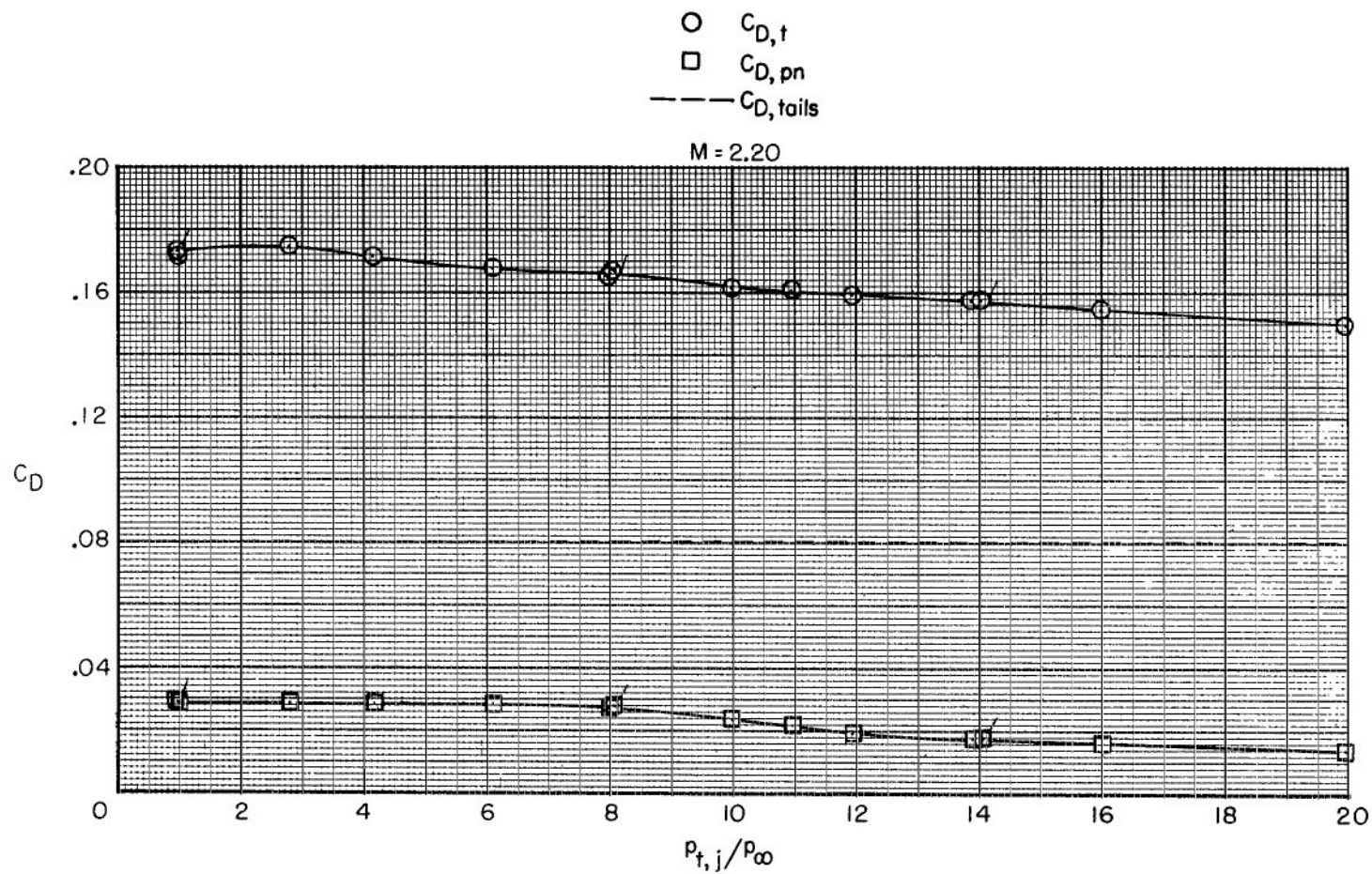
(v) Basic afterbody + aft vertical tail + forward horizontal tail + max. A/B power nozzle.
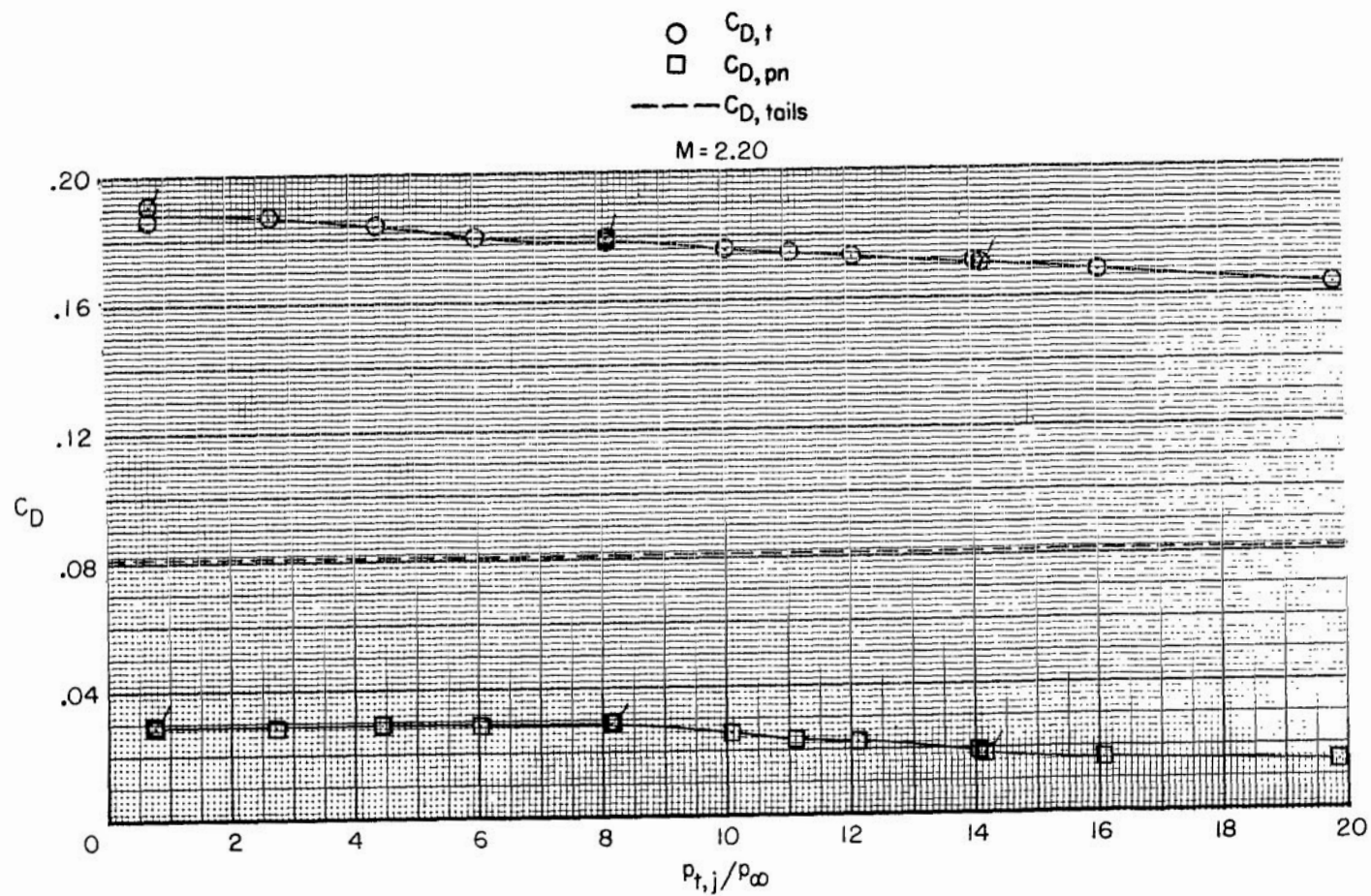
Figure 9.- Continued.

(w) Fully contoured afterbody + forward vertical tail + aft horizontal tail
+ full contour bumps + max. A/B power nozzle.
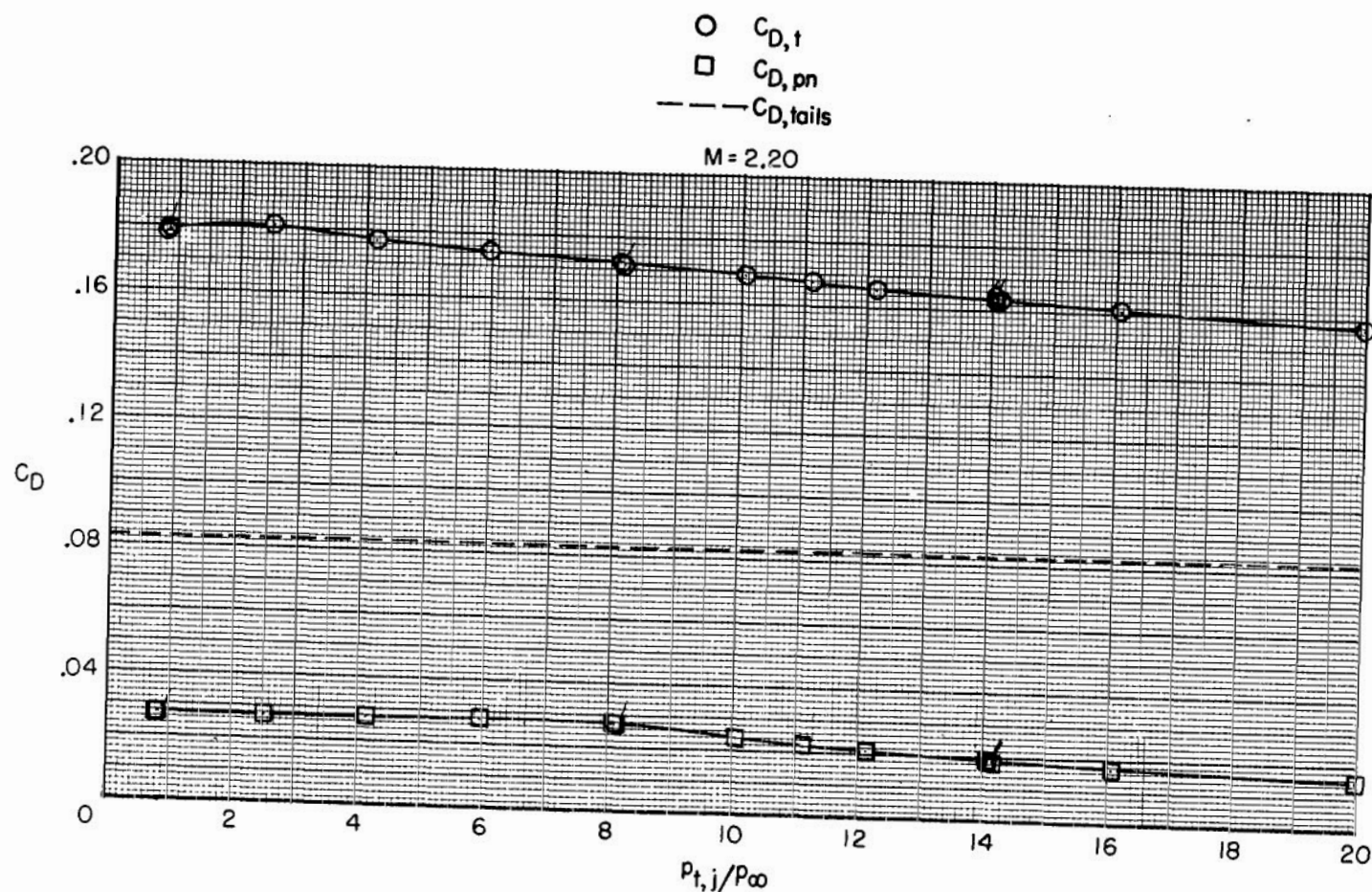
Figure 9.- Continued.

(x) Partially contoured afterbody + forward vertical tail + aft horizontal tail
+ max. A/B power nozzle.

Figure 9.- Concluded.
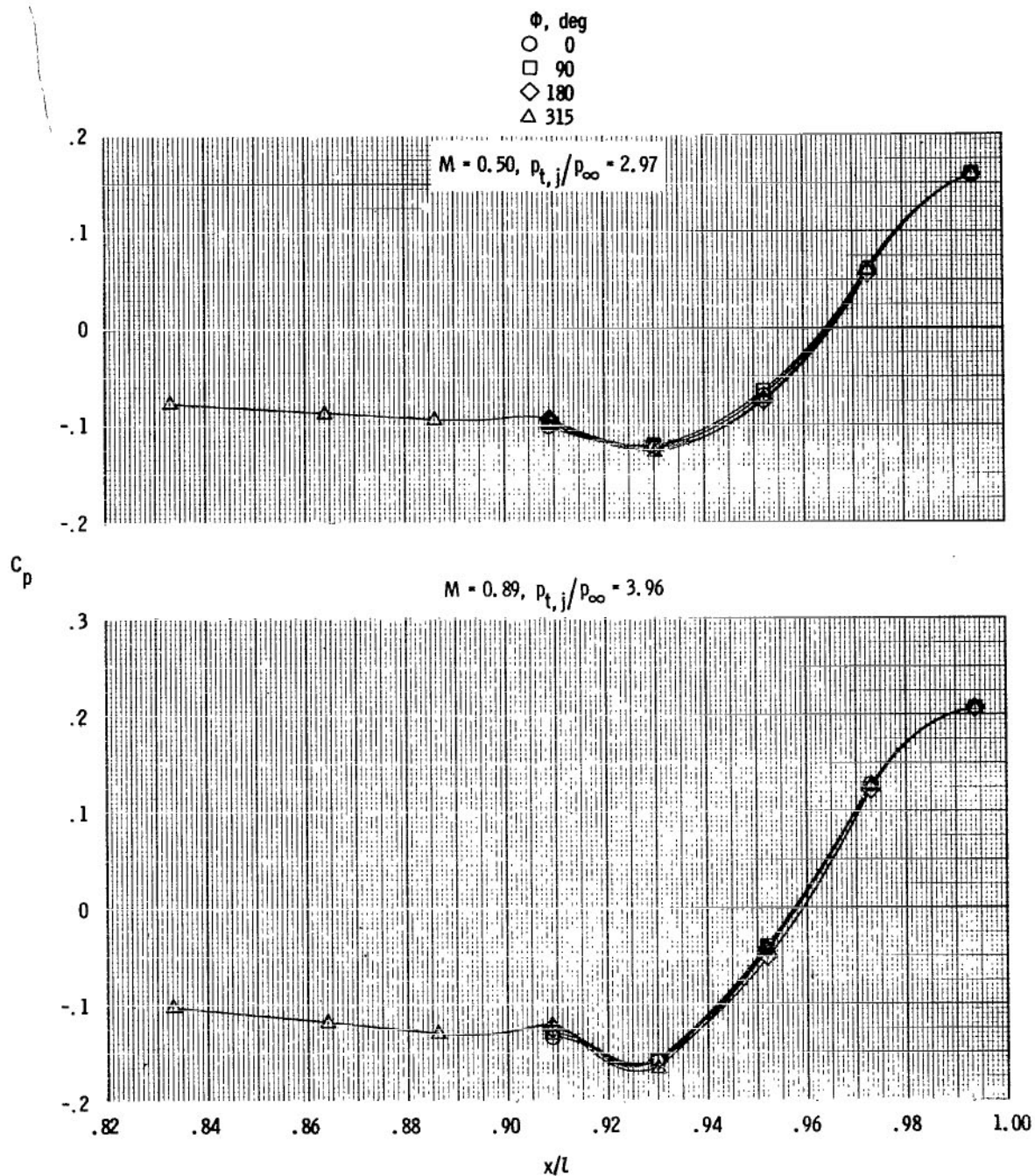
(a) M = 0.50 and 0.89.

Figure 10.- Effect of support system on afterbody/nozzle pressure distribution basic afterbody with dry power nozzle; tails off.
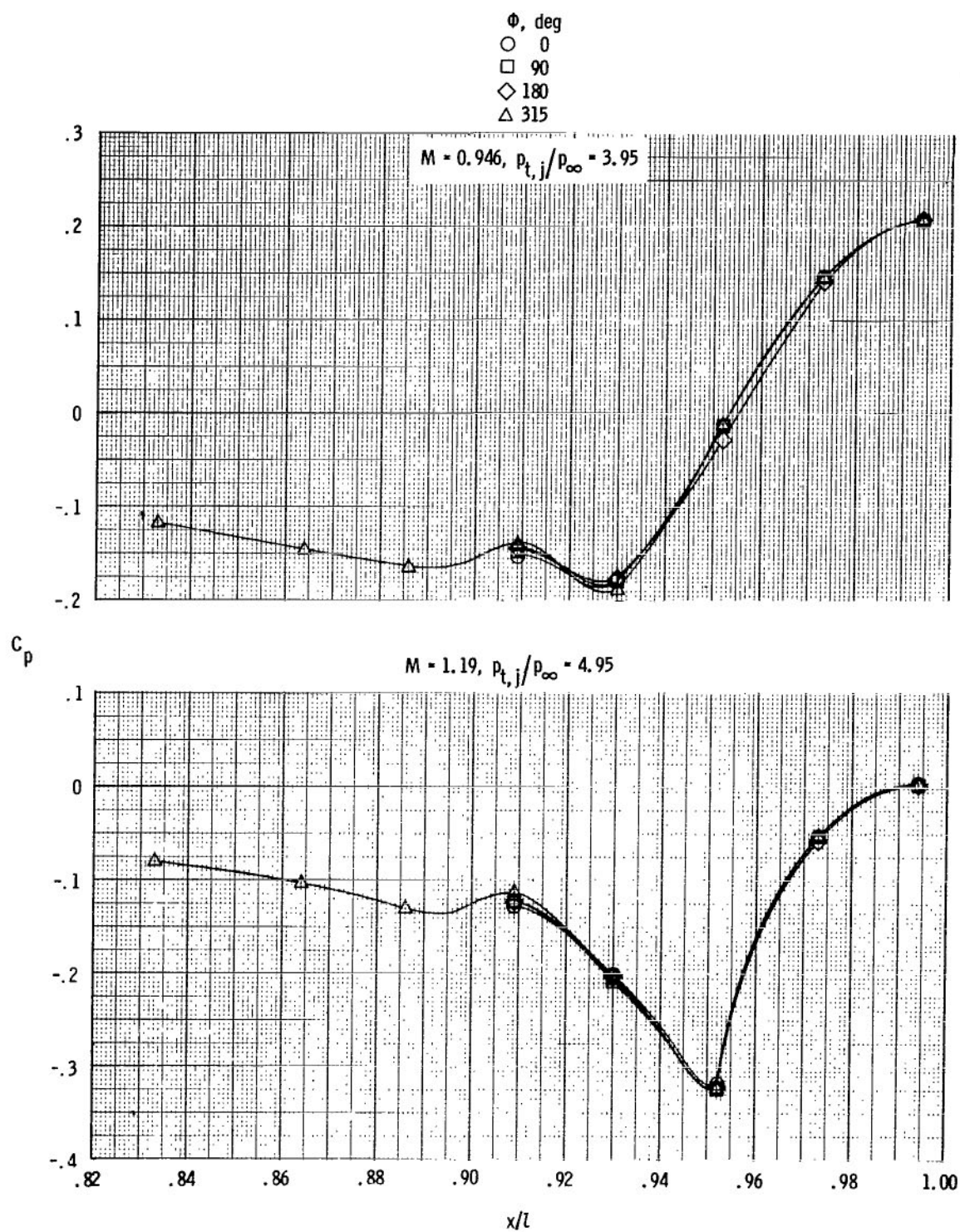
(b) M = 0.946 and 1.19.

Figure 10.- Concluded.
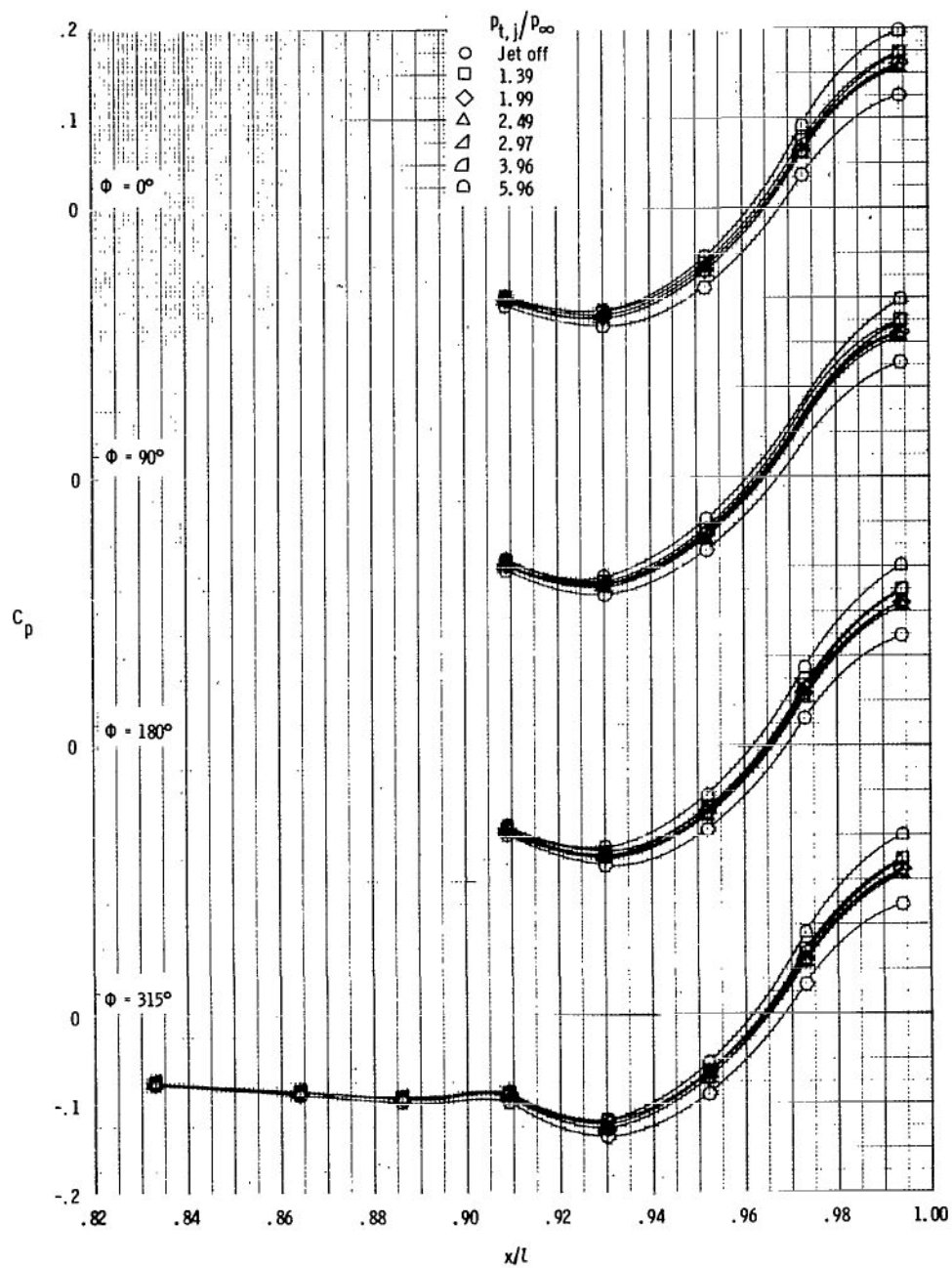
(a) M = 0.50.

Figure 11.- Effect of jet total pressure ratio on afterbody/nozzle pressure
distributions; basic afterbody with dry power nozzle; tails off.
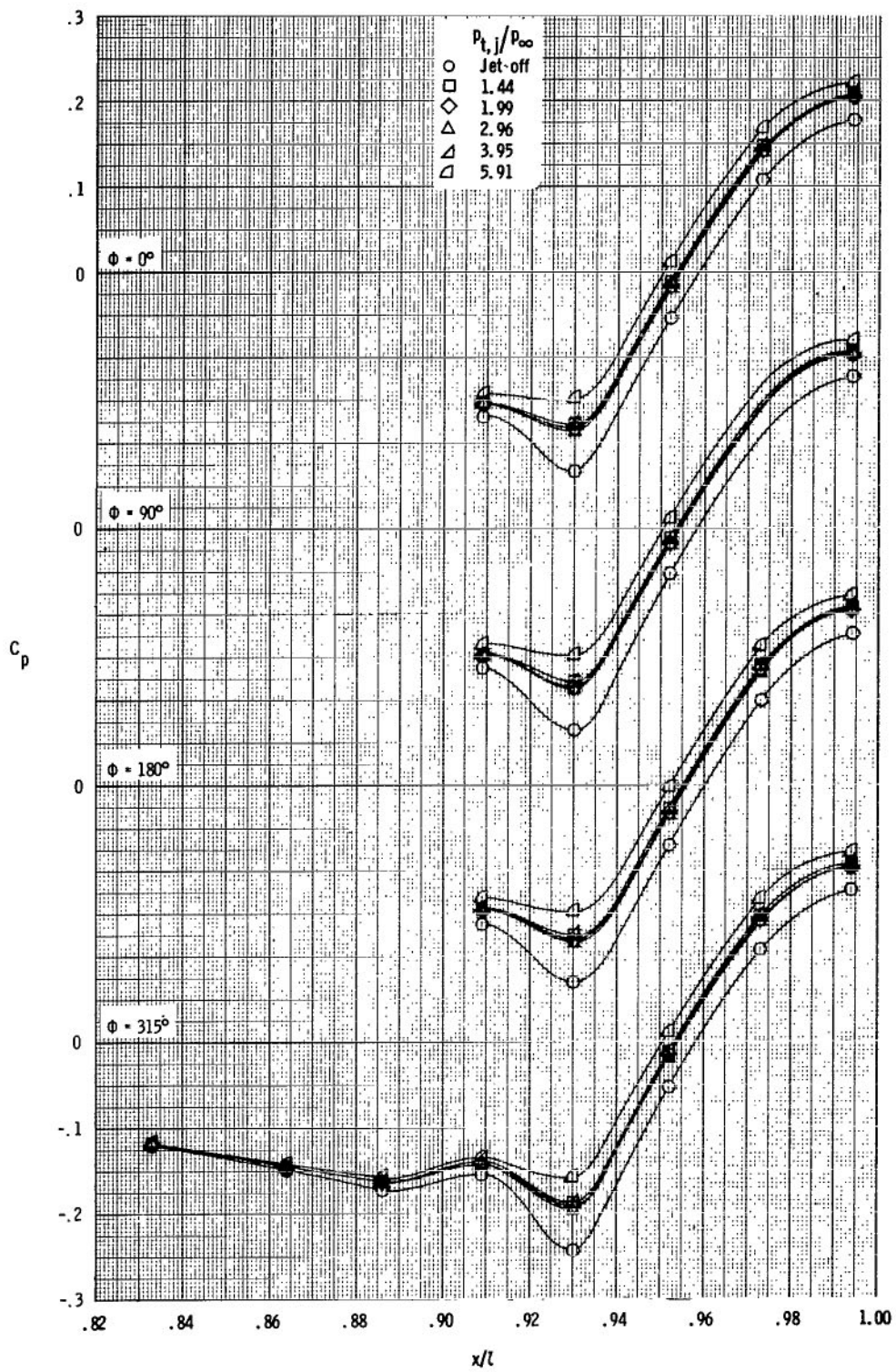
(b) M = 0.945.

Figure 11.- Continued.
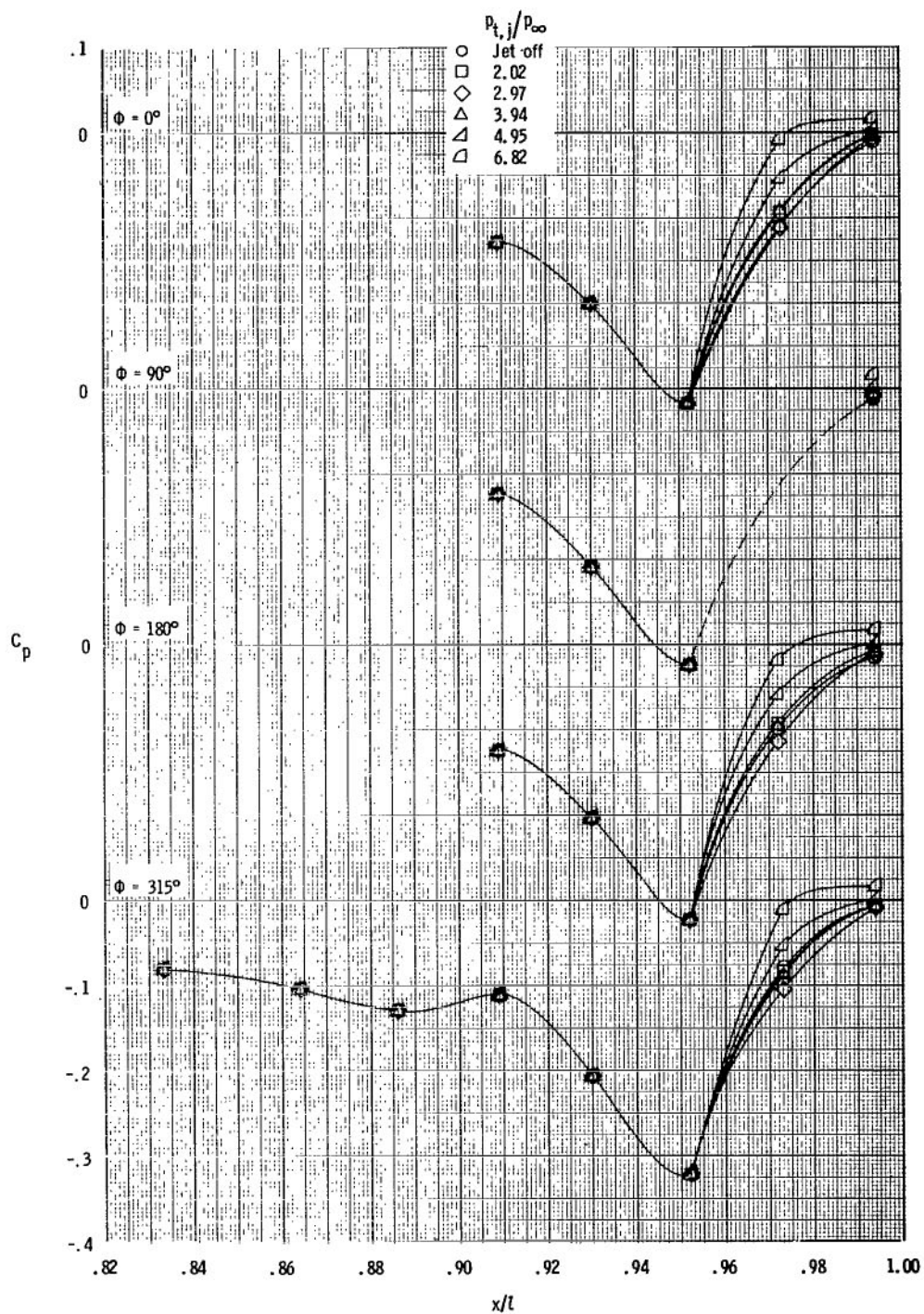
(c) M = 1.19.

Figure 11.- Concluded.
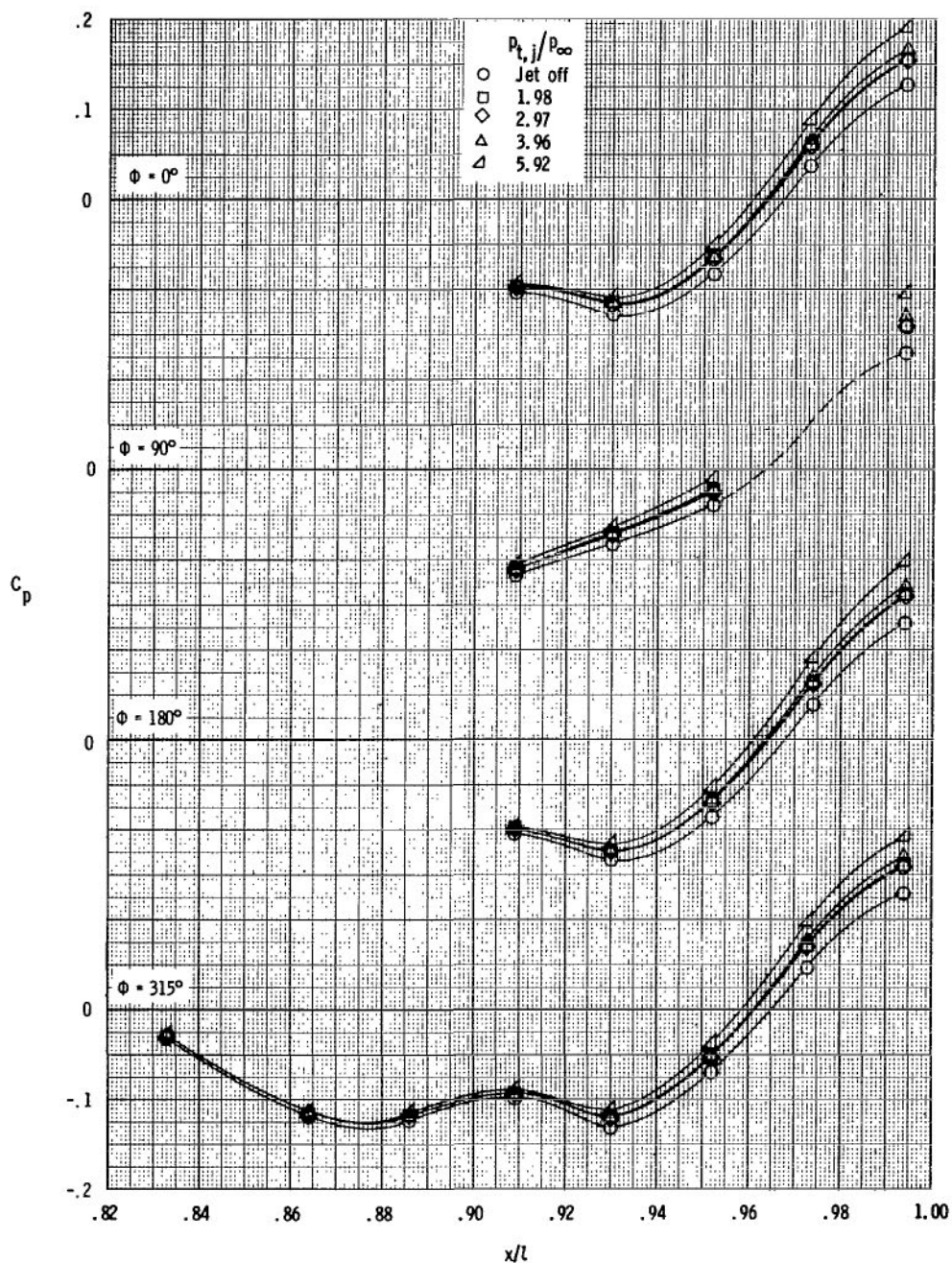
(a)   M = 0.50.

Figure 12.- Effect of jet total pressure ratio on afterbody/nozzle pressure
   distributions; basic afterbody with dry power nozzle, forward vertical
   tail, and aft horizontal tail.

118
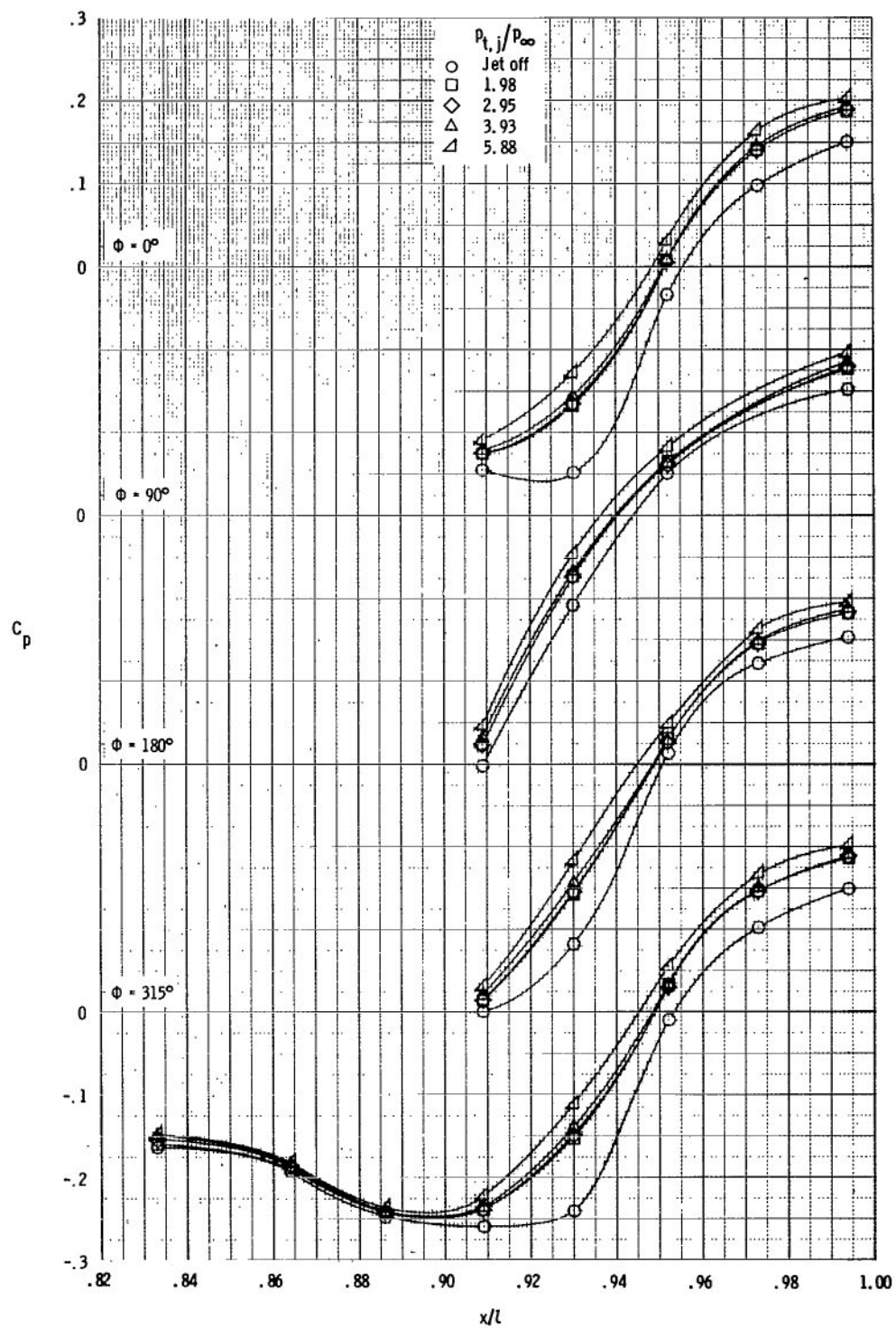
(b) M = 0.944.

Figure 12.- Continued.
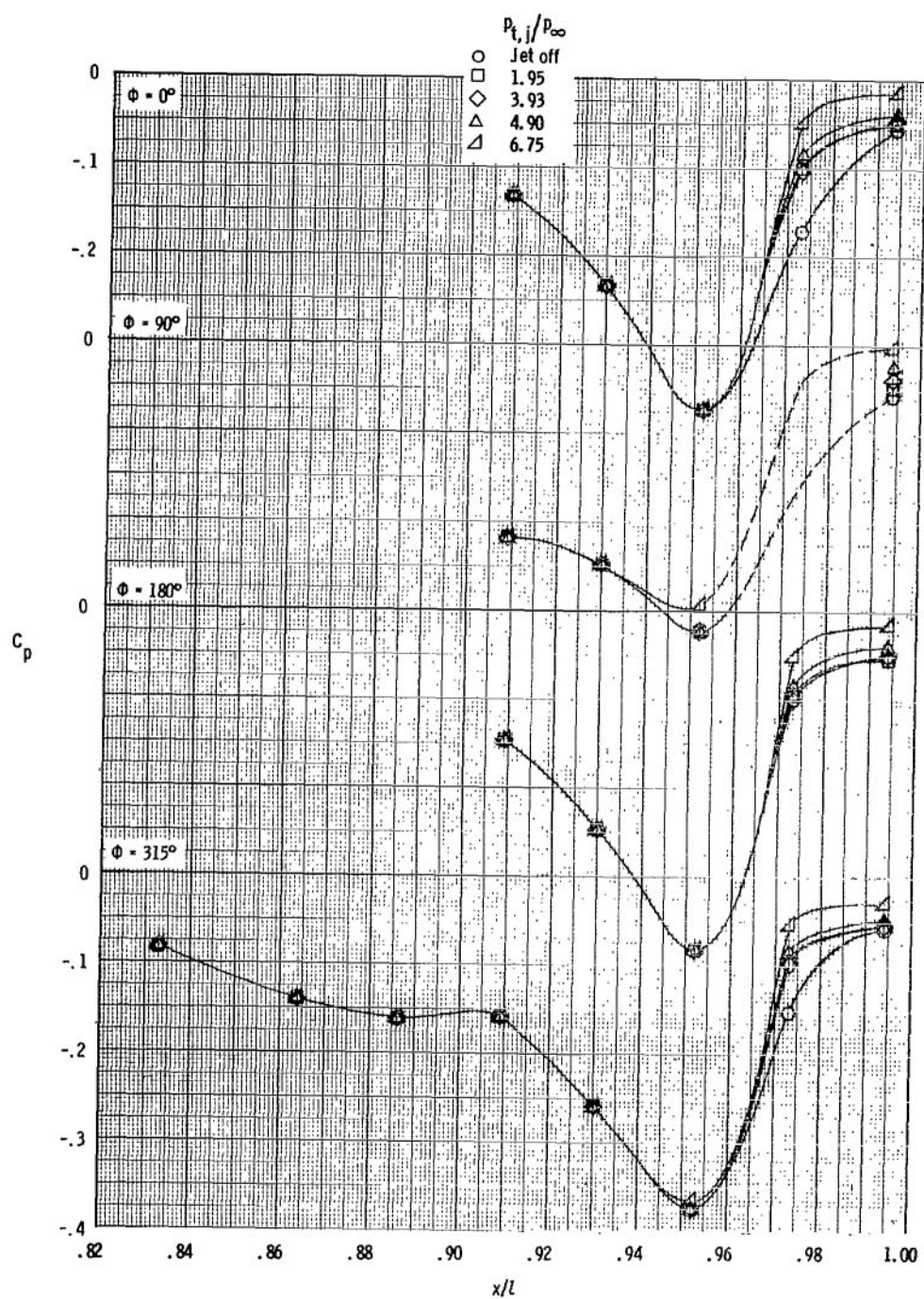
(c) M = 1.19.

Figure 12.- Concluded.
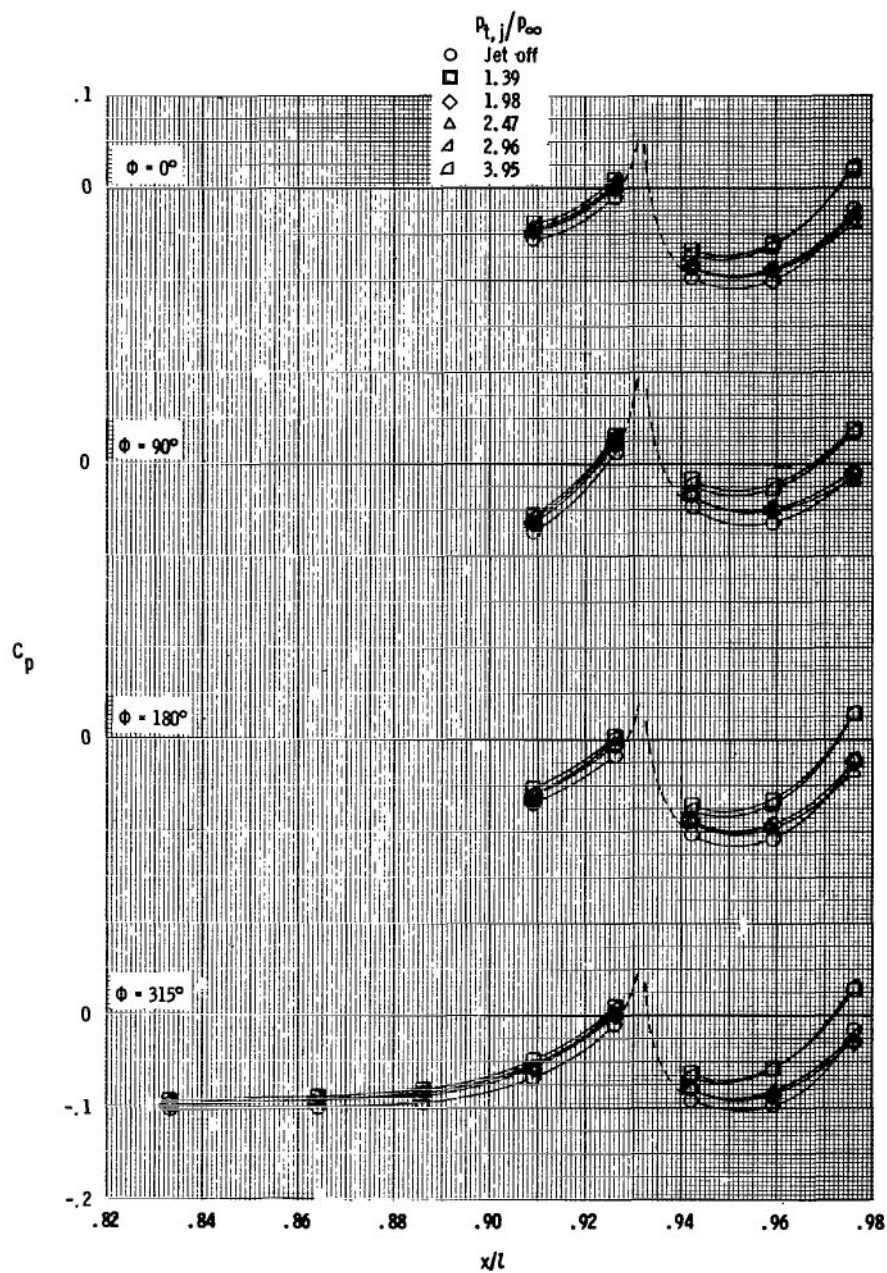
(a) M = 0.50.

Figure 13.- Effect of jet total pressure ratio on afterbody/nozzle pressure
distributions; basic afterbody with max. A/B power nozzle, forward verti-
cal tail, and aft horizontal tail.

121
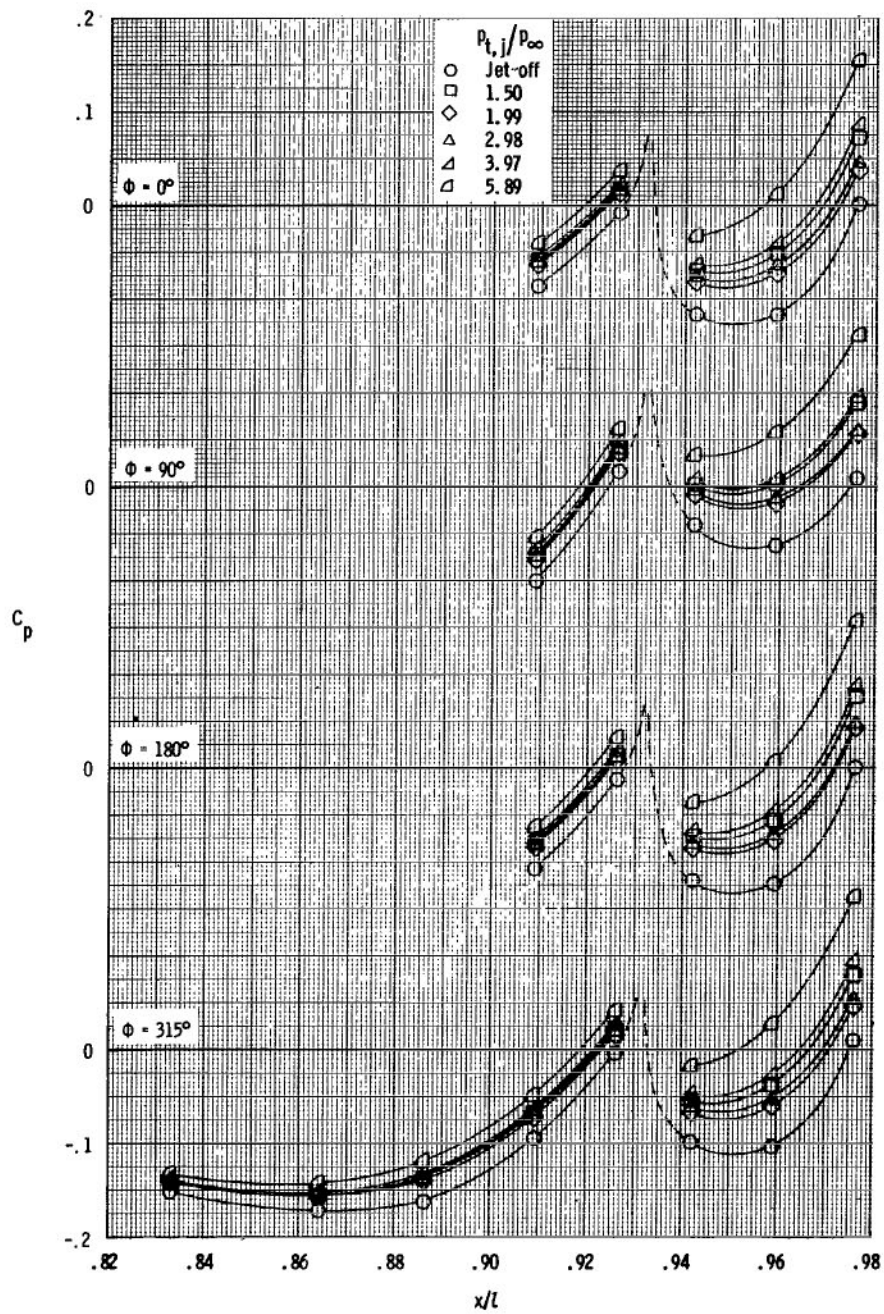
(b) M = 0.89.

Figure 13.- Continued.
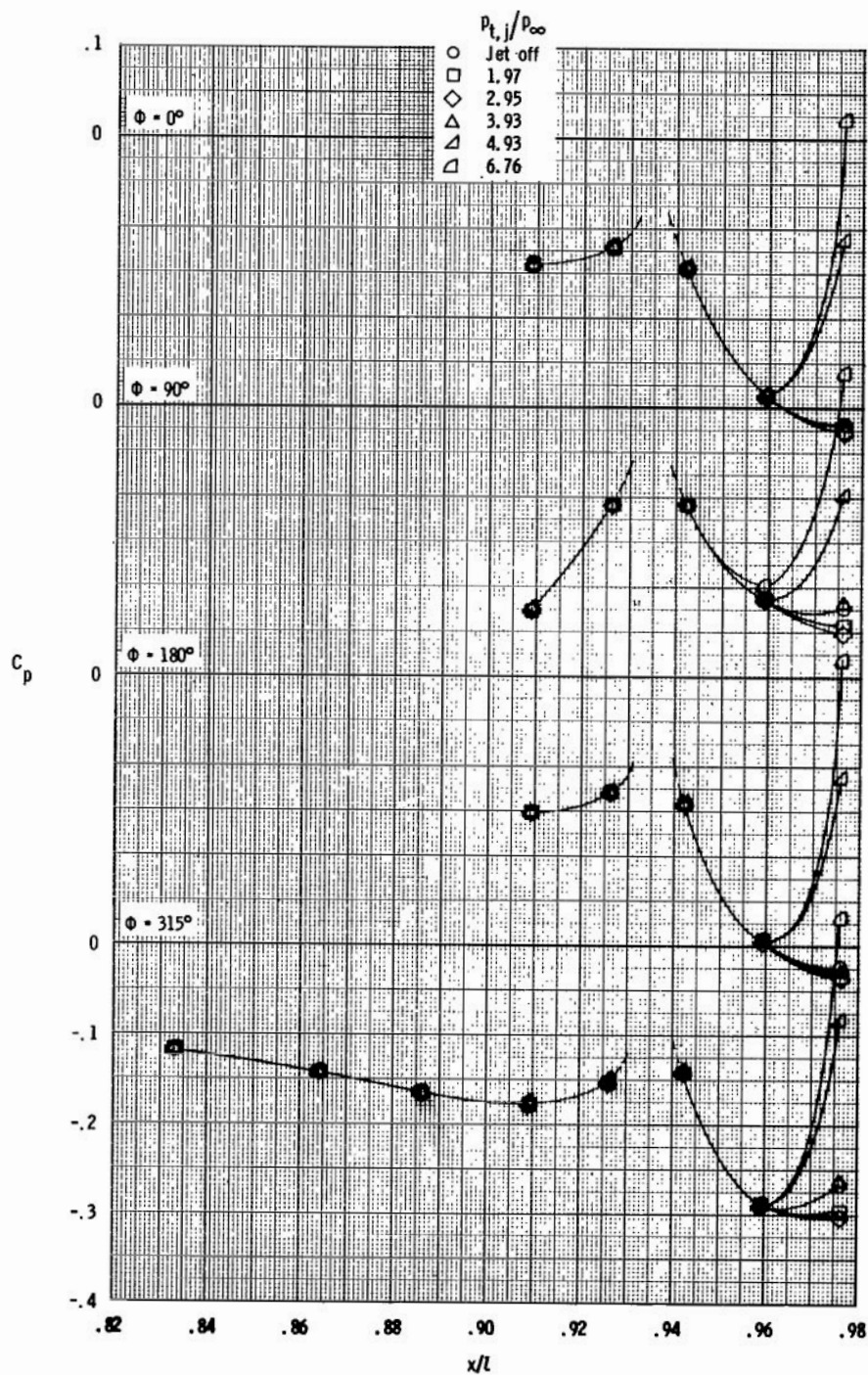
(c)   M = 1.19.

Figure 13.- Continued.
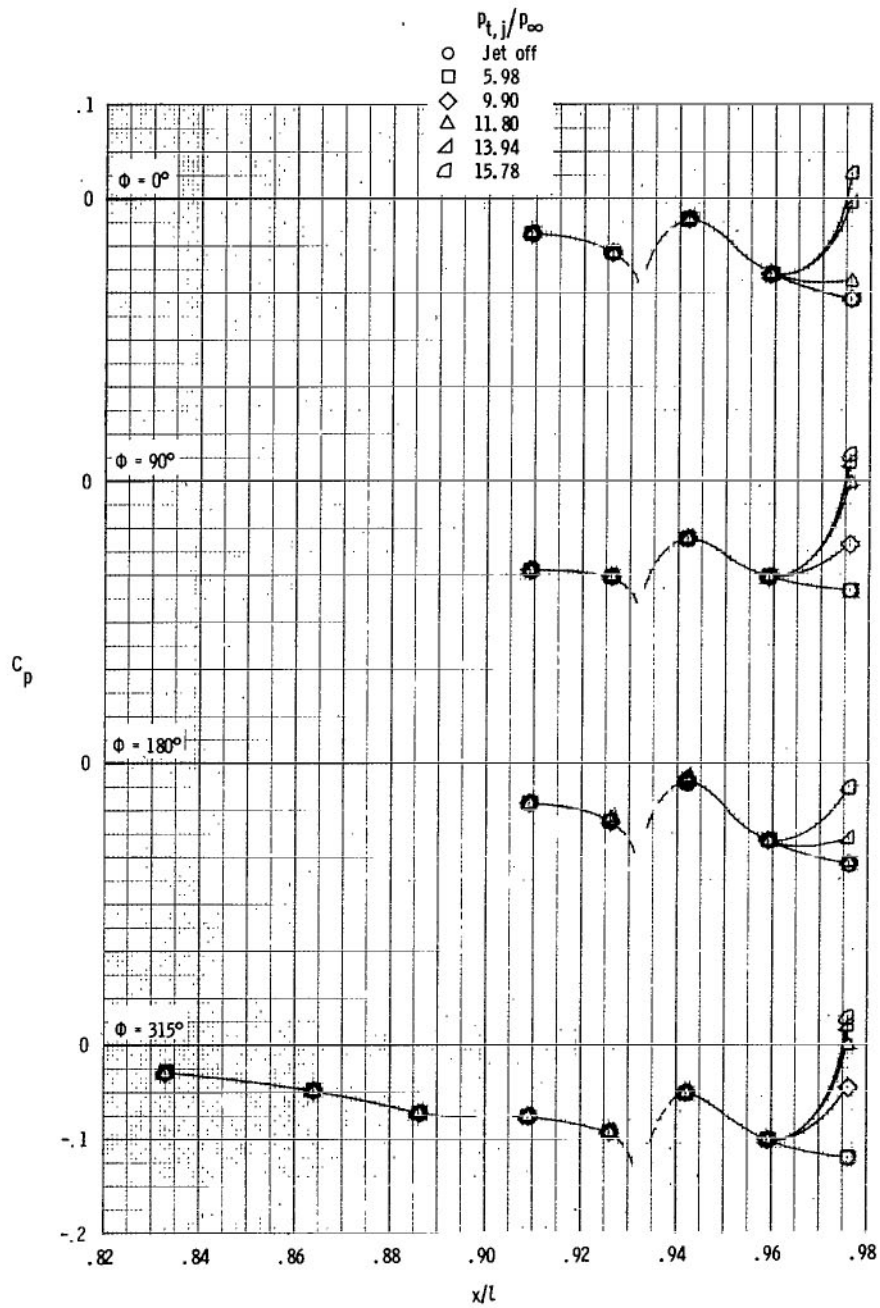
(d)   M = 2.20.

Figure 13.- Concluded.

Tail location
O Tails off
□ Aft vertical tail, aft horizontal tail
◇ Forward vertical tail, aft horizontal tail
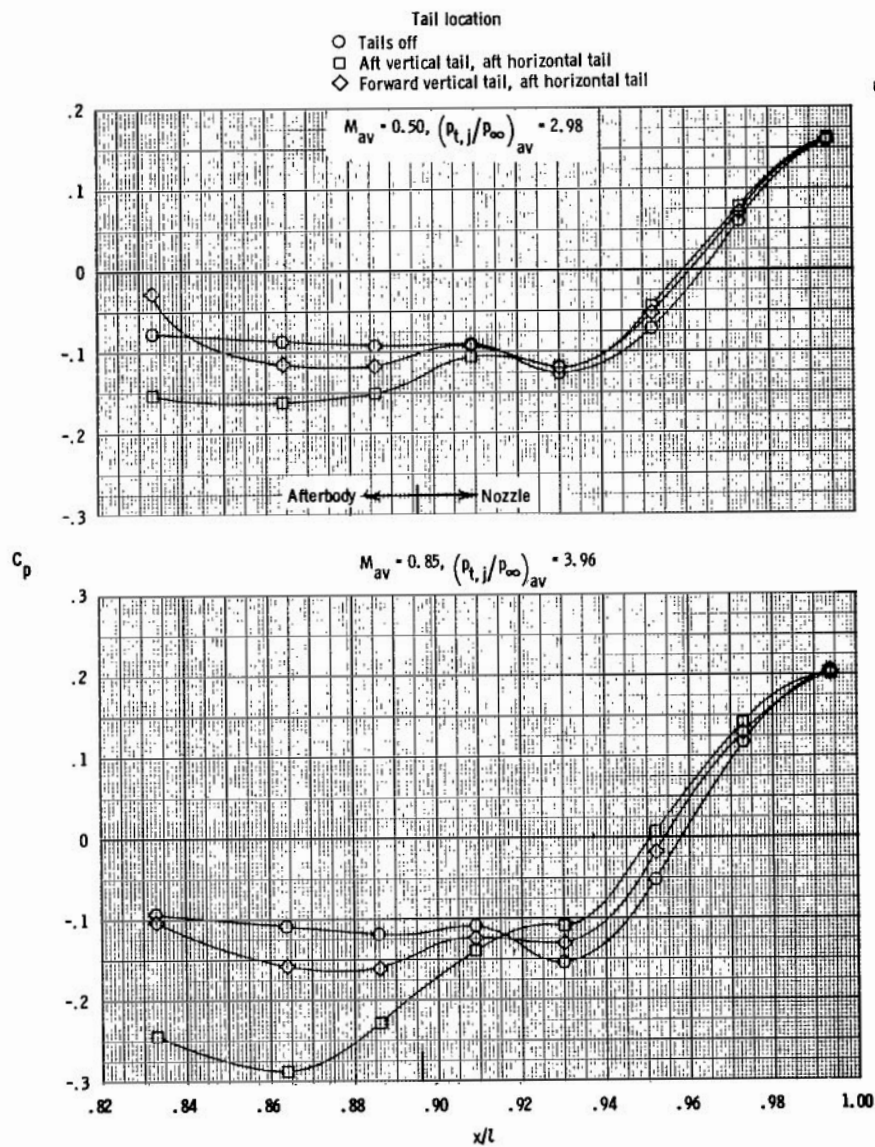
(a) $M_{av} = 0.50$ and 0.85.

Figure 14.- Effect of tail location on longitudinal afterbody/nozzle static-pressure distributions; basic afterbody with dry power nozzle; $\phi = 315^{o}$.
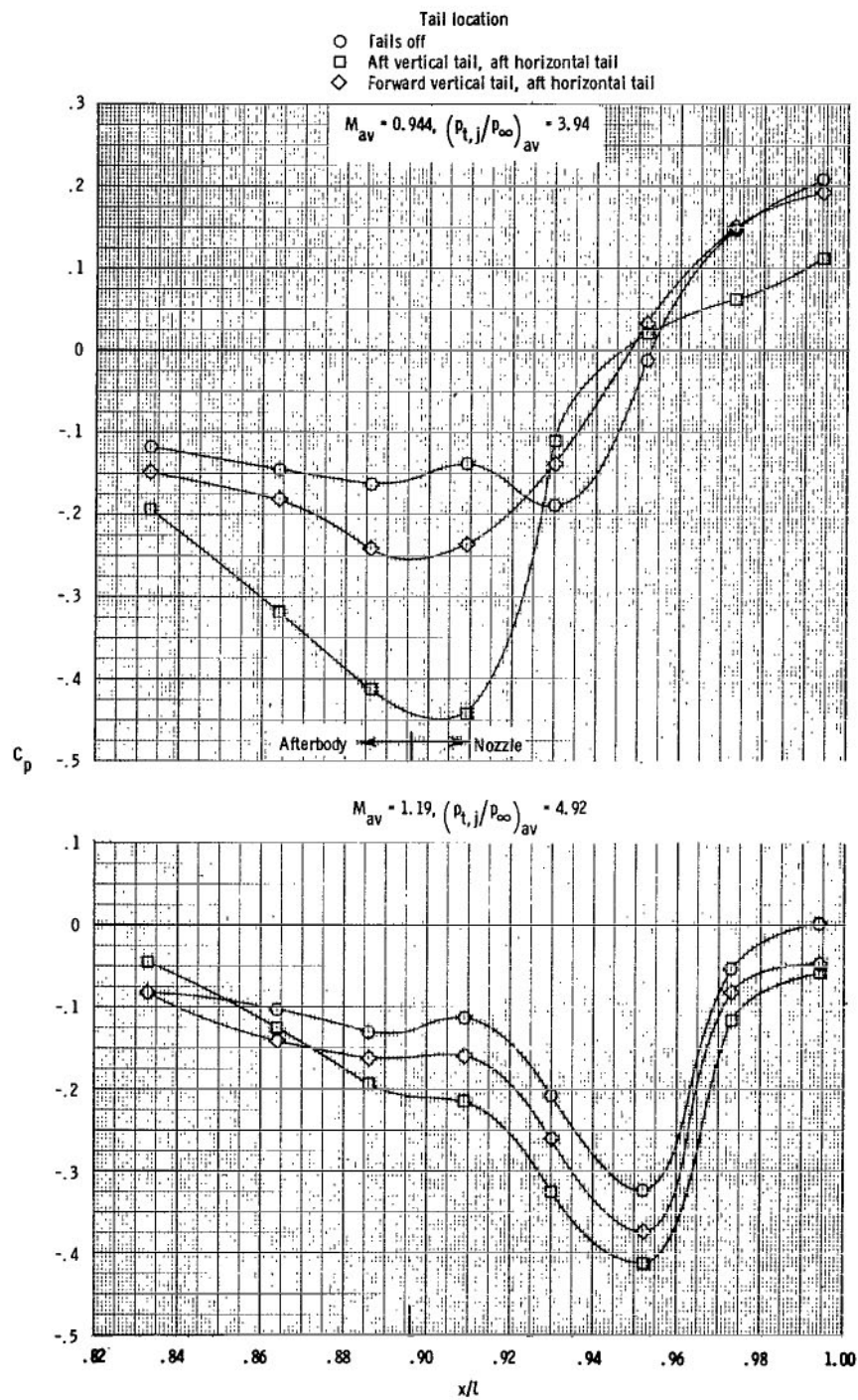
(b) M_{av} = 0.944 and 1.19.

Figure 14.- Concluded.

Tail location
○ Tails off
□ Aft vertical tail, aft horizontal tail
◇ Forward vertical tail, aft horizontal tail

$M_{av} = 0.50$, $\left(p_{t,j}/p_\infty\right)_{av} = 2.96$

$M_{av} = 0.84$, $\left(p_{t,j}/p_\infty\right)_{av} = 3.95$
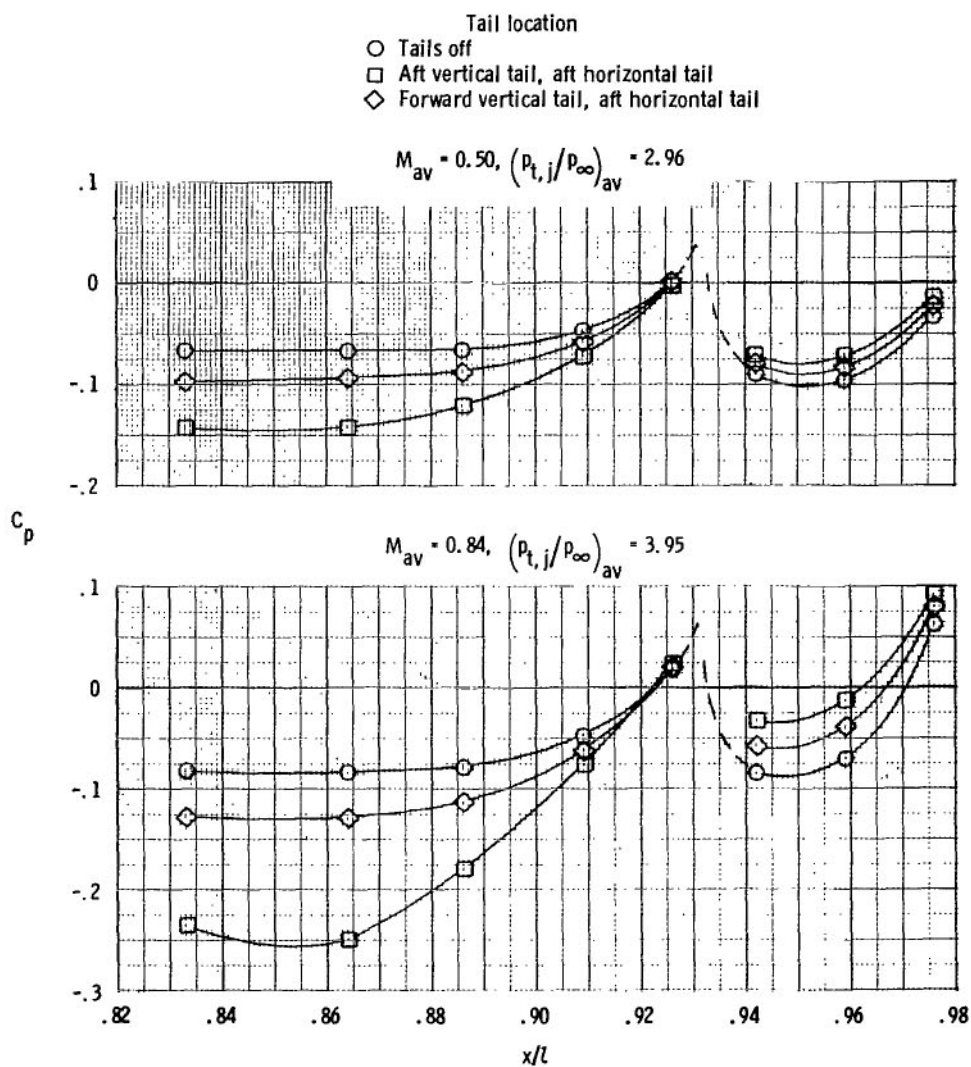
(a) $M_{av} = 0.50$ and 0.84.

Figure 15.-Effect of tail location on longitudinal afterbody/nozzle static-pressure distributions; basic afterbody with max. A/B power nozzle; $\phi = 315^\circ$.

Tail location

○   Tails off
□   Aft vertical tail, aft horizontal tail
◇   Forward vertical tail, aft horizontal tail

$M_{av} = 0.94$, $\left(p_{t,j}/p_{\infty}\right)_{av} = 3.94$

$M_{av} = 1.19$, $\left(p_{t,j}/p_{\infty}\right)_{av} = 4.91$
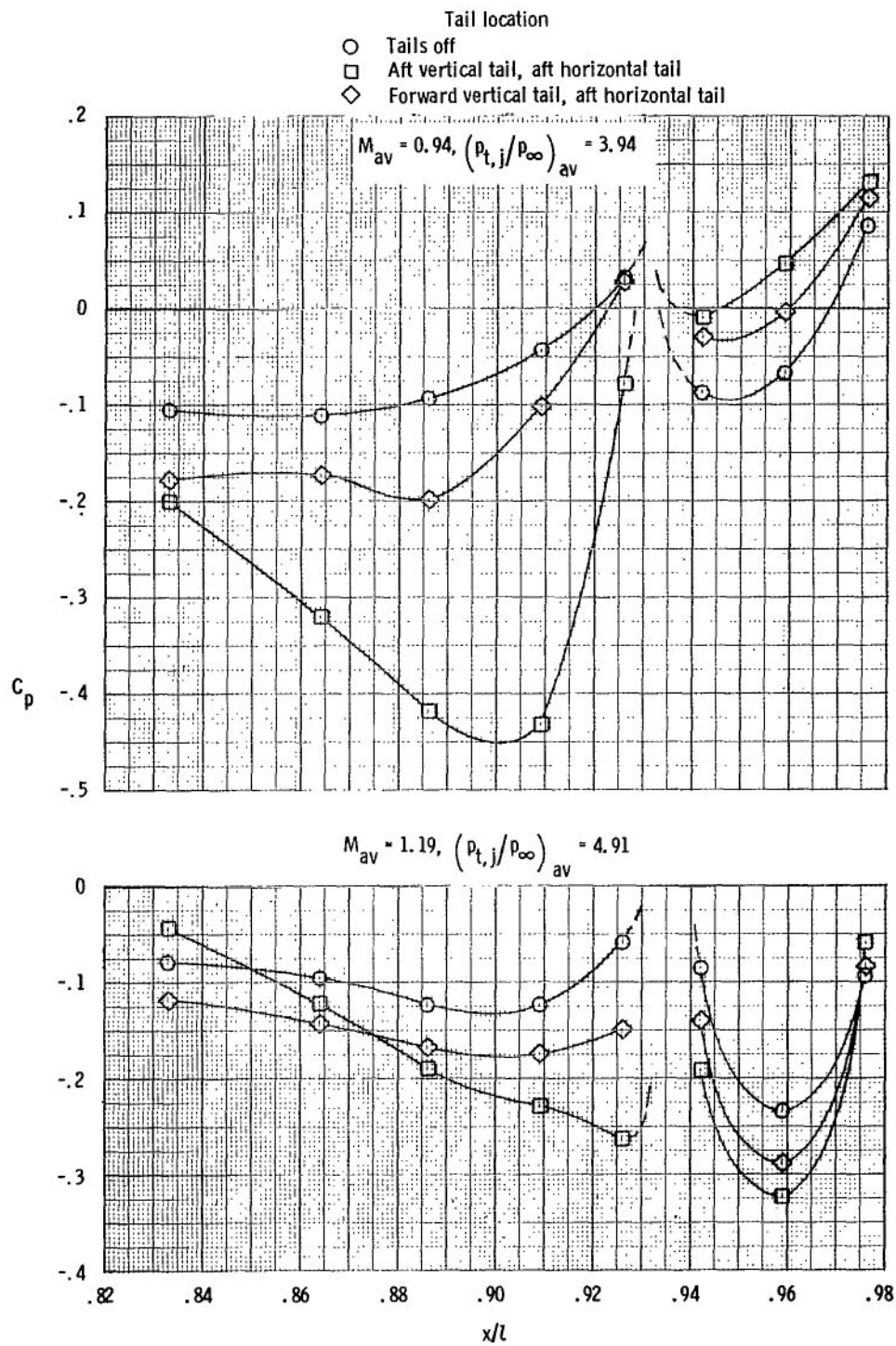
(b) $M_{av} = 0.94$ and 1.19.

Figure 15.- Concluded.
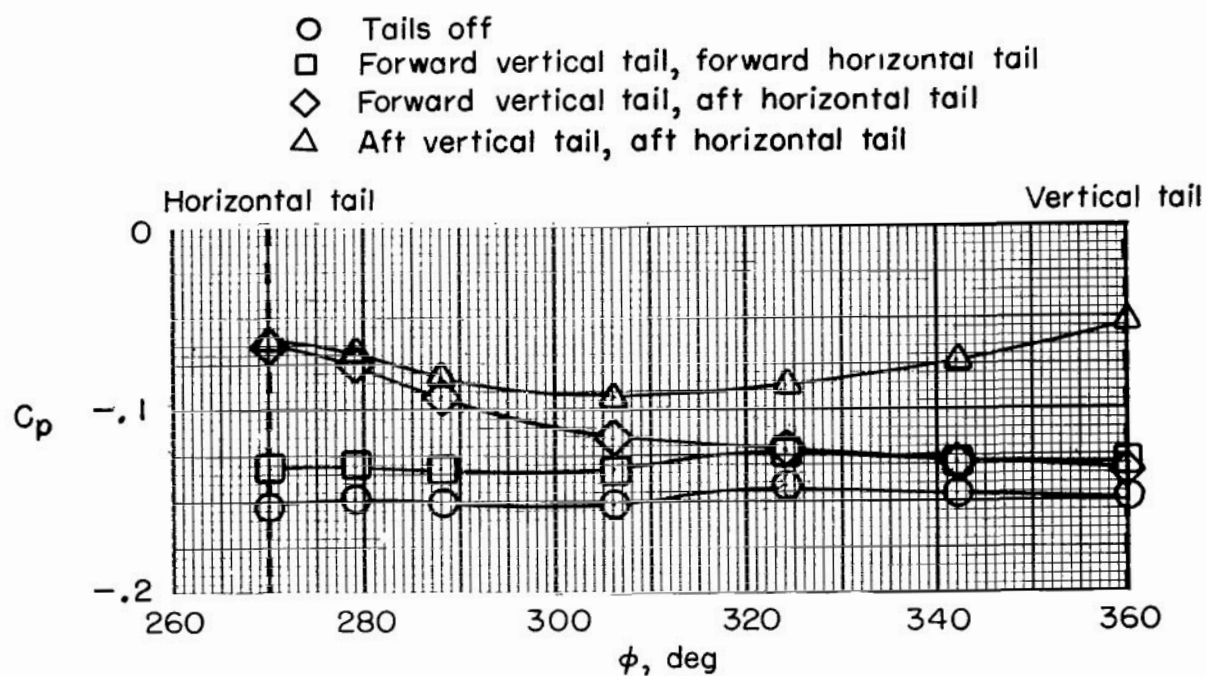
Figure 16.- Effect of tail location on circumferential static-pressure distributions for dry power nozzle. $x/1 = 0.935$, $M_{av} = 0.84$, and $(p_{t,j}/p_\infty)_{av} = 2.96$.

"Contour" bumps
○ Off
□ Partial
◇ Full

$M_{av} = 0.50$, $\left(p_{t,j}/p_{\infty}\right)_{av} = 2.97$

$M_{av} = 0.89$, $\left(p_{t,j}/p_{\infty}\right)_{av} = 3.96$

c_p

x/l
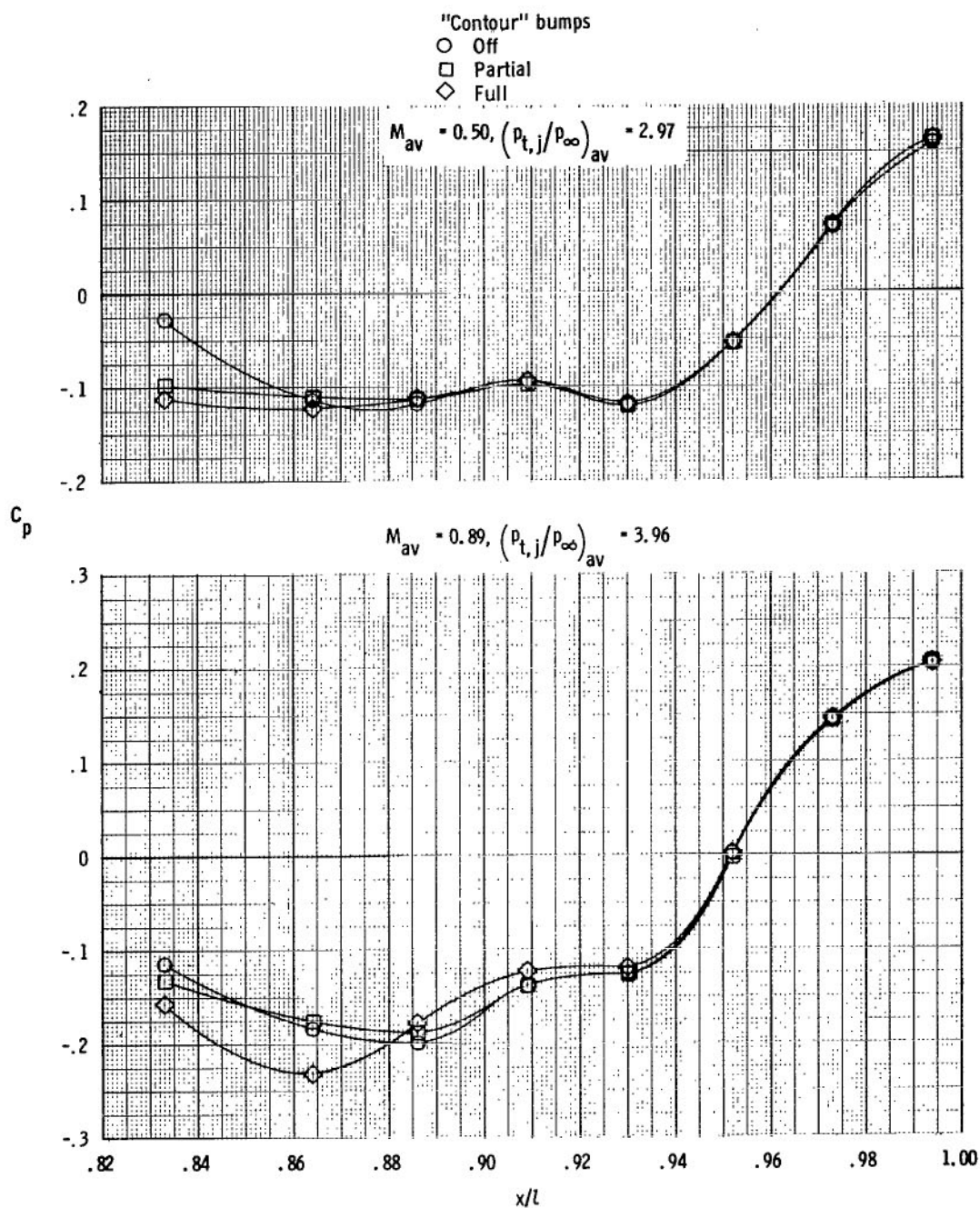
(a) $M_{av} = 0.50$ and 0.89.

Figure 17.- Effect of contour bumps on longitudinal afterbody/nozzle static-pressure distributions; basic afterbody with dry power nozzle, forward vertical tail, and aft horizontal tail; $\phi = 315°$.
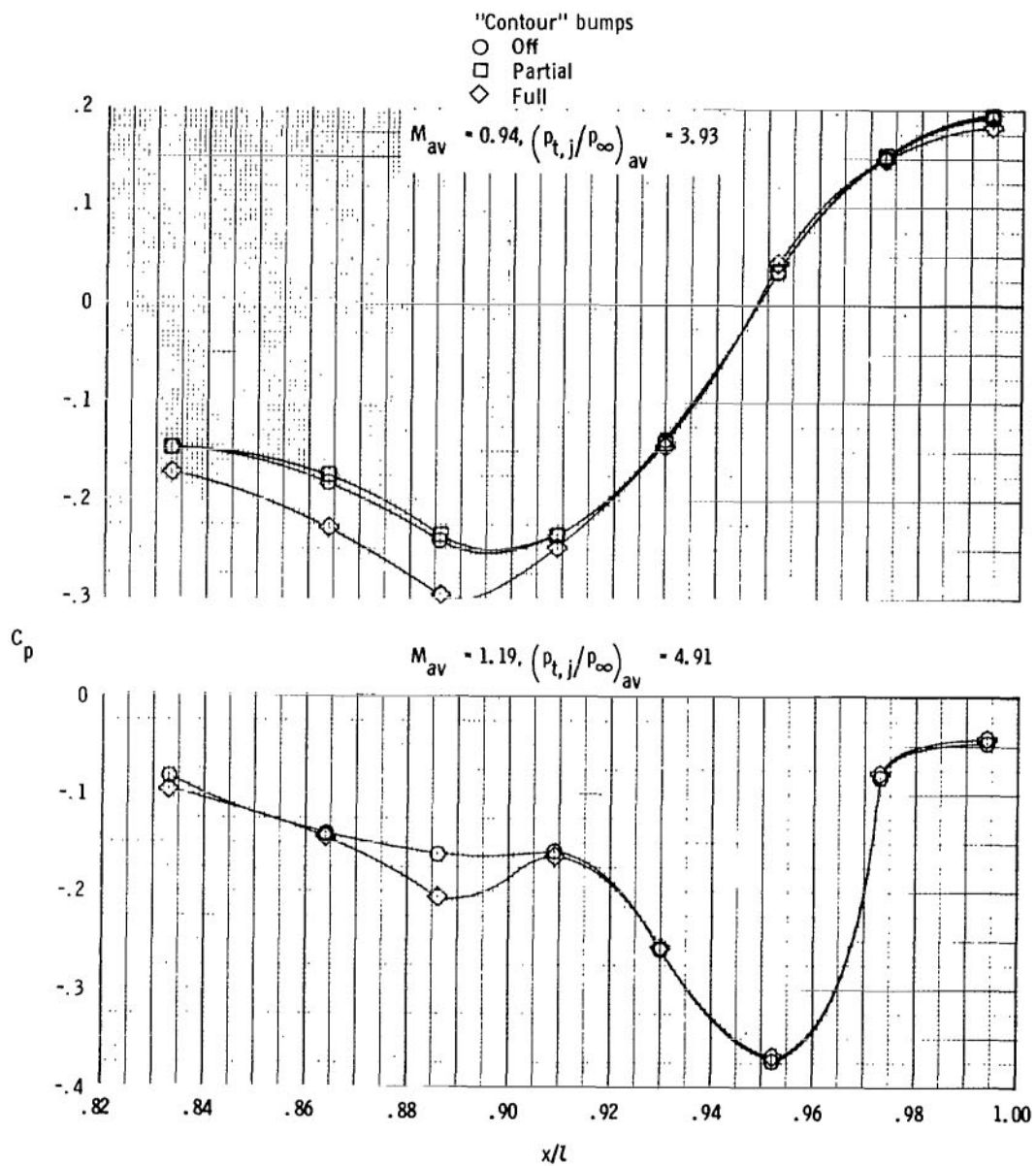
(b) $M_{av} = 0.94$ and 1.19.

Figure 17.- Concluded.

"Contour" bumps
○ Off
□ Full
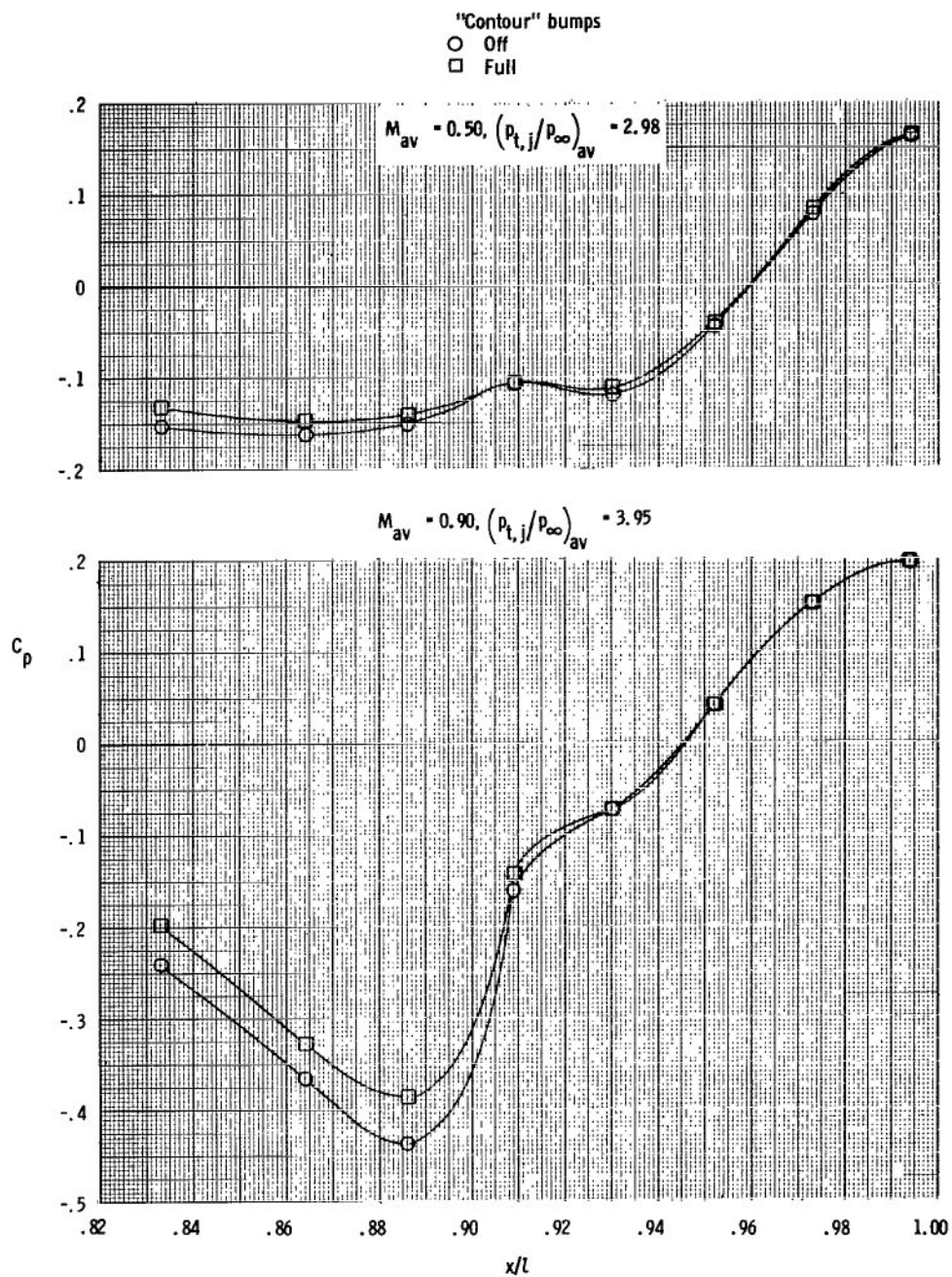
(a) M_{av} = 0.50 and 0.90.

Figure 18.- Effect of contour bumps on longitudinal afterbody/nozzle static-pressure distributions; basic afterbody with dry power nozzle, aft vertical tail, and aft horizontal tail; ϕ = 315°.
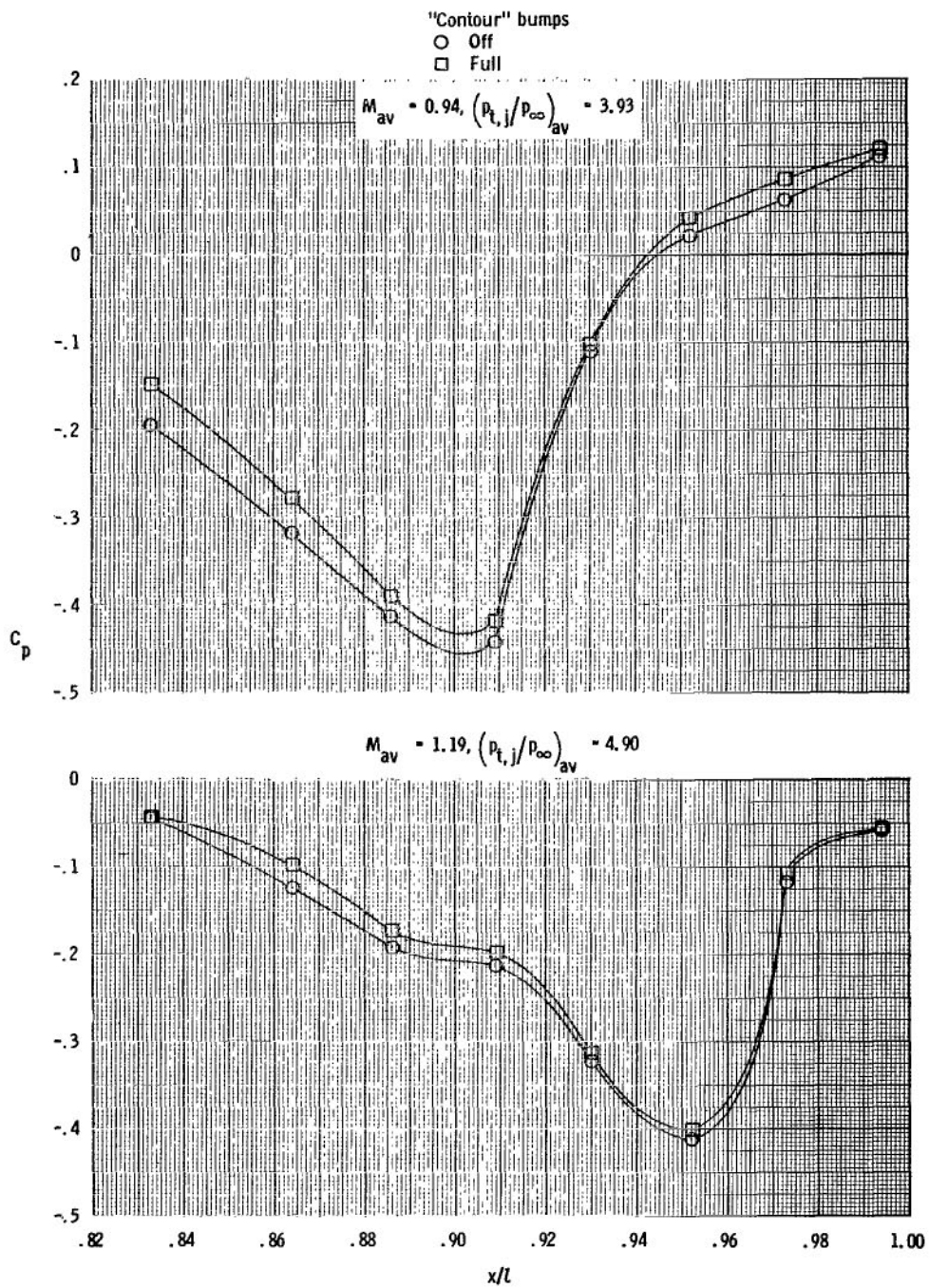
(b) $M_{av} = 0.94$ and 1.19.

Figure 18.- Concluded.
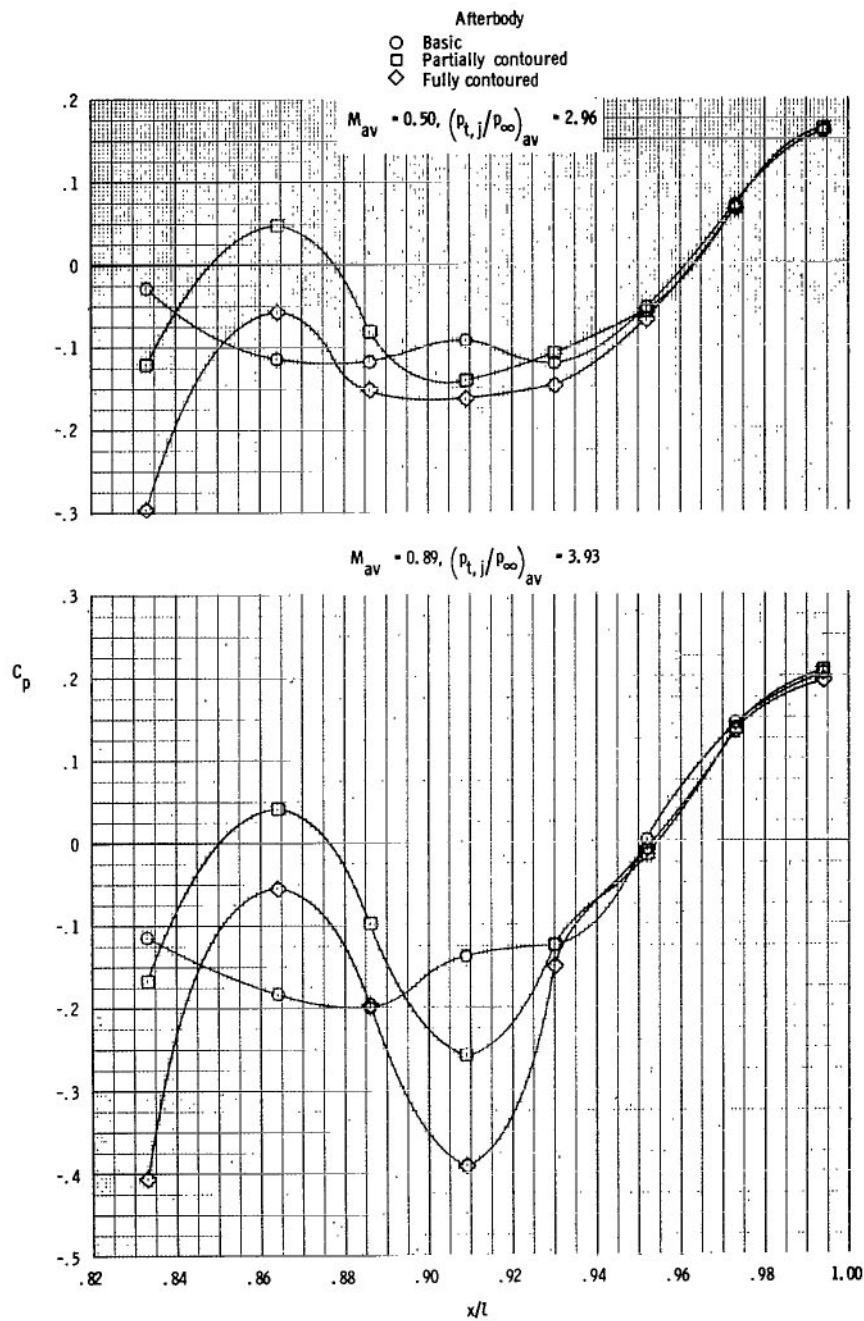
(a) M_{av} = 0.50 and 0.89.

Figure 19.- Effect of afterbody contouring on afterbody/nozzle longitudinal static-pressure distributions; afterbodies with dry power nozzle, forward vertical tail, and aft horizontal tail; ϕ = 315°.

Afterbody
○ Basic
□ Partially contoured
◇ Fully contoured
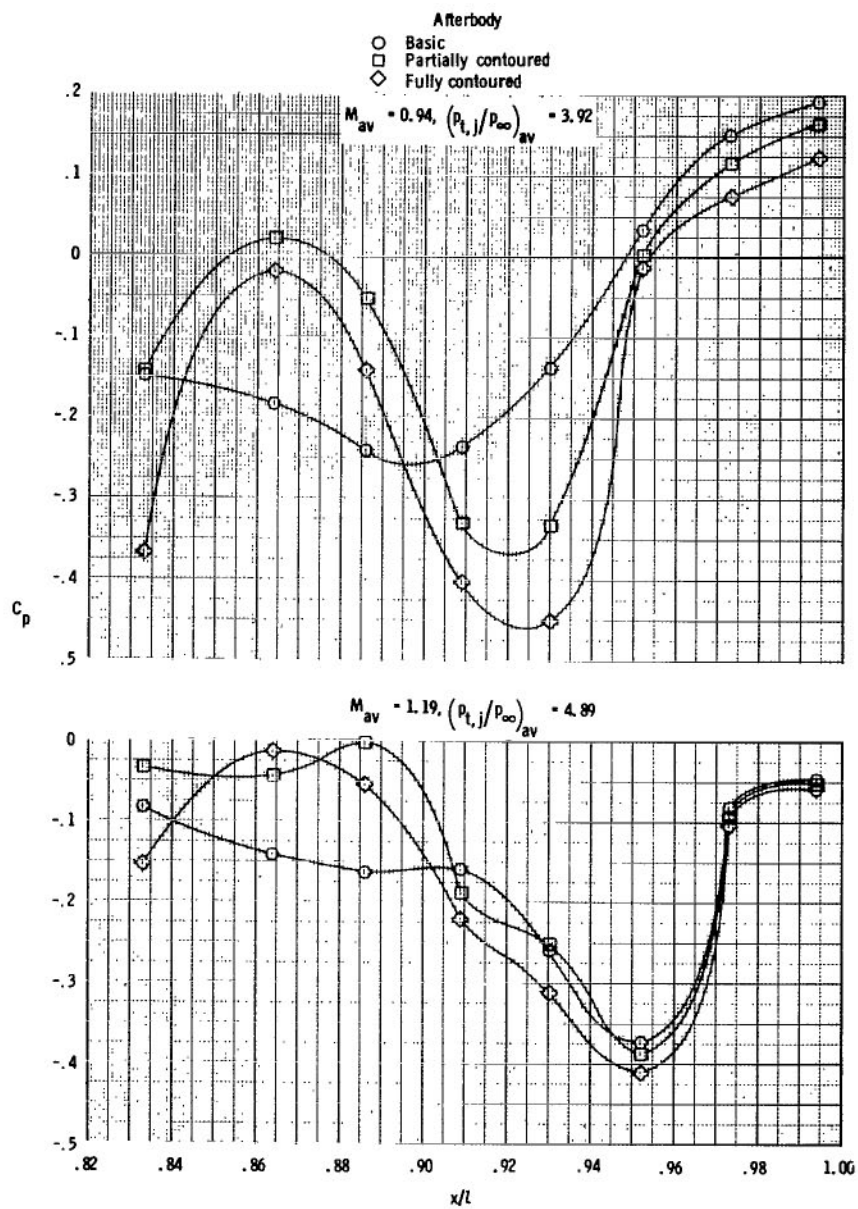
(b) $M_{av} = 0.94$ and 1.19.

Figure 19.- Concluded.

Afterbody
O Basic
□ Fully contoured

$M_{av} = 0.50$, $\left(p_{t,j}/p_\infty\right)_{av} = 2.96$

$M_{av} = 0.84$, $\left(p_{t,j}/p_\infty\right)_{av} = 3.97$

C_p

x/l
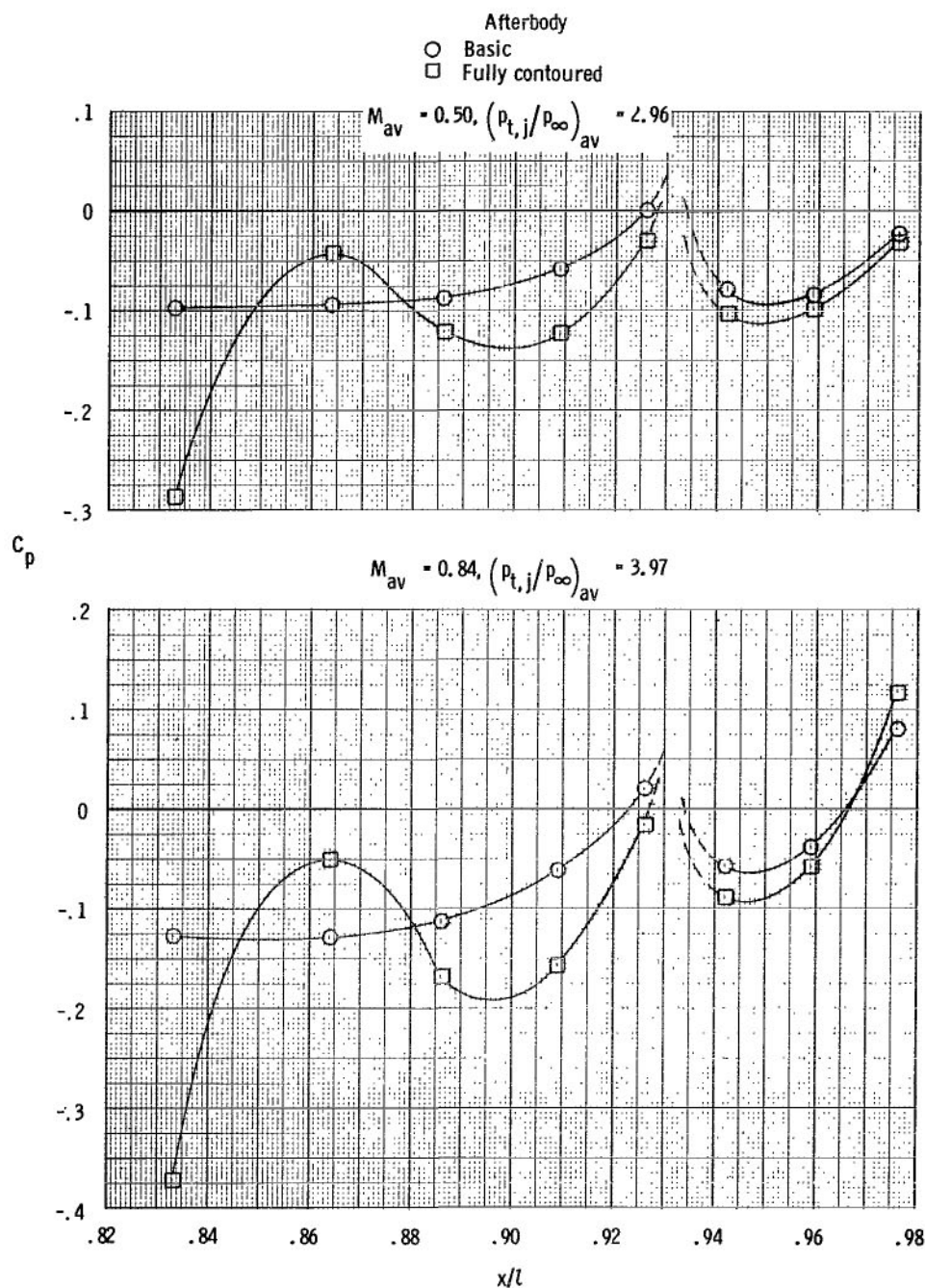
(a) $M_{av} = 0.50$ and 0.84.

Figure 20.- Effect of afterbody contouring on afterbody/nozzle longitudinal
static-pressure distributions; afterbodies with max. A/B power nozzle,
forward vertical tail, and aft horizontal tail; $\phi = 315^\circ$.

136
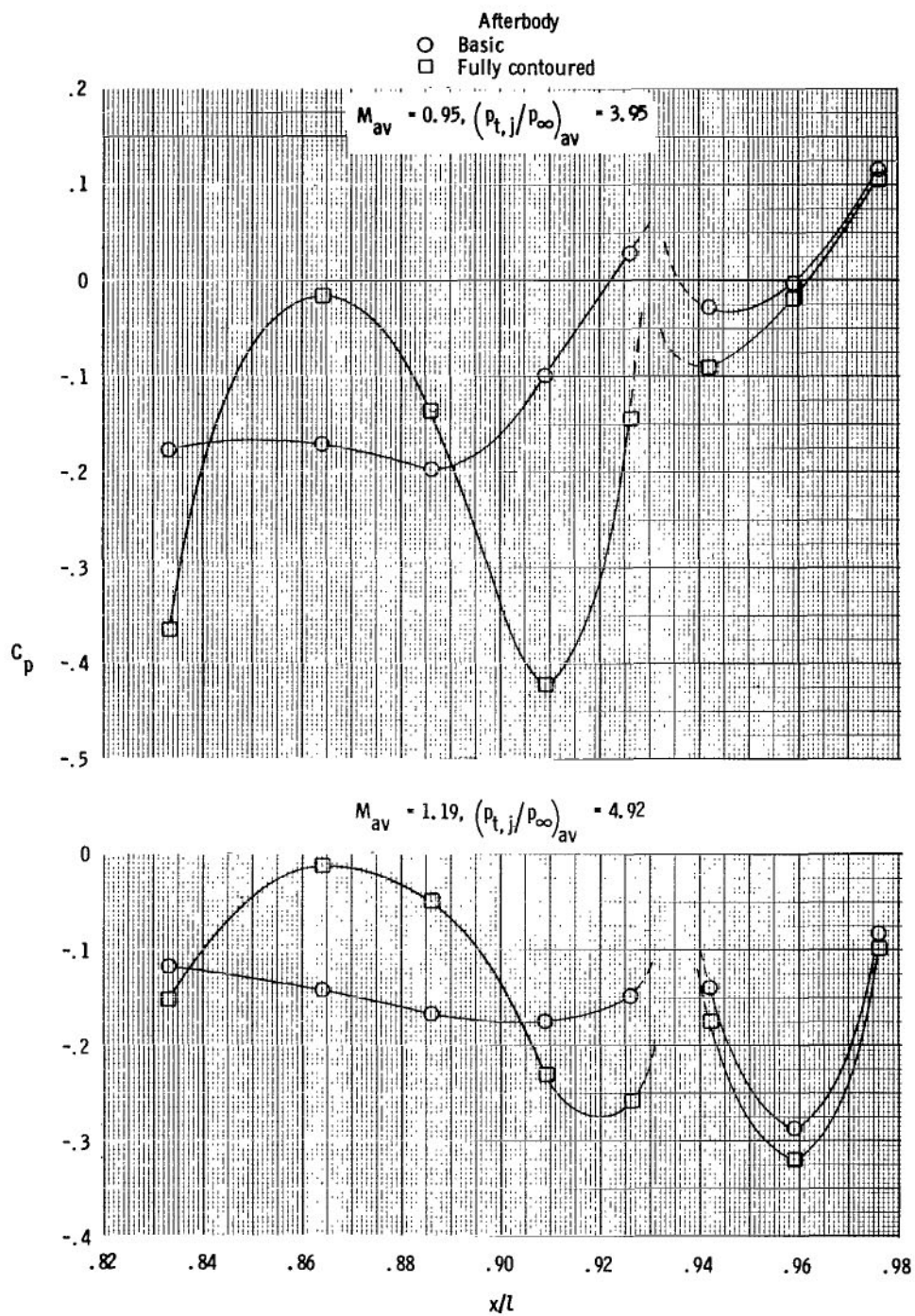
(b) M_{av} = 0.95 and 1.19.

Figure 20.- Concluded.
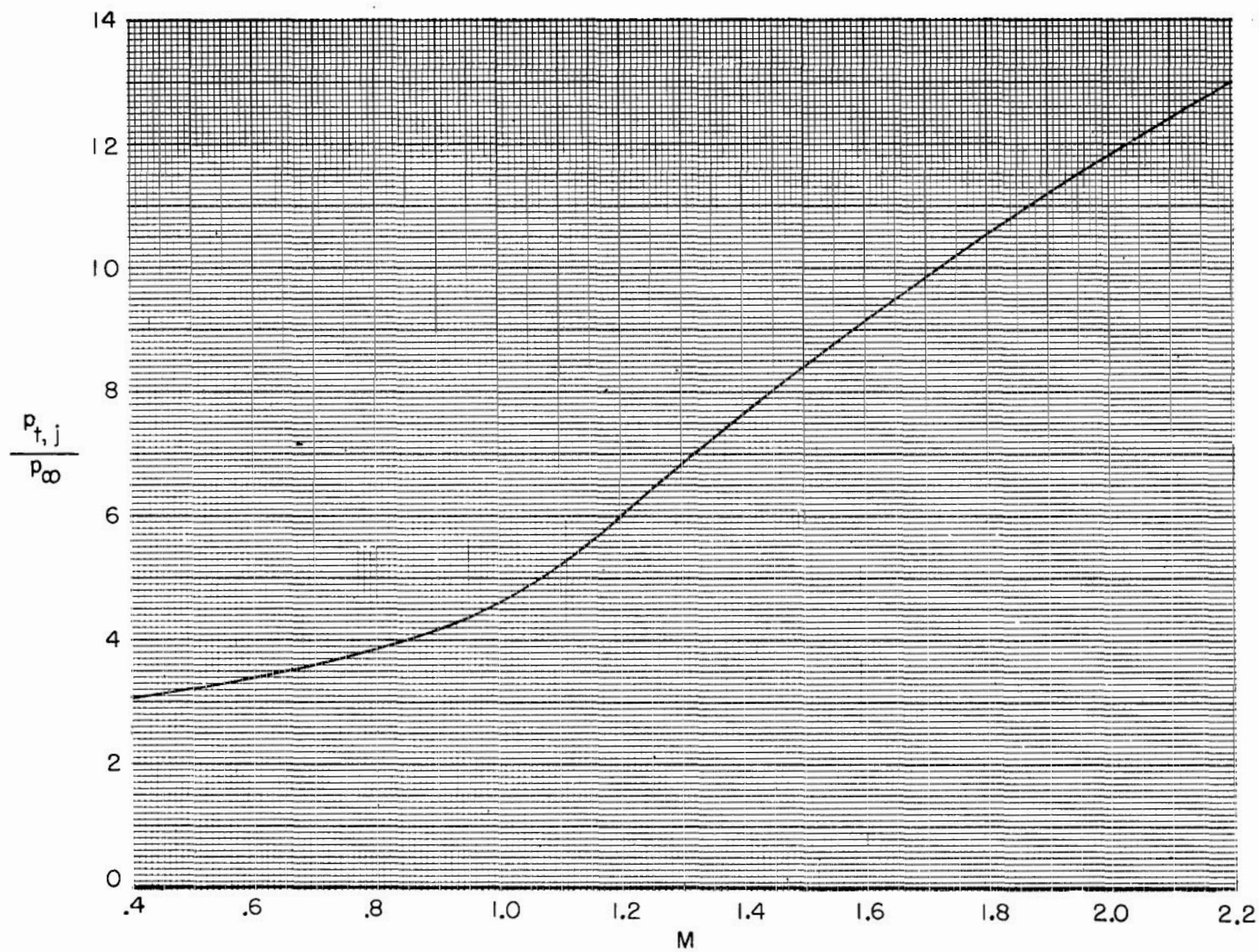
Figure 21.- Typical jet total pressure ratios for a turbofan engine.
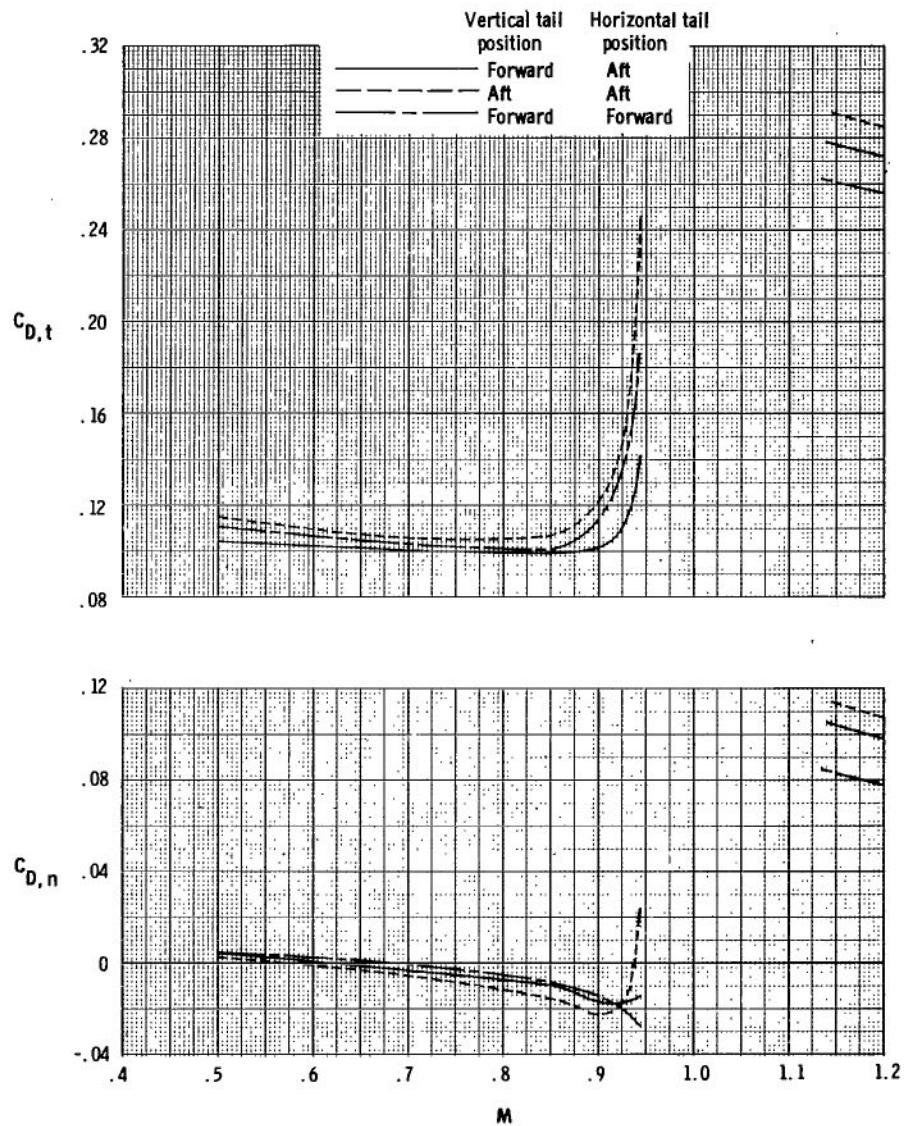
(a) Total and nozzle drag coefficients.

Figure 22.- Effect of empennage arrangement (tail location) on variation of
aft-end drag coefficient components with Mach number for scheduled jet
total pressure ratios; basic afterbody with dry power nozzle.

139
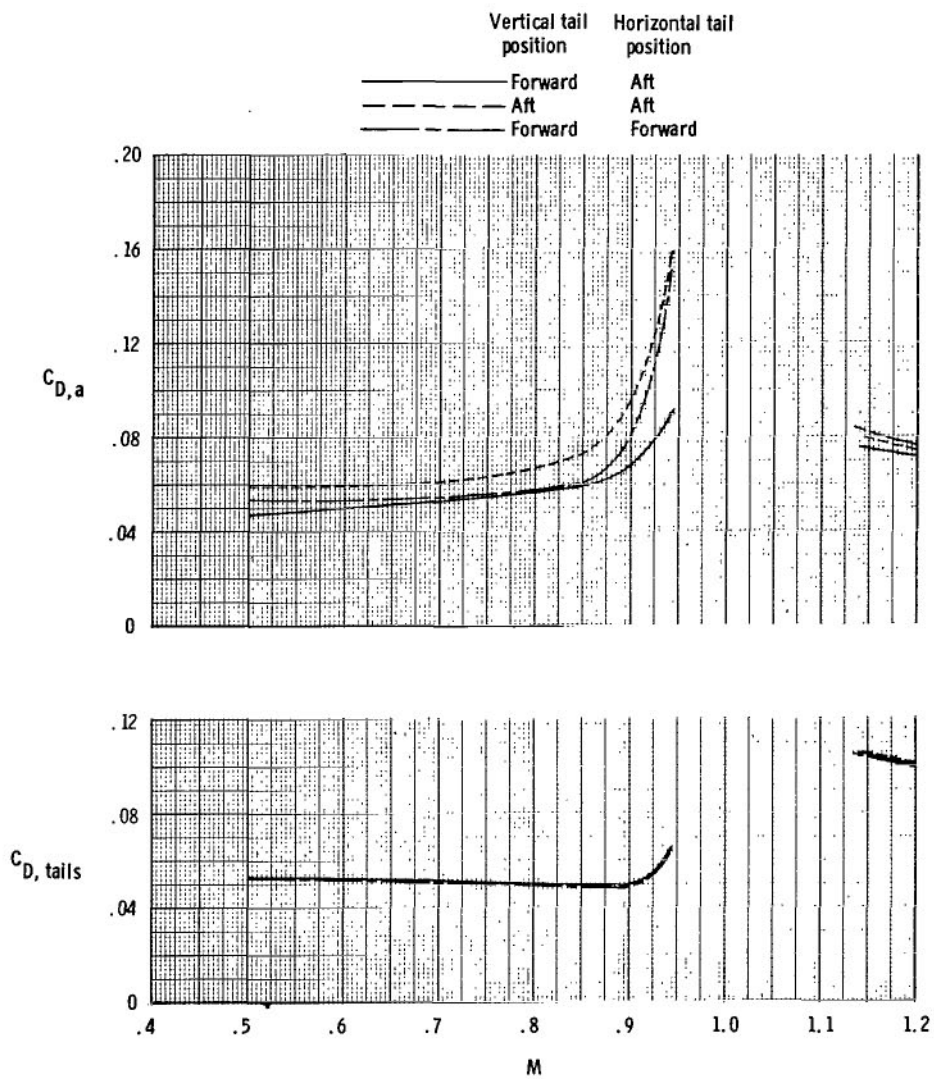
(b) Afterbody and tail drag coefficients.

Figure 22.- Continued.
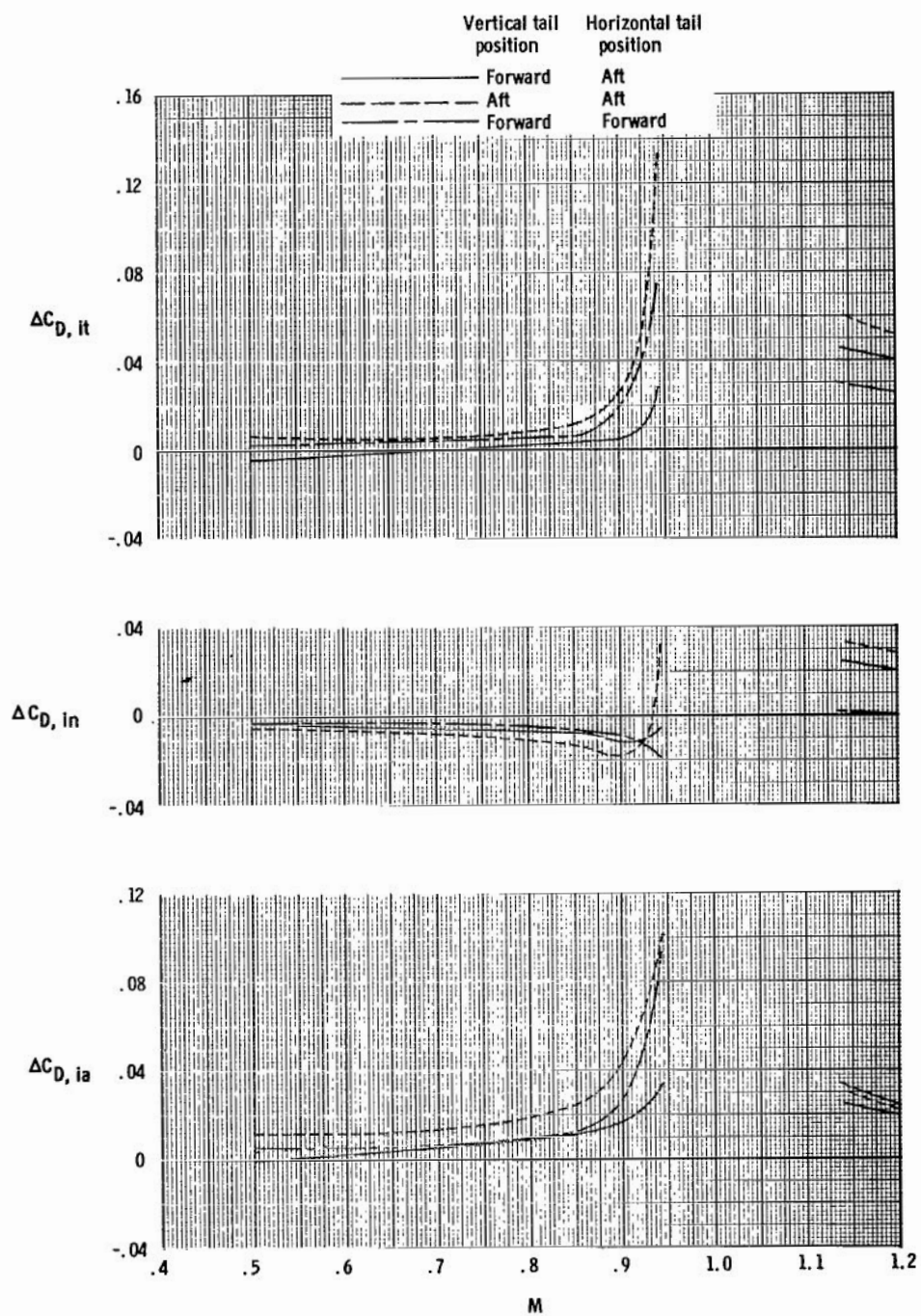
(c) Tail interference-drag coefficient increments on total aft end,
nozzle, and afterbody.

Figure 22.- Concluded.
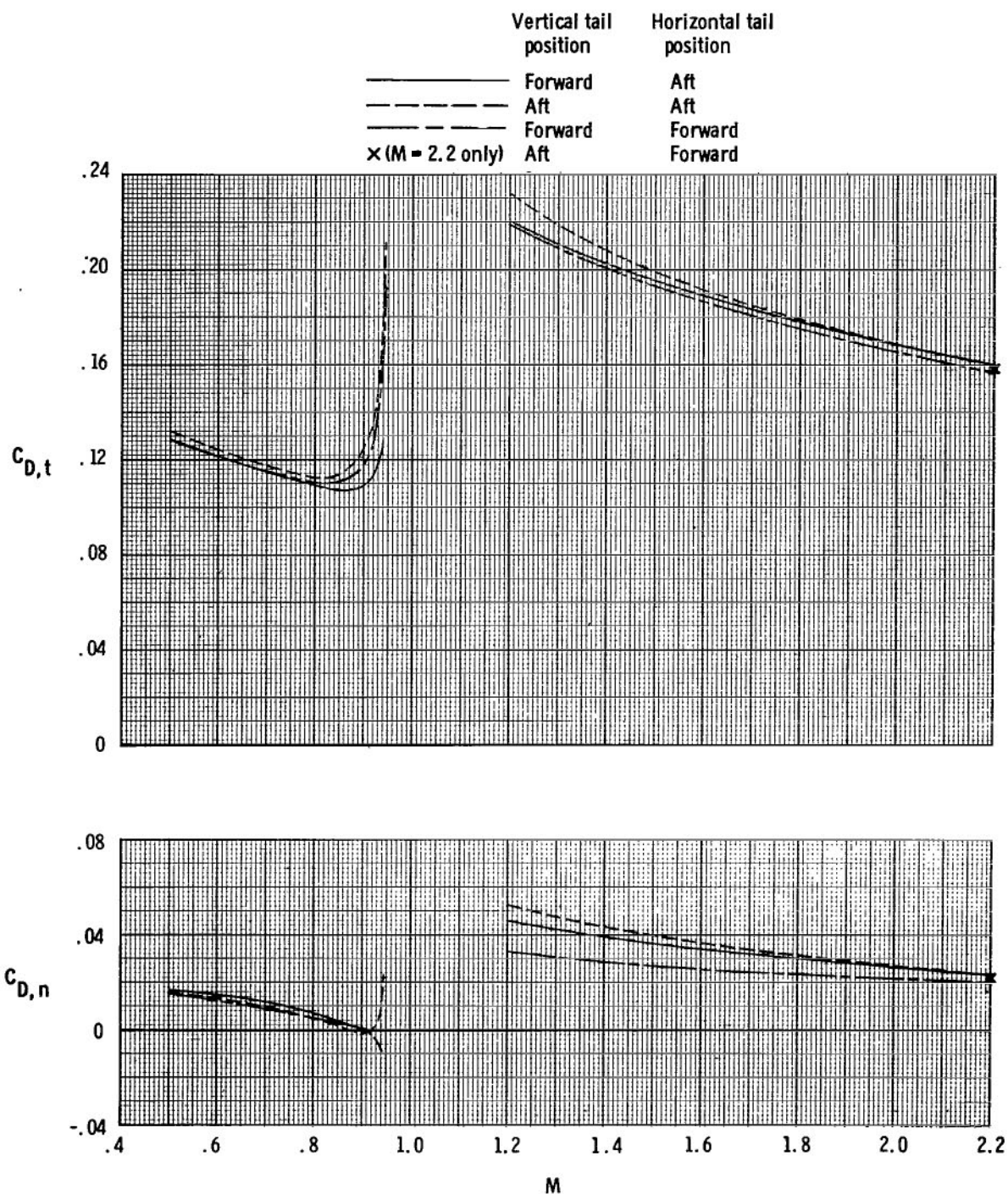
(a) Total and nozzle drag coefficients.

Figure 23.- Effect of empennage arrangement (tail location) on variation of aft-
end drag coefficient components with Mach number for scheduled jet total
pressure ratios; basic afterbody with max. A/B power nozzle.

142
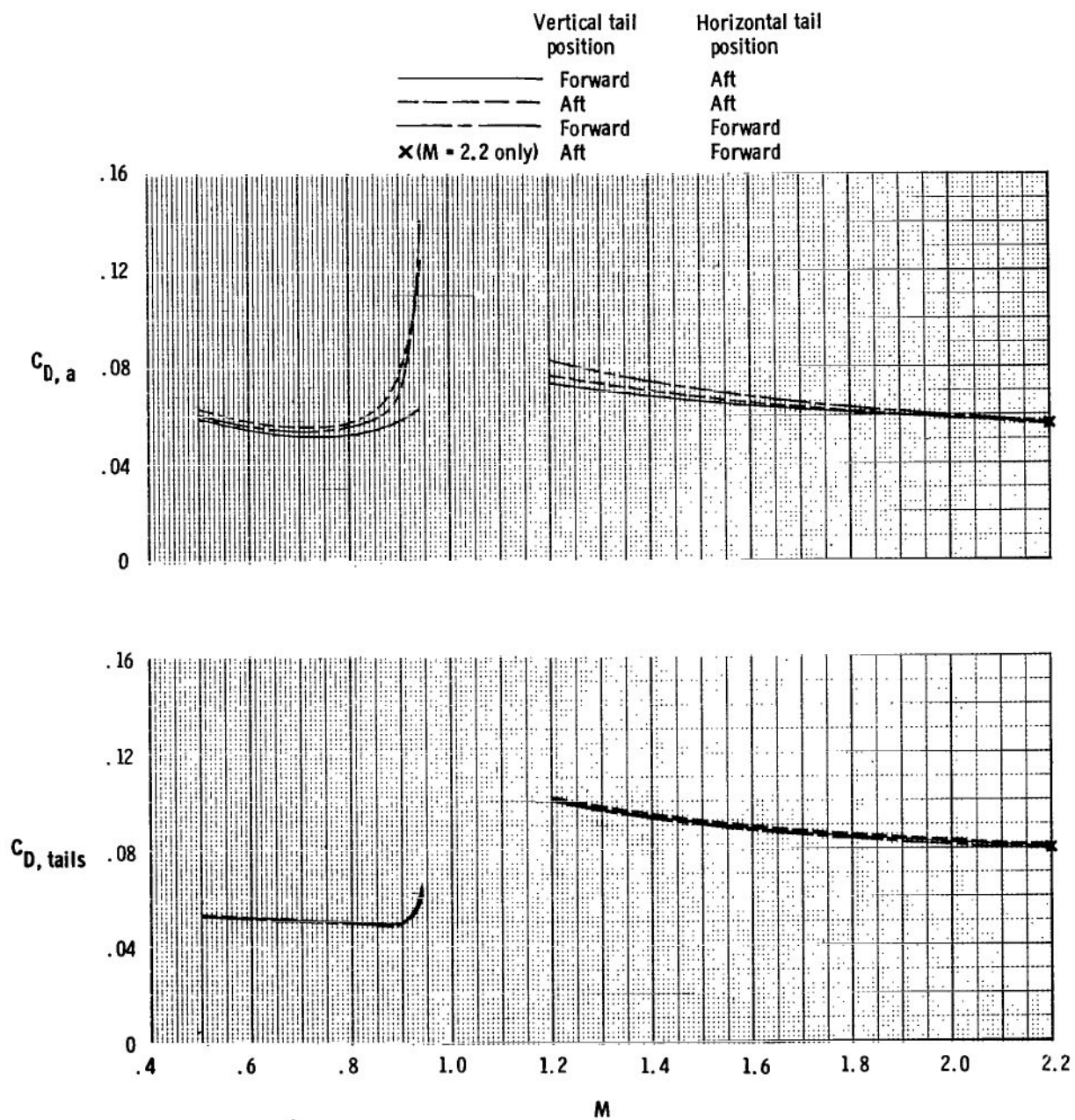
(b) Afterbody and tail drag coefficients.

Figure 23.- Continued.
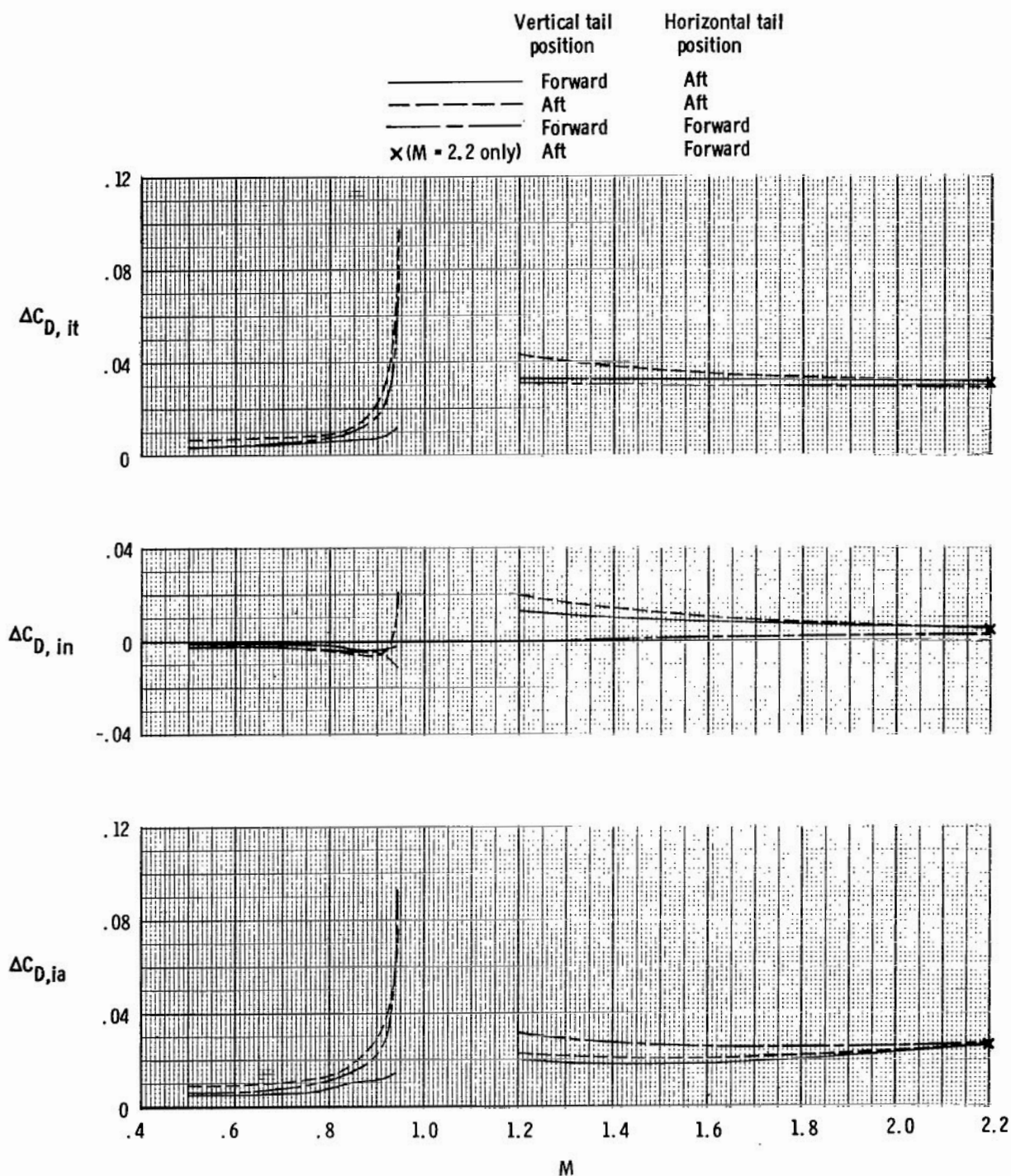
(c) Tail interference-drag coefficient increments on total aft end, nozzle, and afterbody.
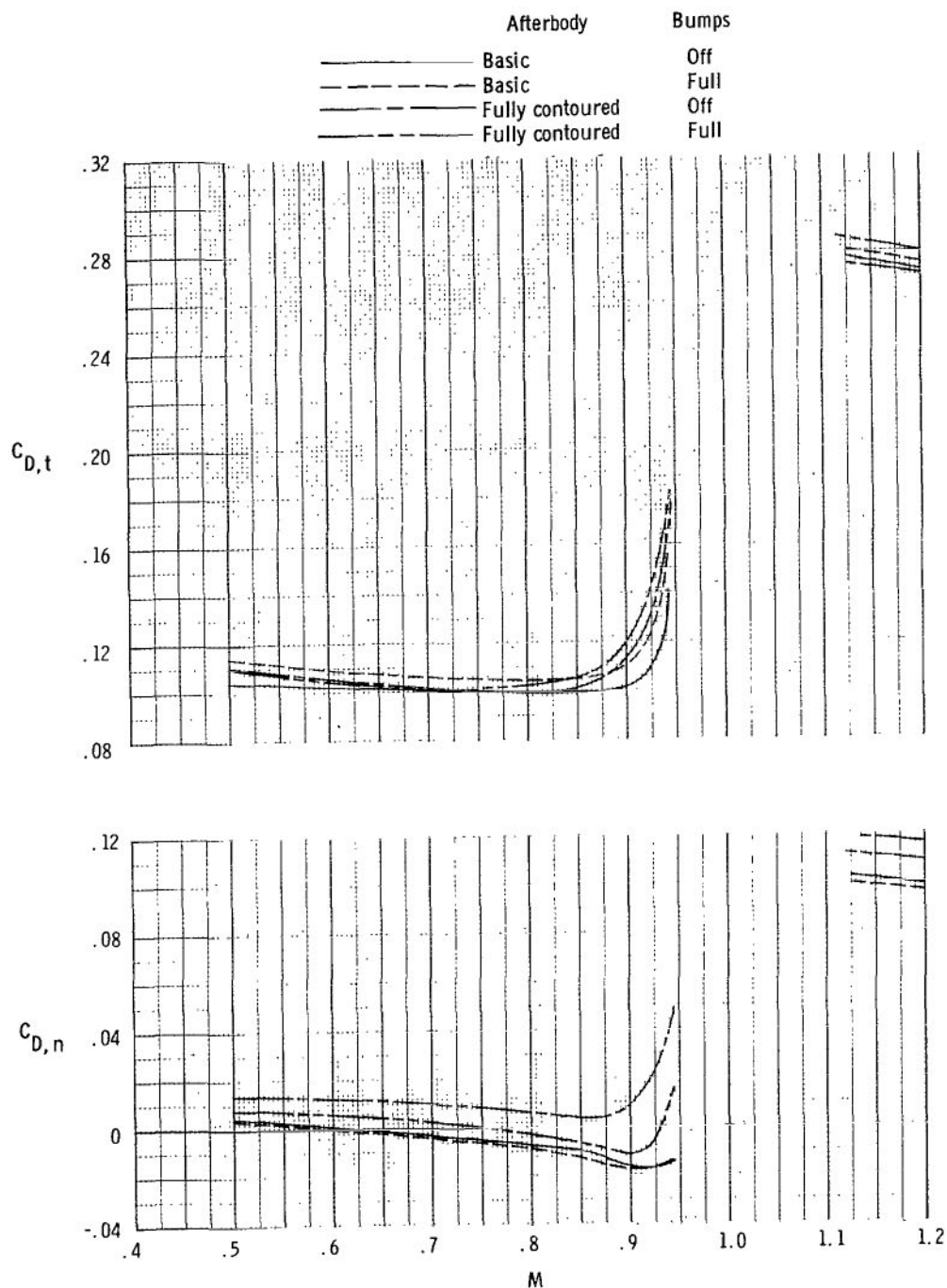
Figure 23.- Concluded.
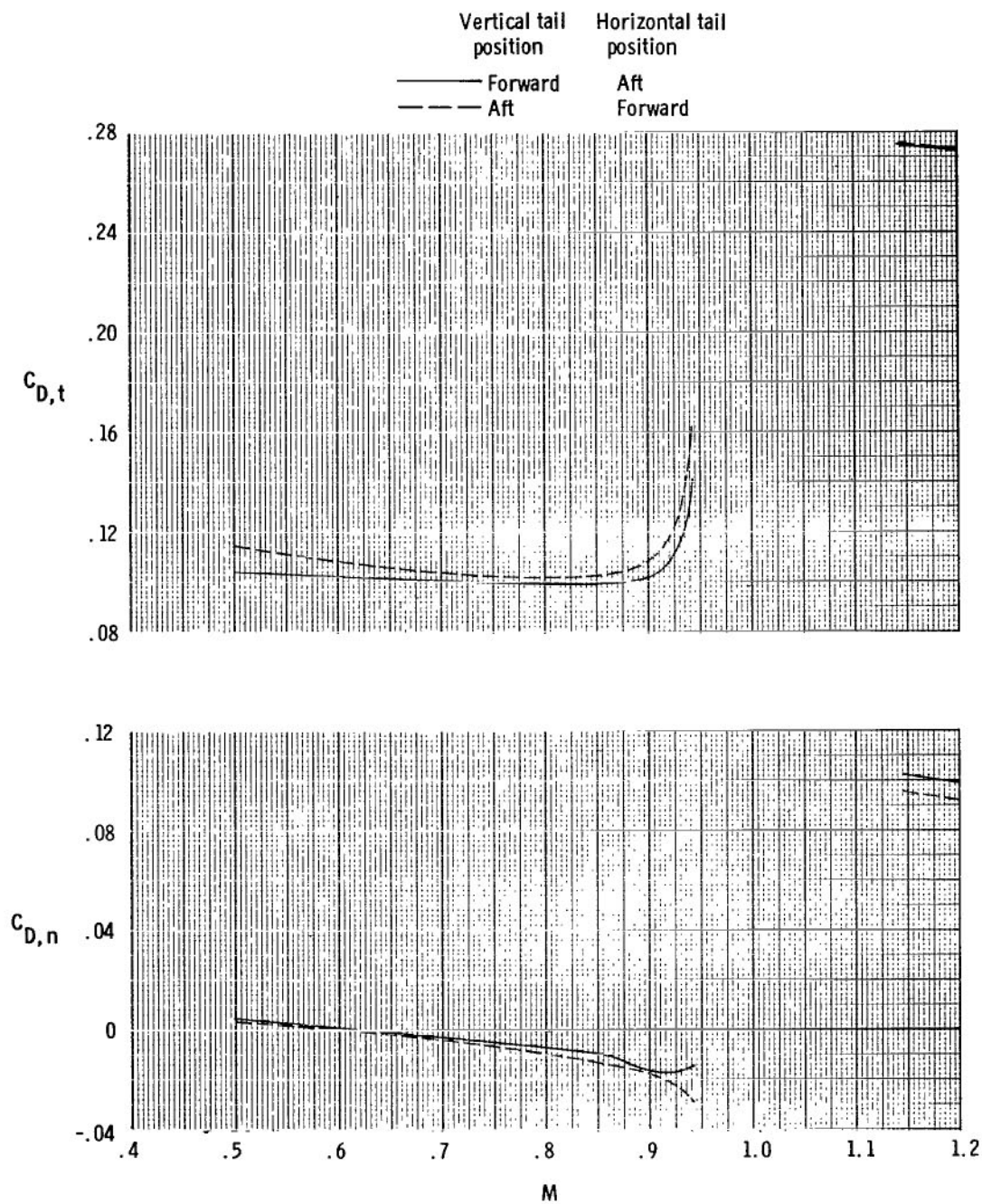
(a) Total and nozzle drag coefficients.

Figure 24.- Effect of method for staggering empennage surfaces on variation of aft-end drag coefficient components with Mach number for scheduled jet total pressure ratios; basic afterbody with dry power nozzle.
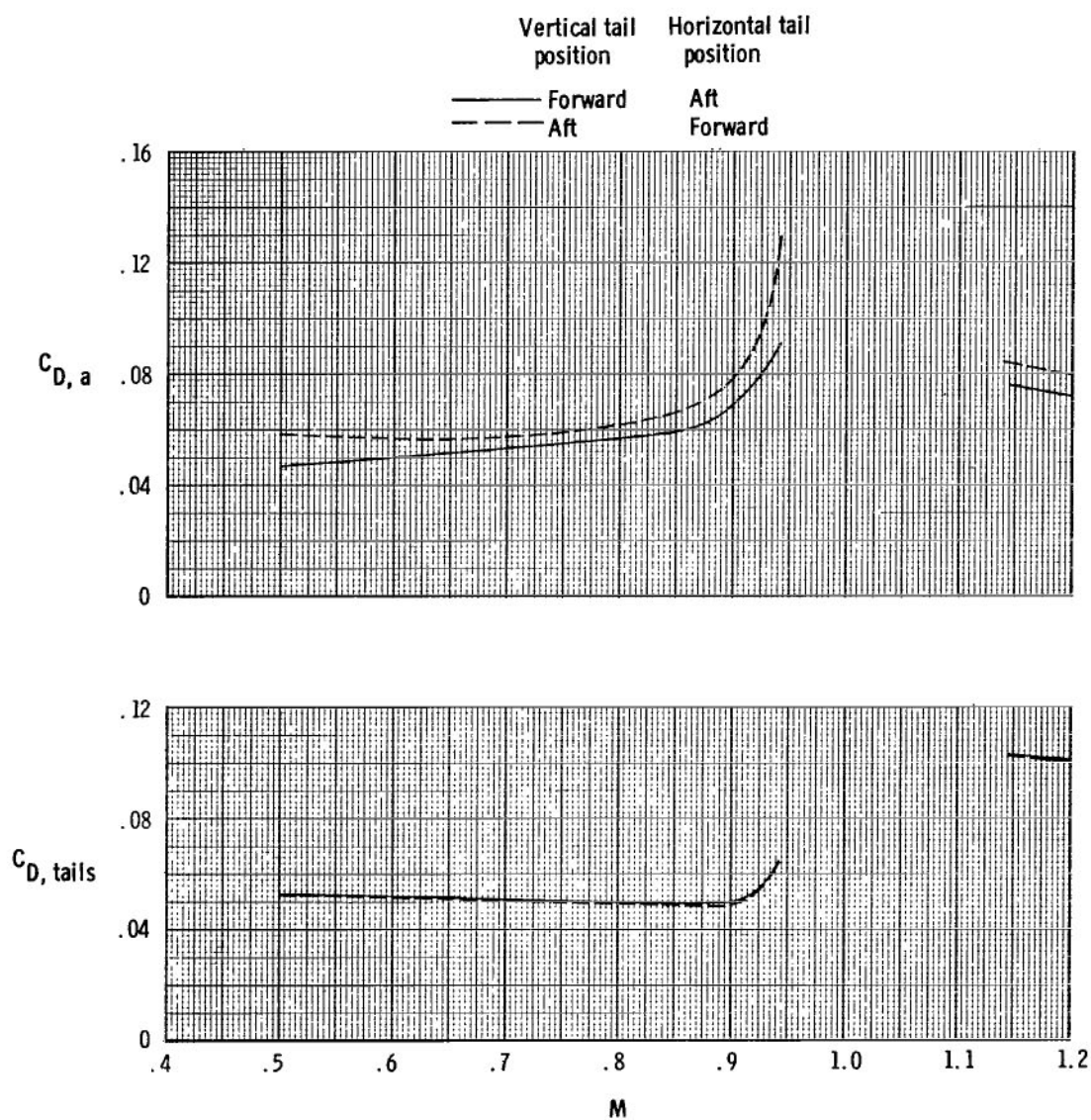
(b) Afterbody and tail drag coefficients.

Figure 24.- Continued.
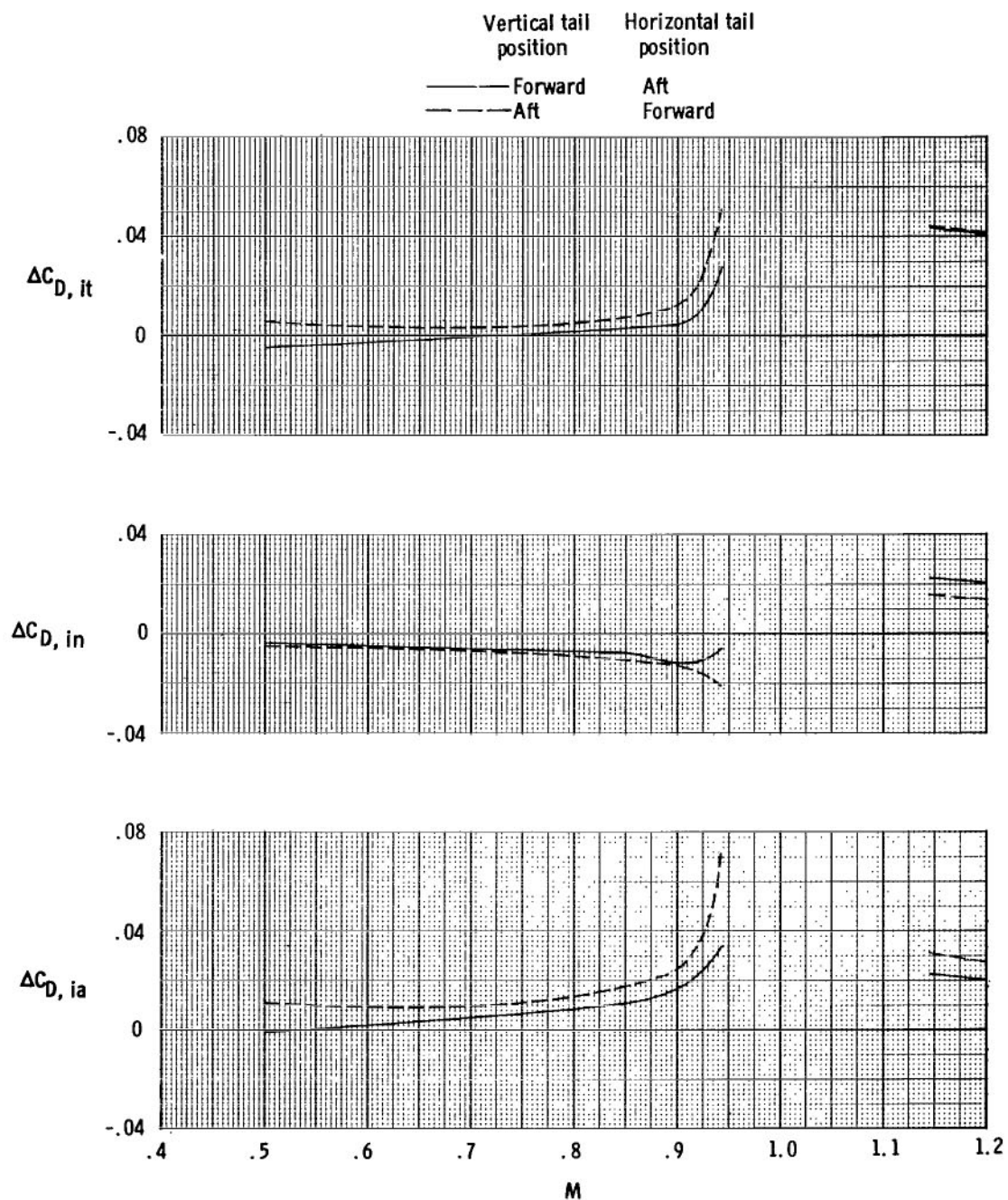
146

(c) Tail interference-drag coefficient increments on total aft end, nozzle, and afterbody.

Figure 24.- Concluded.
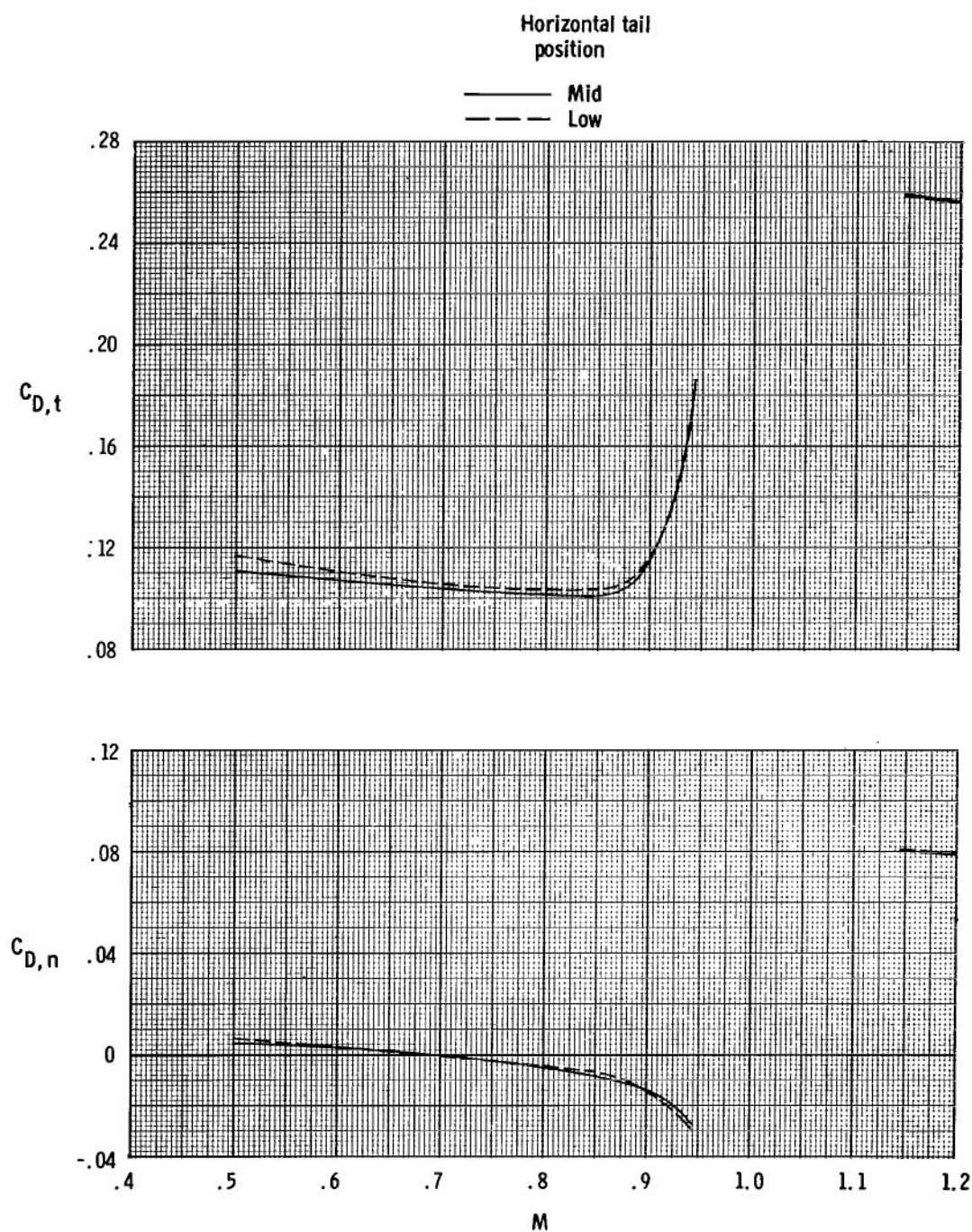
(a) Total and nozzle drag coefficients.

Figure 25.- Effect of horizontal tail height (center-line position or 3.81 cm
   below) on variation of aft-end drag coefficient components with Mach number
   for scheduled jet total pressure ratios; basic afterbody with dry power noz-
   zle, forward vertical tail, and forward horizontal tail.
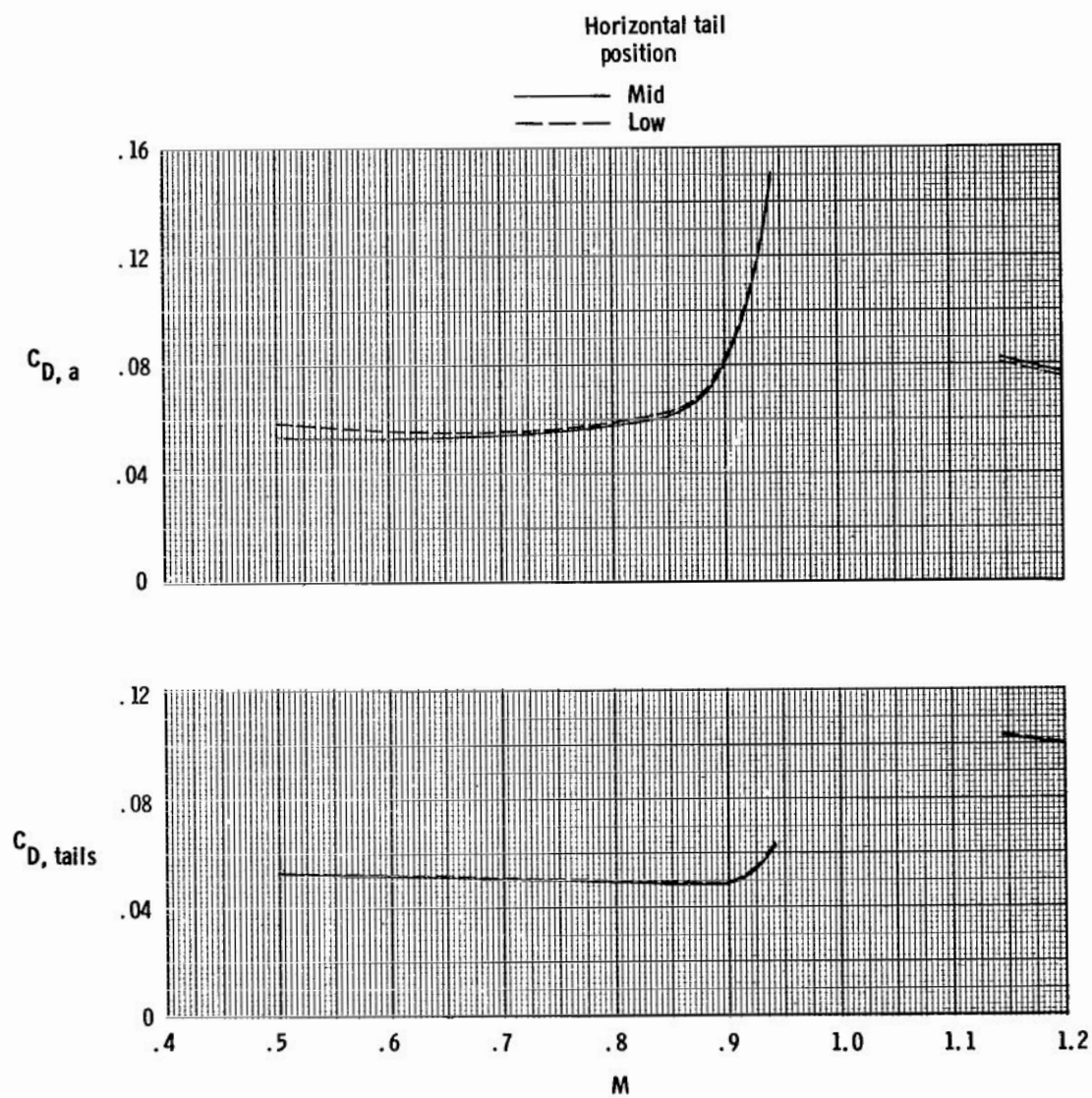
(b) Afterbody and tail drag coefficients.

Figure 25.- Continued.
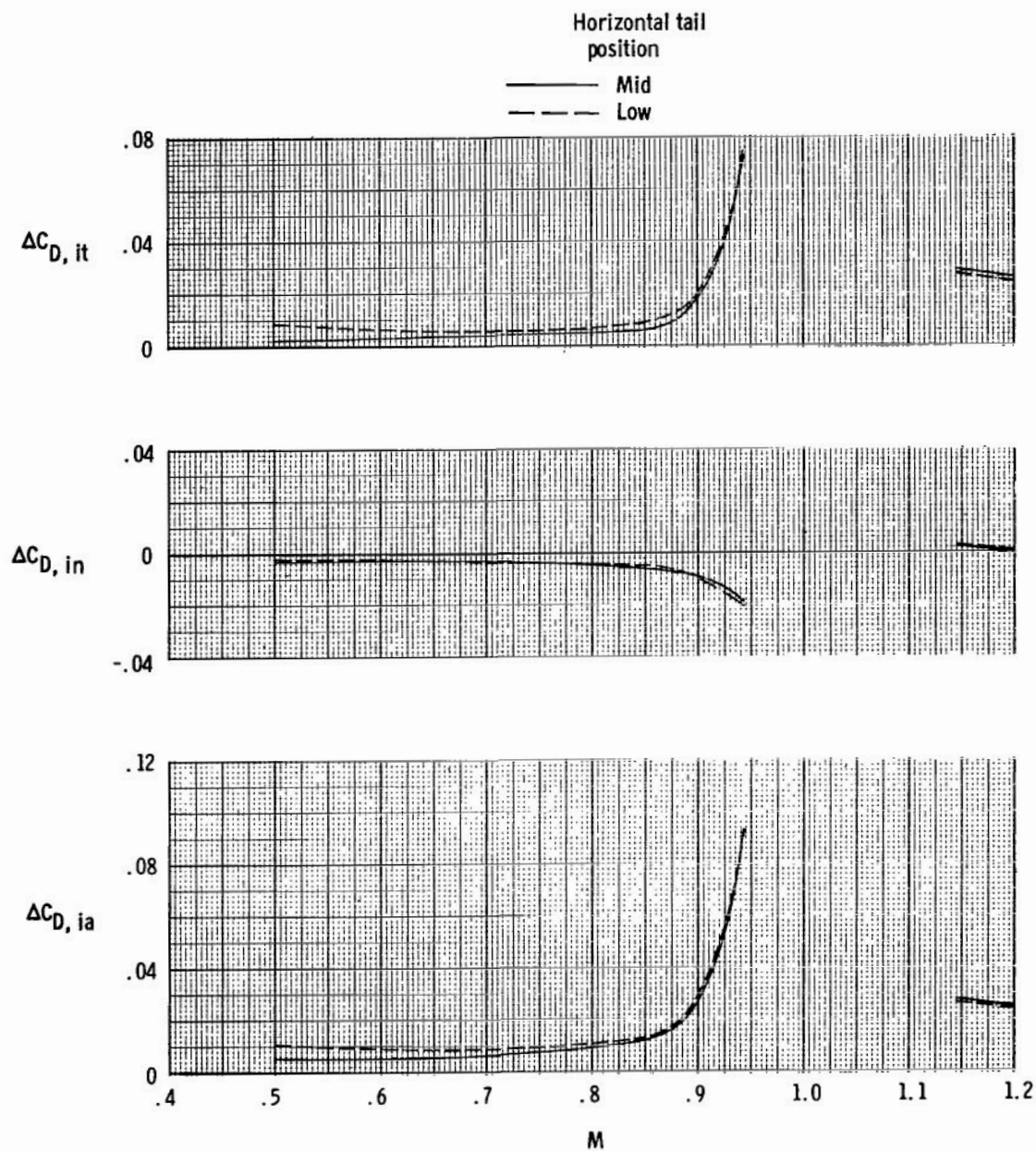
(c) Tail interference-drag coefficient increments on total aft end, nozzle, and afterbody.

Figure 25.- Concluded.
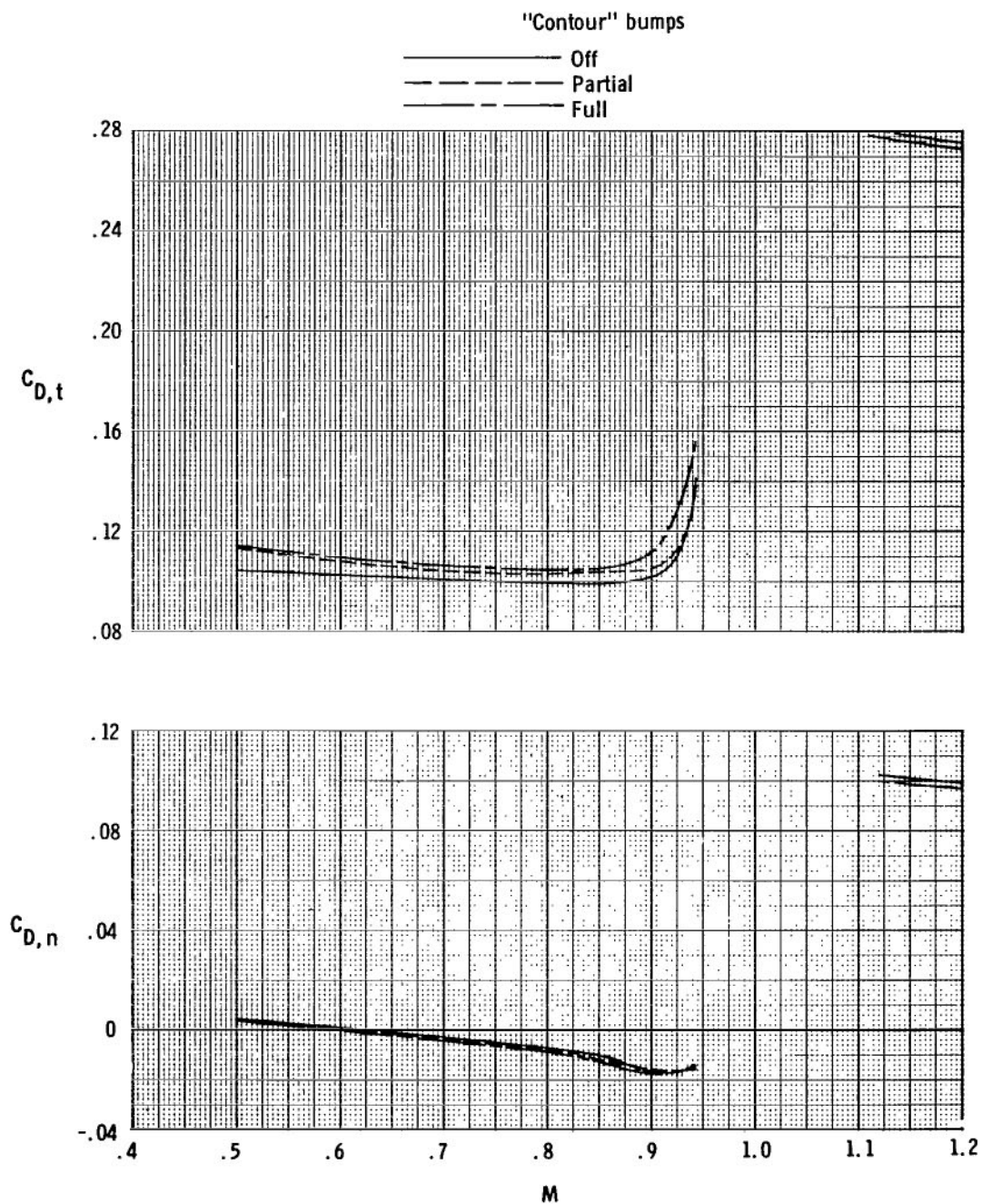
(a) Total and nozzle drag coefficients.

Figure 26.- Effect of contour bumps on variation of aft-end drag coefficient
components with Mach number for scheduled jet total pressure ratios; basic
afterbody with dry power nozzle, forward vertical tail, and aft horizontal
tail.

"Contour" bumps
Off
Partial
Full
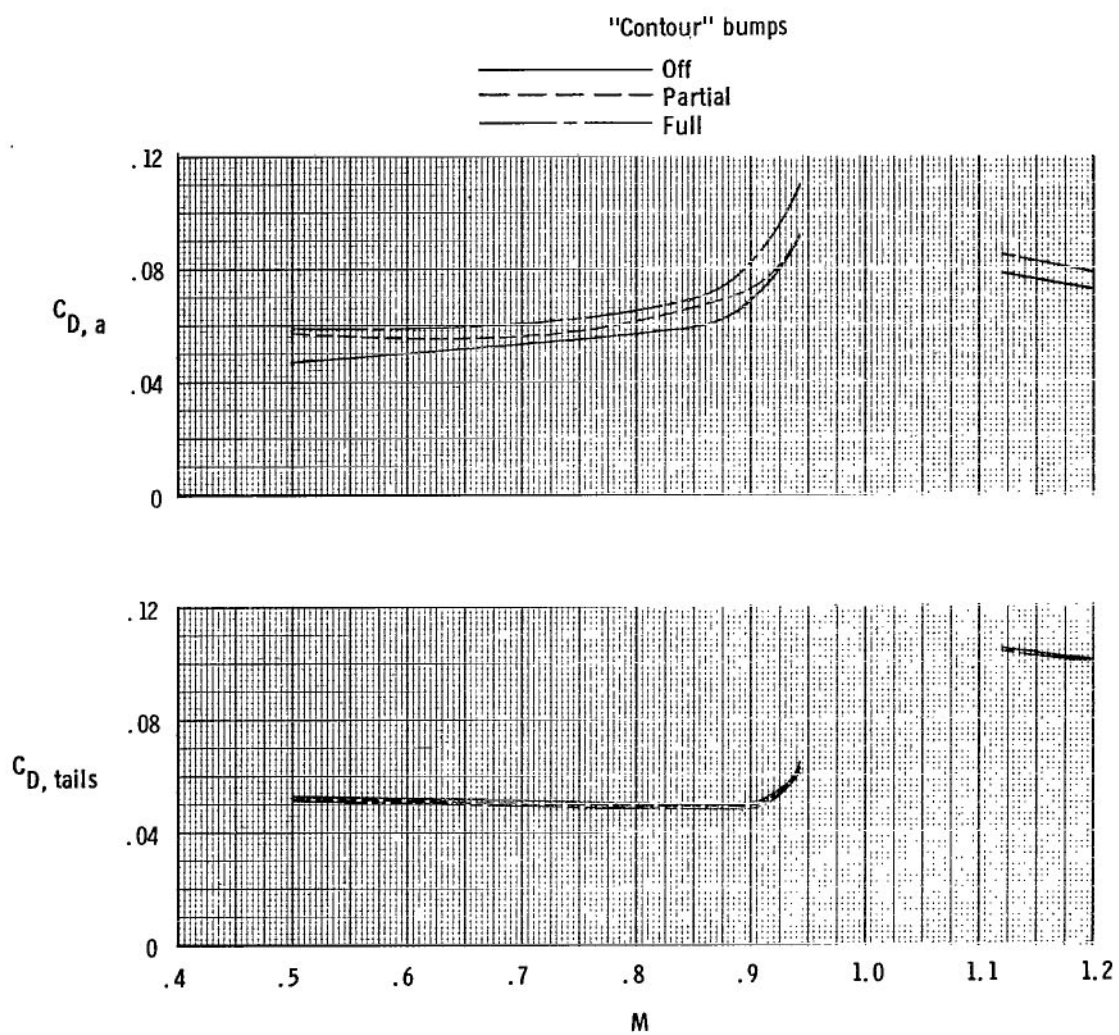
(b) Afterbody and tail drag coefficients.

Figure 26.- Concluded.

152
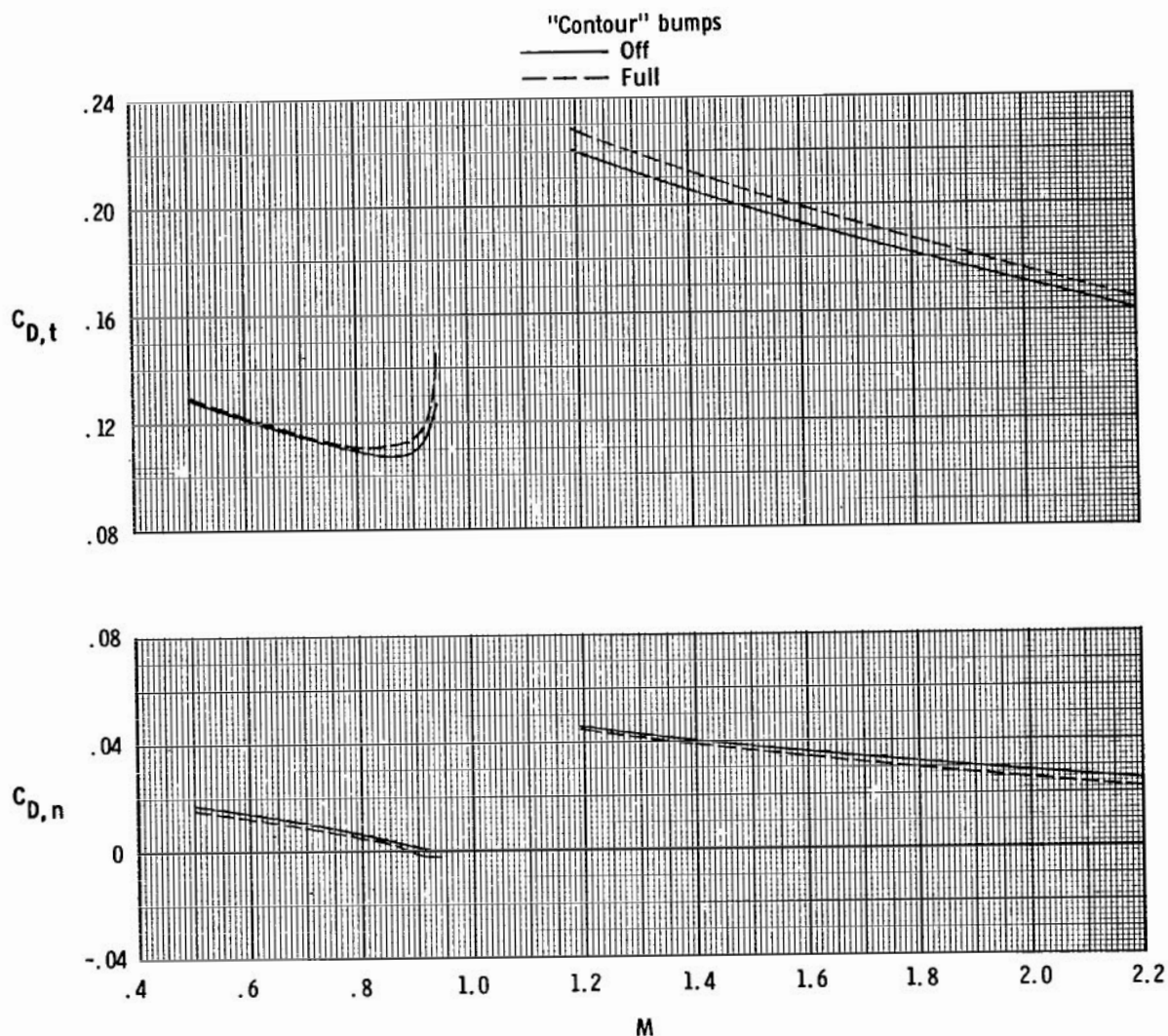
(a) Total and nozzle drag coefficients.

Figure 27.- Effect of contour bumps on variation of aft-end drag coefficient
components with Mach number for scheduled jet total pressure ratios; basic
afterbody with max. A/B power nozzle, forward vertical tail, and aft hori-
zontal tail.
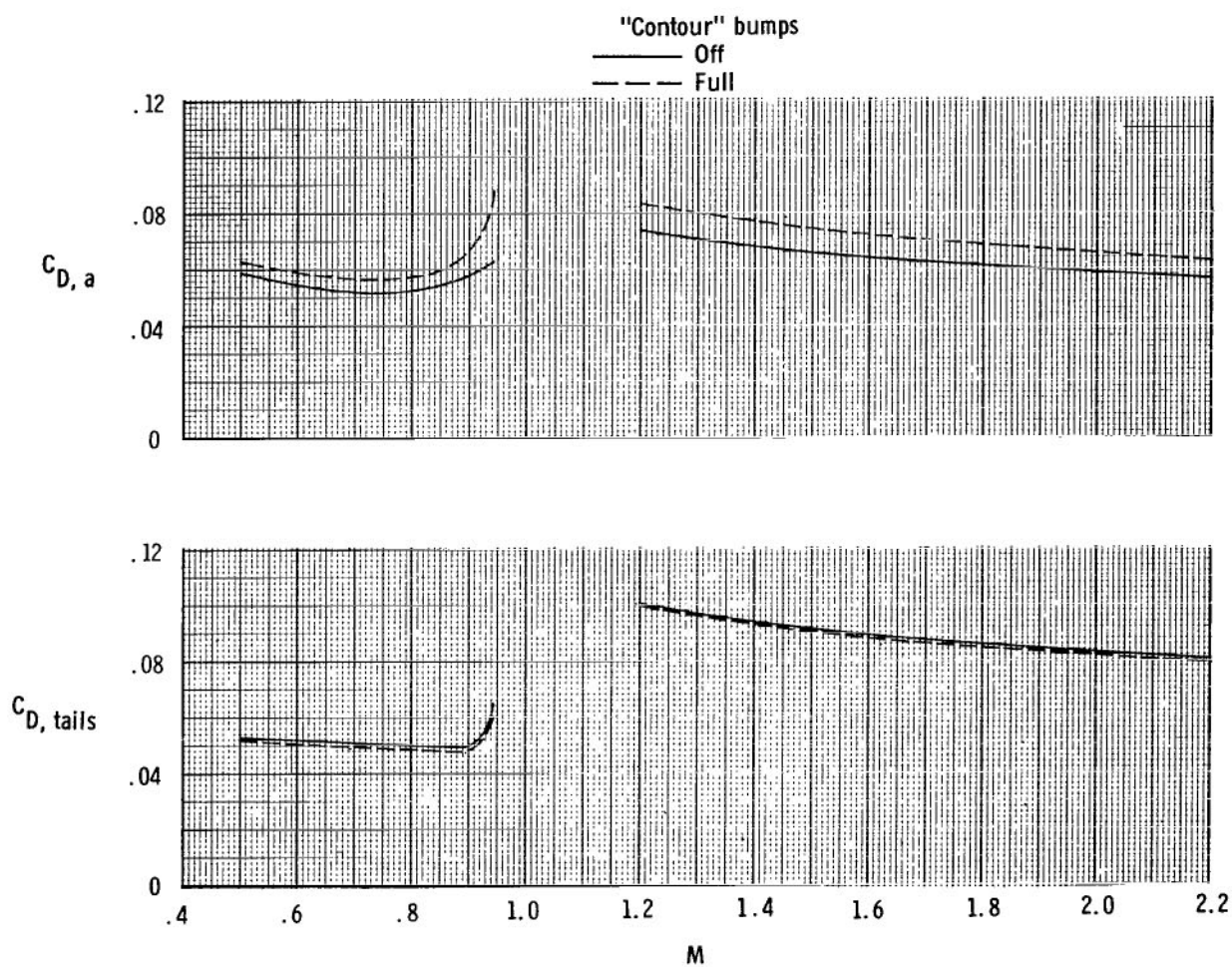
(b) Afterbody and tail drag coefficients.

Figure 27.- Concluded.
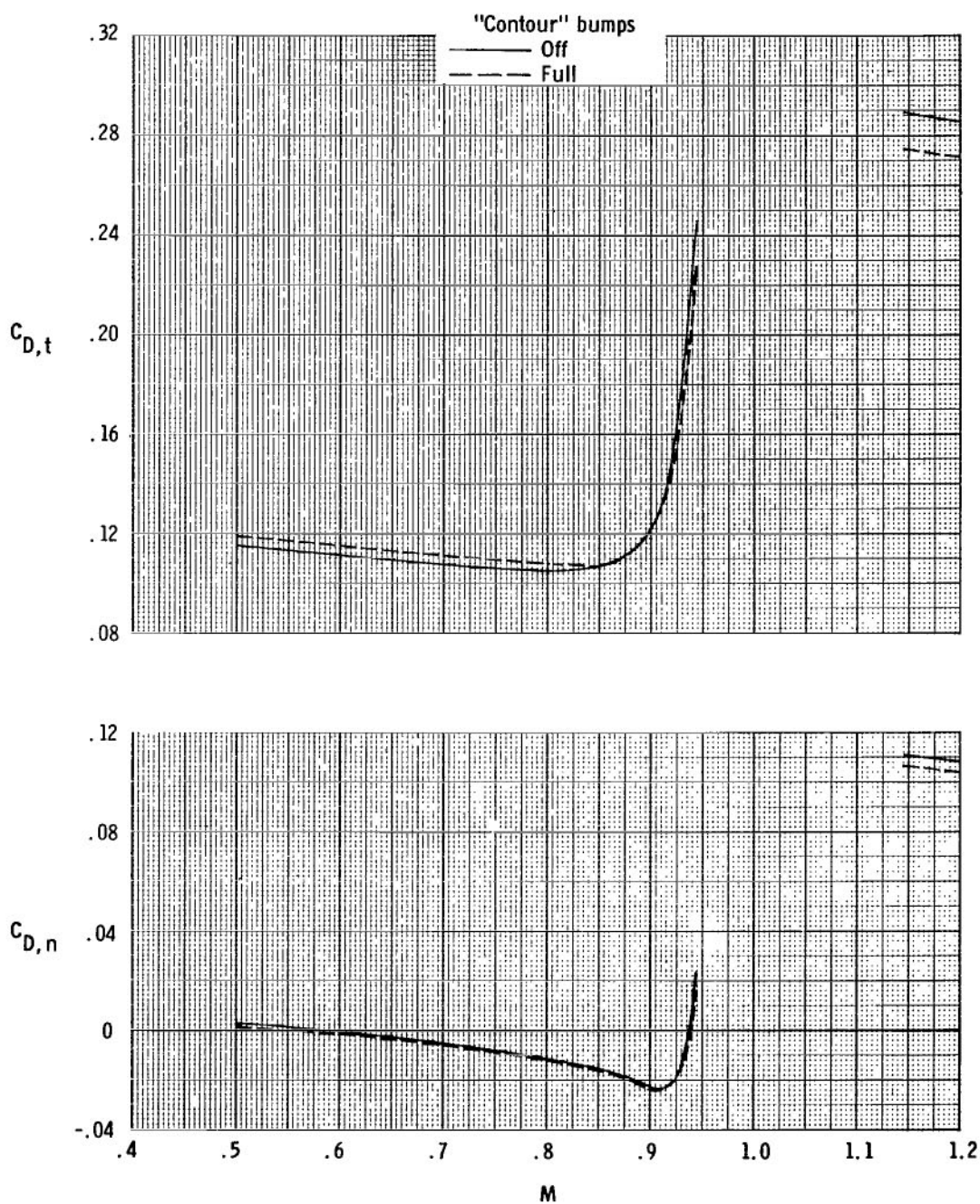
(a) Total and nozzle drag coefficients.

Figure 28.- Effect of contour bumps on variation of aft-end drag coefficient components with Mach number for scheduled jet total pressure ratios; basic afterbody with dry power nozzle, aft vertical tail, and aft horizontal tail.

"Contour" bumps
——— Off
— — — Full
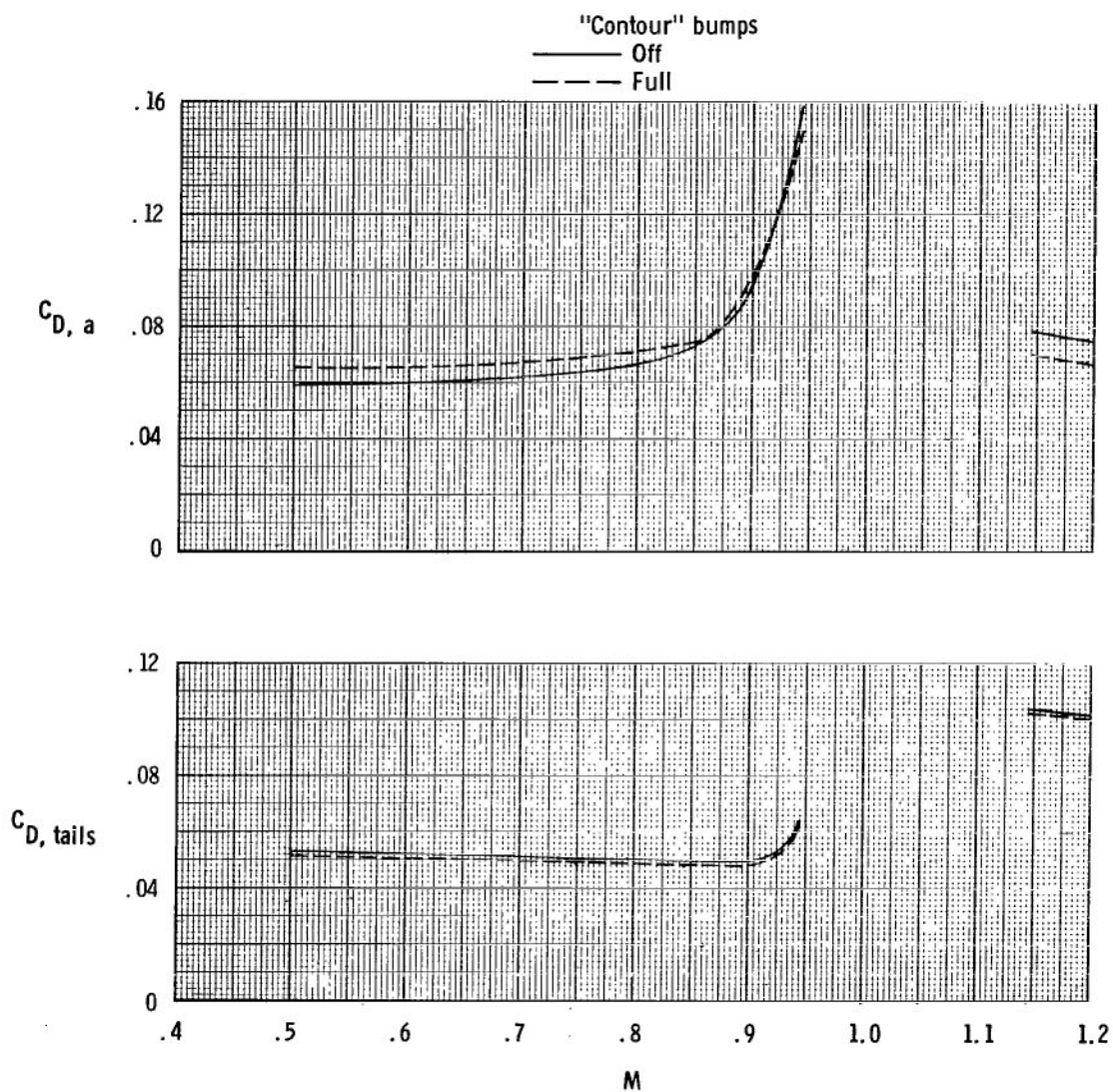
(b) Afterbody and tail drag coefficients.

Figure 28.- Concluded.
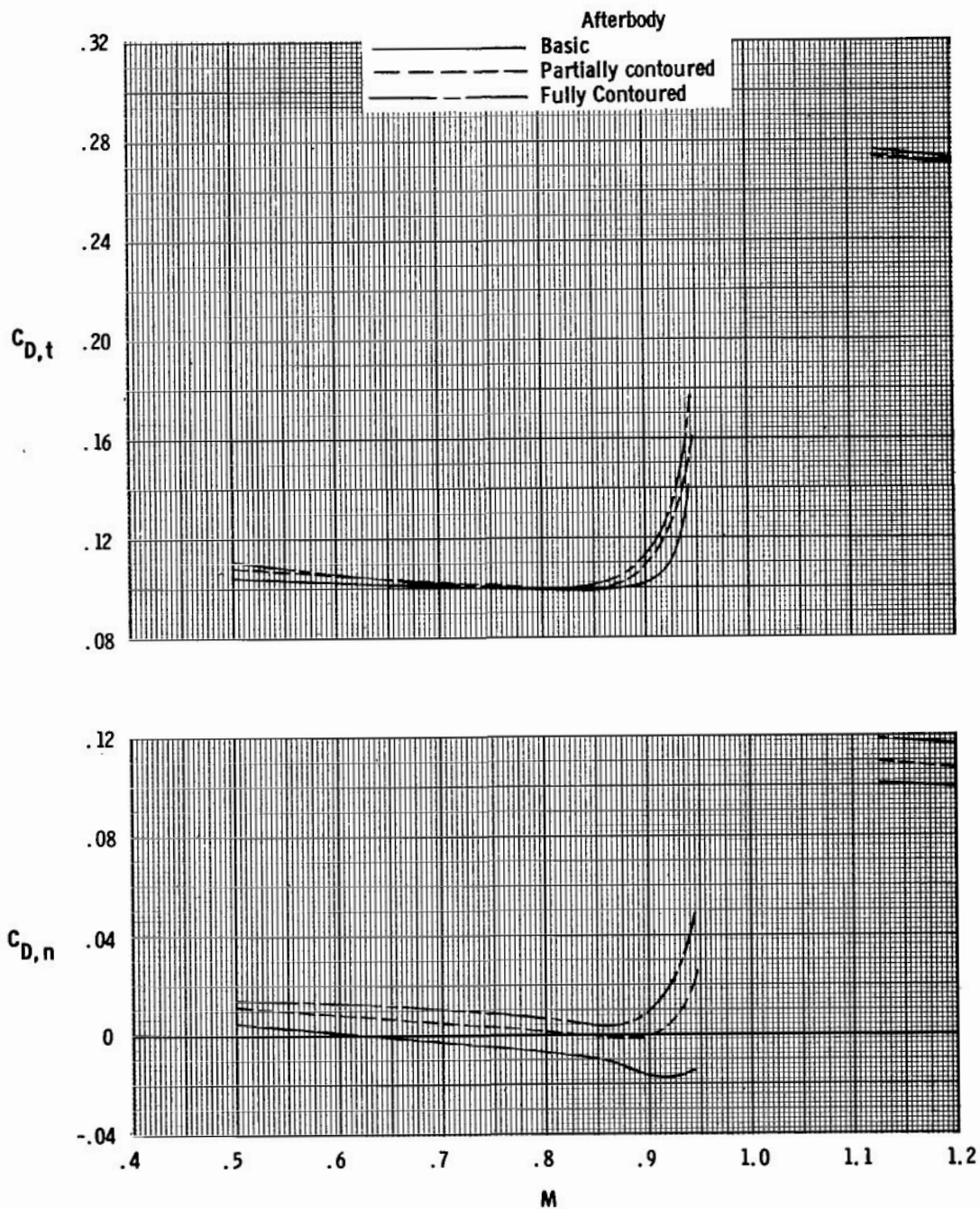
(a) Total and nozzle drag coefficients.

Figure 29.- Effect of afterbody contouring on variation of aft-end drag coefficient components with Mach number for scheduled jet total pressure ratios; dry power nozzle, forward vertical tail, and aft horizontal tail installed.

157

Afterbody
——————— Basic
— — — — — Partially contoured
——— — ——— Fully contoured
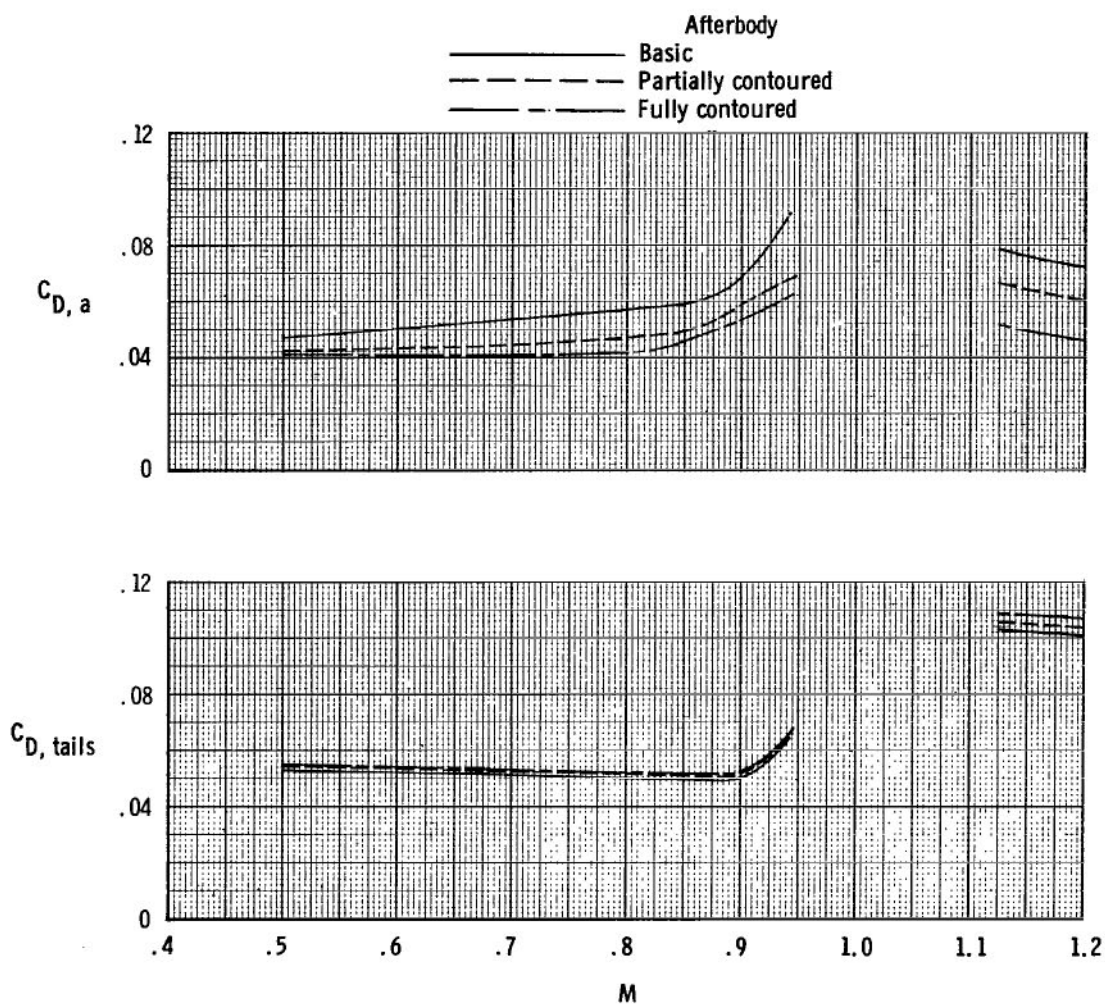
(b) Afterbody and tail drag coefficients.

Figure 29.- Continued.
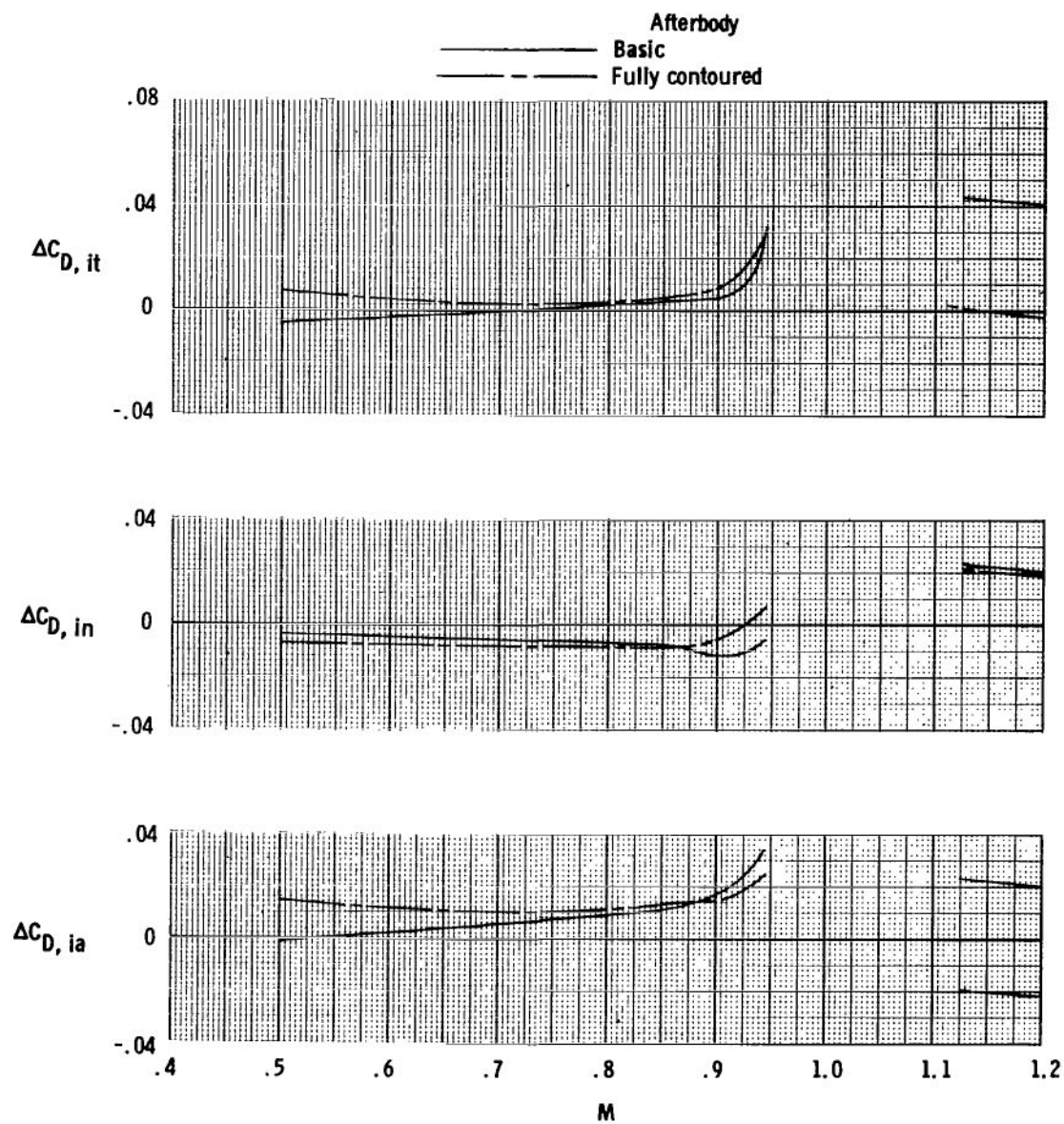
(c) Tail interference-drag coefficient increments on total aft end, nozzle, and afterbody.

Figure 29.- Concluded.
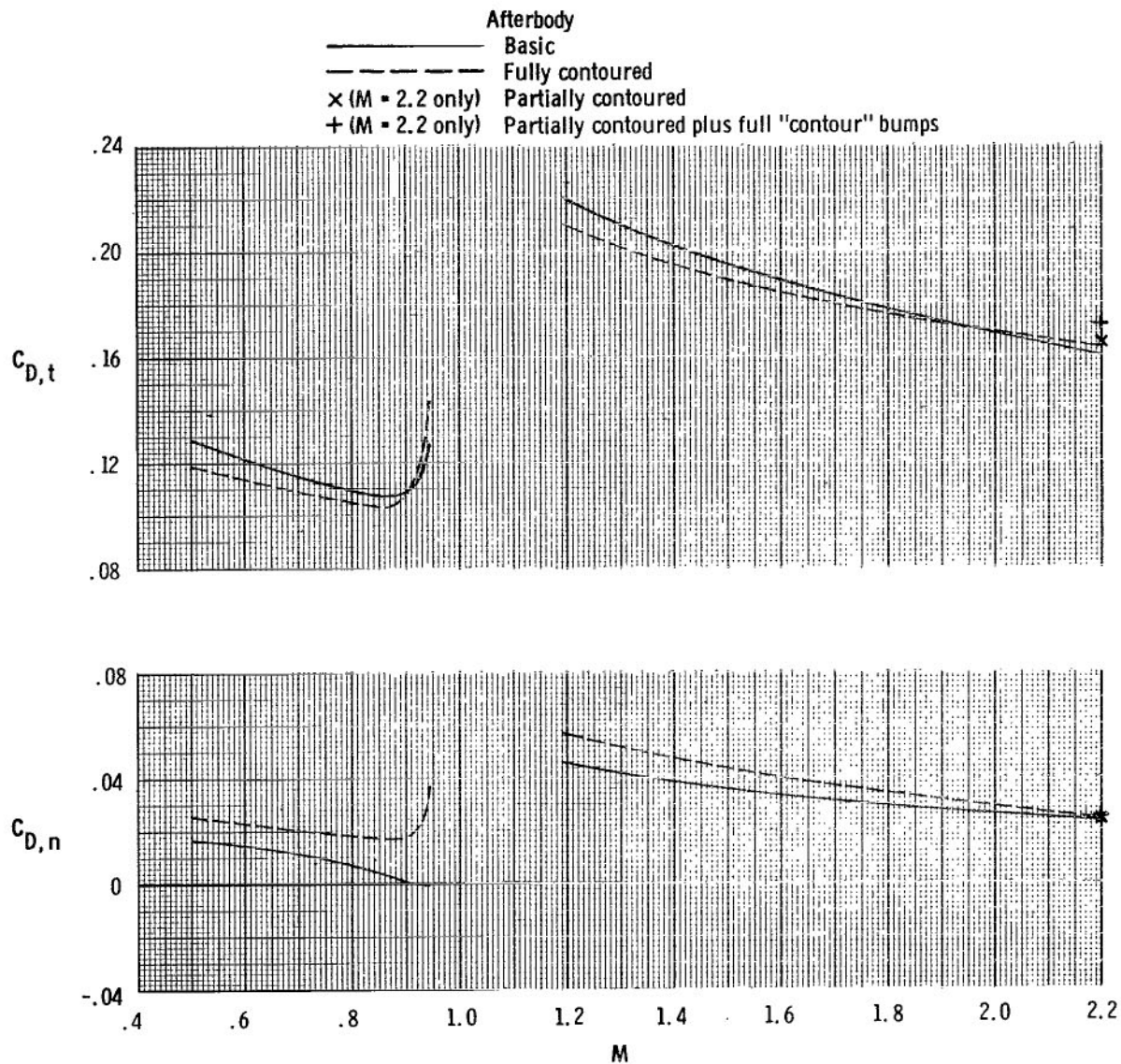
(a) Total and nozzle drag coefficients.

Figure 30.- Effect of afterbody contouring on variation of aft-end drag
coefficient components with Mach number for scheduled jet total pres-
sure ratios; max. A/B power nozzle, forward vertical tail, and aft
horizontal tail.

160
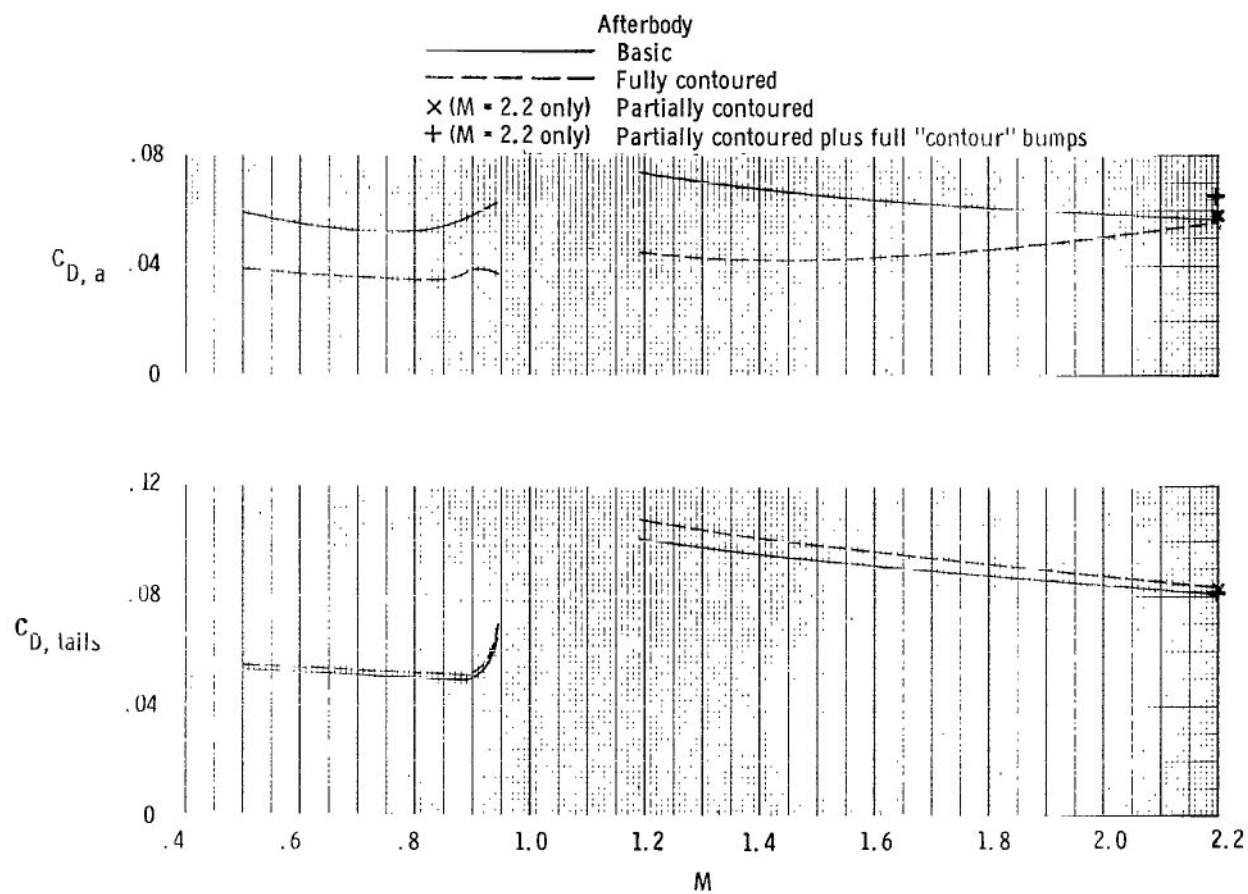
(b) Afterbody and tail drag coefficients.

Figure 30.- Concluded.

Afterbody | Bumps
Basic | Off
Basic | Full
Fully contoured | Off
Fully contoured | Full

(a) Total and nozzle drag coefficients.

Figure 31.- Effect of combined afterbody contouring and contour bumps on variation of aft-end drag coefficient components with Mach number for scheduled jet total pressure ratios; dry power nozzle, forward vertical tail, and aft horizontal tail.

162

Legend:

Afterbody	Bumps
Basic	Off
Basic	Full
Fully contoured	Off
Fully contoured	Full
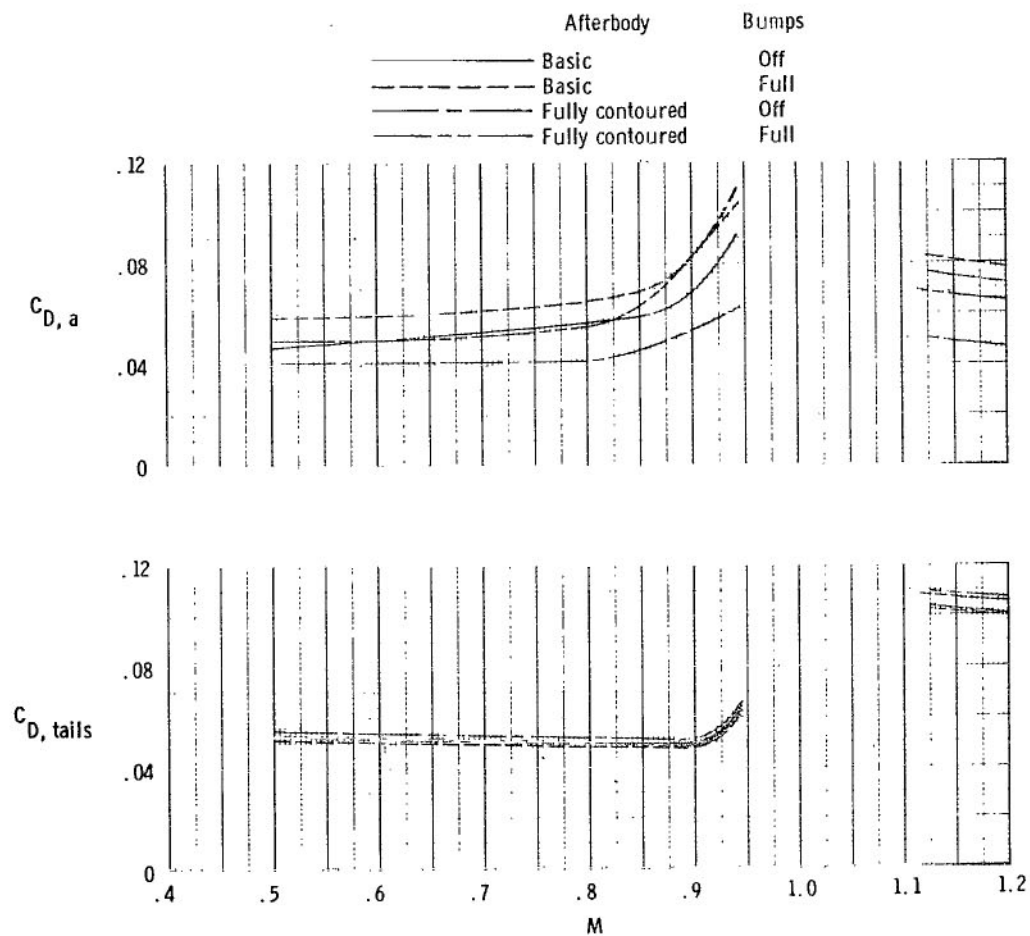
(b) Afterbody and tail drag coefficients.

Figure 31.- Concluded.

——————— Basic configuration, tails on
— — — — — Equivalent body
—— — —— Equivalent body plus tail friction drag
—— — — —— Basic configuration, tails off plus tail drag $\left(C_{D, \text{tails}}\right)$
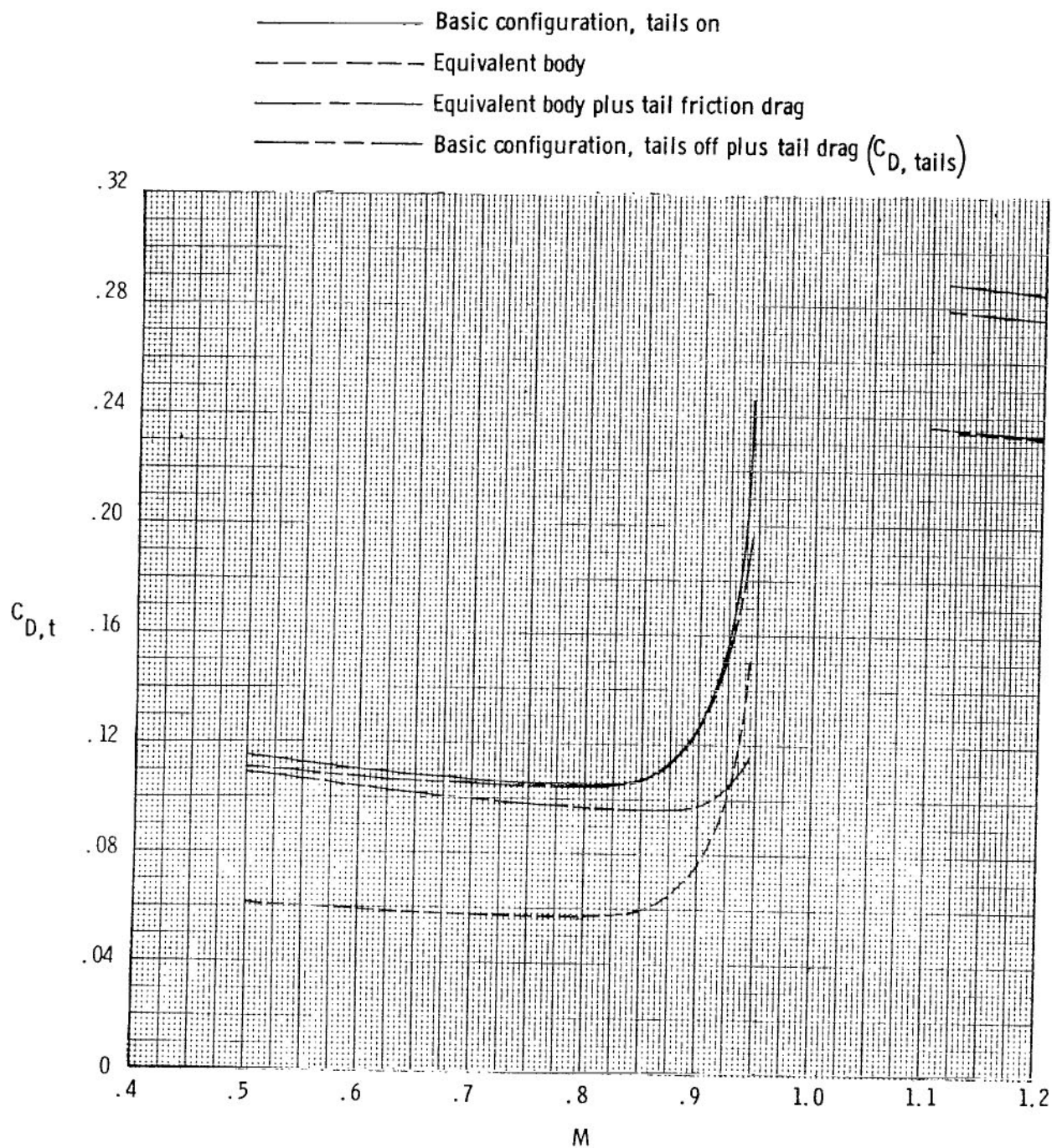
(a) Aft vertical tail, aft horizontal tail.

Figure 32.- Comparison of two indirect methods of obtaining total aft-end drag. Basic afterbody with dry power nozzle.

164
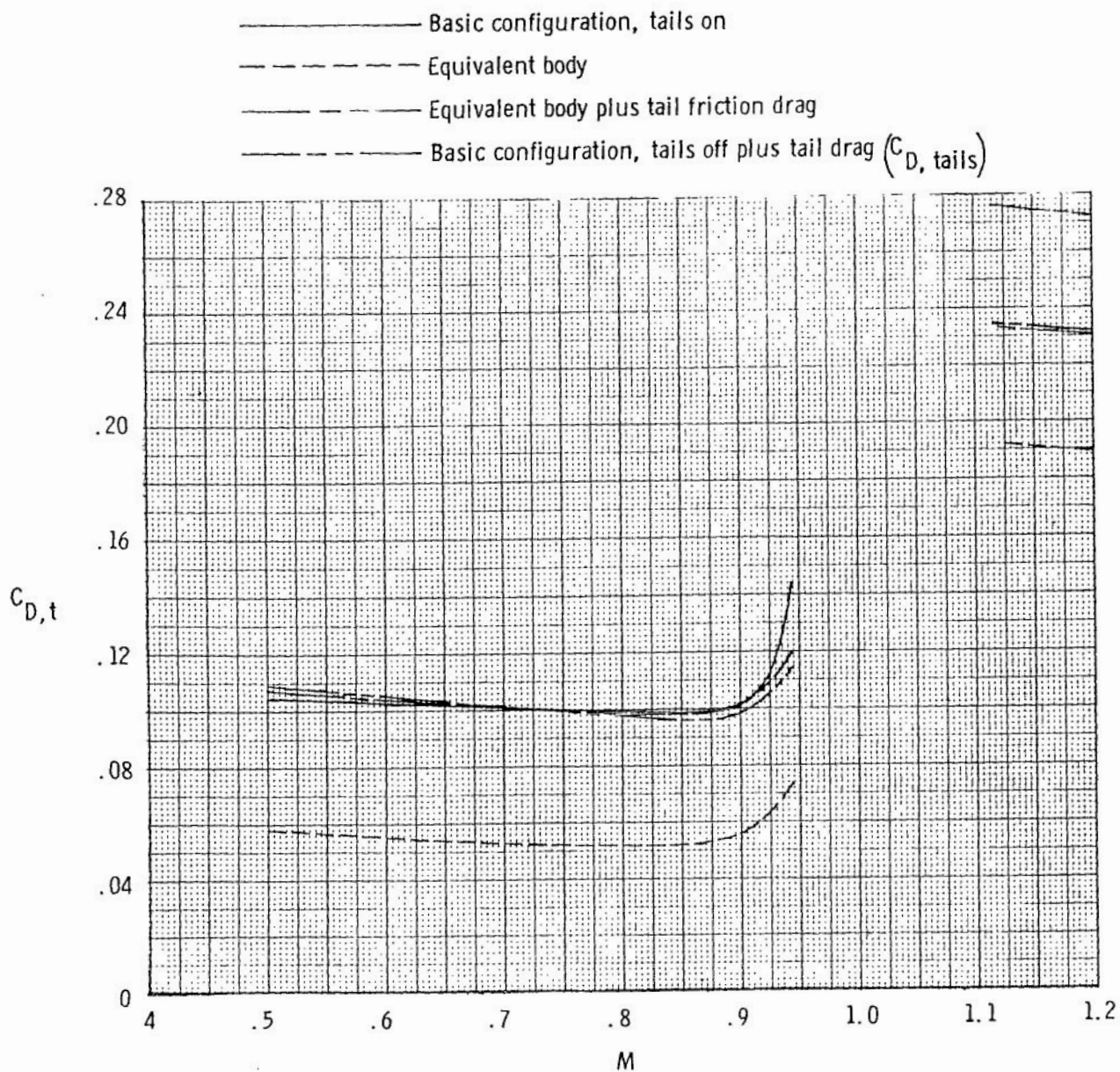
(b) Forward vertical tail, aft horizontal tail.

Figure 32.- Concluded.

Tails off
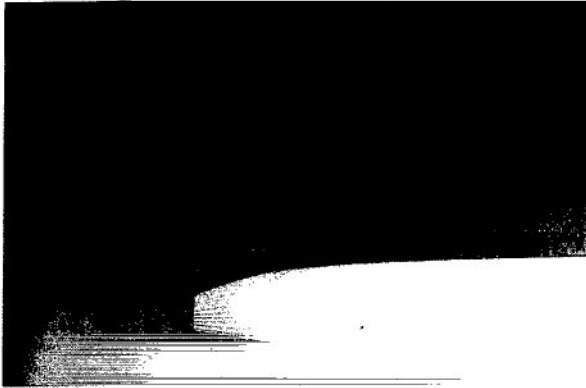
Forward vertical tail, forward
horizontal tail
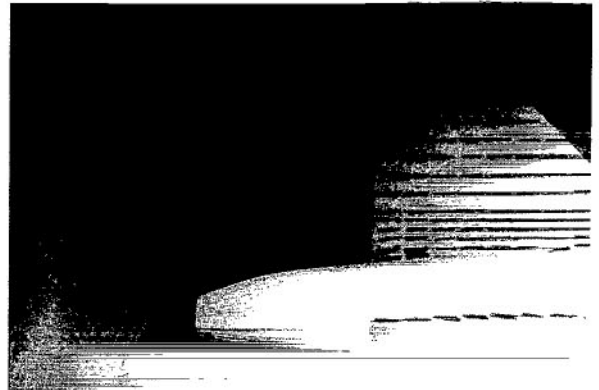
Forward vertical tail,
aft horizontal tail
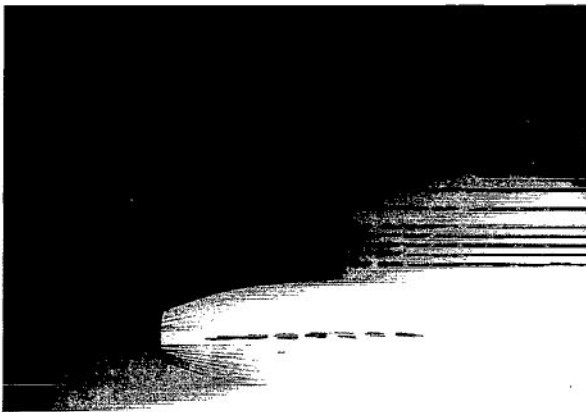
Aft vertical tail,
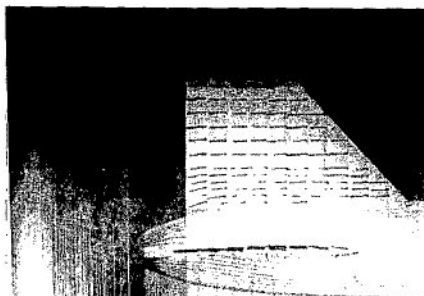aft horizontal tail
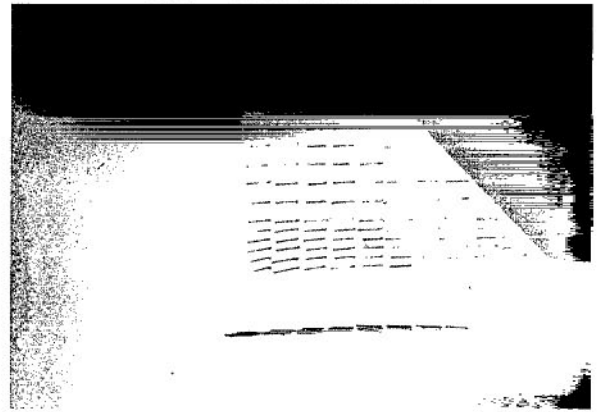
L-76-7505

(a) M = 0.50.

Figure 33.- Ink flow photographs showing effect of tail location on external
afterbody/nozzle flow at several Mach numbers. Jet off.

Tails off
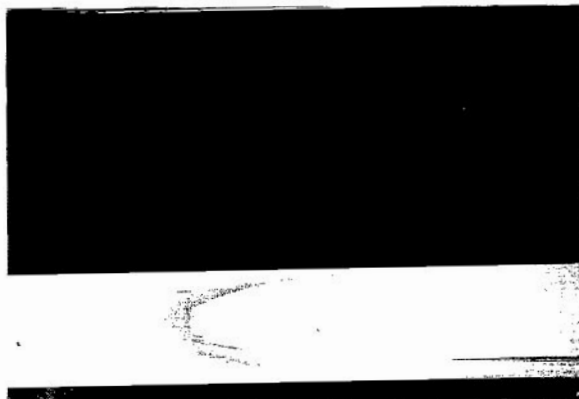
Forward vertical tail, forward
horizontal tail

Forward vertical tail,
aft horizontal tail

Aft vertical tail,
aft horizontal tail
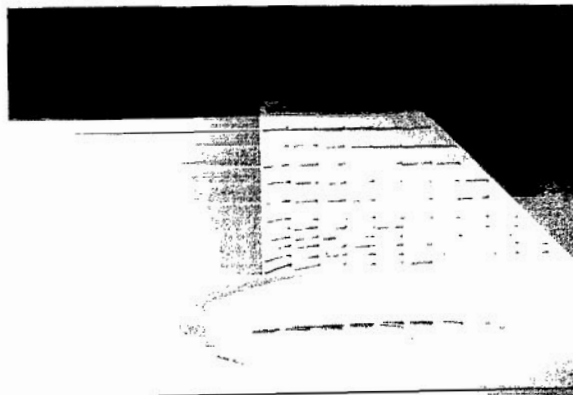
L-76-7506

(b) M = 0.80.

Figure 33.- Continued.
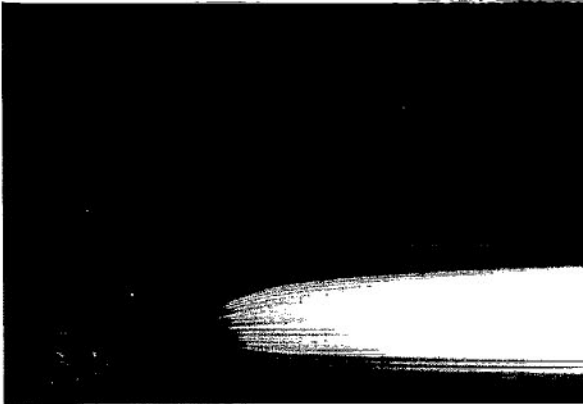
167

Tails off

Forward vertical tail, forward
horizontal tail
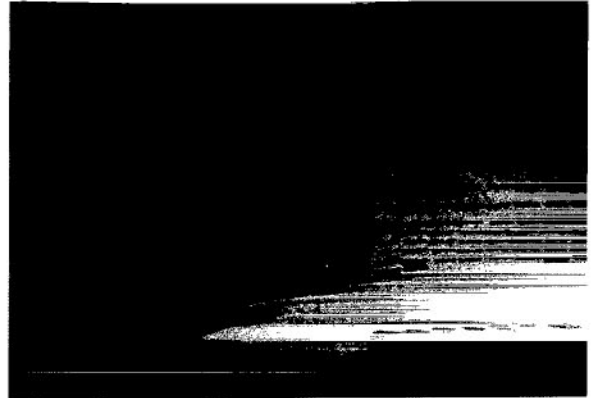
Forward vertical tail,
aft horizontal tail

Aft vertical tail,
aft horizontal tail
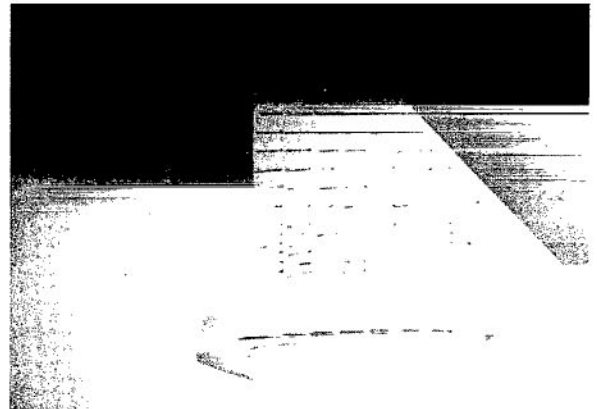
L-76-7507

(c) M = 0.90.

Figure 33.- Continued.
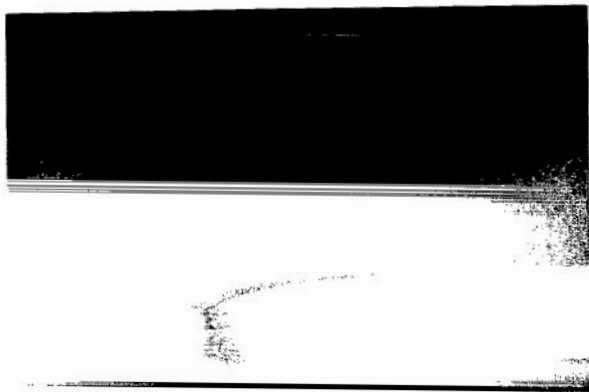
168

Tails off

Forward vertical tail, forward
horizontal tail
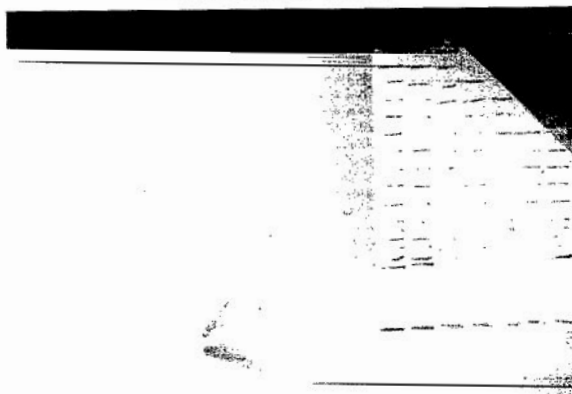
Forward vertical tail,
aft horizontal tail
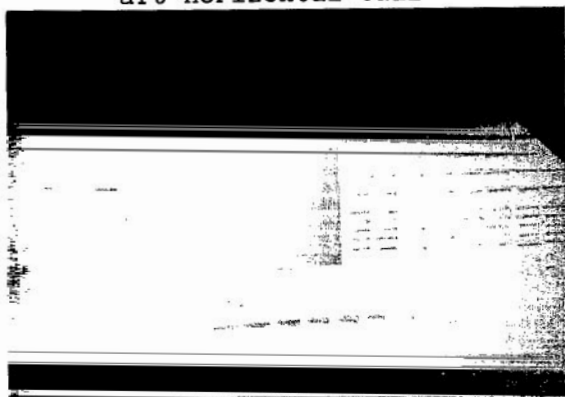
Aft vertical tail,
aft horizontal tail
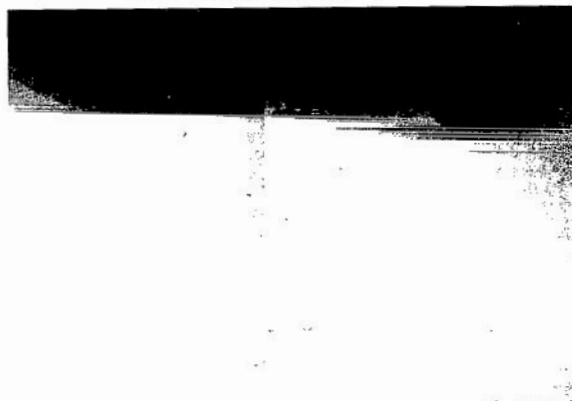
L-76-7508

(d)   M = 0.95.

Figure 33.- Concluded.
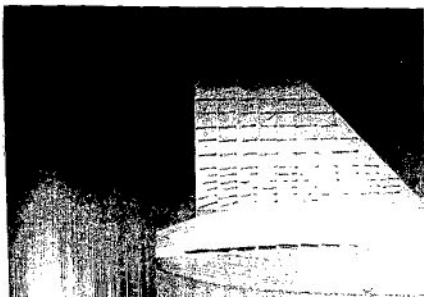
M = 0.80, jet off   M = 0.80, $p_{t,j}/p_\infty$ = 3.0
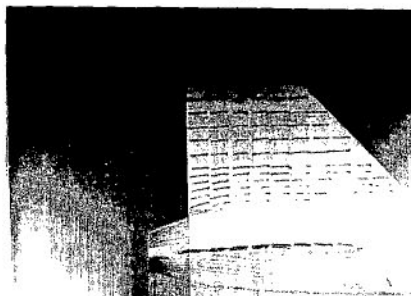
M = 0.85, jet off   M = 0.85, $p_{t,j}/p_\infty$ = 3.0   M = 0.85, $p_{t,j}/p_\infty$ = 6.0
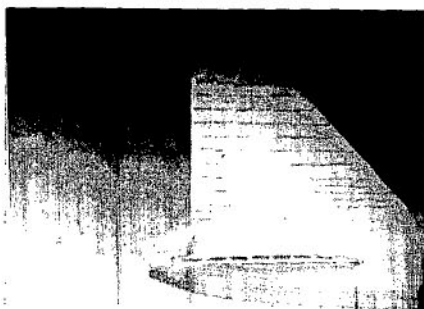
M = 0.95, jet off   M = 0.95, $p_{t,j}/p_\infty$ = 2.0   M = 0.95, $p_{t,j}/p_\infty$ = 6.0
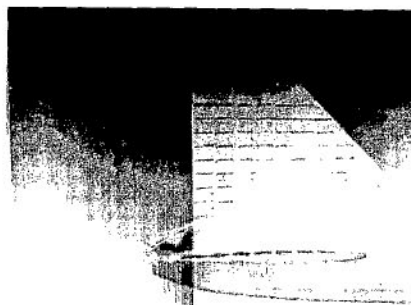
L-76-7509

Figure 34.- Ink flow photographs showing effect of jet exhaust flow on external afterbody/nozzle flow at several Mach numbers. Basic afterbody with dry power nozzle, aft vertical tail, and aft horizontal tail.
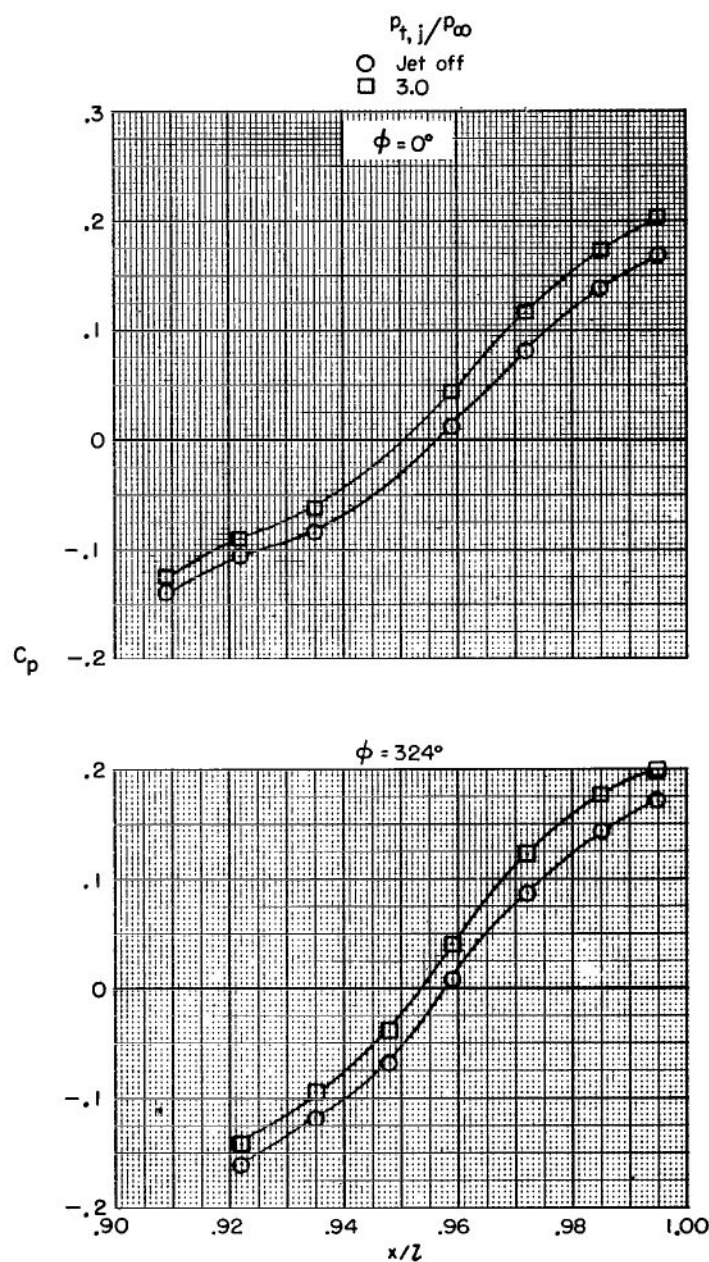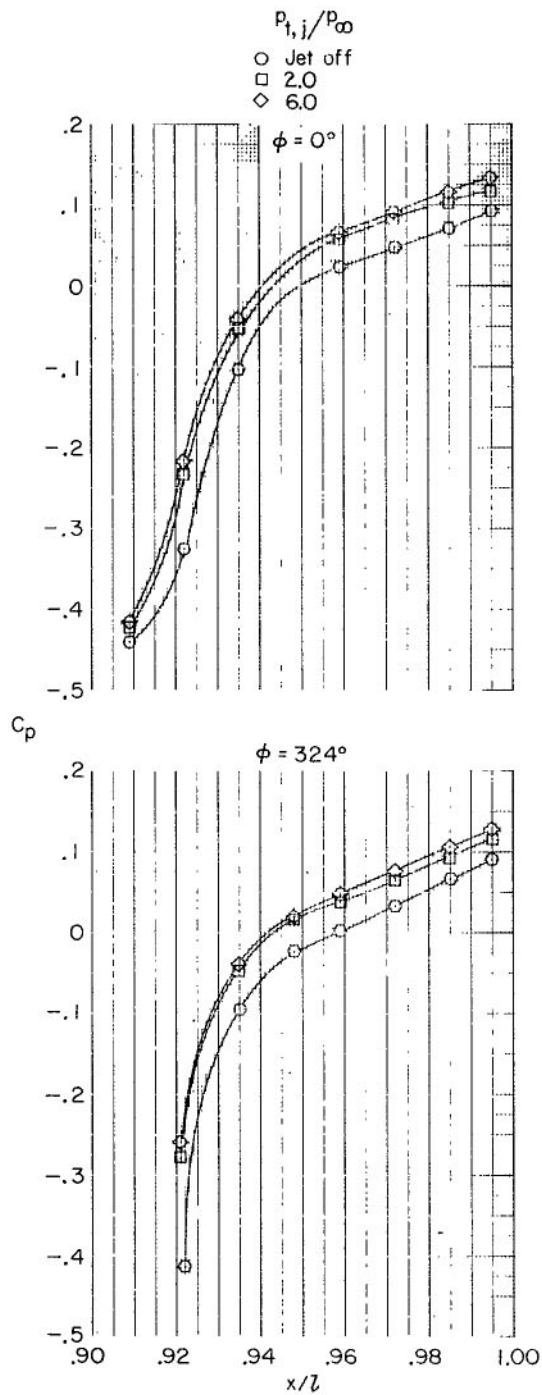
(a) M = 0.80.

Figure 35.- Effect of jet total pressure ratio on nozzle static-pressure distribution. Basic afterbody with dry power nozzle, aft vertical tail, and aft horizontal tail.
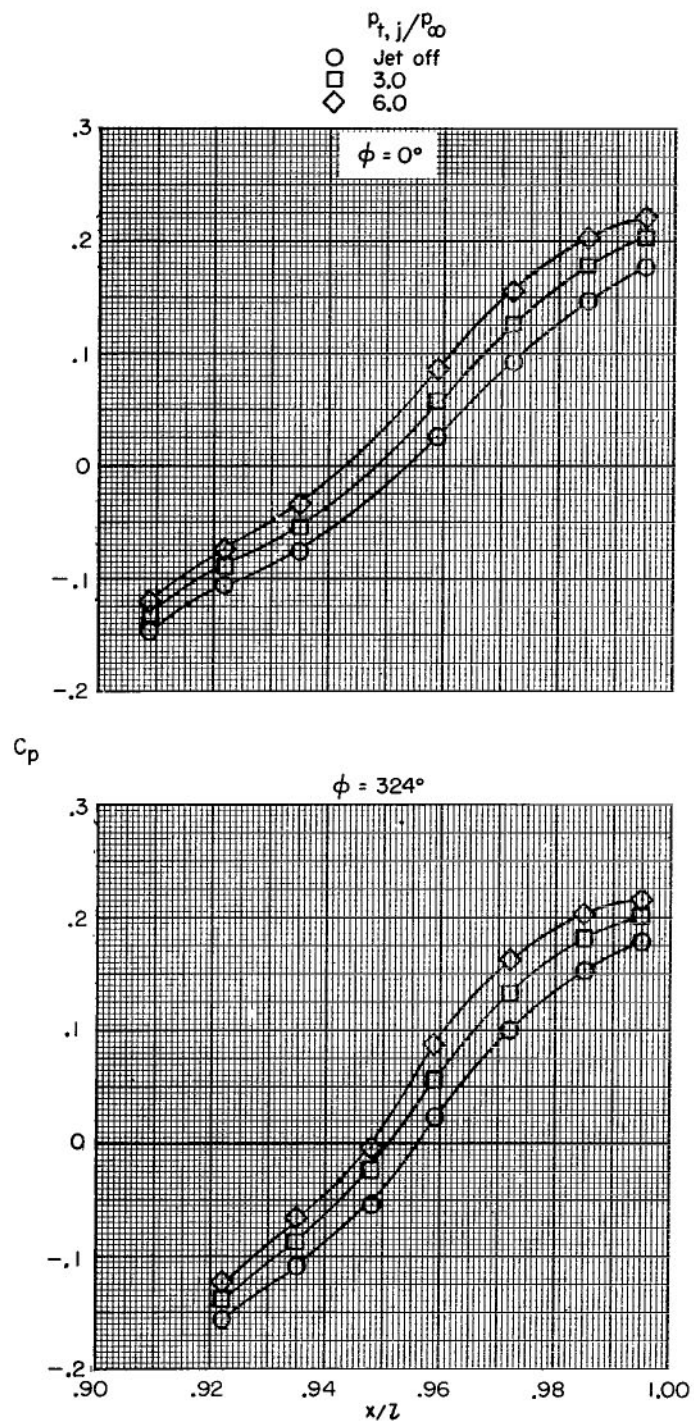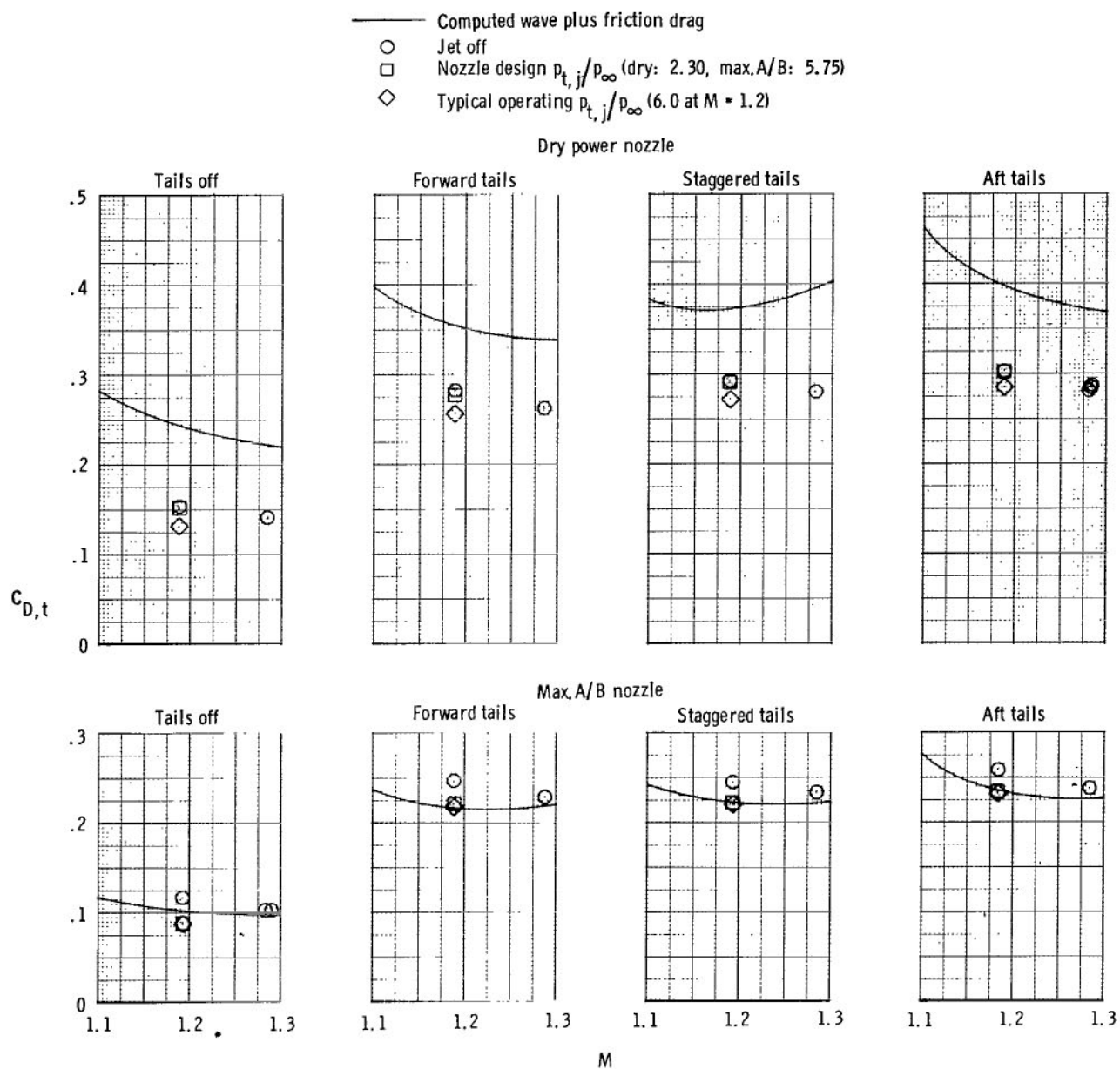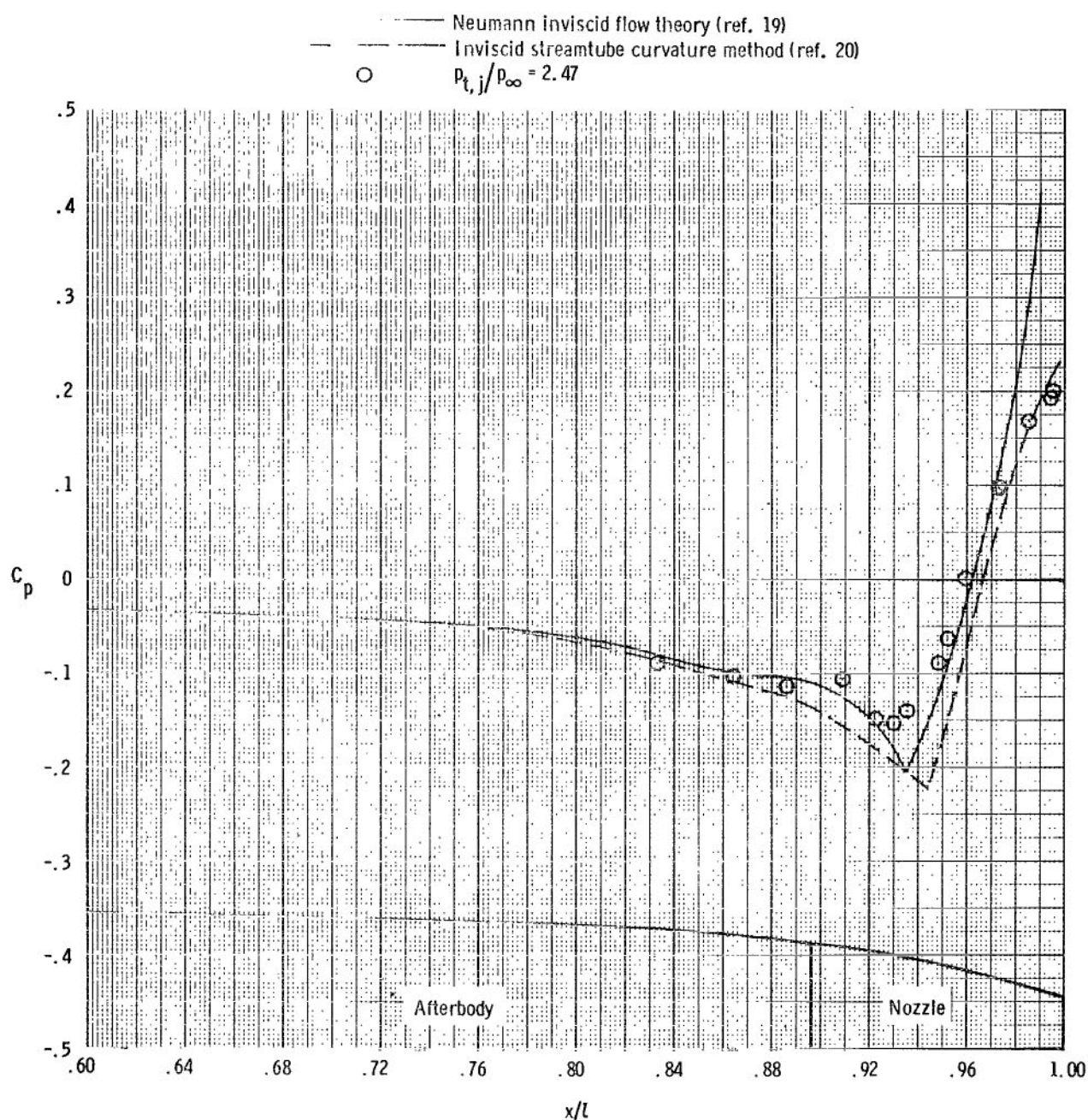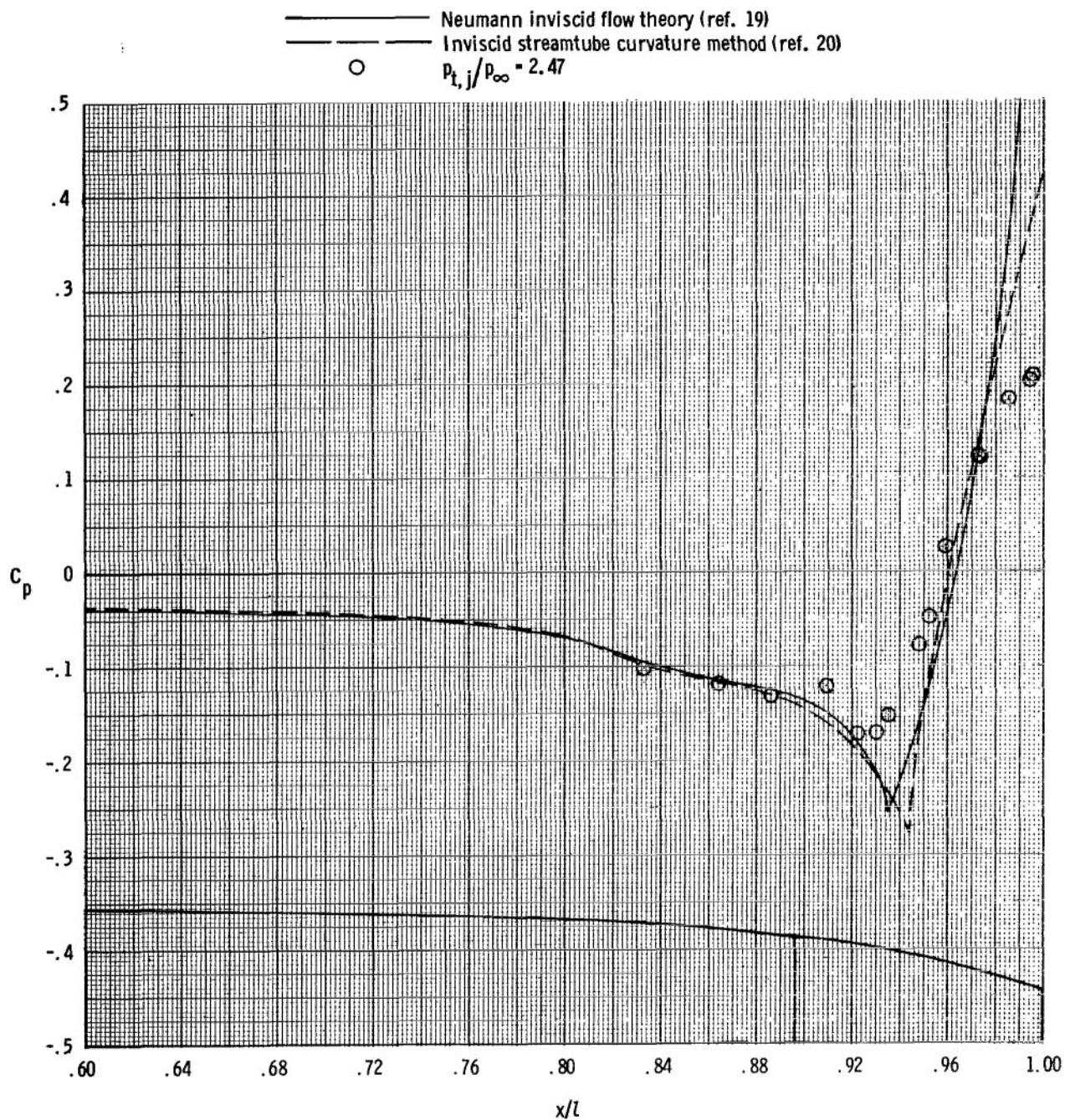
(b)   M = 0.85.

Figure 35.- Continued.

$p_{t,j}/p_\infty$

○ Jet off
□ 2.0
◇ 6.0

$\phi = 0°$

C_p

$\phi = 324°$

x/l

(c)   M = 0.95.

Figure 35.- Concluded.

Figure 36.- Comparison of measured and computed total aft-end drag
coefficients. Basic afterbody.

(a)   M = 0.80.

Figure 37.- Comparison of theoretical and experimental static-pressure distributions on basic afterbody with dry power nozzle. Tails off.

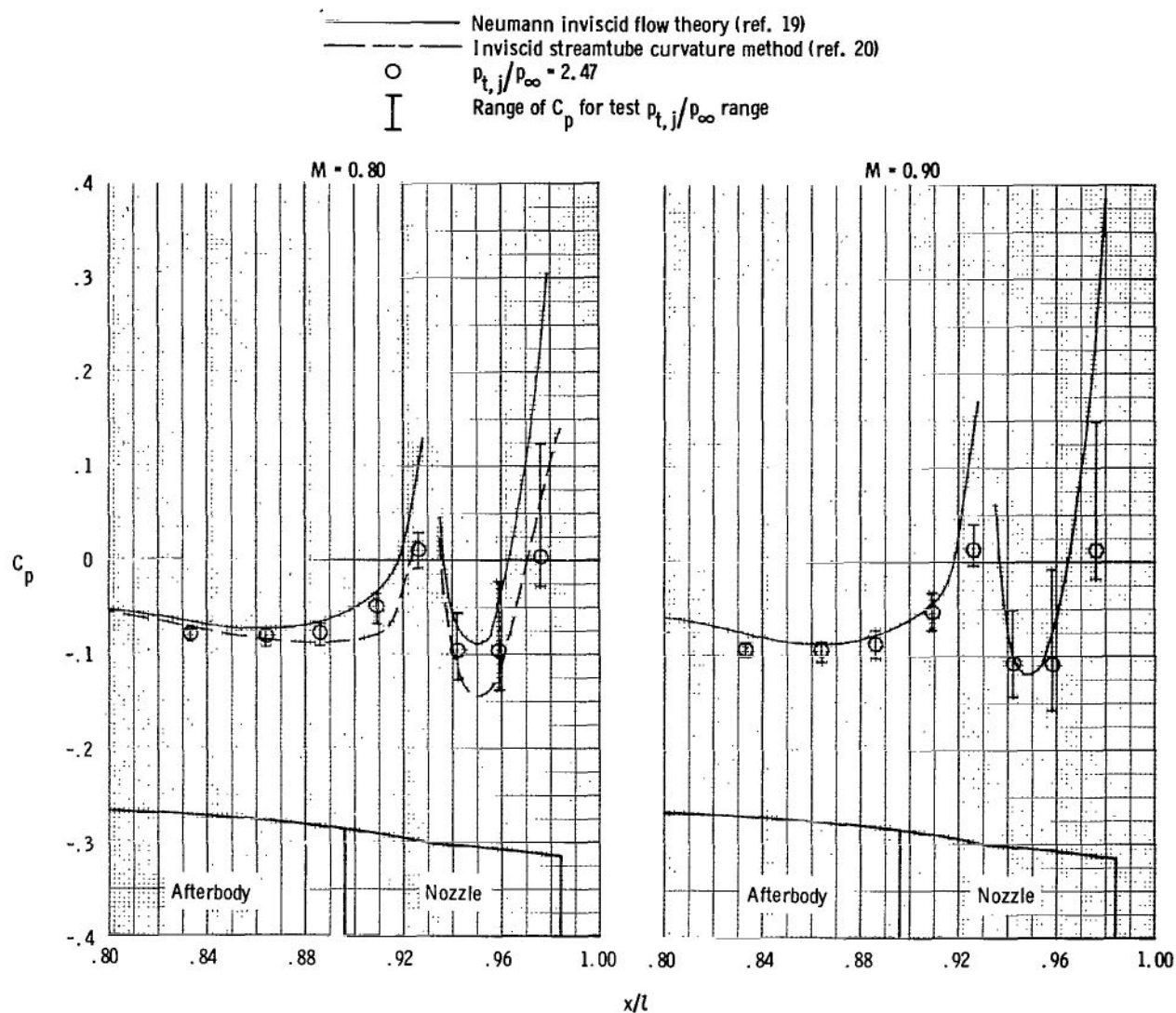(b) M = 0.90.
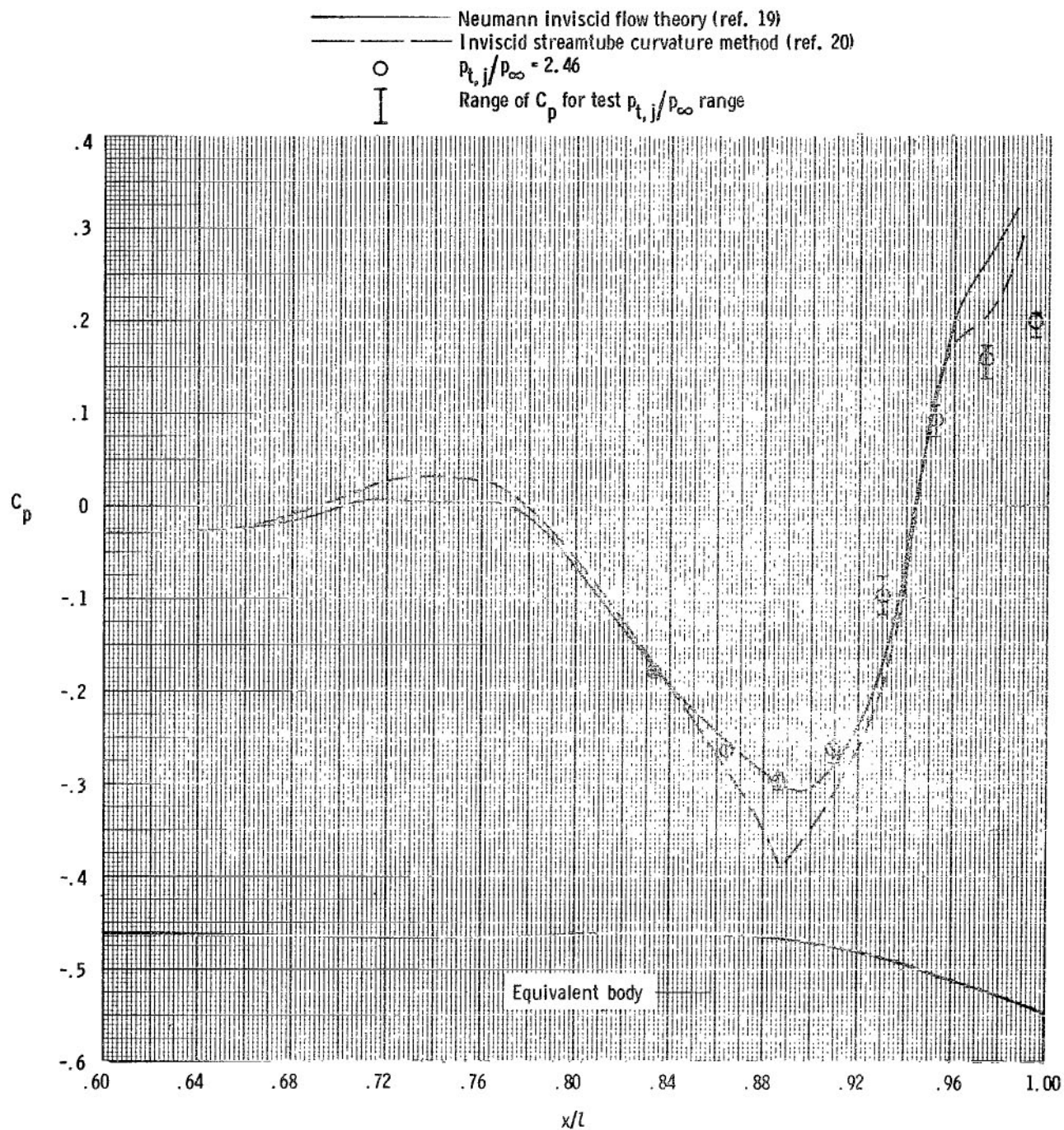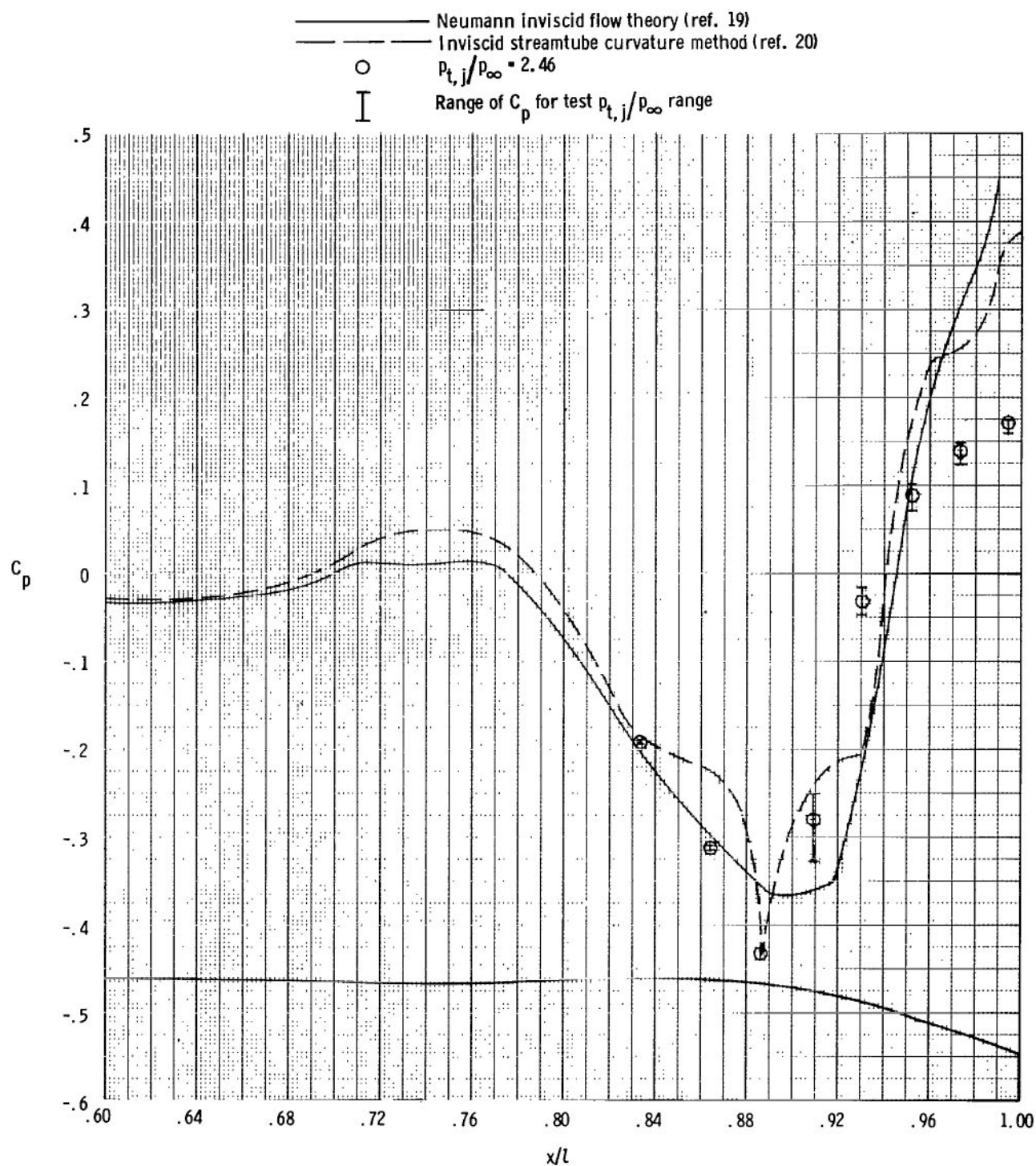
Figure 37.- Concluded.

176

Figure 38.- Comparison of theoretical and experimental static-pressure distributions on basic afterbody with maximum afterburning power nozzle. Tails off.
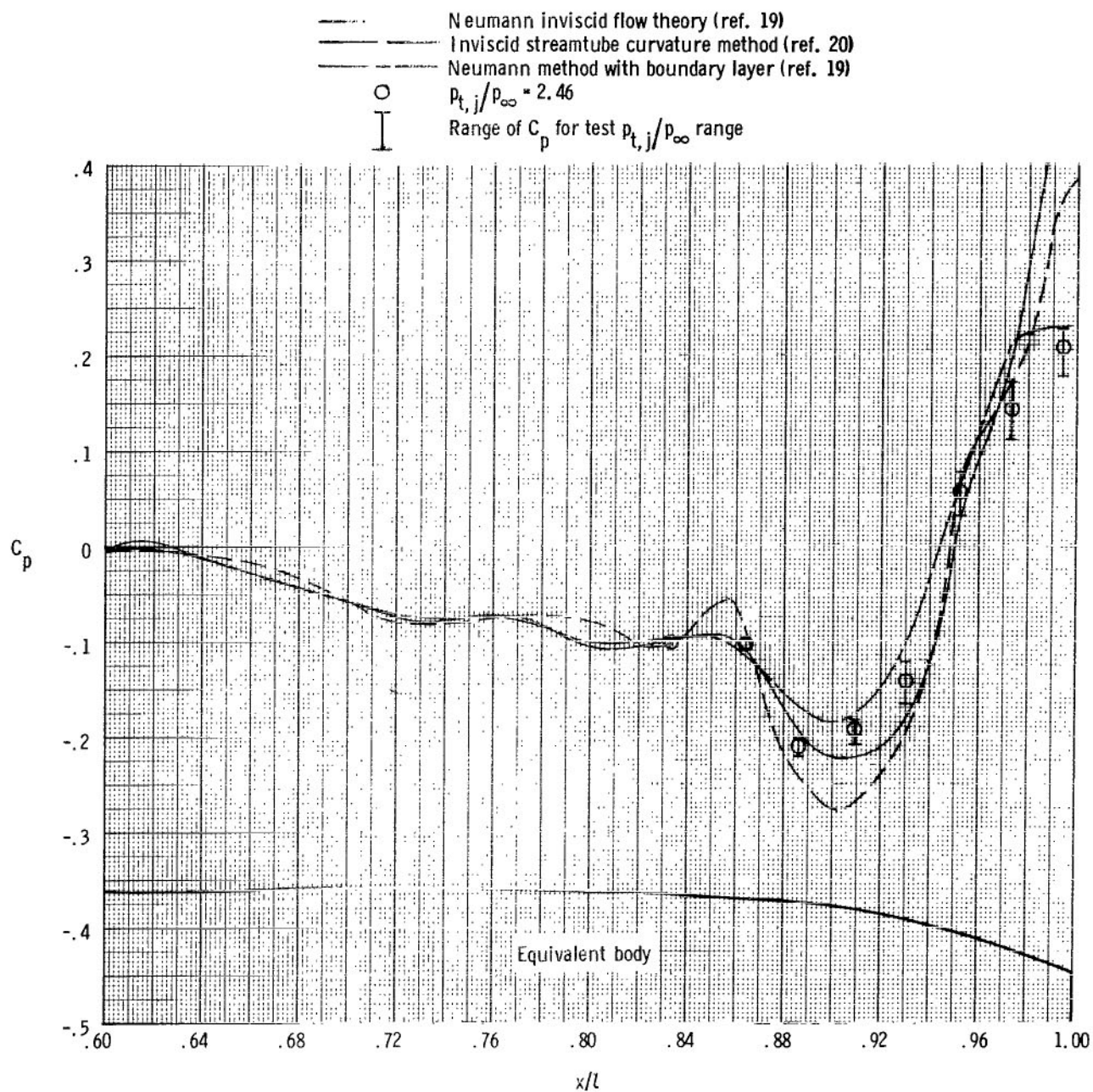
(a) M = 0.80.

Figure 39.– Comparison of theoretical and experimental static-pressure distributions on aft-tail equivalent body with dry power nozzle.

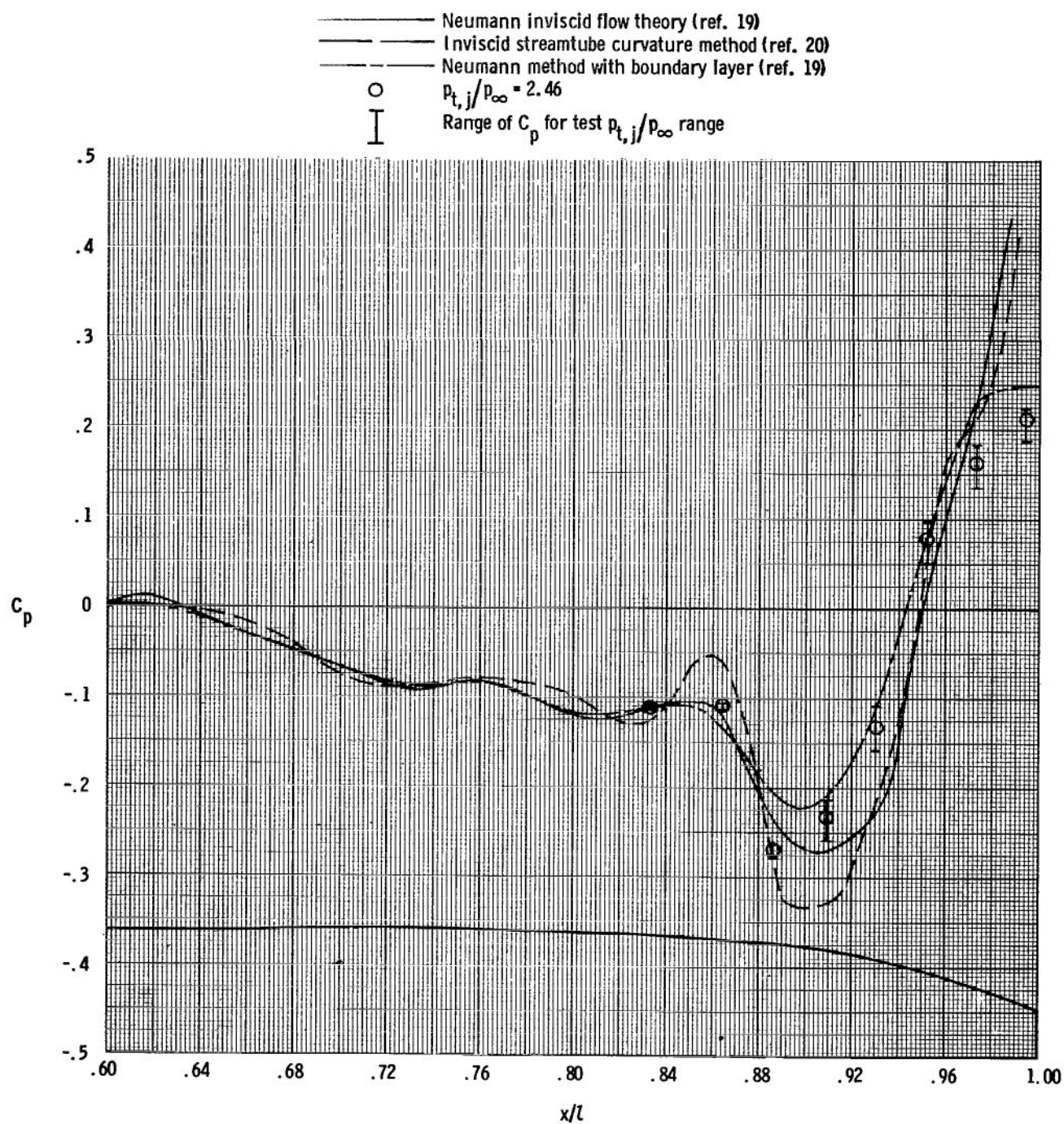(b) M = 0.90.

Figure 39.- Concluded.

(a) $M = 0.80$.

Figure 40.- Comparison of theoretical and experimental static-pressure distributions on staggered-tail equivalent body with dry power nozzle.

Neumann inviscid flow theory (ref. 19)
Inviscid streamtube curvature method (ref. 20)
Neumann method with boundary layer (ref. 19)
$\bigcirc$ $p_{t,j}/p_\infty = 2.46$
I Range of C_p for test $p_{t,j}/p_\infty$ range

(b)   M = 0.90.

Figure 40.— Concluded.

"The aeronautical and space activities of the United States shall be conducted so as to contribute . . . to the expansion of human knowledge of phenomena in the atmosphere and space. The Administration shall provide for the widest practicable and appropriate dissemination of information concerning its activities and the results thereof."
—NATIONAL AERONAUTICS AND SPACE ACT OF 1958

NASA SCIENTIFIC AND TECHNICAL PUBLICATIONS

TECHNICAL REPORTS: Scientific and technical information considered important, complete, and a lasting contribution to existing knowledge.

TECHNICAL NOTES: Information less broad in scope but nevertheless of importance as a contribution to existing knowledge.

TECHNICAL MEMORANDUMS: Information receiving limited distribution because of preliminary data, security classification, or other reasons. Also includes conference proceedings with either limited or unlimited distribution.

CONTRACTOR REPORTS: Scientific and technical information generated under a NASA contract or grant and considered an important contribution to existing knowledge.

TECHNICAL TRANSLATIONS: Information published in a foreign language considered to merit NASA distribution in English.

SPECIAL PUBLICATIONS: Information derived from or of value to NASA activities. Publications include final reports of major projects, monographs, data compilations, handbooks, sourcebooks, and special bibliographies.

TECHNOLOGY UTILIZATION PUBLICATIONS: Information on technology used by NASA that may be of particular interest in commercial and other non-aerospace applications. Publications include Tech Briefs, Technology Utilization Reports and Technology Surveys.

Details on the availability of these publications may be obtained from:

SCIENTIFIC AND TECHNICAL INFORMATION OFFICE

NATIONAL AERONAUTICS AND SPACE ADMINISTRATION
Washington, D.C. 20546